Modelization of the vitrification of sewage sludge using a basaltic matrix

Mariona Tarraqó Avmerich

Universitat de Barcelona

Departament de Mineralogia, Petrologia i Geologia Aplicada

Secció de Cristal·lografia, Mineralogia i Dipòsits Minerals

Modelization of the vitrification of sewage sludge using a basaltic matrix

Mariona Tarragó Aymerich

Tesi Doctoral

2018

UNIVERSITAT DE
BARCELONA

Modelization of the vitrification of sewage sludge using a basaltic matrix

Memòria presentada per **Mariona Tarragó Aymerich** per aspirar al títol de doctora per la Universitat de Barcelona. Aquesta tesi s'ha realitzat dins el **Programa de Doctorat de Ciències de la Terra**, sota la direcció de la **Dra. Maite Garcia Vallès**

Doctorand: Mariona Tarragó Aymerich,
Departament de Mineralogia, Petrologia i Geologia Aplicada

Director: Maria Teresa Garcia Vallès
Departament de Mineralogia, Petrologia i Geologia Aplicada

Tutor: Maria Teresa Garcia Vallès
Departament de Mineralogia, Petrologia i Geologia Aplicada

UNIVERSITAT DE
BARCELONA

Agraïments

Al llarg de l'elaboració de la tesi he tingut la sort de conèixer molta gent que han enriquit aquest llarg viatge, darrerament amb moltes matinades.

A la Dra. Maite Garcia Vallès per haver-me iniciat en la recerca (des de l'any... 2010! Que ja en fa uns quants...) que m'ha permès començar a treballar en l'estudi dels vidres de composicions molt diverses, des de fosfats fins a riolítics. Gràcies per obrir-me un món i una feina fascinants, pel cafè i sobretot per la xocolata!

Al Dr. Salvador Martínez Manent, per haver fet de director oficiós (i molt efectiu) en tots els treballs acadèmics que he dut a terme, per haver compartit amb mi els seus coneixements sobre el vidre i la ceràmica i per recordar-me constantment la importància de la curiositat.

Au Dr. Daniel Neuville, pour m'intégrer dans l'équipe Géomateriaux pendant mes séjours de recherche à l'Institut de Physique du Globe de Paris. Pour me donner accés aux équiments du labo, pour avoir partagé avec moi ses immenses connaissances sur la production et caractérisation du verre, mais surtout pour m'avoir poussé à grandir comme chercheuse. Et non, s'il y a un bout de viande brûlé, il n'est pas à moi!

Al personal dels Centres Científics i Tecnològics de la UB, per facilitar una part molt important dels experiments inclosos en aquesta tesi. Vull fer una menció especial a la Maria Barba i al Dr. Xavier Alcobé, que han resolt tots els meus dubtes i presses en el camp de la Difracció de Raigs X i l'afinament Rietveld; al personal del Taller Mecànic, Manel i Xavi, per arreglar els desastres dels motlles de les provetes de la microscòpia de calefacció; a en Joan Mendoza per la seva ajuda en les sessions de TEM i al Dr. Javier Garcia-Veigas, l'Eva i en David per les sessions de SEM.

A l'Ester Vilalta, per facilitar-me l'accés i l'aprenentatge del l'ús del microduròmetre.

Al Dr. Carles Martín-Closas i el Dr. Alberto Sáez per la seva ajuda en les gestions relacionades amb el seguiment dels estudis de doctorat i la beca. Als membres de la Comissió de Doctorat, Dr. Federico Ortí, Dr. Raimon Pallàs i Dr. José Luis Fernández Turiel, pels seus comentaris constructius.

Al s membres del Departament de Mineralogia, Petrologia i Geologia Aplicada amb qui he tingut la sort de coincidir (amb alguns des de l'època d'estudiant!).

A la Dra. Laura Bayés, per fer més lleugeres les hores de tarugos, bruts i tallats. A Mercedes Aguilar, sempre disposada a ajudar, per les seves habilitats amb el Corel i per deixar-me les eines pertinents en cas de crisi. A Jorge Macridachis, por los pequeños fines de semana de cada día y por las horas de charlas.

To Dr. Rita Cicconi, for your immense help with neverending German paperwork, and for your corrections on my phosphorus manuscript. Grazie mille! Au Dr. Anne-Marie Lejeune pour m'encourager pendant les manips, surtout les particulièrement longues.

A Hugo Esteves, por su colaboración y paciencia en los últimos meses de la tesis. Estoy segura que tu capacidad de trabajo y conocimientos te serán muy útiles en el futuro. Muito obrigado! A tots els estudiants que heu passat pel grup, Ricard, Roger, Anna, Diego, Irene, Claudia i Roger, ja sigui a fer pràctiques, treballs de fi de grau… Explicar-vos conceptes i tècniques m'ha ajudat a haver d'entendre'ls millor.

Vu que je suis une des dernières du groupe à soutenir, j'ai le droit d'appeler tout le monde Dr :). À la magnifique Dr. Rawan El Hayek, pour son soutien infaillible, les longues conversations sur tout et n'importe quoi et son intense suivi de ma thèse, même à distance. To Dr. Alexey Novikov, for ethanol and lighters, for the most cute glass levitation spheres in the world and for cinnamon doughnuts. Au Dr. Lucie Grousset, doyenne du labo, pour ton accueil chaleureux et pour avoir montré que, finalement, on s'en sort de tout. To Cedrick O'Shaughnessy, for the pleasures of the golden foamy liquid that does not taste like sweat anymore and, more important, for the long chats that go with. Au superbe groupe des Bisounours Lab (Dr. Clara Solaro-Müller, Dr. Morgane Brunet, Dr. Géraldine Zdanowicz, Dr. Diane Bonnemains, Dr. Guillaume Boudoir), pour les bo-buns, les soirées et même la Fête Nationale. À Sophie Costis pour les boudins et Jean-Jacques! À Théo Vizerie pour sa curiosité insatiable et surtout à Arnaud Nguyen, parce que derrière les nuages il y a le soleil. Je tiens aussi à remercier Irène Pesty, la première personne que j'ai croisé à l'IPGP, pour faire toujours partie des solutions aux problèmes.

A les meves companyes al Mataró B i al CN Granollers. Als membres dels Castellers de Paris, una petita molt gran colla de 6. À mes coéquipiers de Paris Aquatique, avec qui j'ai vraiment découvert les plaisirs du waterpolo Maîtres et les subtilités du verlan (oufissime!). Mention d'honneur à l'équipe filles pour le match au noir, les soirées et les matchs contre les mecs! A en Jordi Demestre, perquè sempre ens quedarà Paris.

Al Dr. Lluís Aguilar i la resta de l'equip mèdic de la Clínica Teknon, per actuar amb decisió i eficàcia quan el cos va decidir jugar-me una mala passada. Al metge que em va atendre a casa en les primeres hores de la infecció (del qual no he pogut trobar el nom), per confiar en el dubte raonable més que en la inèrcia del costum.

A l'Àngel Llobet, per ser el meu àngel de la guarda geològic (valgui la redundància). A la Mayte Martín i en Jaume, per compartir amb mi la realitat de la mineria a Catalunya.

A la família Albarracín-Calleja i ara també Jacob, sempre a punt per inserir un fragment de vacances en qualsevol moment. La família que sense ser de la mateixa sang, esdevé de la mateixa sang.

A la Rosa Fernàndez, gràcies per una amistat que ha quallat en el moment precís, per les llistes infinites de coses que ens queden per fer i perquè no em tinguis gaire en compte les voltes que faig i et faig fer pel món.

A la meva família, fins al cel. A en Martí, que és el punt de recolzament i a la Roser, per trencar fronteres que de tant llunyanes no sabíem ni que existien. A en Jordi i la Carme (els que diuen que el dia que vaig néixer es van convertir en "els pares de la Mariona"), els meus pares, per la lluita i l'amor constant en tots els fronts. Per ensenyar-me que la Terra i la terra ho són tot.

A tots vosaltres, moltíssimes gràcies!

"La més bella i decorativa de les teories no pot res contra la realitat dels actes"
Caterina Albert

Abstract

Sewage sludge is a high volume, potentially toxic waste generated during the decontamination process of wastewater. Improved solutions for waste disposal require its conversion into an end-product or at least a raw material for new applications. The chemical composition of sewage is similar to that of a basalt enriched in P and Ca, hence it may be inertized by vitrification. The experimental strategy is based on producing glasses from mixtures containing basalt, P and/or Ca to study the production of glass from sewage sludge. Selected glass compositions are then doped with toxic elements (Ba, Cr, Cu, Ni and Zn) to assess the possibility of using the SS-like glass as an inertization matrix for hazardous wastes. Part of these glasses are taken as parent compositions to obtain glass-ceramics, which may offer improved properties.

The characterization of the glasses and glass-ceramics includes the study of their composition (electron microprobe), texture (scanning and transmission electron microscopy), structure (Raman and Mössbauer spectroscopies), thermal behavior (differential thermal analysis) and crystallization (X-Ray diffraction) macroscopic properties (density, viscosity, glass transition temperature and microhardness) and the chemical resistance (leaching tests).

These analyses have shown that the solubility of each element in the basalt glass is limited by either crystallization or phase separation processes. Their large Fe contents cause a pervasive nucleation that has a large influence in the glass transition temperature, crystal growth, viscosity and microhardness and texture. It is of particular importance the delay caused by crystallization in the decrease of viscosity with increasing temperature. However, all the glasses have a viscosity low enough to be melted at temperatures about 1450 ºC . The presence of nuclei also causes the formation of a fine-grained texture of mostly diopside (together with akermanite and nepheline) in the glass-ceramics. In particular, the magnetite nuclei are the germ for the crystallization of diopside.

All the compositions seem to effectively bind the elements in the corresponding glass structure, as the leaching levels comply with the limits for them to be considered inert.

Moreover, their microhardness is in the range of commercial glasses and glass-ceramics used in the construction industry. In conclusion, sewage sludge compositions show potential to be used as raw material for the production of commercial glasses and glass-ceramics following the spirit of circular economy.

List of indexed publications contained in the thesis

Tarrago, M., Pradell, T., Bruna, P., Garcia-Valles, M., Martinez, S. Fe in P-doped basaltic melts: a Mössbauer spectroscopy study. Submitted to Materials Letters (in the second round of review after Moderate Revision)

Tarrago, M., Garcia-Valles, M., Martinez, S., Neuville, D.R. (2018). Phosphorus solubility in basaltic glass: limitations for phosphorus immobilization in glass and glass-ceramics. Journal of Environmental Management, accepted

Tarrago, M., Esteves, H., Garcia-Valles, M., Martinez, S., Neuville, D.R. (2018). Effect of Ca in P-doped basaltic glass-ceramics: Application to waste inertization. Materials Letters 220, 266-268

Tarrago, M., Garcia-Valles, M., Martinez, S. (2017). Valorization of sludge from a wastewater treatment plant by glass-ceramic production. Ceramics International 43, 930 – 937.

Table of Contents

List of Figures

List of Figures

List of Tables

CHAPTER 1 Introduction

Sometimes I think it is because we stopped darning our socks. When I was growing up, Sweden was still a country where people darned their socks. I even learned how to do it in school myself. Then suddenly one day it was over. Socks with holes in them were thrown out. No one bothered to repair them anymore. The whole society changed. "Wear it out and toss it" was the only rule that applied to everybody.

Henning Mankell, The Fifth Woman (1996)

1.1 What is sewage sludge?

Water treatment has two main beneficial effects: the first is a more efficient use of a potentially scarce, non-renewable resource; the second, that it avoids the introduction of potentially toxic elements (PTE) in the environment. For these reasons, it has been potentiated and regulated in the European Economic Community in order to standards of quality by means of Directive 91/271/EEC – modified by 98/15/EC (EEC Council, 1998, 1991). However, water treatment also generates a series of waste that pose environmental issues of their own. The residual sludge accumulated during the treatment of sewage – the mixture of water and refuse piped from human settlements such as towns, cities or industrial zones. The term sludge refers to its mixed solid-liquid nature, resulting in a muddy texture. The volumes and contamination of sewage sludge (SS) tend to increase as the processing of wastewater becomes more effective and regulations on the quality of the output water become more restrictive.

The European Union, in Directive 86/278/EEC (European Council, 1986), considers sewage sludge as the residual sludge from sewage plants generated in either domestic or urban settings and also from septic tanks or any other sewage source. An alternative definition by the United States Environmental Protection Agency (US EPA) considers sewage sludge as solids separated during the treatment of municipal wastewater (including domestic septage) (EPA, 1994). It must not be confused with the term *biosolids*, which include only the treated sewage sludge that meets US EPA requirements for land application and surface disposal (EPA, 1994).

As an output of wastewater treatment plants (WWTP), sewage sludge is a critical biologically active mixture of water, organic matter (derived from human wastes, food wastes, etc.), dead and alive microorganisms (including pathogens), and inorganic and organic toxic contaminants (e.g. metallic trace elements, PAHs) (Kacprzak et al., 2017). Although it only is a few percent of the waste volume processed on the plant, it represents 50 % of the costs.

1.2 Sewage sludge volume

The first issue related to sewage sludge waste is due to its production in large huge volumes. For instance, wastewater processing in the region of Catalonia, which has a population about 7.5 M, generates between 53,059 and 81,250 tons of SS per year. About 5-10% of these sludge are hazardous (Table 1.1).

Sewage sludge production in Catalonia (in t)			
Year	**Hazardous**	**Non hazardous**	**Total**
2016	4,549	66,124	70,673
2015	3,472	77,778	81,250
2014	3,406	63,904	67,310
2013	3,855	56,053	59,908
2012	5,612	47,447	53,059
2011	3,968	70,699	74,667

Table 1.1. Mass of sewage sludge generated yearly in Catalonia, in tons (Agència de Residus de Catalunya, 2018).

Table 1.2. presents the amount of sewage sludge produced in the European Union during the 2006-2015 period. In general, higher population higher GDP are linked to an increase in the production of sewage sludge because both factors increase water consumption. In the two years where more data are available, the amount of sludge is above 9,000 Mt. The major sewage sludge producers are, in this order, Germany, the UK, Spain, and Italy. Each of them averages more than 1,000 Mt per year.

Country/Year	2006	2007	2008	2009	2010	2011	2012	2013	2014	2015	Average per country
Belgium	128	129	140	-	176	-	157	-	-	-	146
Bulgaria	38	40	43	39	50	51	59	60	55	57	49
Czech Republic	203	216	220	207	196	218	263	260	239	210	223
Denmark	-	140	108	-	141	-	-	-	-	-	130
Germany	2,100	2,040	2,053	1,950	1,894	1,946	1,849	1,809	1,837	1,821	1,930
Estonia	28	29	22	22	19	18	22	19	-	-	22
Ireland	78	86	103	107	90	86	72	65	54	58	80
Greece	126	134	136	152	-	147	119	113	116	-	130
Spain	1,065	1,153	1,156	1,205	1,205	-	2,757	-	-	-	1,423
France	-	-	1,087	-	966	-	987	887	962	-	978
Croatia	-	-	-	30	30	31	42	32	16	18	28
Italy	-	-	-	-	1,103	-	-	-	-	-	1,103
Cyprus	-	8	8	9	7	7	7	6	6	7	7
Latvia	24	23	19	22	21	20	20	23	-	-	22
Lithuania	-	-	-	-	51	52	45	41	41	43	46
Luxembourg	15	16	13	-	10	-	8	-	-	9	12
Hungary	238	205	172	149	170	168	159	170	167	157	176
Malta	0	0	0	1	1	6	11	10	9	8	5
Netherlands	373	353	353	350	351	351	346	339	344	-	351
Austria	255	-	254	-	263	-	266	-	239	-	255
Poland	501	533	567	563	527	519	533	540	556	568	541
Portugal	-	189	-	344	-	-	339	-	-	-	291
Romania	226	100	79	121	82	114	85	173	192	210	138
Slovenia	20	21	20	27	30	27	26	27	28	29	26
Slovakia	55	55	58	59	55	59	59	57	57	56	57
Finland	149	147	144	149	143	141	141	-	-	-	145
Sweden	207	217	214	212	204	200	208	208	201	198	207
United Kingdom	1,809	1,825	1,814	1,761	1,419	-	1,137	-	-	-	1,627
Switzerland	210	-	210	210	-	-	-	195	-	-	206
Albania	-	-	-	-	-	-	-	-	91	92	91
Serbia	-	-	-	-	-	-	-	10	8	11	10
Bosnia and Herzegovina	1	1	1	1	1	1	1	1	-	-	1
Total per year	7,846	7,661	8,993	7,690	9,205	4,161	9,718	5,045	5,216	3,552	

Table 1.2. Production of sewage sludge in Europe in Mt (EEC, 2017).

1.3 Composition of sewage sludge

The composition of sewage sludge varies largely and due to several factors (Ansari and Malik, 2010; Guillemet et al., 2009). The most important are the origin of the sludge – for instance, industrial wastes generally contain higher concentrations of PTE than residential wastes; and sludge pretreatment process in the wastewater treatment plant (WWTP). The composition of the sludge depends on the upstream processes that condition the original pollution load on the treated water, and on later treatments. These treatments mainly intend to reduce the water content, the propensity to fermentation and the presence of pathogens in the sludge. The residue after processing becomes enriched in the inorganic fraction of the waste, including the potentially toxic elements. An example of the overall composition of sewage sludge in Austria is presented in Table 1.3.

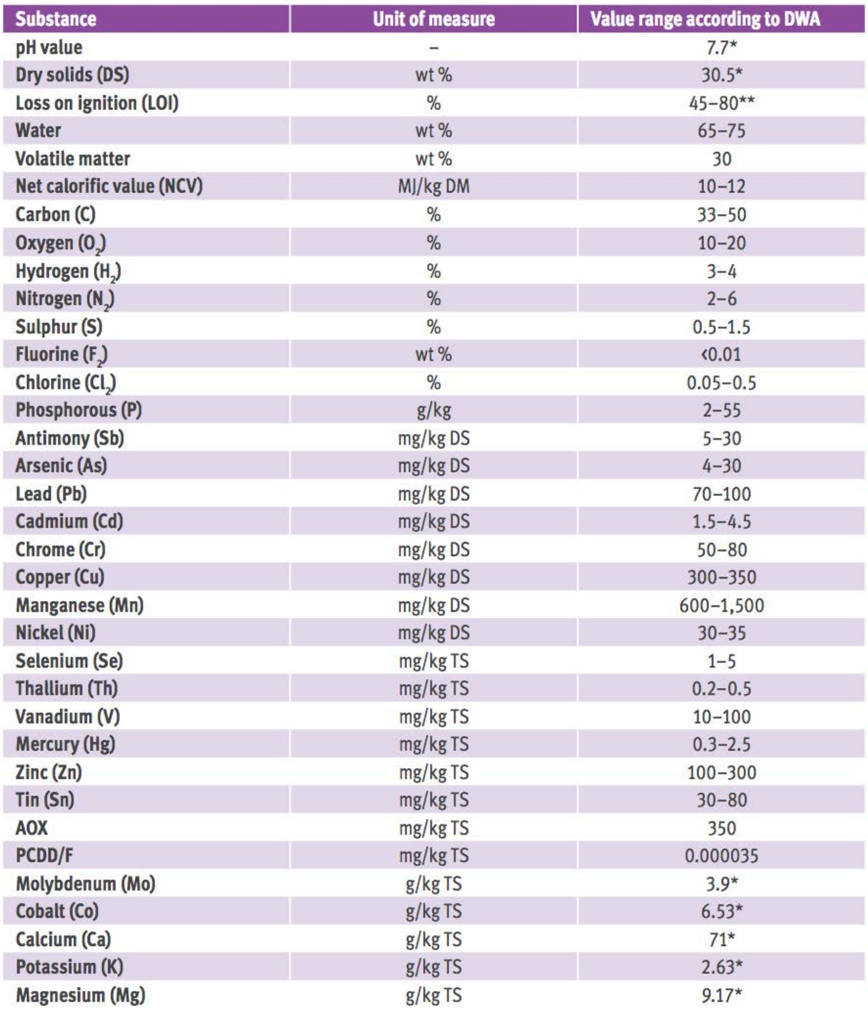

Substance	Unit of measure	Value range according to DWA
pH value	–	7.7*
Dry solids (DS)	wt %	30.5*
Loss on ignition (LOI)	%	45–80**
Water	wt %	65–75
Volatile matter	wt %	30
Net calorific value (NCV)	MJ/kg DM	10–12
Carbon (C)	%	33–50
Oxygen (O_2)	%	10–20
Hydrogen (H_2)	%	3–4
Nitrogen (N_2)	%	2–6
Sulphur (S)	%	0.5–1.5
Fluorine (F_2)	wt %	<0.01
Chlorine (Cl_2)	%	0.05–0.5
Phosphorous (P)	g/kg	2–55
Antimony (Sb)	mg/kg DS	5–30
Arsenic (As)	mg/kg DS	4–30
Lead (Pb)	mg/kg DS	70–100
Cadmium (Cd)	mg/kg DS	1.5–4.5
Chrome (Cr)	mg/kg DS	50–80
Copper (Cu)	mg/kg DS	300–350
Manganese (Mn)	mg/kg DS	600–1,500
Nickel (Ni)	mg/kg DS	30–35
Selenium (Se)	mg/kg TS	1–5
Thallium (Th)	mg/kg TS	0.2–0.5
Vanadium (V)	mg/kg TS	10–100
Mercury (Hg)	mg/kg TS	0.3–2.5
Zinc (Zn)	mg/kg TS	100–300
Tin (Sn)	mg/kg TS	30–80
AOX	mg/kg TS	350
PCDD/F	mg/kg TS	0.000035
Molybdenum (Mo)	g/kg TS	3.9*
Cobalt (Co)	g/kg TS	6.53*
Calcium (Ca)	g/kg TS	71*
Potassium (K)	g/kg TS	2.63*
Magnesium (Mg)	g/kg TS	9.17*

Table 1.3. Composition of bulk sewage sludge in Austria (Oliva et al., 2009).

Sewage sludge has a complex chemical composition that arises from the mixture of inorganic and organic substances together with living microorganisms. Unprocessed sewage sludge contains large amounts of water, even up to 90 wt% (Cieślik et al., 2015). Raw SS contains about 50-70% of organic matter, 30-50% mineral components (including up to 4% organic carbon), 3.4-4.0% N and 0.5-2.5% P together with other nutrients and micronutrients (Fytili and Zabaniotou, 2008). The presence several types of contaminants is significant, including but not restricted to: heavy metals, polycyclic aromatic hydrocarbons (PAHs), polychlorinated biphenyls (PCBs), adsorbable organohalogens (AOX), pesticides, surfactants, hormones, pharmaceuticals, nanoparticles, etc. (Kacprzak et al., 2017).

The scientific literature contains a large amount of compositional measurements of sewage sludge (Albiach et al., 2001; Barbieri et al., 2000; Bernardo and Dal Maschio, 2011; Borowski et al., 2014; Cao et al., 2014; Celis et al., 2008; Dominguez et al., 2006; Domínguez et al., 2008; Ferreiro-Domínguez et al., 2014; Folgueras et al., 2003; Font et al., 2001; Fonts et al., 2012; Forsberg and Ledin, 2006; Garcia-Valles et al., 2013; Gong et al., 2014; Hossain et al., 2009; Ischia et al., 2011; Kikuchi, 1998; Lin et al., 2008; Majima et al., 1978; Menéndez et al., 2005; Metcalf and Eddy, 1991; Monteiro et al., 2008; Montero et al., 2009; Park et al., 2003; Pavšič et al., 2014; Pokorna et al., 2009; Roig et al., 2012; Sánchez et al., 2009; Singh and Agrawal, 2008; Tian et al., 2011; Zhou et al., 2013) that have been combined with previously unpublished compositions reported in chapter 4 to determine their variation. Table 1.4 summarizes the maximum, average, and minimum concentrations of the major inorganic components of sewage sludge. They have been used as a guideline for the choice of the basalt, and in the experimental design to establish the first tentative ranges of P and Ca doping. The main elements have a major influence on the macroscopic properties and the production conditions of any derived product.

Oxide / wt%	**Maximum**	**Average**	**Minimum**
SiO_2	66.24	28.54	5.12
Al_2O_3	30.72	11.61	2.17
MgO	10.68	2.49	0.17
CaO	52.87	16.57	0.16
K_2O	7.29	2.16	0.00
Na_2O	3.00	0.97	0.00
TiO_2	1.45	0.72	0.00
Fe_2O_3	56.50	14.50	0.81
P_2O_5	32.98	13.29	0.00
MnO	3.29	0.16	0.00
Total SO_3	13.34	1.70	0.00
Cl (soluble ppm)	2664.43	331.84	0.00
LOI	37.24	13.23	0.00
Water content	90.96	25.92	0.00
Mn_3O_4	0.19	0.05	0.00

Table 1.4 Summary of the range of concentration of major elements in sewage sludge.

The potentially toxic elements in sewage sludge are summarized in Table 1.5 (Achiba et al., 2010; Angelidis and Gibbs, 1989; Borowski et al., 2014; Dominguez et al., 2006; Guillemet et al., 2009; Gupta and Garg, 2008; He et al., 2009; Hossain et al., 2009; Inguanzo et al., 2002; Li et al., 2012; Nogueira et al., 2010; Sano et al., 2012; Seleiman et al., 2012; Sigua et al., 2005; Tao et al., 2012; Tervahauta et al., 2014; Tian et al., 2011; Wang et al., 2008). The additional data of the two columns on the right – provided in review papers during the 1990s – is consistent with the mentioned values at least in the order of magnitude, hence the heavy metal contents of sewage sludge are definitely a long-term problem (Hsiau and Lo, 1998; Metcalf and Eddy, 1991).

ppm	Maximum	Average	Median	Minimum	Range	Median
Ag	16	9	9	4		
Al	6	3	4	1		
As	300	27	4	0		
B	34	20	20	6	1.1–230	10
Ba	330	247	280	130		
Be	1	1	1	0		
Cd	82	8	3	0	1–3.410	10
Co	430	56	23	3	11.3–2490	20
Cr	1268	263	81	0	10–990,000	500
Cr (VI)	427	151	289	7		
Cu	12701	537	170	0	84–17,000	800
Fe	43826	6709	194	1	1000–154,000	17000
Hg	23	3	1	1	0.6–56	6
La	21	17	17	13		
Mn	488	199	175	0	32–9870	260
Mo	22	9	10	0	0.1–214	4
Ni	1025	172	41	0	2–5300	80
Pb	3519	185	83	0	13–26,000	500
Sb	5	4	5	3		
Se	4	3	4	2	1.7–17.2	5
Sn	130	78	78	36	2.6–329	14
Sr	150	107	107	73		
Va	31	21	21	16		
Y	6	4	5	2		
Zn	31166	1501	403	0	101–49,000	1700
Zr	110	79	85	43		

Table 1.5. Concentrations of potentially toxic elements in sewage sludge.

1.4 Disposal solutions

Waste disposal includes the series of actions intended to either ideally stop the waste from being considered as such or at least minimizing its volume and hazards. The treatment of sewage sludge is considered one of the greatest challenges in wastewater processing (Fytili and Zabaniotou, 2008), as it often contains environmentally toxic elements and the processing costs are expensive, between 150 and 800 €/tons of dry sludge (Figure 1.1). In the best case scenario that all these sludge could be used on land, it would represent an expense of several million euro per year.

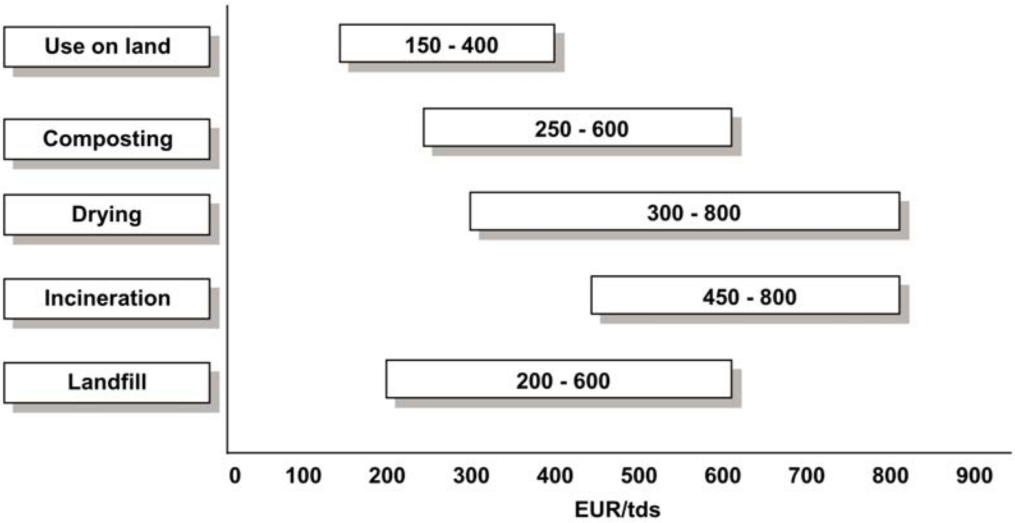

Figure 1.1. Sludge treatment and disposal costs (€/tds) (Hall, 2014).

Dealing with the disposal of sewage sludge in a sustainable way means meeting the requirements of efficient recycling of resources without creating an influx of potentially toxic substances to humans or the environment (Davis, 1996). The European Union promotes the compliance of waste disposal techniques with the principles of a circular design of the economy where most products can be reused as raw materials at the end of their life cycle (Figure 1.2 (European Comission, 2014)). This framework change requires modifying all the value chains, from product design to new business and market models to find new ways of turning waste into a resource together with new modes of consumer behavior.

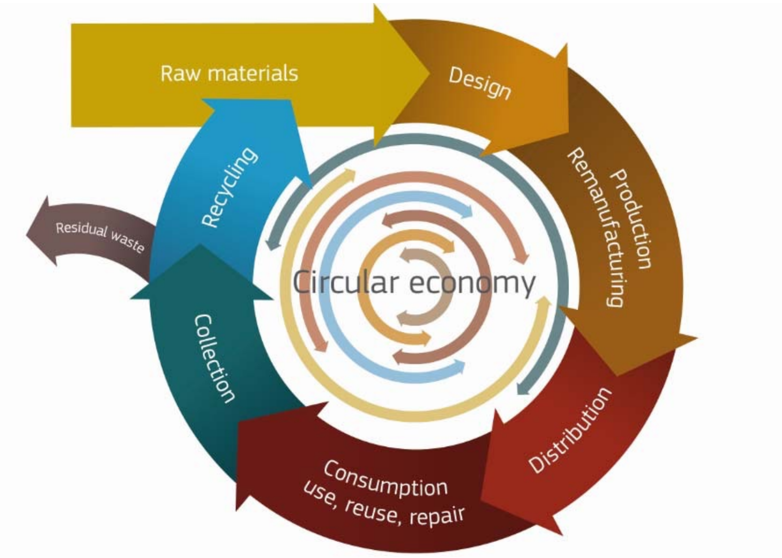

Figure 1.2.Strategies for a circular economy (European Comission, 2014)

Until 1998, most sludge was disposed of at the ocean or used as a fertilizer (Odegaard et al., 2002). However, Directive 98/15/EC forbid the disposal of sewage sludge in the seawaters (EEC Council, 1998). Hence, new solutions had to be promoted or implemented. In 2008, the handling of sewage sludge was done by the following methods: landfilling (40%), agriculture (37%), incineration (11%), and other various applications (12%) such as forestry, silviculture, land reclamation, etc. (Fytili and Zabaniotou, 2008).

Sludge contains compounds of agricultural value such as organic matter, phosphorus, nitrogen and potassium together with pollutants – potentially toxic elements, organic pollutants and pathogens (Cieślik et al., 2015; Kacprzak et al., 2017; Oliva et al., 2009). In consequence, land spreading is limited to certain amounts of toxics – considering both the pollutants in the sludge and their concentration in the application site – in order to prevent soil contamination and risks for the consumer's health. This application is regulated by Directive 86/278/EEC (European Council, 1986), although some countries enforce more restrictive limits. A summary of the allowed concentrations according to the Directive, the regulations of certain countries, and USA law is presented in Table 1.6. In general, the European regulation is more restrictive than the American. Moreover, it is clear that the maximum concentrations of the cited elements in sewage sludge (Table 1.5) exceed in all cases the conditions for their applications in agriculture. In the cases of the countries with more restrictive legislations, the average concentrations may also exceed the permitted values.

Metal	86/278/EEC range	Sweden	Netherlands	France	DIN38414S4	USA
Cd	20-40	2	1.25	20	40	85
Cr	-	100	75	1000	500	3000
Cu	1000-1750	600	75	1000	2000	4300
Hg	16-25	2.5	0.75	10	100	57
Ni	300-400	50	30	200	400	420
Pb	750-1200	100	100	800	500	840
Zn	2500-4000	800	300	3000	4000	7500

Table 1.6. Maximum limits for the application of sewage sludge on the land in the EU, USA and selected countries legislation in mg/kg dry weight. Modified from (Inglezakis et al., 2016)

Landfilling is a method of waste disposal that consists in the accumulation of the residue in an isolated location to prevent it from reaching the environment. It is considered by far the less desirable technique because landfills require the establishment of barriers to confine the waste, a large volume of space, long duration, and they are not always perceived as a desirable addition to the communities that host them. In the EU it is regulated by Directive 1999/31/EC (Council Directive, 1999), which establishes three kinds of landfills: for hazardous waste, for non-hazardous waste and for inert waste. The landfilling of sewage sludge poses two specific issues: the presence of large amounts of water in the sludge increases the volume unless it undergoes a drying process, and the formation of leachates promotes the input of toxic metals and other pollutants the water cycle.

Incineration is a partial disposal technique in the sense that it still generates an output waste in the form of ashes representing about the 30% of the initial volume of the solid fraction (Fytili and Zabaniotou, 2008). However, the increasing limitations on land application and the forbidding altogether of ocean disposal have risen the interest in this method. Its advantages include a large volume reduction (down to 10% of the dewatered sludge), the thermal destruction of toxic organic compounds, recovering some energy in the form of heat, and minimizing odors. The main disadvantages are the generation of gas and gaseous emissions, together with the generation of bottom and fly ash representing about 30-50% of the volume of the sludge. Another issue with incineration is the permanence of dioxins even after a high temperature treatment at about 900 ºC (Mininni et al., 2004). Incineration is the disposal method of choice for about the 10-25% of the sludge produced in several European countries (Lundin et al., 2004).

In the search of an optimal strategy that complies with the principles of circular disposal, several authors have proposed different treatments for sewage sludge. The study of these approaches is out of the scope of this thesis. A detailed review based on End-of-waste criteria, Life Cycle Assessment and circular economy may be found in (Cieślik et al., 2015); it is summarized in Figure 1.3. The authors remark the importance of sewage sludge as a valuable source of matter and energy together with the potential risks posed by the application of those strategies.

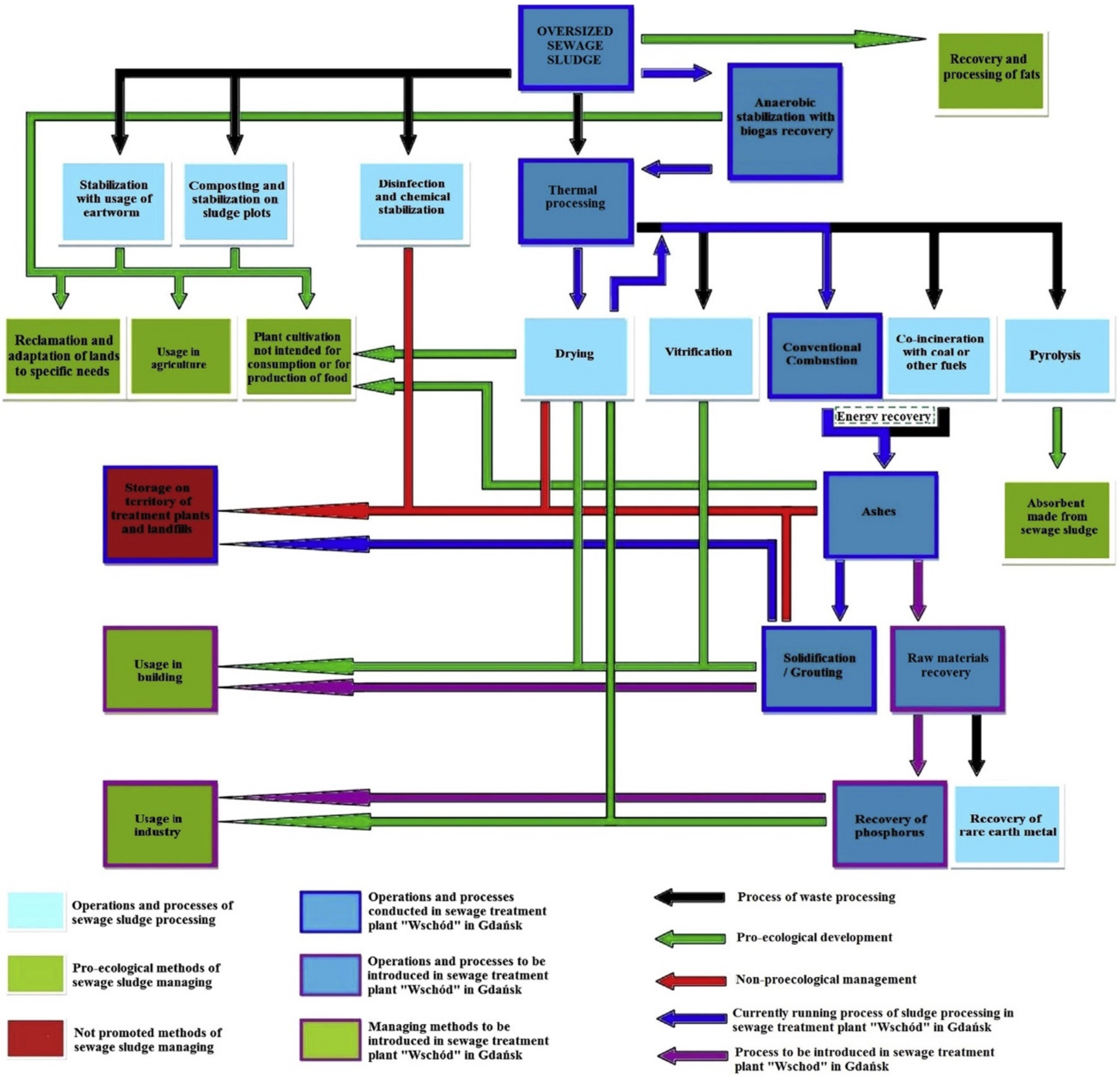

Figure 1.3. Summary of disposal techniques for sewage sludge (Cieślik et al., 2015).

1.5 Description of the elements of interest

This section presents the elements of interest that will be added to the glassy matrix with the aim of explaining the interest of their isolation from the hydrological cycle. They have been chosen due to either their effects on the environment and risks to human health or due to their role in glass formation.

1.1.1 Phosphorus

Environmental contamination with P-bearing materials may happen by the excess application of fertilizers – either industry-produced or the aforementioned sewage sludge. When the amount of P is higher than the necessities of the crops, phosphates are eroded by surface runoff. This creates large inputs of P in aquatic media that cause eutrophication, where the excess P results in an algal bloom, causing oxygen depletion and the formation of a hypoxic or anoxic environment (Correll, 1998; Werner, 2012). The effect of P in the environment and in glass formation is further detailed in the introduction of Chapter 4.

1.1.2 Calcium

The abundance of Ca in sewage sludge is due to its use as a precipitant in wastewater processing. As its abundance in the environment is naturally high, it is not actually a concern in environmental contamination. However, it has a large influence in glass formation. Ca usually plays a network-modifying role, decreasing the connectivity of the silicate network and commonly its viscosity. In some cases it may also act as an intermediate element (De Sousa Meneses et al., 2006). It is also engaged in the crystallization processes of the main silicate minerals such as pyroxene, plagioclase, etc.

1.1.3 Barium

Ba is used in the production of a wide range of lubricants, ceramics, and in alloy manufacture. Its high specific gravity makes it suitable as a loader for paper, soap, rubber, linoleum, and drilling fluids. Ba is also used as an extinguisher for Ra, U and Pu fires. Accumulation on soil may also result from human activity such as the disposal of fly ash and primary and secondary sludge in a landfill, from which it may easily reach the water cycle. The symptoms of Ba intoxication include acute gastroenteritis, loss of deep reflexes and certain degrees of paralysis, hypopotassemia, an increase in the incidence of hypertension, and baritosis (World Health’s Organization, 1990).

1.1.4 Chromium

Chromium is used in many industrial process: in the hardening of steel, in the production of stainless steel, in the production of alloys, in leather tanning, in industrial catalysis, as a pigment (bright green, yellow, red and orange), and in chrome plating; the wastewaters from these industries contain large concentrations of Cr. It is an oligoelement that has a role in glucose metabolism in trace amounts - about 50-200 µg/day of Cr [III] (World Health's Organization, 1988). However, the exposure to chromium compounds – specially chromates and Cr(VI) – has been linked to several health issues (Costa and Klein, 2006; Dayan and Paine, 2001). Other respiratory conditions such as rhinitis, bronchospasm, pneumonia, impaired respiratory dynamics, and bronchial asthma have been attributed to the exposure to chromium compounds. Cr(VI) is a confirmed carcinogenic; chromates are linked to lung cancer (Eastmond et al., 2008).

1.1.5 Copper

Copper contamination of the hydrological cycle may come from several extractive and industrial settings such as tailings and overburdens from copper mining and sewage sludge, together with smelters, iron foundries, power stations and incinerators. Moreover, it is used in cooking utensils and piping systems; fertilizers, bactericides, fungicides, algaecides, and antifouling paints. In the industry, also it has applications as an activator in froth flotation of sulfide ores, production of wood preservatives, electroplating, azo-dye manufacture, as a mordant for textile dyes, in petroleum refining and the manufacture of copper compounds. Although Cu has some essential biological roles – including the formation of catalysts – Cu poisoning causes a variety of effects in humans, such as metallic taste, epigastric pain, headache, nausea, dizziness, vomiting, diarrhea, tachycardia, respiratory difficulty, hemolytic anemia, hematuria, massive gastrointestinal bleeding, liver and kidney failure, and death (World Health's Organization, 1998).

1.1.6 Nickel

Nickel is applied to the production of stainless steels and alloys resistant to both corrosion and temperature which are then used in vehicles, processing machinery, armaments, tools, electrical equipment, household appliances and coinage. Ni compounds may also be used as catalysts, pigments and in batteries. The primary sources of nickel emissions into the ambient air are the combustion of coal and oil for heat or power generation, the incineration of waste and sewage sludge, nickel mining and primary production, steel manufacture, electroplating and other sources such as the fabrication of cement. The main species in polluted air are nickel sulfate, oxides and sulfides. Acute affectations after exposure to nickel include frontal headache, vertigo, nausea, vomiting, insomnia and irritability, which may turn into pneumonia-like symptoms. The pulmonary lesions include hemorrhage, edema, and cellular derangement. The liver, kidneys, adrenal glands, spleen, and brain may also be directly affected. Chronic effects such as rhinitis, sinusitis, nasal septal perforations, asthma, pulmonary changes with fibrosis, and nasal dysplasia have been reported after exposure to nickel in the workplace – in nickel refinery or nickel plating workers (World Health's Organization, 1991). Moreover, nickel is a confirmed carcinogenic (Lu et al., 2005).

1.1.7 Zinc

Zn may reach the water cycle from sources including mining, zinc production facilities, iron and steel production, corrosion of galvanized structures, coal and fuel combustion, waste disposal and incineration, and the use of zinc-containing fertilizers and pesticides. The symptoms of zinc poisoning include gastrointestinal distress, nausea and diarrhea after short-term exposure; continued poisoning is fatal. A disproportionate intake of Zn may imbalance Cu concentrations in the body. Pharmacological dosing of Zn may induce leukopenia (a deficiency of leukocytes in blood) and/or hypochromic microcytic anemia to decreases in serum high-density lipoprotein concentrations (World Health's Organization, 2001).

1.6 Vitrification

Vitrification is an alternative disposal technique that converts the waste into a glass, a stable material capable of isolating elements in its structure. Moreover, the waste becomes a raw material, hence giving two environmental advantages: reducing both the landfilling problem and the volumes of raw materials that have to be mined for the production of glass. Another advantage of vitrification is that the temperatures are higher than those used in incineration, hence permitting the complete elimination of dioxins (Mininni et al., 2004). However, vitrification is cost intensive because it requires a lot of energy compared to most methods. In order to comply with the spirit of the 7th LIFE Program (from the French: L'Instrument Financier pour l'Environnement; the Financial Instrument for the Environment), which proposes improving the economic efficiency of resource management, the environmental footprint of goods has to be reduced all over their cycle. Some of the priorities in waste management lie precisely in converting waste into raw materials, prioritizing prevention, reuse and recycling; as well as progressively abandoning expensive and hazardous techniques such as landfilling.

Urban sewage sludge (USS) has a chemical composition similar to that of basalt (Perez et al., 1996) apart from an excess of P_2O_5 and CaO and a deficit of SiO_2 and MgO. Some typical minerals of basalts, such as pyroxene and spinel, may host PTE as those contained in USS and industrial sludge in their lattices. Hence, once the composition of the sludge is known it may be modified to obtain a glass with the bulk composition of a basalt, where pyroxene and spinel-like phases are stable. Ideally, the best approach would be to add wastes rich in these components; for instance, foundry sands to supply SiO_2. Furthermore, once the material has an appropriate composition, the application of a thermal process may provide a glass-ceramic material with improved inertization capacity. Rincon, in his review of vitrification and sintering applied to industrial wastes points out that the use of "secondary raw materials" (reused wastes) could realistically be applied to the building industry and public works, since they can absorb the large amounts of these wastes generated daily (Rincon, 2016).

1.7 Objectives

This project starts from the hypothesis of the possibility of inertizing sewage sludge by means of vitrification, and the potential of such glasses to be used as a vitrification matrix for the isolation of hazardous wastes bearing heavy metals such as galvanic sludge. The basis for this approach is the rough similarity between the chemical composition of sewage sludge and those of basic rocks that contain minerals that may incorporate the toxic metals in their structure. In this study a basalt is doped with P and Ca – first separately and then together – to simulate the composition of sewage sludge, obtain glasses and characterize their properties, as both elements are much more abundant in sewage sludge than in basalts. It is intended to find which matrix compositions would have appropriate conditions to be made into glass, to gain some insight on their production and determine their macroscopic properties. A precise determination of the effect of the variation of their abundance is necessary to obtain a more consistent framework for the vitrification process. Afterwards, a P-Ca-basalt glass will be chosen to study the incorporation of minor heavy metals (Ba, Cr, Cu, Ni, Zn).

The composition ranges of this study have been established bearing in mind the chemical analyses of sewage sludge available in the literature. This modified basaltic glass may become a form of environmental remediation and valorization of silicate-rich sludges that otherwise would have to be kept in huge expensive landfills. The basalt (which represents the silicate-rich sludge) used as inertization matrix is a cheap and readily available raw material which has a controlled and homogeneous chemical composition. This composition is then modified by adding the selected toxic element in order to evaluate its effect on the properties of glasses and glass-forming melts during and after production.

The objectives of the thesis can be summarized as follows:

- Establish the possibility of inertizing sewage sludge by vitrification and using these glasses as inertization matrix for additional toxic wastes that may enter the glass structure.

- Analyze the influence of the variation of the chemical composition in glass production and glass-ceramics processing, characterize the solubility of each element in the basalt-based glass.
- Study the influence of the compositional variability in the macroscopic properties (density, microhardness, viscosity) of the glasses and specially in their resistance to leaching.
- Evaluate the potential applications of the obtained materials.

1.8 Manuscript structure

The manuscript is divided in eleven chapters.

The first chapter is an introduction to the issue of sewage sludge: definition, origin, composition, volume of sludge produced in the European Union and current disposal solutions. The second chapter focuses on the state of the art on glass formation and structure and in the inertization of sewage sludge and related products by vitrification. This is divided in a general introduction about glass and glass-ceramics and continues explaining recent case studies of waste vitrification. The third chapter is a general Materials and Methods section that summarizes the ensemble of raw materials, equipment and analytical techniques used along the manuscript.

The fourth chapter explains the addition of various amounts of P to the chosen basalt. The addition of P has many implications, among which an unmixing process and the formation of a glass-ceramic from the quenched product. This crystallization improves the resistance of the material. The chapter is presented in form of a Research Article that has been accepted for publication at the Journal of Environmental Management. The fifth chapter deals with the effect of P on the Fe environment and redox state; as well as their effect on the production of the glasses. This chapter is presented in the form of an article under review at Materials Letters. The sixth chapter explains the addition of various amounts of Ca to the chosen basalt and the application of a glass-ceramic process to a selected composition. The addition of Ca has two main effects: controlling both the crystallization of either pyroxene or melilite and the nucleation by increasing the liquidus temperature. The glass-ceramics processing improves the mechanical properties of the material

The seventh chapter includes the definition of the composition of several proposed matrices containing 4 wt% P_2O_5 and various amounts of CaO. Some of the results of this chapter have been published as a paper in Materials Letters. The eight chapter includes the cases of vitrification of potentially toxic elements representing industrial wastes mixed with the model of sewage sludge inertization matrix. The glasses are separately doped with one of the following elements: Ba, Cr, Cu, Ni, Zn. The effect of each element in the glass-forming ability, thermal behavior, crystallization, viscosity, microhardness and leaching are assessed. The chapter also includes the application of the glass-ceramics process to Cr-doped and Ni-doped glasses. The ninth chapter explains the application of vitrification and glass-ceramic process to sewage sludge obtained at a WWTP in El-Sadat, Egypt. It has been published as a Research Paper in Ceramics International. The tenth chapter is a general discussion of the presented results. The eleventh chapter summarizes the conclusions of the thesis.

It must be noted that the chapters corresponding to research papers (either submitted, accepted or published) are presented in the same form as they were submitted.

CHAPTER 2 State of the art

Among the many thousands of things that I have never been able to understand, one in particular stands out. That is the question of who was the first person who stood by a pile of sand and said, "You know, I bet if we took some of this and mixed it with a little potash and heated it, we could make a material that would be solid and yet transparent. We could call it glass." Call me obtuse, but you could stand me on a beach till the end of time and never would it occur to me to try to make it into windows.

Bill Bryson, Notes from a small island

2.1 Generalities on glass

2.1.1 Historical context

Glass is a common product of both natural and industrial processes. It may be found in nature in the form of obsidian (volcanic glass), tektite (resulting of a meteoritic impact) or fulgurite (due to lightning strikes in siliceous sand). Obsidian was even used by prehistoric humans to make tools. Moreover, the glasses of the system CaO-MgO-Al_2O_3-SiO_2 are the most common probes of magmatic melts.

Glass is also one of the earliest man-made materials. Its production started during the Bronze Age – about 4500 years ago – in the Middle East; probably in several sites at the same time (Mysen and Richet, 2005). The earlier glasses all had similar compositions – containing SiO_2, Na_2O, Al_2O_3, K_2O, CaO, MgO, Fe_2O_3 and PbO. It must be noted that the impossibility of accurately controlling the composition of the raw materials and the redox conditions in the kilns made the production of glass tricky and scarcely reproducible. Alongside history, glass became increasingly used for ornaments, as a container – for expensive unguents and perfumes – jewelry (as enamel), in glazes… as well as consolidating its artistic possibilities. However, its composition remained essentially that of a soda-lime silicate (Le Losq et al., 2018), sometimes containing potassium.

The first systematic study of glass composition was made by Otto Schott by the end of the 19th century. The massive production of glass was strongly reinforced by the invention of the float process by Alastair Pilkington in the 1950's. This method provided a perfectly flat, large glass surface; reducing the costs, increasing the efficiency of the glass production process and thus the availability as a construction material (Barker, 1977). The system CaO-Na_2O-SiO_2 remains the base of the most usual industrial melt composition, float window glass.

Nowadays, glasses have several applications such as cookware – for instance the borosilicate Pyrex®, optics, automobile industry, as a building material, for biomedical applications such as Bioglass®, in dentistry, etc. Moreover, the compositional range has far overreached the traditional oxide glasses. Indeed, metallic and chalcogenide glasses are of increasing importance due to their unique mechanical and optical properties.

2.1.2 Definition of glass

Glass is an amorphous solid completely lacking in long range, periodic atomic structure, and exhibiting a region of glass transformation behavior (Shelby, 2005). As glass is generally obtained by quenching of a supercooled liquid, it may also be considered a nonequilibrium, non-crystalline state of matter that exhibits a glass transition, with a structure similar to that of their parent supercooled liquids (SCL) (Zanotto and Mauro, 2017). Both definitions concur in highlighting the importance of the glass transition as a necessary property of the glass-forming melts. The exact relationship between the structure of a glass and that of its parent liquid is still a controversial matter because the structure of the melts is susceptible to change depending on temperature (Mysen and Richet, 2005).

2.1.3 Glass formation

The process of glass formation can be explained from the variation of enthalpy during the cooling process of a melt (Figure 2.1). A melt in thermodynamic equilibrium does not crystallize as long as the environmental conditions do not vary; it flows at a rate depending on its viscosity and it adapts to the shape of the container. A decrease in temperature increases viscosity. Further changes depend on the cooling rate. If the cooling is slow, the melt forms a crystalline solid, which is thermodynamically stable. Some macroscopic properties, such as enthalpy, change abruptly due to the rearrangement of the disordered liquid into the infinitely periodical crystals. During the cooling of a melt, enthalpy decreases continuously until the melting point is reached. As crystallization happens, a discontinuity in the cooling curve marks the step down in enthalpy due to the much lower energy of the crystals. From this point on, the crystalline phase is stable.

If the cooling is too fast to allow for crystal formation, the melting point can be surpassed without crystallization. This transition does not cause any sudden change in the enthalpy vs temperature curve. The supercooled liquid is less stable than the crystalline phase, and it is in a thermodynamic state of metastable equilibrium, hence any small perturbation of the system may cause crystallization. The heat of the reaction rises the temperature back to the melting point and the reaction continues following the normal crystallization path.

If supercooling progresses without crystallizing the enthalpy of the melt goes on decreasing at the same rate until at a certain temperature an elbow appears on the curve together with a remarkable increase in viscosity. This temperature interval is known as the glass transition range and marks the border between the supercooled liquid and the glass. Below this range the enthalpy of the glass decreases more gradually, with a slope similar to that of the crystal. The breadth of the transition range depends on the cooling rate. In this zone, the material is in non-equilibrium conditions and thermodynamically unstable. In summary, above Tg the material is properly referred to as melt, and it is deformable, whereas below Tg the glasses are characterized for being rigid and fragile.

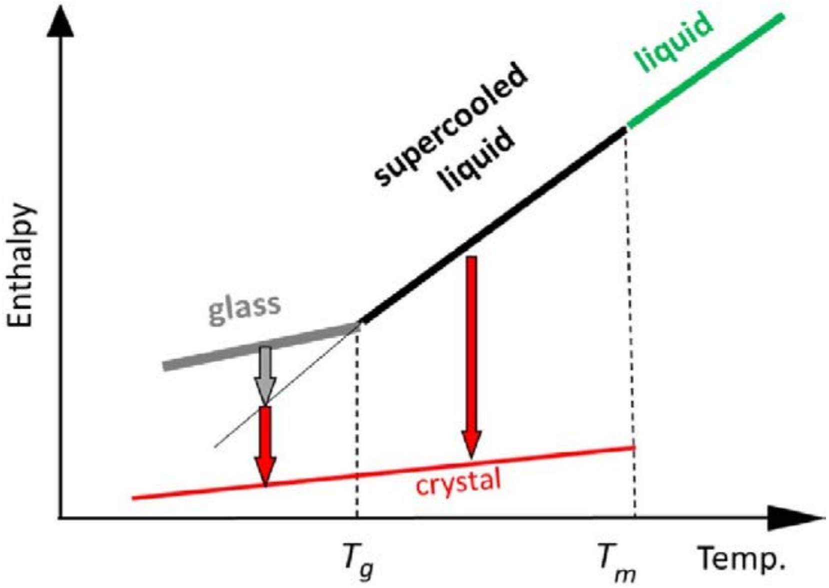

Figure 2.1 Schematic plot showing enthalpy as a function of temperature and the four states: the stable liquid, the supercooled liquid (SCL), the glass (G) and the crystal (C). Tm stands for melting temperature (liquidus) and Tg for glass transition temperature (Zanotto and Mauro, 2017).

2.1.4 Glass transition

The nature of the glass transition may possibly be the major unsolved issue in solid state physics. Its effects on the structure of the melt during vitrification are not precisely understood. Glasses are only ordered at the interatomic scale; thus, they are characterized by an excess energy in comparison to the other states of matter. This results in a change to the liquid or the solid state below their liquidus temperature. The glass transition is the phenomenon permitting the transition from high viscosity supercooled liquid to solid before crystallization occurs. Tg is marked by the continuity of the 1st order thermodynamic properties (volume, enthalpy, viscosity, etc.) and a step in the 2nd order thermodynamic properties (thermal expansion coefficient, heat capacity, etc.).

2.2 Classification of cations according to their role in glass

2.2.5 Network forming cations

Some cations such as Si^{4+}, P^{5+} or B^{3+} can form a glassy network by themselves as they can establish covalent bonds exclusively with oxygen and thus create polyhedra of low coordination numbers (3 or 4) linked by their vertices. They receive the name of network-forming cations or network formers, and are characterized by small ionic radii and high charge. The oxygen linking two different tetrahedra receive the name of bridging oxgen (BO) . In a similar way as in mineral structures, Al^{3+} (and also Fe^{3+}) can be network formers when they are in tetrahedral coordination, although their presence causes a deficit of charge in the structure (Mysen and Richet, 2005).

2.2.6 Network modifiers and charge compensators.

Network modifying cations are large ionic radii and low charge (usually alkalies and alkaline-earth cations) that form ionic bonds with oxygen. These bonds are much weaker than the covalent bonds of the network formers and cause ruptures of the network, creating non-bridging oxygens (as opposed to bridging oxygens, that link two tetrahedra). Their coordination polyhedra are large, between 6 and 12 (Mysen and Richet, 2005).

2.2.7 Intermediate cations

Cations such as Fe^{3+} or Al^{3+} form unbalanced units (FeO_4^- and AlO_4^- respectively). Depending on the bulk glass composition, they will play the role of network formers if another cation balances this excess charge and the role of network modifiers in the opposite case (Mysen and Richet, 2005).

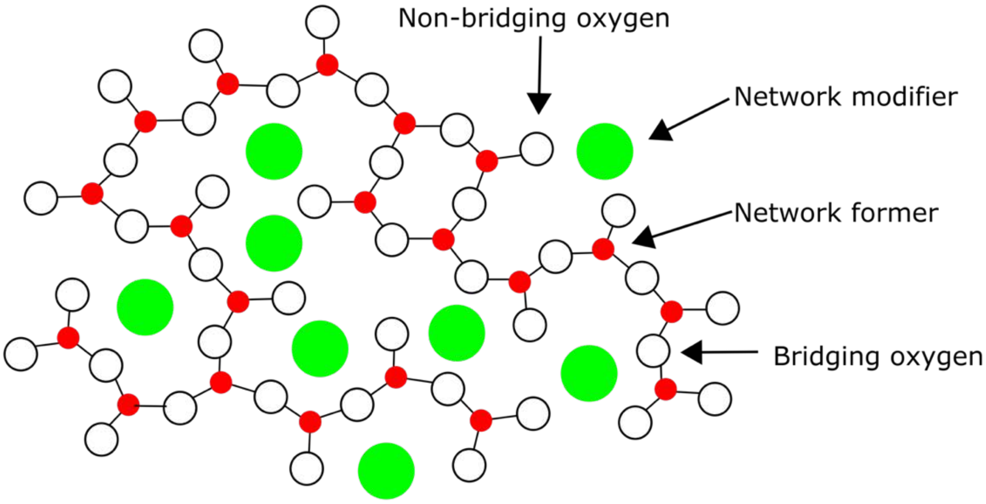

Figure 2.2. 2D scheme of the structure of a binary glass adapted from (Biscoe and Warren, 1938).

2.2.8 Polymerization degree and Q groups

The connectivity of tetrahedra in the glassy network is described using the Q^n notation, where n refers to the number of BO that link two different tetrahedra together (Figure 2.3). In the case of silicates, n varies between 0 and 4; Q^0 refers to a completely depolymerized network – equivalent to nesosilicate minerals – whereas Q^4 is the fully polymerized network where all the tetrahedra are interconnected, e.g. amorphous silica. The substitution of Si^{4+} for Al^{3+} or other intermediate cations creates a distortion on the shape and configuration of the tetrahedra due to the rearrangement required by charge compensation.

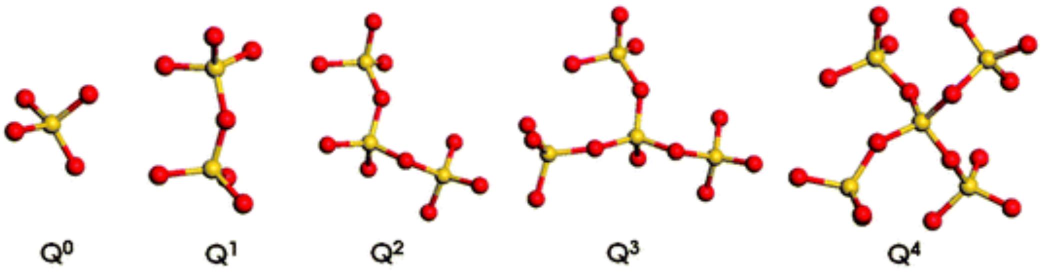

Figure 2.3. Scheme of the different Qn species in glass. The network formers are represented in yellow and oxygen in red.

2.3 General models of glass structure

The study of crystal structure, although not without complications, is largely simplified by the periodicity of the lattice. Although glasses also have a structure, their characterization poses particular issues arising from the lack of long-range ordering. Several authors have proposed models that intend to explain the middle and short-range ordering and linking them to the process of glass formation.

2.3.9 Lebedev crystallite theory

The crystallite theory (Lebedev, 1921) proposes that glasses are in fact constituted of microcrystalline, optically undetectable clusters. For instance, vitreous SiO_2 is constituted by nanoclusters of the one of the SiO_2 polymorphs. In fact, it was proposed that its structure resembles cristobalite. In binary and multicomponent glasses, the crystallites may be either definite chemical compounds or form solid solutions with other components. Therefore, glass structure has to be both micro-heterogeneous and multiphasic by nature. The microcrystals correspond to severely deformed units of a fractional crystalline lattice. This model was abandoned because it failed to explain the variation of macroscopic properties such as density.

2.3.10 Goldschmidt's radius criterion

Goldschmidt proposed that any simple oxide may be a glass former as long as it complies with certain geometrical criteria (Goldschmidt, 1926). The essential condition for vitrification is that the ratio between the radius of the cation (r_c) and the radius of the anion (r_a) has to be between 0.2 and 0.4 (Table 2.1). Some of the major glass formers, such as SiO_2

and P_2O_5, comply with this rule. However, BeO does not form a glass despite having an appropriate r_c/r_a ratio.

Oxide	**R_{cation}/R_{anion}**
SiO_2	0.38/1.4 ~ 0.28
B_2O_3	0.2/1.4 ~ 0.15
P_2O_5	0.34/1.4 ~ 0.25
GeO_2	0.44/1.4 ~ 0.31

Table 2.1. Ionic ratio of the different network-forming elements (Vogel, 1992).

2.3.11 The continuous random network theory

The main aim of previous models was to explain the variation of glass properties from the evolution of the structure. In exchange, Zachariasen’s continuous random network (CRN) focuses primarily on the structure (Zachariasen, 1932).

The atomic arrangement in simple oxide glasses agrees with certain postulates:

- The atomic forces in the glass and the corresponding crystal must be similar.
- Glass consists of a 3D random network
- Glass has a larger internal energy than the corresponding crystal, but it is not high enough to activate crystallization.
- Structural units are similar in glasses and crystals (Figure 2.4).

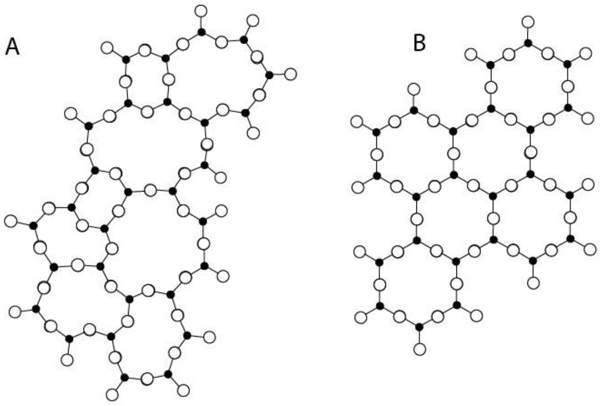

Figure 2.4. Schematic 2D structure of an oxide glass (A) according to the CRN model (Zachariasen, 1932) compared to a crystal of analogous composition. Full and white circles represent cations and oxygen respectively.

Zachariasen’s model established some rules for the formation of binary glasses. A glass of composition A_mO_n may be formed when (Zachariasen, 1932):

- Any oxygen atom is linked to not more than two atoms A.
- The number of oxygen atoms surrounding atoms A must be small.
- The oxygen polyhedral share corners with each other, not edges or faces.
- If the network has to be 3-dimensional, at least three corners in each oxygen polyhedron must be shared.

According to these rules, A_2O and AO oxides cannot be vitrified. Among the others, only those that can of forming oxygen triangles or tetrahedra are capable of forming a glassy network. Thus, A_2O_3, AO_2 and A_2O_5 are the potential network formers. Huang and coworkers recently proved that SiO_2 effectively follows Zachariasen’s rules by observing a 2D thin silica layer grown on graphene in ADF-STEM (Huang et al., 2012) (Figure 2.5).

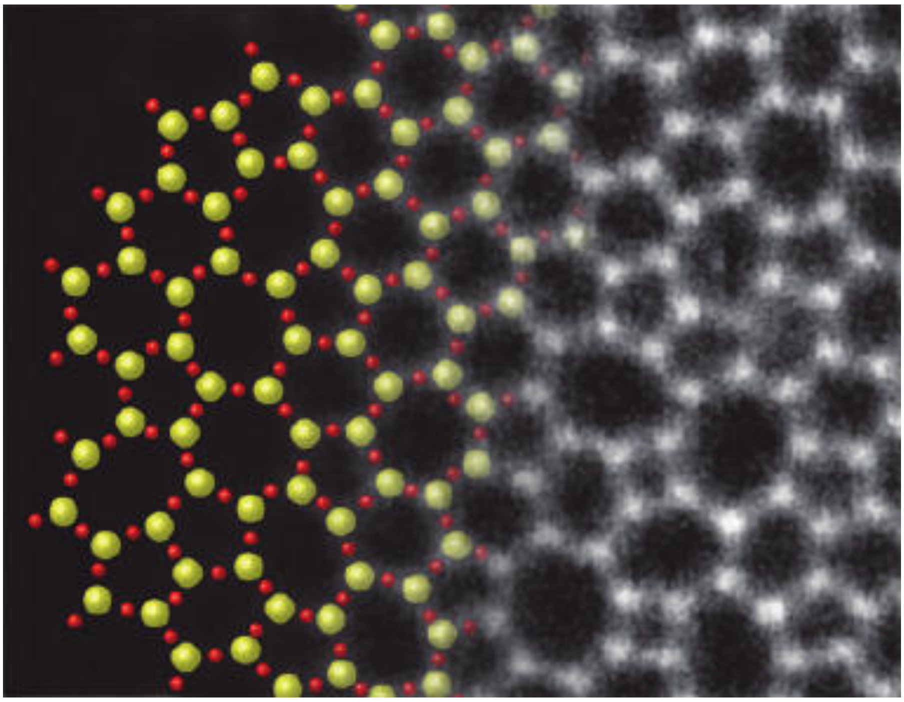

Figure 2.5 Comparison between the CRN model and the ADF-STEM image of SiO2 (Huang et al., 2012; Zachariasen, 1932).

2.3.12 3 Dimensional Continuous Random Network

Warren and Biscoe extended Zachariasen’s model to multicomponent glasses containing not-network forming cations (Biscoe and Warren, 1938) . The addition of an alkali metal into SiO_2 glass breaks some Si-O bonds. This process creates voids for the alkali ions and disrupts the whole network.

2.3.13 Dietzel's field strength theory

The former models are based on the constrains posed by the ionic radii of the atoms to glass formation. Dietzel took into account electronic properties such as charge or polarizability by introducing a factor called "cation field strength", CFS = Z/a^2, where Z is the ion charge and a is the distance between a given ion and O. From this arose a classification of the ions into network formers (Z/a^2 = 1.4-2.0); network modifiers (Z/a^2 = 0.1-0.4); and intermediate cations (Z/a^2 = 0.5-1.0). In general, small highly charged cations tend to be network formers, whereas large low charged cations are preferentially network modifiers (Table 2.2).

Elements	**Valence Z_c**	**r_c**	**A**
Network formers			
P	5	0.31	1.71
V	5	0.49	1.4
Si	4	0.4	1.235
B	3	0.25	1.102
Sb	5	0.74	1.092
Ge	4	0.53	1.074
Intermediate cations			
Ti	4	0.74	0.873
Al	3	0.53	0.805
Zr	4	0.86	0.783
Be	2	0.41	0.61
Mg	2	0.86	0.392
Zn	2	0.88	0.385
Network modifiers			
Ca	2	1.14	0.31
Pb	2	1.33	0.268
Li	1	0.9	0.189
Na	1	1.16	0.153
K	1	1.52	0.117

Table 2.2. Field Intensity (A) of the different cations (Vogel, 1992).

2.3.14 Sun's single bond strength criterion

Sun proposed that the glass-forming ability may be related to the strength of cation-oxygen bonds (Sun, 1947). Stronger bonds will hamper the rearrangement of the melt for crystallization and facilitate vitrification. Using the single bond strength (SBS) criterion –

summarized in Table 2.3,cations can be divided into glass formers (SBS > 80 Kcal/mol), modifiers (SBS < 60 Kcal/mol), and intermediates (60 Kcal/mol ≥ SBS ≤ 80 Kcal/mol). Although this model is suitable for oxide glasses, it does not account for the chalcogenide network formers (SBS ≤ 40 Kcal/mol).

	M in M_mO_n	**Oxidation state**	**Dissociation energy E_d (kcal)**	**Coordination**	**Bond energy (kcal)**
Network formers	B	3	356	3	119
	Si	4	424	4	106
	Ge	4	431	4	108
	Al	3	402-317	4	101-79
	P	5	442	4	111-88
	As	5	349	4	87-70
	Sb	5	339	4	85-68
	Zr	4	485	6	81
Intermediate cations	Zn	2	144	2	72
	Pb	2	145	2	73
	Al	3	317-402	6	53-67
	Zr	4	485	8	61
Network modifiers	Pb	4	232	6	39
	Mg	2	222	6	37
	Li	1	144	4	36
	Pb	2	145	4	36
	Zn	2	144	4	36
	Ba	2	260	8	33
	Ca	2	257	8	32
	Sr	2	256	8	32
	Na	1	120	6	20
	K	1	115	9	13

Table 2.3. Dissociation energies and bond strengths of certain oxides (Sun, 1947).

2.3.15 Smekal's mixed bonding rules

The random arrangement of glass is not compatible with 100% covalent bonding, as it is characterized by distinct bond lengths and angles. However, glass structure also shows a certain directionality that is not compatible with pure ionic or metallic bonding. Smekal suggested (Smekal, 1951) that the bonds in glasses might have intermediate characteristics between the bonds in crystals. Purely ionic materials melt at low temperatures but crystallize relatively easy, whereas materials with mixed linkages such as quartz melt at much higher temperatures and are capable of vitrifying.

2.3.16 Modified random network: multicomponent glasses

The Modified Random Network theory (MRN) proposes a separation between network-forming cations (Si^{4+}, Al^{3+} and Fe^{3+}) and network modifiers (alkaline and alkaline earths). It is based in the formation of distinct local structures, named percolation channels (Figure 2.6), at the nanometer scale, where the NM lie preferentially (Greaves et al., 1981; Le Losq et al., 2017; Vessal et al., 1992). The formation of the channels around silicate tetrahedra is an unmixing process that recuperates the idea of nanoscale heterogeneities contained in the crystallite theory. In contrast to this theory, it appears to be consistent with the evolution of transport properties, conductivity… The MRN was first established for binary compositions and has recently been demonstrated to be applicable also to multicomponent glasses and melts (Le Losq et al., 2017).

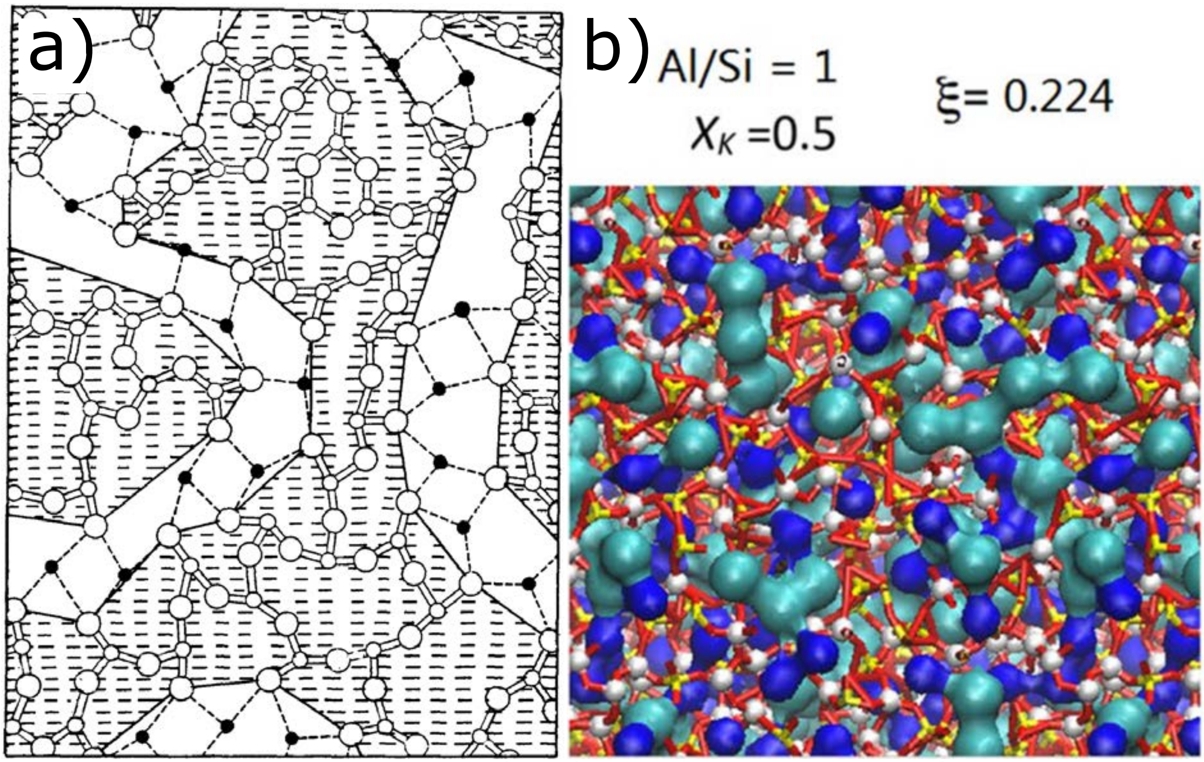

Figure 2.6. Modified Random Network (MRN) model for glass structure. a) Directional network bonds are shown === with ionic interactions marked· • • •. Network regions are shaded to highlight the modifier channels (Greaves, 1985). b) Percolation channels in the mixture Na/K in aluminosilicate melts (Le Losq et al., 2017).

2.4 Unmixing

Unmixing processes are common in nature and even in everyday life such as the separation between oil and water or vinegar. Upon shaking in a closed container, the liquids appear to mix, but the actual process involves droplets of one of the liquids dispersing in the other. When the system goes back to stable conditions, the two liquids separate in a short span of time due to their fluidity. In glasses and melts, the process follows the same principle but the effects are much slower, influenced by their high viscosity at low temperatures. If a liquid is homogeneous at high temperature but enters a miscibility gap, a sharp cooling results in the formation of solid, dispersed droplets in a continuous matrix of the other (Shelby, 2005). In some instances, the phase separation occurs and may observed in the liquid state, such as in phosphate-silicate mixtures. In other cases, the melts are too viscous for the phase separation to develop and the glass seems homogeneous, although droplets of different compositions may be observed at high magnification (electron microscopy). This is the case of some commercial sodium borosilicate glasses (Shelby, 2005).

There are two different types of unmixing processes. The first, nucleation and crystallization, is analogous to the formation of crystals. The phase separation requires a lot of energy and results in the growth of nuclei in regions separated by sharply defined boundaries. The other phase acquires a spherical form because it stays in the liquid state. The second process is spinodal decomposition. It requires less energy as it is more common when the compositional change is small. It forms interconnected separated zones (Neuville et al., 2013).

2.5 Viscosity: (alumino)silicate liquids, phosphate liquids, natural melts

Viscosity is the resistance of a liquid to shear deformation. It is defined by the expression

$$\eta = \frac{F \cdot d}{A \cdot v}$$

where F is the tangential force applied to two parallel planes of area A, which are separated by a distance d. v is the relative velocity of the two planes.

The study of viscosity is essential in the glassmaking process (Fernandez Navarro, 1991; Shelby, 2005). According to the kinetic model, the dependence of viscosity on temperature plays a major role in the control of the glass-forming ability. Glasses form more easily when viscosity is either high at the melting temperature, or alternatively when it increases fast with decreasing temperature. In both cases, high viscosities pose kinetic barriers to the atomic rearrangement that leads to crystallization. When viscosity varies directly with the applied shear force, η is independent of the force and the liquid has a Newtonian behavior. At high shear stresses, many glass-forming melts exhibit an apparent decrease in viscosity with increasing shear stress – known as shear thinning. The unit of viscosity in the SI is Pa·s (N/m^2). Fluidity is considered the opposite of viscosity, although the term is rarely used in the scientific literature about glass.

Viscosity is mainly controlled by two variables: temperature and chemical composition. The effect of temperature on viscosity is related to its configuration. In solids, atoms are emplaced in local minima of the interatomic potential. In a crystal, these potentials are symmetrical and periodical on the long range, whereas in a glass these distances vary greatly. As a consequence, at low temperature the atoms vibrate upon an increase in energy, whereas over a certain threshold – about the magnitude of the potential energy – the atoms are capable of trespassing the potential barriers of the different configurations, causing a certain atomic mobility. Chemical composition influences viscosity through its control of the degree of connectivity of the network. Viscosity then depends on the coordination number and the type of bond between the tetrahedra and the rest of cations. For instance, amorphous silica has a high viscosity because all the tetrahedra are interconnected. In exchange, the presence of Na in a network modifying role makes albite melts less viscous.

The viscosities that are relevant for the production of glass in an industrial setting are grouped under the term *workability points.* The viscosity ranges are named according to the process that happens inside them (Shelby, 2005):

- Practical melting range (1-10^2 Pa·s) refers to the range where fining, bubble removal and homogeneity can be obtained in a short time. It is used as a reference viscosity but it must not be confused with the actual melting point of crystals.
- Glass conditioning (10^2-10^3 Pa·s) is the process that ensures that the thermal profile inside the glass is appropriate for the continuity of the processing in the forming range.
- Forming range (10^3-10^8 Pa·s) refers to the span of viscosities low enough that the glass can be deformed by its own weight or by small loads, hence it acquires a definite shape upon cooling. The Littleton softening point refers to the temperature where the viscosity equals $10^{6.6}$ Pa·s. However, it can only be used for compositions with densities similar to that of the soda-lime silicate glas.
- Annealing range (10^{12}-$10^{13.5}$ Pa·s) is the range of viscosities were the internal stresses are relieved in time span between a few minutes (annealing point, at 10^{12} Pa·s) and a few hours (strain point, at $10^{13.5}$ Pa·s).

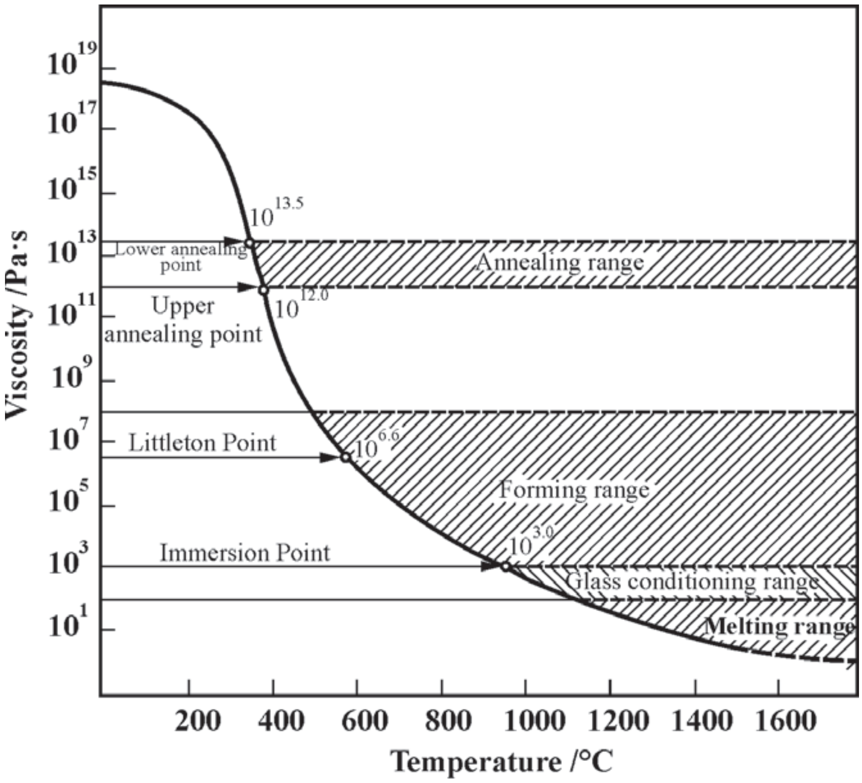

Figure 2.7. Dependence of viscosity on temperature.

2.6 Vitrification as an inertization technique

Vitrification is an inertization technique based on the transformation of a waste – or a mixture of wastes, sometimes with additional reagents – into a glass. It is the state-of-the-art technique for the inertization of radioactive waste to ensure a long-term isolation (Donald et al., 1997; Gin et al., 2013; Vienna, 2010). Other current proposals on the inertization by vitrification include soil decontamination (Careghini et al., 2010; Navarro et al., 2013), mine wastes (Alfonso et al., 2016; Arancibia et al., 2013) or incineration ashes, which are easily vitrifiable due to the abundance of silica (Cheng, 2004; Cheng et al., 2002; Haugsten and Gustavson, 2000; Kang et al., 2017; Kavouras et al., 2003; Romero et al., 2001; Varitis et al., 2015). It must be taken into account that waste vitrification is currently economically unviable when applied to non-radioactive wastes (Bingham and Hand, 2006). However, the evolution of environmental legislation points to a scenario where the increasing cost of landfilling and the stimuli to the development of environmentally friendly solutions might shift this balance. The interest of vitrification is patent in the large number of waste inertization studies that use this technique, either in alone or combined with others (Table 2.4).

Using melting temperatures between 1400 and 1600 ºC ensures the destruction of pathogens and organic compounds. The fabrication of glass-ceramics also receives its fair share of attention due to the large possibilities arising from the versatility and the potential improvements of the physical properties of the glasses related to crystallization. It is of particular interest the production of glass-ceramics combining different kinds of waste (Binhussain et al., 2014; Mymrin et al., 2014). The organic fraction of the sludge may be used to provide additional power for the thermal equipment (Cao and Pawłowski, 2012; Król and Poskrobko, 2012; Rulkens, 2008). This reduces the need for additional fuel and CO_2 emissions.

No.	Type of waste	Description	References
1	Fine coal, rock dust	From mining and mineral processing	[30]
2	Contaminated soils	Agriculture and horticulture	[31]
3	Bio-waste	Forestry, fisheries, food preparation, and processing	[22]
4	Wood and paper	Manufacture of furniture, pulp, paper, and paperboard	[22]
5	Tannery sludge	Processing operations of leather and fur	[32]
6	Hydrocarbons	Petroleum refining, natural gas purification, and pyrolysis of coal	[22]
7	Chemicals	Inorganic chemical processes and photographic industry	[33]
8	Paints and varnishes	The production of paint, varnish, adhesives, and sealants	[34]
9	Fine-grained scraps	Mechanical surface treatment of metals	[35]
10	Construction aggregates	Construction and demolition of buildings	[36]
11	Medical waste	Sharps, organs and body parts, sanitary towels, bandages, reagents, drugs	[37]
12	Sewage sludge	Municipal and industrial water treatment	[38]
13	Ash and slag	From power plants and other energy facilities	[39]
14	Sludges and filter cakes	From machining of steel, aluminium, lead, zinc, copper and precious metals, and from electroplating and coating of metals	[40]
15	Glass and ceramics	From glassworks during glass processing and from households and industrial plants	[41]
16	Cement, lime, and plaster	From manufacture of mineral binders and from lime and cement industry	[42]
17	Radioactive waste	From production and processing of nuclear fuel and from the mining of uranium ore	[43]
18	Asbestos waste	From manufacture of textile articles, fibers, roof panels, water, and sewage pipes	[44]

Table 2.4. A brief summary of waste for vitrification (Borowski, 2015). The reference numbers are those of the original article.

2.7 Glass-ceramics

Glass-ceramics are polycrystalline materials composed by inorganic glasses and ceramics that are produced by controlled crystallization of the glassy phase (Holand and Beall, 2012). The name applies either to both highly crystalline materials up to 98% and those that contain substantial residual glass (about 70%). They may be composed by single or several glassy and crystalline phases; their composition changes during the crystallization process. Not all the glass compositions produce suitable glass-ceramics: some glasses – such as albite glass – do not crystallize, whereas some other compositions crystallize fast and spontaneously, complicating the growth of the crystals in a preferred orientation.

Crystallization consists of two steps that may be partially overlapped: nucleation at low temperature and crystal growth at high temperature. Nucleation concerns the formation of submicroscopic nuclei in the first stages of ordering. Crystal growth refers to the formation of macroscopic crystals from the nuclei. The formation of crystals confers glass-ceramics new properties that are clearly differentiated of from those of glasses. These differences depend on the size, the distribution and the composition of the newly formed phases. Crystallization may be achieved both by heating glasses – as in the glass-ceramic process – and by decreasing the temperature of melts – such as in the petrurgic process or the cooling of magmas.

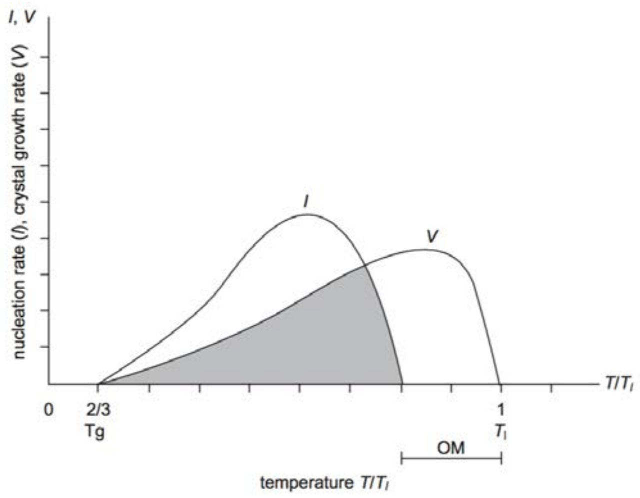

Figure 2.8. Nucleation/crystal growth rate as a function of temperature from (Holand and Beall, 2012).

2.8 Vitrification of sewage sludge

The inertization of sewage sludge by vitrification – either by itself or in combination with other processes – has attracted a certain interest in recent studies on waste inertization and management. In their 2003 review, Colombo and coworkers summarized the research on wastes that showed potential to be inertized by vitrification (evelopments of the last decade.) such as municipal solid waste (MSW) fly ash, coal fly ash, steel plant fly ash, stainless steel fly ash, steelwork slag, Zn hydrometallurgy slag, mud from Be extraction, dredging spoils, and asbestos containing residues (Colombo et al., 2003). The summary includes mixtures between wastes and additives. Bingham and Hand focused on the vitrification of MSW and sewage sludge ashes in their review (Bingham and Hand, 2006). The authors highlight the importance of standardizing wastewater processing to reduce the variability of its by-products. This section reviews the research on sewage sludge and sewage sludge ash vitrification after the two beforementioned reviews, focusing in the developments of the last decade.

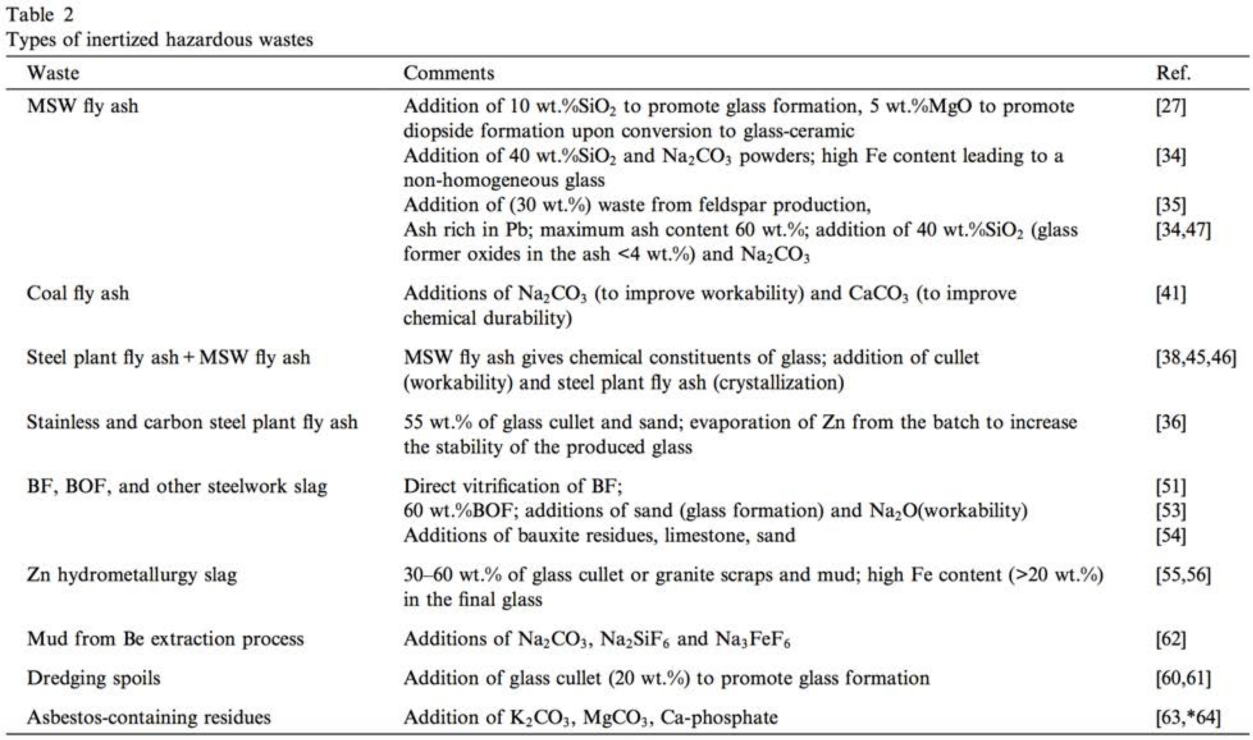

Table 2
Types of inertized hazardous wastes

Waste	Comments	Ref.
MSW fly ash	Addition of 10 wt.%SiO_2 to promote glass formation, 5 wt.%MgO to promote diopside formation upon conversion to glass-ceramic	[27]
	Addition of 40 wt.%SiO_2 and Na_2CO_3 powders; high Fe content leading to a non-homogeneous glass	[34]
	Addition of (30 wt.%) waste from feldspar production,	[35]
	Ash rich in Pb; maximum ash content 60 wt.%; addition of 40 wt.%SiO_2 (glass former oxides in the ash <4 wt.%) and Na_2CO_3	[34,47]
Coal fly ash	Additions of Na_2CO_3 (to improve workability) and $CaCO_3$ (to improve chemical durability)	[41]
Steel plant fly ash + MSW fly ash	MSW fly ash gives chemical constituents of glass; addition of cullet (workability) and steel plant fly ash (crystallization)	[38,45,46]
Stainless and carbon steel plant fly ash	55 wt.% of glass cullet and sand; evaporation of Zn from the batch to increase the stability of the produced glass	[36]
BF, BOF, and other steelwork slag	Direct vitrification of BF;	[51]
	60 wt.%BOF; additions of sand (glass formation) and Na_2O(workability)	[53]
	Additions of bauxite residues, limestone, sand	[54]
Zn hydrometallurgy slag	30–60 wt.% of glass cullet or granite scraps and mud; high Fe content (>20 wt.%) in the final glass	[55,56]
Mud from Be extraction process	Additions of Na_2CO_3, Na_2SiF_6 and Na_3FeF_6	[62]
Dredging spoils	Addition of glass cullet (20 wt.%) to promote glass formation	[60,61]
Asbestos-containing residues	Addition of K_2CO_3, $MgCO_3$, Ca-phosphate	[63,*64]

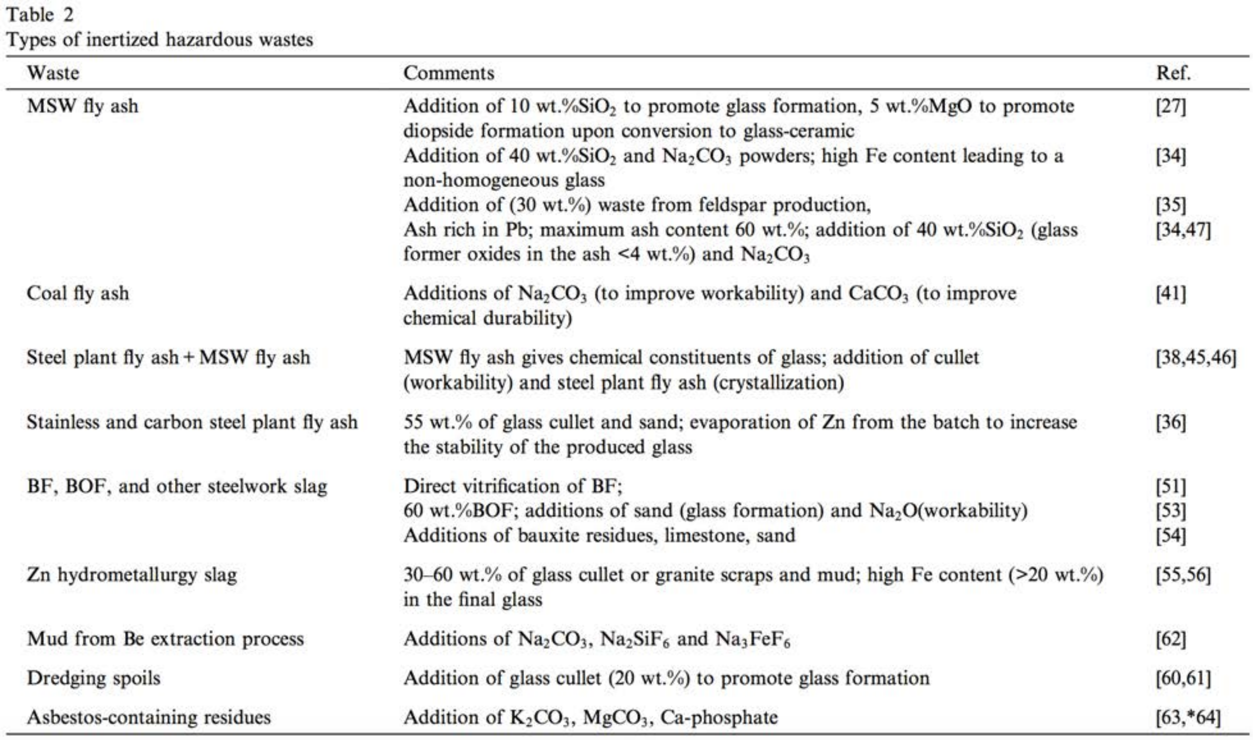

Table 2
Types of inertized hazardous wastes

Waste	Comments	Ref.
MSW fly ash	Addition of 10 wt.%SiO_2 to promote glass formation, 5 wt.%MgO to promote diopside formation upon conversion to glass-ceramic	[27]
	Addition of 40 wt.%SiO_2 and Na_2CO_3 powders; high Fe content leading to a non-homogeneous glass	[34]
	Addition of (30 wt.%) waste from feldspar production,	[35]
	Ash rich in Pb; maximum ash content 60 wt.%; addition of 40 wt.%SiO_2 (glass former oxides in the ash <4 wt.%) and Na_2CO_3	[34,47]
Coal fly ash	Additions of Na_2CO_3 (to improve workability) and $CaCO_3$ (to improve chemical durability)	[41]
Steel plant fly ash + MSW fly ash	MSW fly ash gives chemical constituents of glass; addition of cullet (workability) and steel plant fly ash (crystallization)	[38,45,46]
Stainless and carbon steel plant fly ash	55 wt.% of glass cullet and sand; evaporation of Zn from the batch to increase the stability of the produced glass	[36]
BF, BOF, and other steelwork slag	Direct vitrification of BF;	[51]
	60 wt.%BOF; additions of sand (glass formation) and Na_2O(workability)	[53]
	Additions of bauxite residues, limestone, sand	[54]
Zn hydrometallurgy slag	30–60 wt.% of glass cullet or granite scraps and mud; high Fe content (>20 wt.%) in the final glass	[55,56]
Mud from Be extraction process	Additions of Na_2CO_3, Na_2SiF_6 and Na_3FeF_6	[62]
Dredging spoils	Addition of glass cullet (20 wt.%) to promote glass formation	[60,61]
Asbestos-containing residues	Addition of K_2CO_3, $MgCO_3$, Ca-phosphate	[63,*64]

Table 2.5. Types of wastes inertized by vitrification from (Colombo et al., 2003). The reference numbers are those of the original article.

Park and Heo investigated the production of glasses and glass-ceramics from incinerated MSW mixed with SiO_2, MgO, and TiO_2 (Park and Heo, 2002). The mechanical properties of the glass-ceramics are adequate in the light of potential applications – hardness of 6.37 GPa, fracture toughness of 1.86 MPa·$m^{1/2}$ and bending strength of 127 MPa. Moreover, Mg addition caused the crystallization of diopside as the main phase of the glass-ceramics. The concentration of heavy metals in the leachate was very low, complying with the Korean regulations – which permit concentrations on the same order of magnitude as European norms.

Hannant and coworkers studied the environment of iron in simulated and real sewage sludge ashes (SSA) by a combination of Mössbauer spectroscopy and X-Ray Absorption spectroscopy (XAS) (Hannant et al., 2009, 2008). Apart from the inertization of SSA waste itself, these studies are relevant in the inertization of intermediate legacy-level nuclear wastes. The authors report that it was necessary to add up to 34 mol% CaO to permit a full vitrification at 1450 ºC. CaO reduced Tg and at concentrations above 29 mol% enabled the formation of

4-fold coordinated Fe^{3+}. This influence the redox reactions, as the authors found $^{IV}Fe^{3+}$ more likely to take part in redox reactions than $^{VI}Fe^{3+}$. Moreover, $^{VI}Fe^{3+}$ seems to increase due to the lack of charge-balancing in the ferric state. Fe^{2+} occupies both 6-fold and 8-fold coordinated environments.

Tian and coworkers studied the evolution of the crystallization, microstructure, and properties of a sewage sludge-based glass and glass-ceramics prepared by microwave heating (Tian et al., 2011). Melting in the Microwave equipment reduced the crystallinity of the glass as it generated a latent heat that suppressed crystal growth. The glass-ceramics obtained by heating the glass between 900 and 1000 ºC contained anorthite and wollastonite. Concerning their mechanical properties, Vickers microhardness ranged between 6.12-6.54 GPa and the thermal expansion coefficient between $5.29\text{-}5.75\cdot10^{-6}\,{}^{o}C^{-1}$. All the glass-ceramics immobilized heavy metals against leaching.

Sobiecka and Szymanski analyzed the thermal vitrification process of a set of mixtures of fly ash and chromium-rich sludge (Sobiecka and Szymanski, 2013). The vitrificates fromed easily due to their compositions in the lime aluminosilicate system and successfully reduced the leaching from several ppm/L in the wastes to the low ppb/L range. Their Vickers hardness was between 3.089 and 5.002 GPa (increasing with the proportion of fly ash). The authors also point that the use of two different hazardous wastes reduces the cost of the process without increasing its environmental impact, which is uncommon in plasma vitrification technology.

Barbieri and coworkers made alkali and alkaline-earth glasses and glass-ceramics from municipal and industrial sewage sludge (Barbieri et al., 2000). The authors mixed MSW bottom ash with glass cullet to increase the concentration of Na, which is the flux agent. Moreover, they added steel fly ash – rich in Fe_2O_3 and ZnO – to catalyze the crystallization of the glass-ceramics. The resulting glasses had negligible leaching, good chemical durability and rendered basaltic glass-ceramics – bearing wollastonite, diopside, anorthite and Fe oxides – by a surface devitrification mechanism. Another study focused on the structure, chemical durability and crystallization behavior of incinerator-based glassy systems (Barbieri et al., 2008). In this case, both bottom and fly ash from the incineration of MSW were mixed with glass cullet, feldspar and clay by-products. The obtained glasses were interesting because of their good chemical resistance, specially in alkaline environment. They were deemed suitable to make glass-ceramics and to be manufactured into fibers or tiles.

Lin and coworkers studied the production and characterization of glazed tiles containing incinerated sewage sludge (Lin et al., 2008). The composition of the glaze was modified by the addition of one of four different colorants: Fe_2O_3 (red), V_2O_5 (yellow), $CoCO_3$ (blue), or MnO_2 (purple) and was sintered on the tiles at 1050 ºC. The glazes formed a film that protected the surface – enhancing abrasion resistance – and limited water absorption on the tiles proportionally to the % of glaze.

Ischia and coworkers studied the co-pyrolysis of SS and clay using thermogravimetry and evolved gas mass spectrometry (Ischia et al., 2011). The clay high surface/area ratio catalyzed the pyrolysis reaction of the sludge and released water between 450-500 ºC, enhancing the gasification of part of the carbon residue of the inorganic components. Moreover, the final residue of the SS-clay blend was a vitreous matrix that immobilized the heavy metals in SS. The sludge mass was reduced in 52 % up to 600 ºC.

Baowei and coworkers studied the structure and performance of glass.ceramics from Bayan Obo mine tailing and fly ash (Baowei et al., 2013). The compositions of the obtained glass-ceramics lie in the CMAS system and crystallize into diopside as the main phase. This gives the glass-ceramics a hardness of 7.17 GPa and shows potential for construction application.

Menéndez and coworkers explained the vitrification of the solid residue of microwave treatment and gasification of SS (Menéndez et al., 2005). The process includes drying, pyrolysis and gasification of SS, giving rise to a gas with a high CO and H_2 content and an oil with a low PAH content. The high temperatures during the process result in a partially vitrified residue with a low micro- and mesopore volume. The authors also state that microwave melting produces a less porous, more resistant to leaching material.

Park and coworkers investigated the control of the crystalline phase in glass-ceramics obtained from sewage sludge fly ash (Park et al., 2003). Thermal treatments yielded diopside and/or anorthite glass-ceramics. The former had better physical and chemical properties due to the interlocking microstructure of diopside crystals.

Borowski studied the vitrification of sewage sludge ash and highlighted the versatility of this technique to produce objects with specific shapes and dimensions, therefore being appropriate for both the ceramic and the construction industries (Borowski, 2015). The author obtained vitrified pellets of ashes that may replace mineral and artificial aggregates used in road construction. Another product were mini-glass balls that may be used as additional proppants in hydraulic fracturing of shale gas and oil. In another study, Borowski proposed the production of vitrified briquettes from SS (42%) mixed with crushed waste glass (50%) and cement (8%) (Borowski, 2013). Heating the mixture up to about 1100-1200 ºC caused surface vitrification and sintering. This treatment process prevented the migration of dangerous substances from the briquettes and the leaching of heavy metals, turning them into environmentally safe products. These products may replace the aggregates used in the construction of paved roads, embankments and banks.

Grigiante and coworkers proposed a two-step pyrolysis-vitrification process that achieved a leach-resistant material applicable to the ceramic industry or as road bed (Grigiante et al., 2010). This technique recovered 44% of the energy of the sludge; the difference was used to reduce the moisture of the sludge from 80% to 10-20%.

Bernardo and Dal Maschio proposed the integration of vitrification and glass-ceramic production by simple viscous flow sintering with pyrolysis – where SS is used as a fuel – in order to design a process which did not produce any waste requiring disposal (Bernardo and Dal Maschio, 2011). Their final product was comparable to natural stones in terms of both mechanical strength and chemical stability. Franus and coworkers sintered sewage sludge to obtain a lightweight aggregate (Franus et al., 2016). These aggregates can be applied to the filling of wooden frames or curtain walls.

Bien and coworkers (Bień et al., 2013) proposed the vitrification of mixtures of tannery sewage sludge – bearing high chromium contents due to the chromium salts used in the tanning process of leather – with waste moulding sands, dolomite flotation waste, and flux agents. The mixtures with higher silica contents were found to be more effective in the binding of heavy metals, whereas an excess flux was responsible for a decrease in microhardness. All of their compositions apart from the most enriched in Cr were satisfactorily vitrified. The vitrificates with higher amounts of fluxes look glassier.

Garcia-Valles and coworkers studied the incorporation of heavy metals in mineral phases through a glass-ceramics process of a vitrified mixture of sewage sludge and galvanic sludge bearing large concentrations of Cr (Garcia-Valles et al., 2007). The mixture also contained fluorite (CaF_2) as a fluxing agent. The glass-ceramics contained spinel, magnetite (which oxidized to maghemite), gehlenite, anorthite and fluorapatite, thus obtaining minerals that hosted the toxic elements such as Cr. The process improved the microhardness of the glass.

Garcia-Valles and coworkers studied the production of glasses from different sources of sewage sludge in Egypt and measured their viscosities (Garcia-Valles et al., 2013). The study also includes the development of the Hot-Stage software that is used to treat the pictures obtained during HSM experimental runs. The thermally treated glasses had a lower viscosity due to crystallization specially at low temperature.

Although all the presented studies are both interesting and readily applicable, most research has focused on the vitrification of as-obtained wastes. Hence, there is a gap in the research for systematic studies of the effect of compositional variations of these wastes in the vitrification range and glass properties. Another important insight is the combination of several types of wastes with the aim of obtaining more suitable compositions and providing a more efficient disposal route.

2.9 Take-home message

- Glass is an amorphous material characterized by the absence of a long range ordering and by the phenomenon of the glass transition.
- The viscosity of a glass is the essential parameter controlling its production.

- The vitrification of sewage sludge and sewage sludge incineration ashes is an effective inertization technique but requires of a better knowledge of the production process and obtaining a marketable product in order to compensate for its high cost
- .

CHAPTER 3 Material and Methods

Je suis de ceux qui pensent que la science est d’une grande beauté. Un scientifique dans son laboratoire est non seulement un technicien : il est aussi un enfant placé devant des phénomènes naturels qui l’impressionnent comme des contes de fées.

("I am among those who think that science has great beauty. A scientist in his laboratory is not only a technician: he is also a child placed before natural phenomena which impress him like a fairy tale.")

Marie Curie

3.1 Materials

The glasses for this study have been produced from batch mixtures of basalt and reagent grade chemical products.

3.1.1. Basalt from Sant Joan les Fonts

The Sant Joan les Fonts' basalt from Boscarró quarry (la Garrotxa, Girona, Catalonia) has been chosen for this study as its chemical composition (Table 3.1) is quite similar to the ranges determined for sewage sludge (Araña et al., 1983). Moreover, the basalt is a homogeneous, readily accessible, inexpensive material. The basalt fits well within the range of USS compositions apart from its P_2O_5 and MgO contents (highlighted with *).

Oxide	**SiO_2**	**Al_2O_3**	**CaO**	**MgO**	**Na_2O**	**K_2O**	**TiO_2**	**FeO**	**P_2O_5**	**MnO**
Basalt	46.00	14.60	10.12	9.21*	3.61	2.09	2.50	10.04	0.36*	0.17
USS	33-53	12-21	8-38	2-7	1-5	1-4	1-3	5-10	3-5	0.1-0.4

Table 3.1. Chemical composition (major and trace elements) of the Sant Joan les Fonts Basalt (Araña et al., 1983) *compared to typical concentrations in urban sewage sludge.*

3.1.2. Laboratory chemical reagents

The addition of phosphorus, calcium and PTE to the basalt has been made using reagent grade chemical products. The materials are summarized in Table 3.2.

Element	**Reagent**	**Producer**	**Code**	**CAS**	**Purity**
P	$NH_4H_2PO_4$	Panreac	131126	7722-76-1	99%
Ca	$CaCO_3$	Panreac	121212	471-34-1	99%
Ba	$BaCO_3$	Acros Organics	423440025	523-77-9	99+%
Cr	Cr_2O_3	-	-	1333-82-0	-
Cu	CuO	Alfa Aesar	41692	1317-38-0	99.7%
Ni	NiO	Alfa Aesar	12359	1313-99-1	99%
Zn	ZnO	Panreac	131786	1314-13-2	99.0%

Table 3.2 Chemical reagents used for the production of glass.

Each set of glasses is named after its chemical composition. The glass made using only the original basalt is named B0. The P-doped series are named BXP, where B corresponds to basalt, and X corresponds to the amount of added P. In the same fashion, the Ca-doped series are named BYCa, where Y corresponds to the amount of added Ca. Finally, the matrix glasses are named MZE, where M corresponds to matrix, Z is the amount of added PTE and E the chemical symbol of the added PTE (Table 3.3).

In summary, the different sets of glasses and glass-ceramics are made from:

- Basalt + P mixtures
- Basalt + Ca mixtures
- Basalt + P + Ca mixtures – sometimes referred to as "matrix glasses".
- Matrix glasses + PTE (either Ba, Cr, Cu, Ni or Zn) mixtures
- Glass made from sewage sludge from El Sadat City WWTP (Egypt).

The glass-ceramics are named by adding the letters GC to the name of their parent glasses.

Sample	wt% element	Sample	wt% added element
B0	none		
		M1Ba	1.27
B2P	2.55	**M5Ba**	6.01
B4P	4.54	**M10Ba**	12.37
B8P	8.52		
B16P	16.47	**M1Cr**	1
B32P	32.38	**M5Cr**	5
		M15Cr	15
B1Ca	10.58		
B2Ca	11.73	**M1Cu**	1.06
B4Ca	13.44	**M5Cu**	5.23
B8Ca	16.52		
B16Ca	24.44	**M05Ni**	0.46
B24Ca	28.84	**M1Ni**	1.02
B32Ca	36.56	**M15Ni**	10.91
M14Ca	14.04	**M1Zn**	1.16
M23Ca	22.10	**M5Zn**	5.72
M30Ca	30.21	**M10Zn**	11.24

Table 3.3. Summary of the names of the glass samples obtained for this study and the concentration of the element of interest in wt%.

3.2 Methods

3.2.1 Glass synthesis

3.1.2.1. Classical quenching

Each glass batch has been prepared to make about 100 g of glass. The mixtures have been homogenized in a ball mill and melted in platinum-rhodium crucibles placed inside a globular alumina equipped with SuperKanthal™ heating elements, Pt-Rh thermocouples, and a Eurotherm® 902 programmer. According to their composition, the melting process varies slightly, as detailed in the corresponding chapters. It can be summarized as follows:

- When ADHP is present in the mixture, a 2 h isothermal step at 200 ºC ensures its decomposition by the following reaction: $NH_4H_2PO_{4(s)} \rightarrow NH_{3(g)} + P_2O_{5(s)} + 3H_2O_{(g)}$
- When $CaCO_3$ is added to the mixture, it is decomposed at 950 ºC for 1 h according to the following reaction: $CaCO_{3(s)} \rightarrow CaO_{(s)} + CO_{2(g)}$
- When $BaCO_3$ is added to the mixture, it is decarbonated at 1200 ºC for 1 h according to the following reaction: $BaCO_{3(s)} \rightarrow BaO_{(s)} + CO_{2(g)}$

Regardless of the intermediate steps, all the compositions have then been melted at 1450 ºC for 4 h and quenched by casting on a Cu plate. The quenching rate using this method is about 15 ºC/s (Neuville et al., 2008a). The samples that proved too viscous to be cast have been quenched by immersing the bottom of the crucible in cold water. Finally, part of each glass has been annealed at 500 ºC during 12 h in a muffle furnace to remove internal tensions.

3.1.2.2. Melting on the heating wire

In an effort to obtain higher quenching rates, some glasses of the P-doped basaltic glass series were remelted at 1450ºC and 1600ºC using a Pt-Rh alloy wire heating system originally designed to obtain spectroscopic data of silicate melts at the Institut de Physique du Globe de Paris (IPGP) (Mysen and Frantz, 1992; Neuville et al., 2014b) (Figure 3.1). The system takes only some mg of glass per melting cycle, thus increasing the quenching rate. The wires had previously been calibrated using salts with known melting points in order to achieve reliable temperature determination.

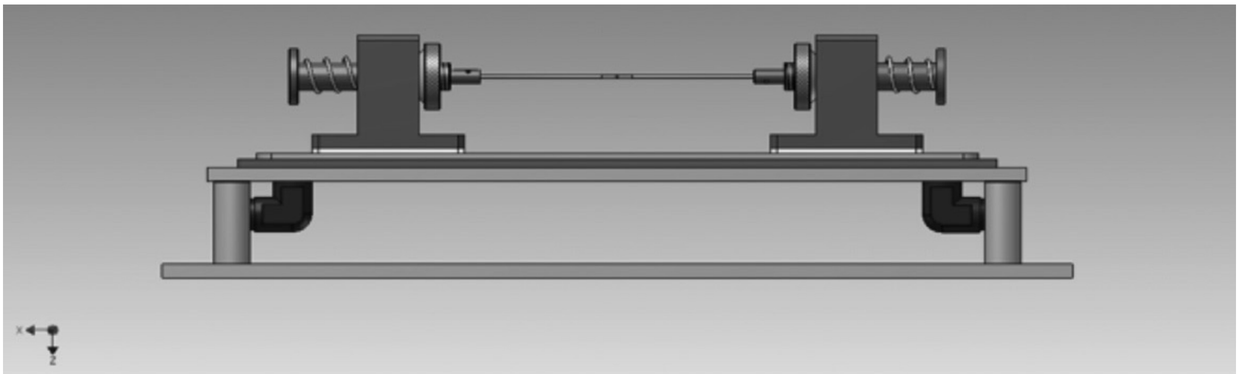

Figure 3.1. Scheme of the heating wire system at IPGP (Neuville et al., 2014b).

3.1.2.3. Aerodynamic levitation

Selected samples of the P-doped basalt series have been remelted by aerodynamic levitation at the Centre National de la Recherche Scientifique-Conditions Extrêmes et Matériaux: Haute Température et Irradiation (CEMTHI-CNRS, Orléans, France). The device has been used to remelt partially crystallized glasses obtained by classical quenching and make glass spheres. It consists of an aerodynamic device coupled with two CO_2 lasers (Coté et al., 1992; Hennet et al., 2006) where a piece of small ceramics is placed into the levitator's nozzle, heated up to a temperature just above the liquidus – determined optically – by means of the lasers. Each sample has been held at high temperature to enable bubble removal and then quenched by turning the power of the lasers off (Figure 3.2). The levitation spheres have been used for density measurements.

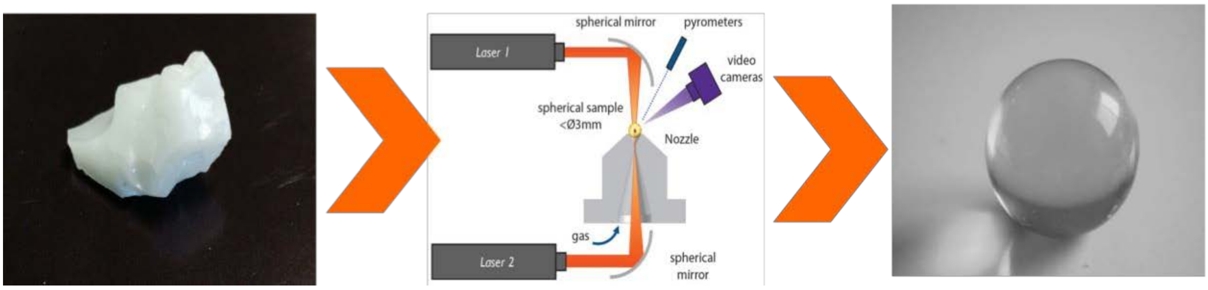

Figure 3.2 Schematic representation of glass synthesis from ceramic samples using the levitation device. Courtesy of A.N. Novikov (Novikov, 2017).

The cooling rate of the melt during the quench with this technique is around 300 °C/s

(Neuville et al., 2008b), expanding the glass-forming range. However, this technique is limited by the possible volatilization of elements that may change the melt's composition. Another disadvantage is the size of the sample, which is generally between 1-3 mm and never exceeds 4 mm in diameter. The highest quenching rates can only be obtained with the smallest samples.

3.1.2.4. Glass-ceramics synthesis

The synthesis of the glass-ceramics products has been made in the same furnaces used for the melting of the raw mixtures. Fragments of the glass are placed in an inert ceramic container and next to the Pt-Rh thermocouple to provide the most accurate temperature measurement possible. The production of each glass-ceramic is detailed in the corresponding chapters.

3.2.2 Chemical composition

3.1.2.5. XRF (basalt)

The chemical composition of the basalt has been analyzed by X-Ray fluorescence in a sequential X-Ray spectrophotometer Phillips PW2400 at Centres Científics i Tecnològics de la Universitat de Barcelona (CCIT-UB). Two different modes of sample preparation available at CCiT-UB have been used: pearls for the main elements and pressed pellets for the trace elements.

3.1.2.6. Electron Microprobe Analysis

Electron Microprobe Analysis at CCIT-UB has been used to verify the chemical composition and homogeneity of the quenched products. The glasses are cut, mounted in epoxy resin and polished. Quantitative chemical composition profiles of the obtained glasses (a longitudinal and a transversal profile; 10 spots each) has been measured using a JEOL JXA 8230 electron microprobe. Quantitative electron microprobe analyses were obtained in wavelength-dispersive spectroscopy (WDS) mode, operating with an accelerating voltage of 20 kV, a beam current of 16 nA for Al, Si, Ti, Ca, K, Mg, Fe, Mn, 8 nA for Na and 6 nA for P, and a beam diameter of 5 μm. Corundum (AlKα), wollastonite (SiKα, CaKα), rutile (TiKα), orthoclase (KKα), apatite (PKα), periclase (MgKα), albite (NaKα), synthetic Fe_2O_3 (FeKα), rhodonite (MnKα), barite (BaKα), Cr_2O_3 (CrKα), CuO_2 (CuKα), Ni^0 (NiKα), and sphalerite (ZnKα) were used as standards. The employed analyzing crystals were TAP for Al, Si, P; PETJ for Cr, Ti, Ca, and K; TAPH for Mg and Na; and LIFH for Fe, Mn Ni, Cu, Ba, and Zn.

3.2.3 Electron microscopy

The microstructure and microchemistry of selected samples has been studied by means of both Scanning Electron Microscopy (SEM) and Transmission Electron Microscopy (TEM). Both microscopes are available at CCIT-UB.

3.1.2.7. Scanning Electron Microscopy

Textural information and qualitative punctual chemical analysis of the glasses, the crystalline phases formed during production, and the products of crystallization treatments have been obtained from carbon-coated, polished glass fragments. The equipment is a JEOL J-7100 field emission scanning electron microscope with EDS detector and backscattered electron detector (FE-SEM-EDS) with the operating conditions of 20 kV and 5 nA. A Co standard has been used to calibrate the microanalysis system.

3.1.2.8. Transmission Electron Microscopy

A thin section of sample B32P has been prepared by ionic beam polishing. The analysis has been performed in a Hitachi H-800-MT transmission electron microscope with energy dispersed analysis of X-rays (EDX), operating at 200 Kv in STEM mode using the dark field detector. The beam size used in this mode is around 15 nm. The spectrometer is an Oxford Instruments INCA x-sight, with Si (Li) detector. The map acquisition is accomplished using the INCA Microanalysis Suite, software version 4.09. X-ray maps are obtained selecting the characteristic X-ray peaks for Si, Al, Ca, Fe, Mg and P.

3.2.4 Differential Thermal Analysis

Differential Thermal Analysis (DTA) has been used to establish the glass transition, crystallization and melting temperatures of the studied compositions; together with the nucleation temperatures of selected compositions. All the glasses have been treated to at least one crystallization temperature to identify which phases crystallize during the heating. The analyses have been performed at the DMPGA in a Netzsch STA 409 vertical furnace. In all cases the reference material is aluminum oxide 0419-0197 from Perkin Elmer.

Standard DTA experiments are done using about 120 mg of powdered glass in Pt-Rh crucibles, under dry air atmosphere, with a flow rate of 80 mL/min and a heating rate of 10ºC/min from room temperature to 1400ºC followed by free cooling. The sample/reference ratio is about 3/1 and it has been optimized to obtain a larger signal while ensuring the completion of the reaction. The data has been processed with the Netzsch Proteus Analysis® software. The error of the temperature measurement is about 0.3 ºC.

The study of the determination of the temperatures of maximum nucleation rate have been designed according to Xu and coworkers (Xu et al., 1991). Their research established that the temperature of maximum nucleation rate can be determined from the shift of the temperature of exothermic peak of the crystallization reaction. This approach should provide a distinctive peak for each of the nucleating phases.

The determination of calorimetric Tg by DTA is done using the tangents method to calculate of the inflection of the curve during the endothermal event corresponding to the glass transition (point B in Figure 3.3).

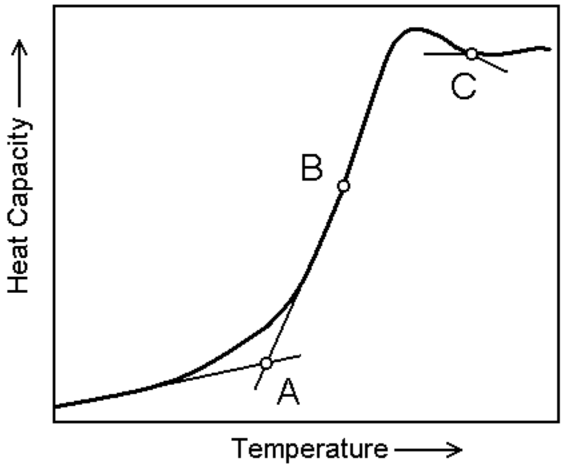

Figure 3.3. Calculation of calorimetric Tg by the tangents method. From (Flügel, 2007).

3.2.5 Dilatometry

Glass transition temperature (Tg) has been also obtained by dilatometry in a Linseis L76/1550 horizontal push-rod dilatometer. 20 mm long bars were cut from each glass, then placed in the sample carrier and heated up to around 750ºC at 10ºC/min. The samples that were too viscous to be cast into bars have been analyzed using powdered glass, inside a SP5856/3605/10 sample carrier. In the case of oxide glasses, certain studies establish that calorimetric Tg measured at 10 ºC/min is reached at a viscosity of 10^{12} Pa·s (Yue, 2008).

For the dilatometry measurements, annealed glass samples are cut into bars of about 20x5x5mm. If necessary, the two smaller faces are flattened and polished in order to improve their stability in the sample holder. Dilatometric Tg is calculated at the inflection of the curve representing deformation as a function of temperature (Figure 3.4). The measurement is done using the tangents method.

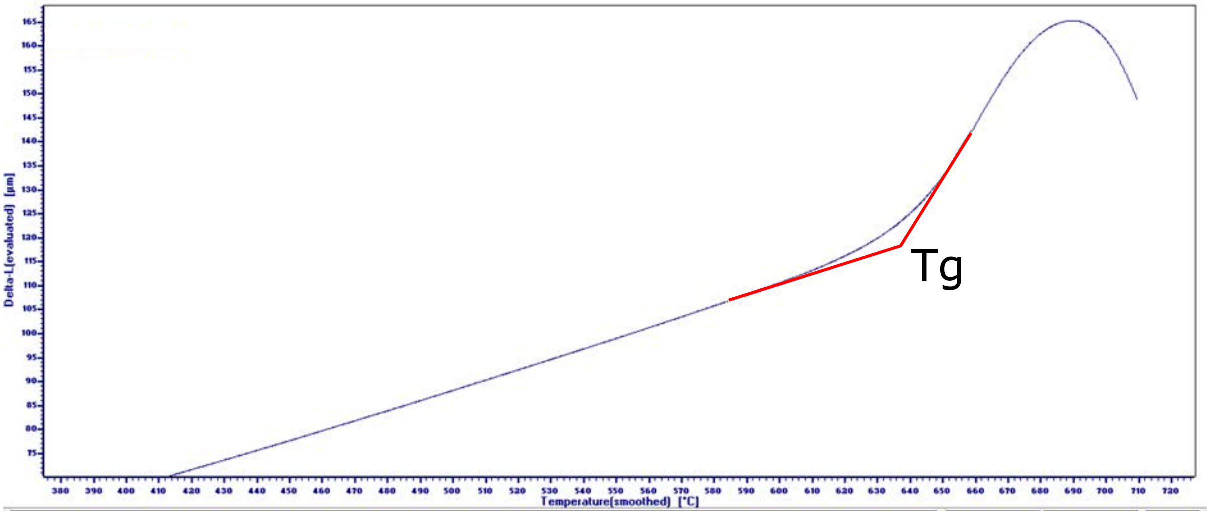

Figure 3.4. Calculation of dilatometric Tg by the tangents method. The tangents are represented by the red lines.

3.2.6 X-Ray Diffraction

XRD has been used for several purposes on the course of this work:

- To verify the amorphous character of the quenched products.
- To qualitatively identify any crystalline phases formed during quenching or upon the established thermal treatments.

- To obtain a quantification of the mineral species present in selected samples by means of the Rietveld refinement of the XRD profile.
- To study crystallization *in situ* during a thermal treatment, in a High Temperature XRD chamber. The variation of the intensity of the peaks reflects the evolution of the crystal size with temperature.

The preparation of the samples for X-Ray powder diffraction preparation is as follows: the glass powders (grain size below 45 μm) are placed inside a cylindrical sample holder and then pressed with the help of a glass plate to obtain a flat surface. The regular sample holder is a cylindrical container 16 mm wide and 2.5 mm high. In the experiments to determine the phases that crystallize during the exothermal events, the powdered thermally treated glass preparations have been made in zero background sample holders following the same procedure due to the small volume that can be treated in each DTA cycle to ensure maximum crystallization (between 120-160 mg).

X-Ray diffraction spectra are obtained in a Bragg-Brentano PANAnalytical X'Pert Diffractometer system (graphite monochromator, automatic gap, Kα-radiation of Cu at λ = 1.54061 Å, powered at 45 kV – 40 mA, scanning range 4 – 100º with a 0.017º 2θ step scan and a 50 s measuring time). Identification and semiquantitative evaluation of phases has been made on PANanalytical X'Pert HighScore software.

Rietveld refinement of selected samples has been performed using FullProf v3.0 software (Rodríguez-Carvajal, 1993). Some of these samples have been mixed with 30 wt% ZnO as an internal standard for the quantification of the amorphous phase.

3.2.7 Glass synthesis

The mineralogical evolution during the heating treatment of selected samples was determined by X-Ray Diffraction (XRD) carried out under vacuum atmosphere in an Anton Paar HTK1200N High Temperature chamber (HT-XRD), coupled to a PANalytical X′Pert PRO MPD Alpha1 powder diffractometer in Bragg-Brentano θ/2θ geometry (radius of 240 mm), Cu $K_{\alpha1}$ radiation (λ=1.5406Å), work power 45 kV–40 mA, scanning range 4–80° 2θ with step size of 0.017° and measuring time 50 s. The sample was placed in a Pt sample holder. The temperatures of spectra acquisition are detailed in the corresponding sections. In all cases, they include a spectrum before heating and a final spectrum after the cooling cycle. 7 spectra have been taken at each of the temperatures of interest. Data from the HT-XRD patterns were used to determine how the intensity of certain peaks varies with temperature as well as to calculate the coherent size of the crystallites of each mineral phase nucleated during the thermal treatment from Scherrer's equation (Equation 3.1) (Monshi et al., 2012).:

Equation 3.1

$$\tau = \frac{K\lambda}{\beta \cos\theta}$$

In this equation τ stands for the average size of the crystalline domains; K is a dimensionless shape (0.9), λ is the X-Ray wavelength (1.5406); β is the full width of the peak at half maximum minus the instrumental line broadening, in radians; and θ is the Bragg angle – in radians.

3.2.8 Glass synthesis

Hot-Stage microscopy is an indirect experimental method for the determination of the evolution of viscosity as a function of temperature. It consists on the observation of the deformation of a powdered glass cylinder during a heating cycle. The variation of the shape of the cylinder as viscosity decreases is independent of the chemical composition of the sample. Certain shapes correspond to the fixed viscosity points, and thus have been assigned viscosity values (Pascual et al., 2001). They are summarized in Table 3.4 and Figure 3.5.

The cylinders are prepared by binding about 45 mg of powdered glass (diameter <45 μm) in a uniaxial press with a 1/20 solution of Elvacite®. Test tubes are heated at 5ºC/min up to 1450ºC in air. This process is recorded with ProgRes Capture Pro software and the picture analysis is performed using Hot-stage software (Garcia-Valles et al., 2013).

Fixed viscosity point	Viscosity (Pa·s)
First shrinkage	$10^{7.9}$
Maximum shrinkage	$10^{6.9}$
Softening	$10^{5.6}$
Half ball	$10^{3.5}$
Flow	$10^{2.1}$

Table 3.4 Fixed viscosity points of HSM (Pascual et al., 2001)

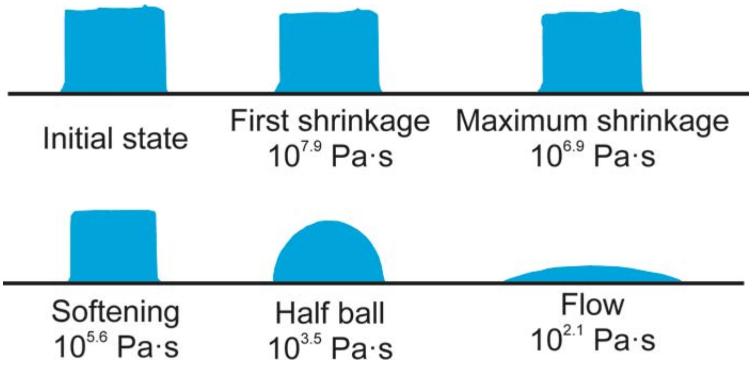

Figure 3.5 Shapes of the deformed cylinder at each fixed viscosity point.

The images during the heating cycle have been obtained using a prototype HSM at the DMPGA equipped with a Jenoptik ProgRes CT3 camera and ProgRes Capture Pro software version 2.9.9. The process is recorded by taking a picture every 3 min until shrinking starts. The acquisition is then changed to every 3 s (which is the maximum period of the equipment).

The treatment of the recorded images has been done using the Hot-stage software (Garcia-Valles et al., 2013). This software measures the evolution of certain parameters (height, width…) of the sample to measure its deformation. The viscosity-temperature curves are then plotted using the values of the fixed viscosity points.

HSM offers a fast method for the determination of viscosity. However, as analysis is performed during a single heating cycle, it is impossible to avoid the crystallization range of the studied glasses.

3.2.9 Raman spectroscopy

Raman spectroscopy in standard conditions requires no preparation apart from having a fragment of the material that is small enough to fit in the microscope. Although Raman spectroscopy is not as specific as XRD in the identification of mineral phases, it is much more sensitive to nanoscale ordering, hence it can show the onset of crystallization processes.

Raman spectra have been obtained at IPGP using a T64000 Jobin-Yvon Raman spectrometer equipped with a CCD detector. The light source is an Ar^+ ion laser operating at 488 nm with a typical output of 100 mW on the sample. The integration time is 300 s and the spectral range is between 100 – 1500 cm^{-1}. The spectra have been subtracted a splines baseline using as explained by (Di Genova et al., 2015), treated with the Long correction (Long, 1977; Neuville et al., 2014b) and normalized to the total area with the Fityk software (Wojdyr, 2010). The changes in the Raman spectra due to subtracting a background change the height of the phenomena, but their position is unmodified.

3.2.10 Mössbauer spectroscopy

The Fe environment and redox ratio of selected samples have been analyzed by Mössbauer spectroscopy at the Departament de Física of the Universitat Politècnica de Catalunya. Room temperature Mössbauer spectra have been collected in transmission geometry over the velocity range ±4 mm/s using a constant acceleration spectrometer, with a 25 mCi source of $^{57}Co(Rh)$. Several sets of paramagnetic doublets have been fitted to the spectra, using a Voigt curve profile with a natural width (half with at half maximum of 0.24 mm/s) (NORMOS programs R.A. Brand, Laboratorium fur Angewandte Physik, Univ. Duisburg) to take into account the Gaussian distribution of hyperfine parameters associated to the variability of sites due to cation substitution in crystalline structures and in disordered and glass structures. The hyperfine parameters fitted for each doublet are the isomer shift (IS), relative to α-Fe, the quadrupole splitting (QS) and the full width at half maximum of the absorption lines (Γ). The Fe^{2+} and Fe^{3+} ratios with respect to total Fe, are based on fitted peak areas.

3.2.11 Density measurements

The density of the glasses of this study has been measured at IPGP using the Archimedean method. It based on the displacement of a volume of liquid during the immersion of a solid being equal to the volume of this solid. Toluene – the immersion liquid – is an appropriate solvent because it does not react with glasses and it has a high wetting power.

The only sample preparation that may be involved is breaking the glass into fragments small enough to fit the basket of the experimental setting. Density measurements are an ~~excellent~~ probe for the homogeneity of glasses.

The variation of the density of toluene with temperature is corrected using

Equation 3.2

$$\rho_t = 0.8845 - 0.9159 \cdot 10^{-3} T + 0.368 T^2$$

where T is the temperature in ºC.

Al least ten glass fragments of each composition have been weighted in air and then immersed in toluene. According to Archimedes' principle, glass density will be obtained from

Equation 3.3

$$\rho_g = \frac{\rho_t \cdot m_a}{m_a - m_t}$$

where ρ_g stands for the density of the glass, m_a is the mass of the fragment in air and m_t is the mass of the glass when it is fully immersed in toluene.

3.2.12 Microhardness Vickers

The microhardness of the samples has been analyzed on the polished glass probes previously used for EMPA. The measurements have been performed in a Galileo Isoscan OD Vickers microindenter at the Departament de Ciència de Materials i Enginyeria Metal·lúrgica (Facultat de Química, UB). The measurements have been performed by applying loads between 100-300 g during 15 s. The actual value of the load does not affect the measurement as long as the sample is not fractured.

3.2.13 Leaching tests

Elementary analysis of the leachates are used to evaluate the stability of the glasses and glass-ceramics according to DIN 38414-S4 (DIN-38414S4, 1984). The test is performed in 10 g of dried sample (particle size between 2 and 4 mm), mixed in 100 mL of deionized water. The mixture is agitated in a rotating shaker at room temperature during 24 h and the liquid is separated from the solid using a 0.45 μm pore size filter. The leachates have been analyzed by at CCIT-UB inductively coupled plasma optical emission spectrometry (ICP-OES, Optima 3100×, PerkinElmer) and inductively coupled plasma mass spectrometry (ICP-MS, Elan 6000, PerkinElmer).

CHAPTER 4 Phosphorus solubility in basaltic glass: limitations for phosphorus immobilization in glass and glass-ceramics

Ohne Phosphor, Kein Gedanke

(Without phosphorus there would be no thoughts)

Ludwig Büchner

4.1 Introduction

Vitrification is a widespread inertization technique that can be applied to the remediation of both hazardous and non-hazardous wastes to reduce the volume of the disposal material (and thus the necessity of landfills) and to immobilize the toxic elements of the raw waste in the glass structure. Several examples of inertization by this approach can be found in the literature: polluted soils (Careghini et al., 2010; Navarro et al., 2013), radioactive wastes (Ciecińska et al., 2015; Davydov et al., 1996; Hrma et al., 2014; Pioro et al., 2001), incineration ashes (Cheng, 2004; Cheng et al., 2002; Haugsten and Gustavson, 2000; Jung et al., 2005; Kavouras et al., 2003; Romero et al., 2001). The production of glass-ceramics from these glasses enables further inertization due to the emplacement of toxic elements in the structure of minerals (Binhussain et al., 2014; Garcia-Valles et al., 2007; Mymrin et al., 2014; Varitis et al., 2015). The glass-ceramic process also provides recycled materials with superior mechanical properties (Marinoni et al., 2013; Teixeira et al., 2014). These glasses and glass-ceramics – apart from those made using radioactive wastes – may have applications in the building industry such as pavements or wall covers (Romero and Rincón, 1997).

Sewage sludges (SS) from urban wastewater treatment plants (UWWTP) have a good potential as one of the raw materials for an inertization matrix because their compositions are roughly similar to that of basalt (Rincon, 2016) (Table 1). This matrix could be tested to host contaminant and hazardous wastes like galvanic sludge (Garcia-Valles et al., 2007). However, the higher abundance of some elements, such as phosphorus and calcium, in the sludge compared to basalts or any natural igneous system requires experimental studies to understand how the compositional variation affects their properties and their long-term stability.

Phosphorus is an essential nutrient, as it is present in the structure of several biomolecules such as DNA or RNA, in cell membranes, and in the inorganic fraction of bone. Low phosphate levels limit the growth in both terrestrial and aquatic systems, hence the amount of soil phosphate has long been complemented using fertilizers. Sewage sludge may be a substitute for these (European Council, 1986). However, an exceeding amount of phosphorus may cause two environmental issues:

1. Euthrophication: excessive growth of algae and aquatic plants due to a great supply of nutrients resulting in oxygen overconsumption and depletion. Hypoxic conditions cause animal death and stop biological purification of water (Correll, 1998; Werner, 2012). It is considered the greatest threat for surface waters worldwide.
2. Heavy metal input in the soil due to high Cd contents in fertilizers (Werner, 2012).

The application of sewage sludge in agriculture is then limited and requires additional recycling methods (Mininni et al., 2015).

In rock-forming silicate melts, the effect of phosphorus on both melt structure and properties is considered of great importance despite its scarcity (natural igneous melts usually have less than 1 wt% P_2O_5) because it has a strong influence on phase relationships, physical and chemical properties (Dupree et al., 1989; Gan and Hess, 1992; Mysen et al., 1981; Ryerson and Hess, 1980; Toplis et al., 1994a; Wyllie and Tuttle, 1964). Even small amounts of P_2O_5 may cause structural variations in the liquid that alter the values of the trace-element partition coefficient by tenths percent (Ryerson and Hess, 1978). The addition of phosphorus to silicate melts is known to influence a number of properties and processes, including the redox state of iron, viscosity and density (Toplis et al., 1994a), the formation of an immiscibility gap (Wyllie and Tuttle, 1964), the shifts of the liquidus boundary of the silicate minerals, an increase in the silica activity coefficient and the expansion of the liquid immiscibility volume (Ryerson and Hess, 1980).

This paper focuses on the addition of phosphorus to basalt to simulate the inertization of sewage sludge, an appropriate glass-making composition due to its low viscosity at high temperature (<1300°C). The amount of P that may be bound in basalt is established by determining its solubility in the melt together with an analysis of the structure, thermal evolution, rheological behavior, and macroscopic properties in order to constrain the production process. The obtained materials underwent hardness and chemical resistance tests to establish potential uses.

4.2 Experimental methods

4.2.1 Choice of compositional range

The chemical compositions of a series of sewage sludge (SS) from wastewater treatment plants (WWTP) and a basalt from Sant Joan les Fonts (Girona, Catalonia) (Table 1) have been analyzed by X-ray fluorescence (XRF), using a sequential X-ray spectrophotometer Phillips PW2400. The range of phosphorus concentration in sewage sludge has been complemented with data from the literature (Borowski et al., 2014; Folgueras et al., 2003; Forsberg and Ledin, 2006; Hossain et al., 2009; Kikuchi, 1998; Montero et al., 2009; Roig et al., 2012; Wang et al., 2008). Its maximum is 32.98 wt% P_2O_5 (Wang et al., 2008).

4.2.2 Glass production

A basaltic rock of La Garrotxa (Girona, Catalonia) is doped with $NH_4H_2PO_4$ (ADHP, Reag-Ph.Eur, PA-ACS 131126.1211) to simulate a SS-like matrix. The mixtures are homogenized in a ball mill for 30 min and melted in a Pt-Rh crucible placed inside a globular alumina furnace equipped with SuperKanthal™ heating elements and an Eurotherm® 902 programmer. Each sample is heated at 200 ºC for 2 h to decompose the ADHP and then above the melting point at 1450 ºC, for 4h. Part of the quenched glass has been annealed for 12 h at 500 ºC.

Some mg of each glass have been remelted at 1450ºC and 1600ºC using a Pt-Rh alloy wire heating system originally designed to obtain spectroscopic data of silicate melts at high temperatures (Mysen and Frantz, 1992; Neuville et al., 2014b; Neuville and Mysen, 1996). The wires have previously been calibrated using salts with known melting points in order to achieve reliable determination of temperature.

4.2.3 Electron microscopy

Textural information and qualitative punctual chemical analysis of the glasses and the crystalline phases formed during production have been obtained using a JEOL J-7100 field emission scanning electron microscope with EDS detector and backscattered electron detector (FE-SEM-EDS). A thin section of the sample most enriched in P (labeled B32P) has been analyzed using a Hitachi H-800-MT transmission electron microscope (TEM) with energy dispersed analysis of X-rays (EDX), operating at 200 kV in STEM mode using the dark field detector. The beam size used in this mode is around 15 nm. The spectrometer is an Oxford Instruments INCA x-sight, with Si (Li) detector. The map acquisition is accomplished using the INCA Microanalysis Suite, software version 4.09. X-ray maps are obtained selecting the characteristic X-ray peaks for Si, Al, Ca, Fe, Mg and P.

4.2.4 Density measurements

The densities of glass fragments are measured with the Archimedean method using toluene as the immersion liquid. The masses of several glass fragments are measured in air (M_a) and in toluene (M_t). The variation in the density of toluene, ρT, is corrected using the temperature T of toluene and its equation of state. The density of the glasses is calculated using the following equation $\rho = M_a * \rho T / (M_a - M_t)$.

4.2.5 Raman spectroscopy

Raman spectra are obtained using a T64000 Jobin-Yvon Raman spectrometer equipped with a CCD detector. The light source is an Ar^+ ion laser operating at 488 nm with a typical output of 100 mW on the sample. The integration time is 300 s and the spectral range is between 100 – 1500 cm^{-1}. The spectra are treated with the Long correction (Long, 1977; Neuville et al., 2014b) and normalized to the total area.

4.2.6 Thermal Analysis

Crystallization temperatures during thermal treatments have been determined using Differential Thermal Analysis (DTA) in a Netzsch STA 409 vertical furnace. The experiments have been performed using Pt-Rh crucibles in air, with a flow rate of 80 mL/min and a heating rate of 10ºC/min from room temperature to 1300ºC followed by free cooling. The reference material is aluminum oxide 0419-0197 from Perkin Elmer.

4.2.7 X-Ray diffraction

X-Ray diffraction has been used both to assess the amorphous character of the glasses right after production and to determine which phases crystallize during thermal treatments. X-Ray diffraction spectra have been obtained from powdered samples (particles under 45 µm) in a Bragg-Brentano PANAnalytical X'Pert Diffractometer system (graphite monochromator, automatic gap, Kα-radiation of Cu at λ = 1.54061 Å, powered at 45 kV – 40 mA, scanning range 4 – 100º with a 0.017º 2θ step scan and a 50 s measuring time). Identification and semiquantitative evaluation of phases has been made on PANanalytical X'Pert HighScore software.

4.2.8 Dilatometry

Glass transition temperature (Tg) has been obtained by dilatometry in a Linseis L76/1550 horizontal dilatometer. 20 mm long bars were cut from each glass, then placed in the sample carrier and heated up to around 750ºC at 10ºC/min. When samples are too viscous to be cast into bars the analysis is performed in powdered glass, inside a SP5856/3605/10 sample carrier. A value of 10^{12} Pa·s has been assigned to Tg (Yue, 2008).

4.2.9 Hot-stage microscopy

The temperatures of the fixed viscosity points (Pascual et al., 2001) for Hot-Stage Microscopy (HSM) are determined by optical observation of the deformation of 3 mm-high test tube conformed using powdered glass (<45 μm) bound in a uniaxial press using a 1/20 solution of Elvacite®. Test tubes have been heated at 5ºC/min up to 1450ºC in air. The process is recorded with ProgRes Capture Pro software and the picture analysis has been performed using Hot-stage software (Garcia-Valles et al., 2013). The error in the determination of temperature using this method is ± 10 ºC (Pascual et al., 2001).

4.2.10 Microhardness

The microhardness of the samples has been measured on polished glass probes using a Galileo Isoscan OD Vickers micro-indenter with a load of 300 g.

4.2.11 Leaching tests

The elementary analysis of the leachates has been used to evaluate the stability of the glasses according to DIN 38414-S4 (DIN-38414S4, 1984). The test has been performed in 10 g of dried sample (particle size between 2 and 4 mm), mixed in 100 mL of deionized water. The mixture is agitated in a rotating shaker at room temperature during 24 h and the liquid is separated from the solid using a 0.45 µm pore size filter. The leachates have been analyzed by inductively coupled plasma optical emission spectrometry (ICP-OES, Optima 3100×, PerkinElmer) and inductively coupled plasma mass spectrometry (ICP-MS, Elan 6000, PerkinElmer).

4.3 Results

1.1.1 Sewage sludge compositions

The chemical compositions of a series of sewage sludge from UWWTP are presented in Table 4.1. The main components of the sludge are Al_2O_3, SiO_2, CaO, Fe_2O_3 and P_2O_5. The high amount of P – common in urban sewage sludge – is due to the predominance of porcine farming in the source area. The abundance of Al_2O_3, SiO_2 and Fe_2O_3 supports the use of basalt as an analogous. Low concentrations of silica could be increased by adding low cost wastes such as spent foundry sands, which typically contain about 88 wt% of silica (Siddique et al., 2010)

	Centelles	Vic	Taradell	Torelló	Manlleu	Tona	Prats	Roda	St. P. Ribes	Basalt
Al_2O_3	10.40	10.55	11.29	5.35	9.92	11.20	11.35	9.86	13.71	14.37
SiO_2	16.60	17.45	24.19	10.54	19.49	23.59	20.69	18.33	31.6	44.63
CaO	21.25	19.64	14.92	14.34	21.46	22.4	18.85	18.61	30.27	10.26
TiO_2	0.80	0.59	0.75	0.41	0.61	0.96	0.57	0.59	2.00	2.55
Na_2O	1.94	2.19	2.97	1.09	1.27	1.64	1.53	1.85	1.53	3.36
MgO	3.94	3.04	2.35	2.15	2.91	4.85	3.00	3.23	3.36	10.20
MnO	-	0.25	-	-	-	-	-	0.16	0.00	0.17
Fe_2O_3	16.96	21.17	19.97	37.16	18.37	3.03	17.01	20.73	4.32	12.86
K_2O	4.00	1.26	3.00	1.63	2.39	7.22	4.04	2.36	1.80	2.01
P_2O_5	22.29	17.52	19.56	25.64	22.57	23.78	21.15	20.29	7.74	0.56
SO_3	0.92	1.61	0.16	0.37	-	0.38	0.18	0.46	2.86	-
Cr_2O_3	-	3.93	-	0.13	-	-	0.86	2.22	0.00	0.04
NiO	-	-	-	0.13	-	-	0.14	-	0.82	0.02
CuO	0.32	0.28	0.33	0.2	0.15	-	0.27	0.42	0.10	0.01
ZnO	0.18	0.31	0.16	0.63	0.21	0.23	-	0.65	-	0.01
SrO	0.24	0.23	0.16	0.23	0.36	0.58	0.23	0.23	0.12	0.10
BaO	0.17	-	0.18	-	0.29	0.14	0.12	-	0.12	0.07

Table 4.1. Chemical composition (wt%) of sewage sludge from wastewater treatment plants in Catalonia and the basalt used as a raw material for the production of glass. The WWTPs are identified by the name of the town they serve.

4.3.12 Texture and density: effect of P on the homogeneity of the glasses

The nominal compositions of the glasses are shown in Table 4.2. In the glasses with more than 8 wt% P_2O_5 phase separation process – observed by the presence of two phases of different average atomic number in the backscattered electron mode of SEM and TEM (Figure 4.1 and Figure 4.2) – prevents obtaining consistent experimental bulk chemical compositions. However, the calculations are considered accurate because there is no significant weight loss during melting. The relative concentrations of Al_2O_3, CaO, Na_2O and K_2O correspond to the metaluminous field ($[CaO]+[Na_2O]+[K_2O] > [Al_2O_3] > [Na_2O]+[K_2O]$).

wt%/Samples	Basalt	B0	B2P	B4P	B8P	B16P	B32P
Al_2O_3	14.37	14.37	14.08	13.8	13.22	12.07	9.77
SiO_2	44.63	44.63	43.74	42.85	41.06	37.49	30.35
CaO	10.26	10.26	10.06	9.85	9.44	8.62	6.98
TiO_2	2.55	2.55	2.50	2.45	2.35	2.14	1.73
Na_2O	3.36	3.36	3.29	3.23	3.09	2.82	2.29
MgO	10.2	10.20	10.00	9.79	9.38	8.57	6.94
MnO	0.17	0.17	0.17	0.16	0.16	0.14	0.12
FeO	11.88	11.88	11.64	11.41	10.93	9.98	8.08
K_2O	2.01	2.01	1.97	1.93	1.85	1.69	1.37
P_2O_5	0.56	0.56	2.55	4.54	8.52	16.47	32.38

Table 4.2. Nominal chemical compositions (wt%) of the major components of the glasses.

The glasses up to 4 wt% P_2O_5 are homogeneous at the SEM scale (Figure 4.1). At higher phosphorus contents, a dark light Si-rich phase separates from a bright heavy P-rich phase. At 8 wt% P_2O_5 the onset of this immiscibility can be observed in the form of a Si-rich groundmass where a P-rich liquid phase is segregating in the form of nebula-like clusters (Figure 4.1A). Further addition of phosphorus up to 16 wt% P_2O_5 causes the exsolution of larger, rounded P rich regions from the Si - P groundmass (Figure 4.1B). In this case, circular Si-rich areas separate inside the P-rich region. At 32 wt% P_2O_5 the groundmass is constituted by a Ca-Mg-Fe phosphate phase, which encloses dark circular Si-rich areas (Figure 4.1C). The boundaries between the two regions are sharp. Dendritic stanfieldite ($Ca_4(Mg^{2+}, Fe^{2+}, Mn^{2+})_5(PO_4)_6$) crystals have grown due to the crystallization of the phosphorus-rich region (Figure 4.1D). The overall P-rich phase dominates the mix in this case because the bulk amount of P_2O_5 in the glass exceeds that of SiO_2. Fe is associated to P due to the formation of Fe^{3+}-PO_4^{3-} complexes (Ryerson, 1985; Toplis et al., 1994a).

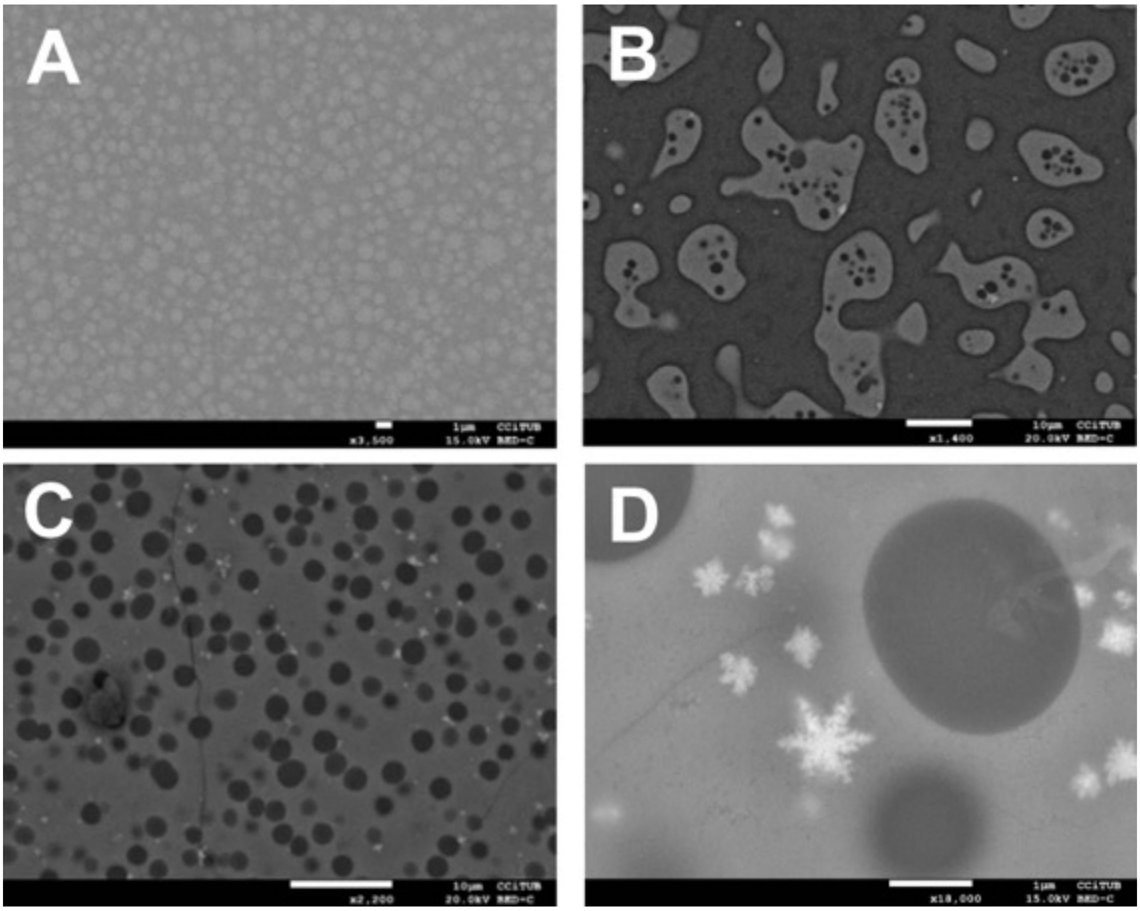

Figure 4.1. SEM micrographs of the immiscibility of a phosphate-rich and a silicate-rich phases upon phosphorus addition in as-quenched materials. A) Incipient separation in sample B8P. B) The phosphate phase coalesces and the separation with the silicate phase becomes sharper in sample B16P. C) The two phases are in mostly differentiated regions in sample B32P. D). Detail of the sharp separation between the silicate and the phosphate phases.

A characterization of the separation by TEM has provided the chemical compositions of the two unmixed phases in sample B32P (Figure 4.2a). The crystalline phosphate phase has an average of 28.56 mol% P_2O_5. Other major components are MgO (40.02 mol%), CaO (16.39 mol%) and Fe_2O_3 (3.86 mol%). According to these proportions, the limiting component in the crystallization of stoichiometric stanfieldite is CaO. The excess Mg^{2+} and PO_4^{3-} may be forming complexes. The phosphate phase also contains 4.43 mol% Al_2O_3 and 5.13 mol% SiO_2. The silicate phase is mainly constituted by SiO_2 (79.65 mol%) and Al_2O_3 (10.75 mol%), together with 5.31 mol% P_2O_5 and traces of the other components of the basalt. Compositional profiles on the location marked in Figure 4.2b show a sharp border between the two phases

(Figure 4.2c and d). Moreover, electron diffraction confirms that this phase is amorphous (Figure 4.2e). The elementary mapping undertaken in a region showing a whole sphere evidences that the aluminosilicate (Figure 4.2f and g) region is scarce in alkalis and alkaline earths that would act as charge compensators, and which lie mostly in the phosphate phase (Figure 4.2 i, j, k, l).

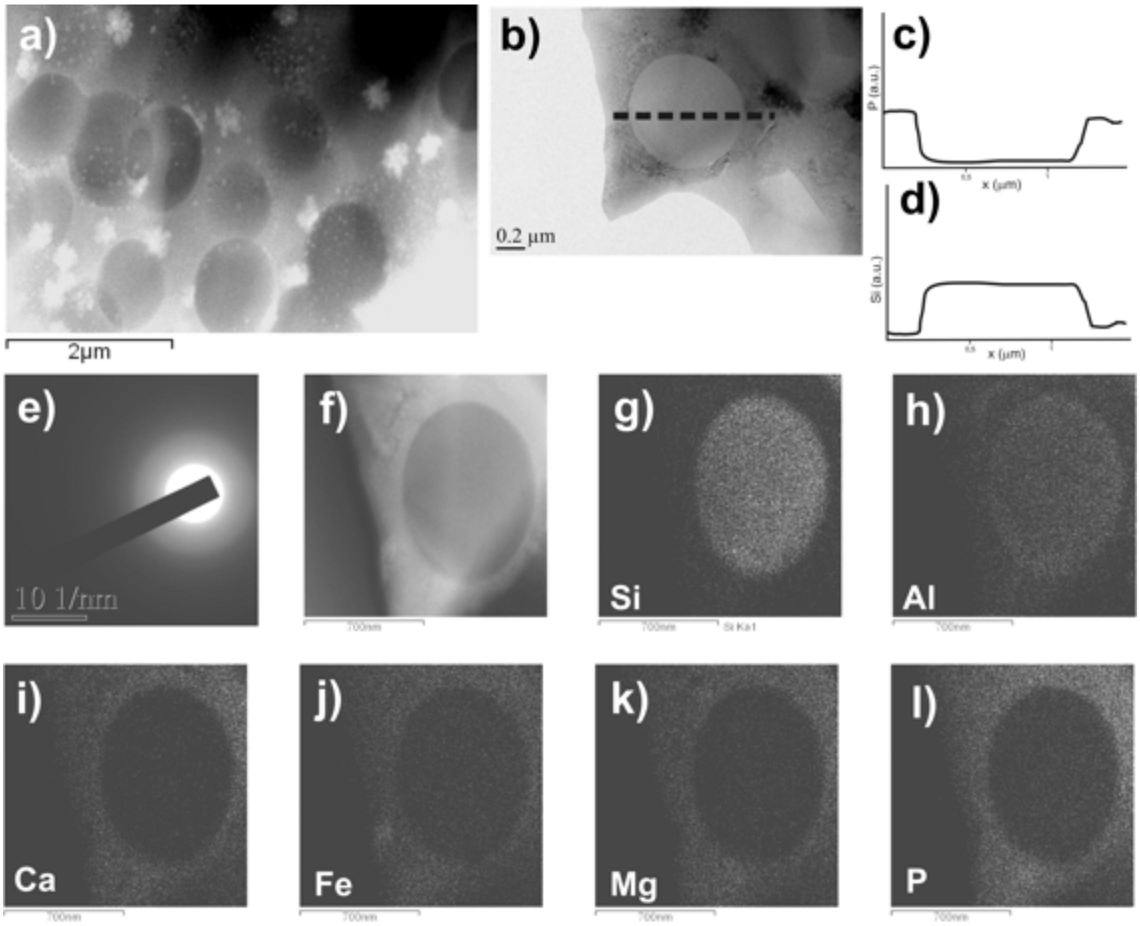

Figure 4.2. TEM micrographs showing the two unmixed phases in sample B32P (a), elementary composition profiles (b: measured profile, c: P profile; d: Si profile), the electron diffraction profile of the silicate phase (e), location of the mapping (f) and elementary mapping for Si (g), Al (h), Ca (i), Fe (j), Mg (k), P (l).

From this point, the materials of this study can be divided in two groups: samples bearing up to 8 wt% P_2O_5 are amorphous at the XRD scale, whereas the unmixed samples have to be considered glass-ceramics.

The addition of phosphorus causes a decrease in the average density of the basaltic glass due to the higher free volume of PO_4 tetrahedra compared to SiO_4 tetrahedra (Toplis et al., 1994a). Figure 4.3 presents the average densities and the standard deviation of the measurements on 10 different fragments of each composition (vertical error bars). It must be noted that the scatter of the density values shown by the error bars is much larger than the experimental error of ± 0.001 g/cm^3 of the density measurements. Moreover, it increases with P addition, reaching even 0.2 g/cm^3 in sample B32P. This variation of a macroscopic property within a single composition is an indicator of heterogeneities. Thus, the density of the bulk glasses and glass-ceramics actually corresponds to the contribution from the density of nuclei/crystals and the density of the amorphous phase. The higher density values correspond to glass shards enriched in crystalline material. For instance, the highest measured value for sample B32P is 2.95 g/cm^3, close to the actual density of stanfieldite, 3.15 g/cm^3.

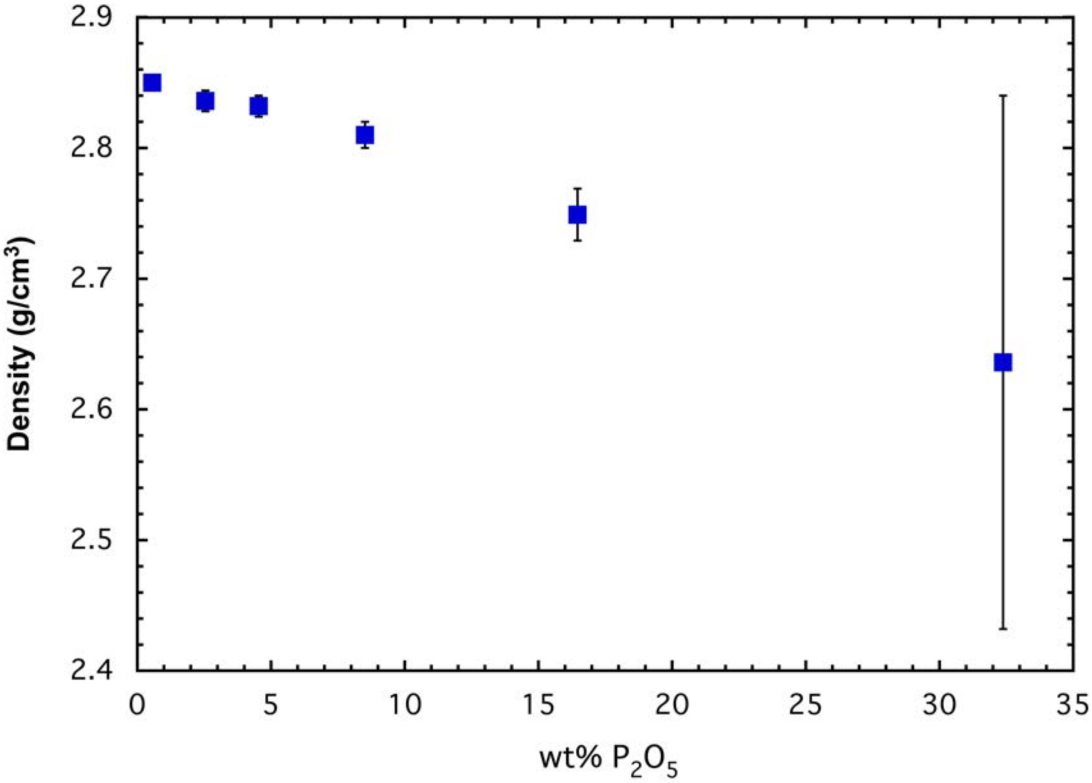

Figure 4.3. Average densities of the glasses. The error bars show the scatter of the measurements, due to the presence of nanocrystalline domains.

4.3.13 Raman spectroscopy: ordering at the nanoscale

Figure 4.4 shows the Raman spectra obtained at room temperature of small amounts of glass – some mg at most – molten on the heating wire (Neuville et al., 2014b). This melting process achieves faster cooling rates, thus providing a more amorphous material. All samples have been remelted at 1450 ºC (Figure 4.4a) and at 1600 ºC (Figure 4.4b).

Raman spectra of basalts are composed of 3 wide bands: the low frequency envelope (LF) from 200 to 600 cm^{-1}, the middle frequency envelope (MF) from 600 to 800 cm^{-1}, and the high frequency (HF) envelope from 800 to 1200 cm^{-1}. The narrow vibrations that arise from the major bands in the spectra account for the formation of nanocrystalline domains during the supercooling process.

In the series molten at 1450 ºC the main band around 673 cm^{-1} at low P contents corresponds to the A_{1g} vibration of magnetite (Shebanova and Lazor, 2003) and it masks the contributions of the LF and MF. These magnetite nanolites are not visible by classic electron microscopy observation because of its very small size. However, Neuville and coworkers identified a mix of magnetite and hercynite with a size of 10·10·5 nm in High Resolution TEM (Neuville et al., 1996). These nanolites might probably be the starting point of the nucleation process. At 8 wt% the bands seem to merge, showing the collapse of the glass structure. The band near 965 cm^{-1} is assigned to the ν_1 mode of crystalline phosphate (Penel et al., 1997); it becomes more intense and shifts to higher frequencies with increasing P. In the series molten at 1600 ºC (Figure 4.4b) the main feature is a band arising from the HF envelope at 965 cm^{-1}. As in the former case, it corresponds to a crystalline phosphate (Penel et al., 1997) of a high melting point. For instance, apatite has a melting point between 1608 and 1622 ºC (Bhatnagar, 1969). There is no evidence for the presence of magnetite – the melting point of pure magnetite is 1594 ºC (Deer et al., 1992).

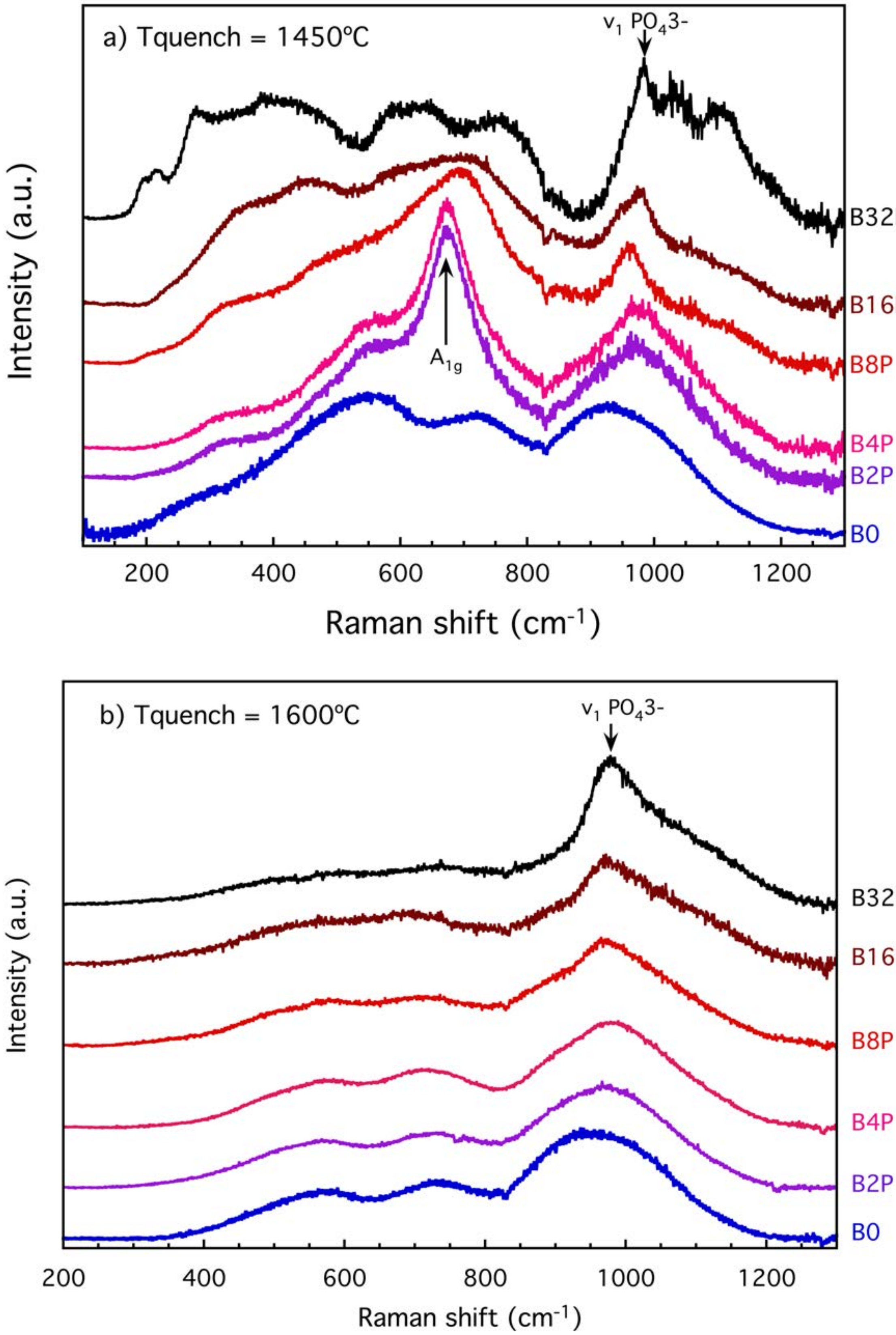

Figure 4.4. Raman spectra of the glasses remelted at a) 1450 ºC and b) 1600 ºC on the heating wire.

The LF envelope is generally assigned to vibrations of the bridging oxygens (BO) forming rings of three or more Si^{4+} tetrahedra (Bell et al., 1968; McMillan and Piriou, 1982; B. O. Mysen et al., 1980; Mysen, 2003; Neuville et al., 2014a; Neuville and Mysen, 1996; Pasquarello and Car, 1998; Seifert et al., 1982; Umari et al., 2003). A band below 800 cm^{-1} generally dominates the MF region and is attributed to the inter-tetrahedral bending mode of polymerized species. Its intensity decreases with decreasing silica content (Matson et al., 1983; McMillan, 1984a; Mysen and Toplis, 2007). The HF envelope contains the vibrations corresponding to the T-O^- bonds – T represents fourfold coordinated cations (mainly Si^{4+}, Al^{3+}, Fe^{3+} and P^{5+}) and O^- are the non-bridging oxygen – and the structural effect of the network-modifying or charge balancing cations (Bell and Dean, 1972; Cicconi et al., 2016, 2015; Cochain et al., 2012; Furukawa et al., 2011; Hehlen and Neuville, 2015; Magnien et al., 2008, 2006; McMillan, 1984a; Mysen, 2003; Neuville et al., 2014a). The LF asymmetric envelope is centered around 550 cm^{-1} and overlaps the MF region.

4.3.14 Thermal analysis and crystallization

The evolution of the thermal behavior and crystallization of the synthetic samples has been studied with a combination of DTA (Figure 4.5) and XRD (Figure 4.6). The DTA runs of the samples with low P contents show an exothermal event about 850 ºC that shifts to higher temperatures with increasing P (Figure 4.5). In the basalt glass (B0) the event is assigned to the crystallization of pyroxene and titano-magnetite ($Fe_{3-x}Ti_xO_4$). The addition of phosphorus destabilizes the pyroxene; rhönite ($Ca_2(Mg^{2+}\ Fe^{2+}\ Fe^{3+}\ Ti^{2+})_6(Si,Al)_6O_{20}$), a 4-chained inosilicate, is formed instead (Figure 4.6). Rhönite is considered a scarce mineral in magmatic rocks, although it is usually present in undersaturated alkali basalt. A common phase association in rocks of similar composition includes Ti-augite, olivine, nepheline, plagioclase, titanomagnetite and Ti-Ca-amphibole (Kunzmann, 1999). P preferentially stays in the amorphous phase at this stage. The formation of inosilicates and spinel-like phases such as titano-magnetite is interesting because they can host potentially toxic elements such as Zn, Cr, etc.

Further addition of P ≥ 8 wt% P_2O_5 changes the behavior of the melt as the phase separation starts. The main event corresponds to the crystallization of phosphate phase stanfieldite $Ca_4(Mg,Fe^{2+},Mn)_5(PO_4)_6$, that must form from the amorphous phosphate phase. Sample B16P lacks an evident exothermal event; the mineral content is limited to the stanfieldite formed during production. Sample B32P undergoes an exothermal event at 688 ºC corresponding to the crystallization of tridymite in the silicate phase. The virtual lack of crystallization of the last samples is consistent with the formation of a glass-ceramic during quenching.

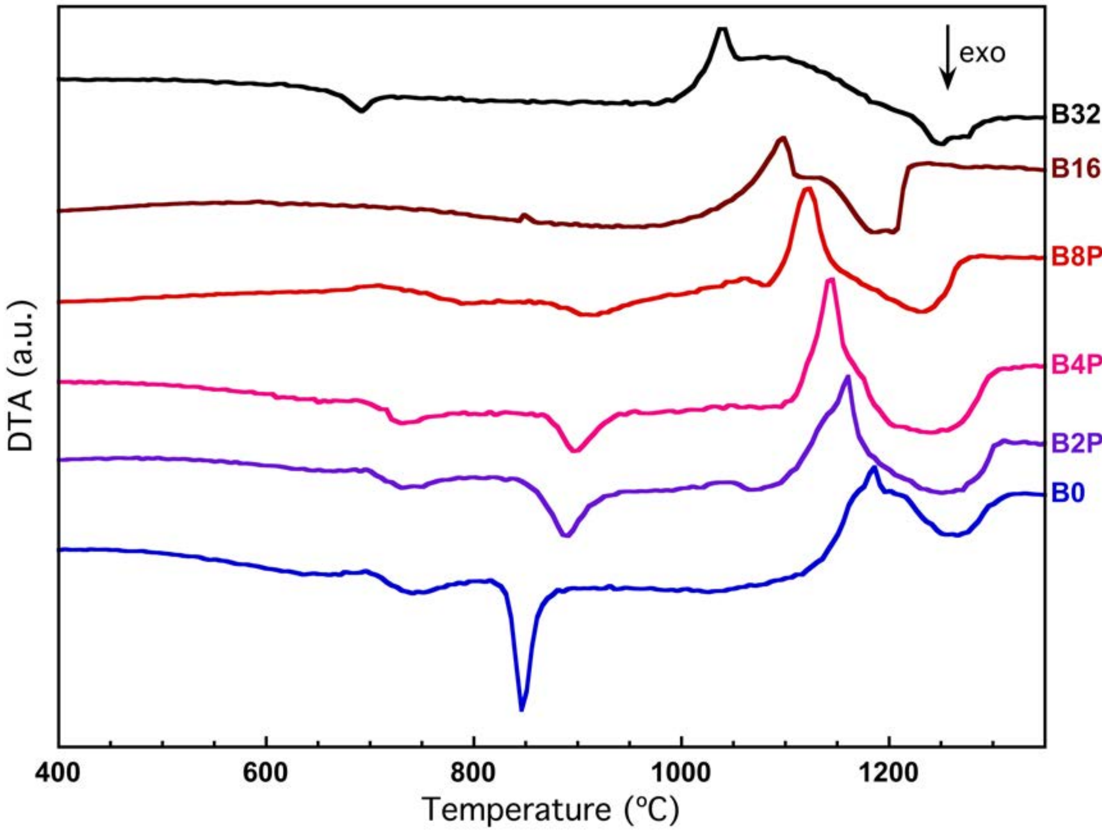

Figure 4.5. Evolution of the thermal behavior as a function of P contents. The experiments have been performed at a heating rate of 10 ºC/min.

The temperatures of the endothermal events linked to the melting of the system decrease around 170 ºC – from 1200 ºC in the glass of original basalt composition to 1031 ºC in the glass bearing the highest phosphorus concentration (Figure 4.5). The depression of liquidus temperature due to the presence of P in silicate systems has previously been reported in albitic and granitic melts, whose liquidus temperatures drop several degrees with P_2O_5

addition. For instance, the melting temperature of albite + 6 wt% P_2O_5 is 150ºC lower than that of the original albite (Wyllie and Tuttle, 1964). The phase diagrams of the pure $Ca_3(PO_4)_2$ - $Mg_3(PO_4)_2$ system show the eutectic melting of the stanfieldite composition at 1120ºC (Ando, 1958). Measured melting temperature is lower due to the higher number of components in the system, which causes impurities to enter the stanfieldite structure.

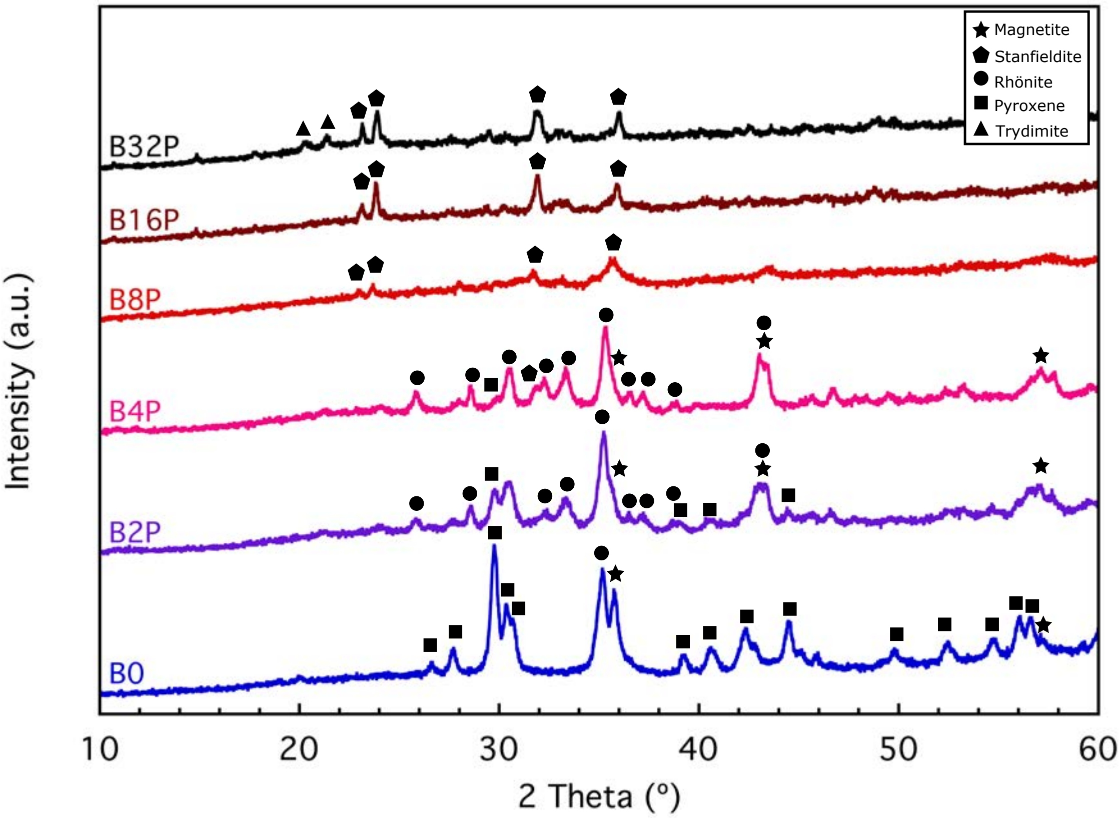

Figure 4.6. XRD patterns of the thermally treated glasses.

The mineral association constituted by pyroxene and magnetite has been described in studies about the crystallization of natural melts of basaltic composition (Burkhard, 2001; De Vicente Mingarro et al., 1991). The maximum concentration of P in magmas is around 2 – 3 wt% P_2O_5 (Mysen et al., 1999), hence, much lower than the maximum of 32 wt% considered in this study. Increasing P changes the thermal behavior due to the increasing crystallization upon glassmaking. The conditions leading to stability of stanfieldite destabilize the rest of mineral phases: at high P contents, Ca and Mg previously emplaced in the pyroxene structure move to the stanfieldite structure. Fe is also influenced by P both because Fe^{2+} can replace Mg^{2+} in the stanfieldite structure and because of the formation of Fe^{3+}-PO_4^{3-} complexes in the melt. This process also inhibits the crystallization of magnetite, which is consistent with the structural collapse observed on the Raman spectrum of sample B8P quenched at 1450 ºC (Figure 4.4a).

4.3.15 Rheological behavior and production process

Determining viscosity is essential in establishing the temperatures required for industrial glassmaking and processing. Table 4.3 summarizes the glass transition temperatures (T_g), the temperatures of the fixed viscosity points and the calculated temperatures corresponding to the viscosities of the workability points (annealing, forming, conditioning and melting ranges) (Fernandez Navarro, 1991). T_g values are around 640ºC.

Viscosity/Pa s	**B0**	**B2P**	**B4P**	**B8P**	**B16P**	**B32P**
T_g/10^{12}	629	637	639	643	643	650
First shrinkage/10$^{7.9}$	766	799	773	790	943	966
Maximum shrinkage/10$^{6.9}$	946	916	960	880	980	1069
Softening/10$^{5.6}$	1158	1048	1171	1049	1127	1200
Half ball/10$^{3.5}$	1220	1205	1284	1172	1219	1292
Flow/10$^{2.1}$	1254	1305	1317	1238	1276	1323
Annealing range/10$^{13.5\text{-}12}$	579-629	578-637	590-639	589-643	570-643	534-650
Forming range/10$^{8\text{-}3}$	763-1232	795-1241	769-1296	786-1196	838-1239	958-1303
Conditioning range/10$^{3\text{-}2}$	1232-1281	1241-1384	1296-1343	1196-1290	1239-1321	1303-1347

Table 4.3. Glass transition temperature, measured temperatures corresponding to HSM fixed viscosity points (according to Pascual et al 2001) and calculated approximative temperatures corresponding to viscosities which are significant for glass production.

Viscosities have been plotted as a function of the inverse of temperature (10000/T) of the fixed viscosity points of HSM and compared to viscosity measurements on remelted basalt from Piton de la Fournaise (GBa98) (Villeneuve et al., 2008) (Figure 4.7). The plots show an anomalous step in the decrease of viscosity during heating, especially remarkable below 10^8

Pa·s. The cause of the deviation is the growth of nuclei formed during glass production detected by Raman spectroscopy in melts quenched at 1450 ºC. These nuclei cause apparent viscosity to be higher than the actual viscosity of a crystal-free melt of the same composition due to the formation of a biphasic system. At the lower limit of the HSM experiments, the viscosity of the P-doped glasses is similar to that of the remelted natural basalt but at the upper limit – corresponding to the temperature of the flow point; the highest value being 1323ºC for sample B32P – the viscosity is significantly higher than that of the remelted basalt used for comparison.

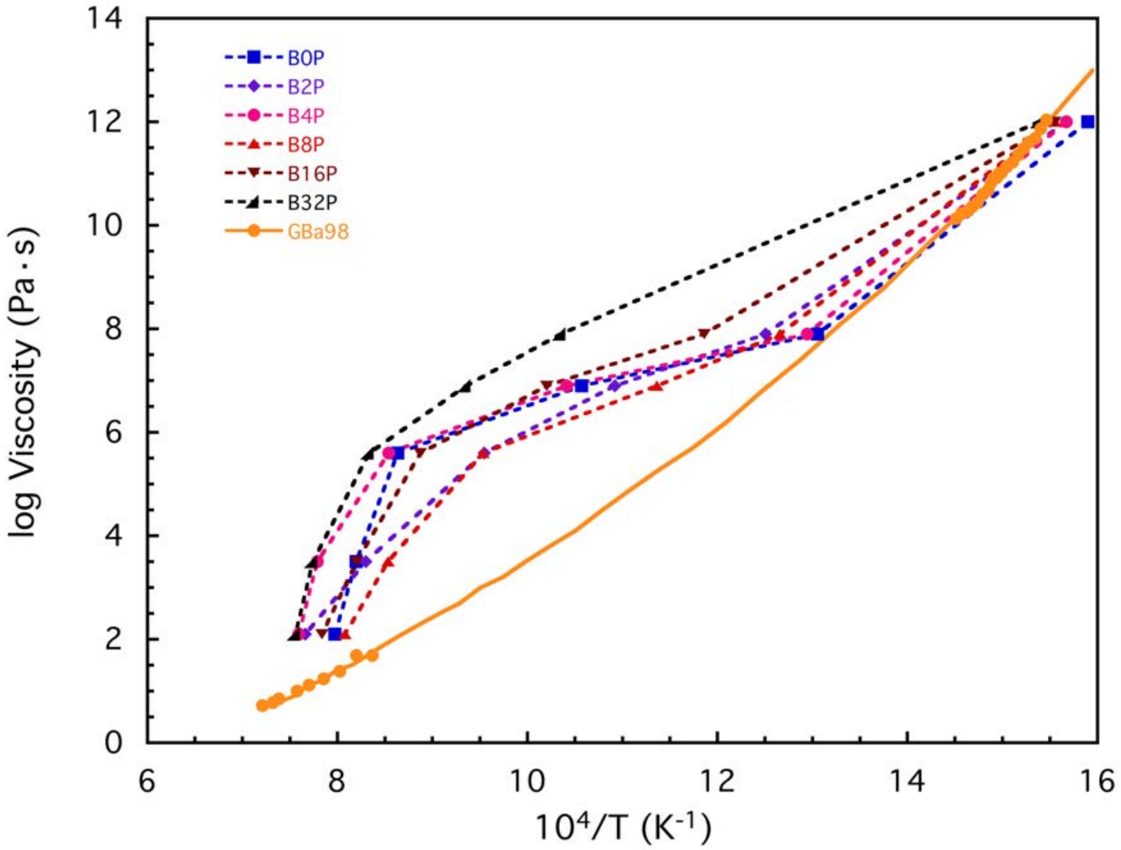

Figure 4.7. Plot of the viscosity as a function of the inverse of the temperatures of the fixed viscosity points of the glasses and viscosity-temperature curve of a remelted basalt (Villeneuve et al., 2008). Discontinuous lines are only intended as a guide for the eye.

The variations of viscosity as a function of phosphorus content are influenced by the phases that crystallize during the heating process and by the progress of the immiscibility. In samples from B0 to B4P, when phosphorus contents increase, the onset and the peak of the exothermic

(Figure 4.5) events shift to higher temperatures due to a delay in crystallization and the increase of apparent viscosity. However, this is in conflict with the increasing degree of crystallinity due to further P addition, which increases viscosity again. The phase separation is another major controller of the evolution of viscosity: in composition B8P the phosphate phase plays the role of a low viscosity liquid where the silicate regions are immersed. The apparent viscosity in compositions B16P and B32P rises again when both the immiscibility and the crystallinity of the phosphate phase increase.

At low concentrations and in depolymerized melts, phosphorus has been reported to cause a non-linear variation of viscosity. This is attributed to the competition between the depolymerizing effect due to the oxidation of Fe^{2+} – viscosity is decreased – and the polymerizing effect related to the removal of network-modifying cations and formation of Si-O-Si bonds creating highly polymerized regions caused by the addition of P – viscosity is increased (Toplis et al., 1994a). This behavior is absent in iron-free compositions; hence it must be attributed to the presence of Fe (Toplis and Dingwell, 1996). P also behaves differently in acidic than in basic melts. Viscosity has an Arrhenian decrease in P-doped haplogranitic melts with increasing P_2O_5 (Dingwell et al., 1993). This increase in viscosity may be attributed to copolymerization of P^{5+} in the silicate network rather than behaving as a network modifier (Ryerson and Hess, 1980). Another point is that the dependence of structural deformation on temperature seems to decrease with increased crystallization caused by P addition.

The melting temperatures during production have to be over the flow point (in this case between 1357 – 1411ºC). According to these results, a production temperature of 1450ºC would be appropriate to cover all the compositional range up to 4 wt% P_2O_5.

4.3.16 Microhardness

The possibility of using the new materials in the building industry depends on their mechanical properties. The average microhardness of the P-doped basaltic glasses decreases with phosphorus addition from 7.7 GPa in the basaltic glass to 5.4 GPa in sample B32P (Figure 4.8). These values are similar to the range of 5.16 – 6.28 GPa reported by

Mingarro (De Vicente Mingarro et al., 1991) and 7.7 GPa obtained by Jensen and coworkers (Jensen et al., 2009) for basaltic glasses. All these measurements lie in the range of the majority of conventional glasses and glass-ceramics (Evans and Wilshaw, 1976; Rincón and Capel, 1985). When analyzed in detail, the decrease of microhardness follows two different trends (Figure 4.8). It has a steep slope until the immiscibility begins; the gradient then becomes much smaller. This is consistent with the formation of a glass-ceramic during the quenching process. The formation of a crystalline phosphate improves the resistance of the final product. The decrease of hardness with P addition can be attributed to the inferior resistance of phosphate materials in comparison to silicates. The most common phosphate mineral, apatite, has a hardness around 5.2 GPa and stanfieldite ranges between 2.0 and 5.2 GPa. On the other hand, the hardness of silicate minerals such as quartz is much higher, between 10.82 and 12.36 GPa.

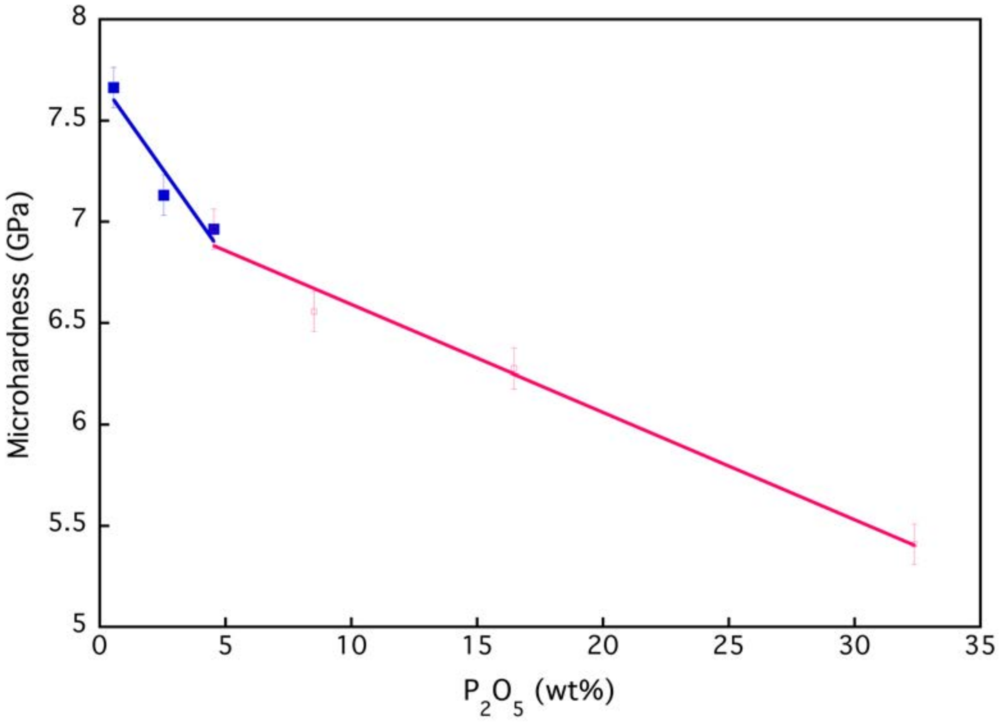

Figure 4.8. Microhardness (Vickers) of the obtained materials as a function of P contents. The change of the slope between the two fitted lines is due to the diminution in the decrease of microhardness caused by crystallization.

4.3.17 Chemical stability

The low chemical resistance of phosphate glasses has long been reported in the literature (Brow, 2000; Kreidl and Weyl, 1941), hence creating the necessity to verify that it does not increase the solubility of the basaltic glasses – as it is intended to use them as an inertization matrix. The elementary concentrations in the leachate of the major elements are generally lower than in the deionized water used as a blank (Table 4.4). Even Si and P, the two major elements, only leach some ppm's, accounting for the stability of the material. Considering the potentially toxic elements, the obtained glasses comply with the limits established in norm DIN 38414-S4 for them to be considered inert. Crystalline phosphate phases such as stanfieldite are considered stable in the long term in terrestrial soils (Qian and Jiang, 2014). However, it has to be noted that the amount of P in the leachate doubles between samples B16P and B32P. The leaching of Mg also follows this trend but neither Ca nor Fe do, thus the the leaching has to be limited to the excess unstable Mg^{2+}-PO_4^{3-} complexes. In exchange, the concentration of Si in the leachate increases from sample B0 to B2P and is then reduced as the immiscibility progresses, hence the silicate phase must be becoming more stable. This might signal the onset of the separation actually happens before it can be distinguished in SEM.

[ppm] in sol	**Si**	**Al**	**Ca**	**Mg**	**Na**	**K**	**Fe**	**P**
B0P	1.71	BDL	BB	0.96	0.20	0.23	BDL	BDL
B2P	2.47	BDL	BB	1.16	0.38	0.32	BDL	BB
B4P	2.19	BDL	BB	1.02	0.99	0.34	BDL	BB
B8P	1.67	BDL	BB	2.22	0.49	0.27	BDL	BB
B16P	1.28	BDL	BB	2.63	0.00	0.28	BDL	1.88
B32P	0.35	BDL	BB	3.44	0.06	0.09	BDL	3.83

[ppb] in sol	**As**	**Ba**	**Cd**	**Cr**	**Cu**	**Hg**	**Mn**	**Ni**	**Pb**	**Ti**	**Zn**
B0P	BDL	BB	0.14	BDL	4.03	BDL	BB	BDL	BB	26.14	BB
B2P	BDL	BB	BDL	0.67	BB	BDL	BB	BDL	BB	1.83	BB
B4P	BDL	BB	BDL	BDL	BB	BDL	0.42	BDL	BB	1.90	BB
B8P	BDL	BB	0.00	BDL	3.35	BDL	0.04	BDL	BDL	1.60	BB
B16P	BDL	BB	0.01	BB	BB	BDL	3.63	BDL	BB	4.80	BB
B32P	BDL	BB	BDL	BDL	BB	BDL	5.72	BDL	BB	42.71	BB
DIN38414-S4	500		40	500	2000	100		400	500		4000

Table 4.4. Elementary analysis of the leachates after immersion of glass bits in deionized water. BB stands for "below the blank" and BDL for "below detection limit".

4.4 Discussion: solubilization of P and immiscibility

It is possible to add large amounts of phosphorus to basaltic glass although it triggers a phase separation. Its development at high P_2O_5 concentrations causes the initially homogeneous glass to evolve into a glass-ceramic. The separation of silicate and phosphate phases can be interpreted in the framework of the Modified Random Network theory (MRN) (Greaves, 1985; Greaves et al., 1981; Le Losq et al., 2017). The MRN model states that in silicate glasses there is a segregation between the network formers (Si^{4+}, Al^{3+} and Fe^{3+}) and the network modifiers (the alkaline and alkaline earth cations) leading to the development of differentiated local structures, called percolation channels, at the nanometer scale (Greaves et al., 1981; Vessal et al., 1992). The formation of percolation channels around silicate tetrahedra is in itself an unmixing process because it separates the aluminosilicate region, rich in network formers (NF), from the network modifiers (NM).

The evolution of the system can be summarized in the following steps (Figure 4.9):

- From 0 to 4 wt% P_2O_5 the glasses are homogeneous (scheme 0). The T_g signal becomes less intense. There is a slight depolymerization related to the diminution of SiO_2 and no gain in polymerization due to the formation of phosphate chains.
- 4 < wt% P_2O_5 < 6 is the beginning of channel formation (scheme 1). Around 6 wt% the nucleation probably starts (scheme 2), hence at 8 wt% P_2O_5 the immiscibility can be observed in SEM although it is still XRD-amorphous. The presence of an amorphous phosphate phase decreases the overall viscosity.
- > 8 wt% the combination of immiscibility and nucleation results in increasingly pervasive nanocrystallization and growth in the phosphate phase (scheme 3-4). The formation of a glass-ceramic increases the viscosity of the melt. Crystallization improves microhardness and leachability compared to a scenario where the material stayed in glassy form. For instance, from the extrapolation of the trend of the decrease of microhardness at low P contents (Figure 4.8), the value of 5.40 GPa at 32 wt% P_2O_5 would be reached at 13.08 wt% P_2O_5 if crystallization had not occurred.

-

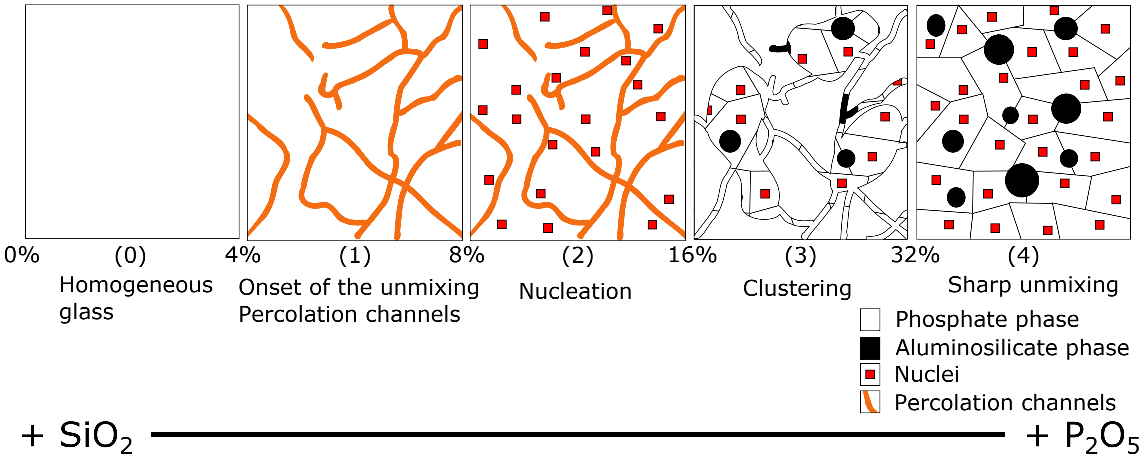

Figure 4.9. Scheme of the incorporation of phosphorus to the glass structure: from a homogeneous glass to a glass-ceramics.

The bulk compositions of the P-doped glasses and glass-ceramics lie in the metaluminous range ([CaO] + [Na_2O] + [K_2O] > [Al_2O_3] > [Na_2O] + [K_2O]). P^{5+} can form strong complexes due to its high field strength. Once formed, these complexes reside outside the silicate network. Divalent cations, in this case Ca^{2+}, Mg^{2+}, Fe^{2+} and Mn^{2+}, form stable complexes with P according to reaction (Ryerson and Hess, 1980):

$$2\text{Mg-O-Si} + \text{P-O-P} \leftrightarrows 2\text{Mg-O-P} + \text{Si-O-Si}$$

This reaction causes a polymerization of the network that enhances the separation of the aluminosilicate spheres (the NF-rich region of the MRN model) and decreases the activities of the NM due to the complexation with P (Gan and Hess, 1992). In the network modifier-rich region, the NM-phosphate groups are more extensive and may be acting as a precursor to the crystallization of stanfieldite that hosts all the main divalent cations in its structure $Ca_4(Mg,Fe^{2+},Mn)_5(PO_4)_6$.

The polymerization of the network progresses even further in the aluminosilicate region of sample B32P (around 80 mol% SiO_2, 11 mol% Al_2O_3 and 5 mol% P_2O_5) according to the reaction described by Gan and Hess for the solubilization of P in peraluminous melts of the $Al_2O_3 – SiO_2 – K_2O – P_2O_5$ system:

$$2\text{Al-O-Si} + \text{P-O-P} \leftrightarrows 2\text{Al-O-P} + \text{Si-O-Si}$$

where P reacts with excess Al to form $AlPO_4$ species, furthering the polymerization of the silicate network by creating silica-rich clusters (Gan and Hess, 1992). This high polymerization degree enables the spheres to stay amorphous. Although $AlPO_4$ units are electrically neutral, excess Al needs to be charge-balanced as there is a lack of alkali and alkaline-earth elements. This could be achieved by the formation of five- or six-fold coordinated Al (Neuville et al., 2006). An attempt to verify this affirmation by electron energy loss spectroscopy in the TEM equipment has been unsuccessful due to the insufficient concentration of Al.

Although it has not been possible to obtain direct evidence of this fact, the boost in viscosity would be consistent with unmixing beginning in the liquid state. The arrangement has to be either very fast to happen during the few seconds that the melt is effectively flowing or already present in the melt, which is consistent with sample B32P having the highest T_g and viscosity. P_2O_5

4.5 Conclusions

Basaltic liquids accept a certain amount of phosphorus, showing potential for the use of sewage sludge as a raw material in the production of glass. The immiscibility between an aluminosilicate and a Ca-Mg-Fe phosphate phase is the limit of single glass formation. After the separation, the phosphate phase will crystallize thus giving glass-ceramics that are capable of hosting and stabilizing large amounts of P.

The rheological behavior of the P-doped basaltic melts is controlled by the nucleation of magnetite and stanfieldite during the melting and the quenching processes. Subsequent growth of these nuclei increases the temperatures at which the viscosity of the melt reaches the forming and glass conditioning ranges (viscosities from 10^8 to 10^2 Pa·s).

The devitrification caused by thermal treatments is constrained by the liquid-liquid immiscibility. At low P contents the glass will crystallize into magnetite and either pyroxene or rhönite. This association stands out because of the possibility that further inertization could be achieved by means of a glass-ceramic process – due to the ability of inosilicates and spinel-like phases (magnetite) to host potentially toxic elements such as Cr or Ba. At high P contents the separation forces the crystallization of the phosphate rich phase into stanfieldite, whereas the silica rich phase mainly stays amorphous due to both its high Si contents and the lack of nucleating agents such as Fe or Ti.

The microhardness of the glasses is comparable to other petrurgic basaltic materials. According to the leaching tests, the glasses can be considered inert because the cations are bound in the structure of the glass especially at low P contents. The inertization of high amounts of phosphorus is possible because crystallization of a phosphate phase/stanfieldite buffers the loss of mechanical and chemical resistance typical of phosphate glasses.

CHAPTER 5 Fe in P-doped basaltic melts: a Mössbauer spectroscopy study

Do not wait to strike till the iron is hot;

But make it hot by striking

William Butler Yeats

5.1 Intoduction

Sewage sludge (SS) is a high volume, potentially toxic waste. The European Union proposes its use in agriculture in substitution of fertilizers due to its high concentrations of phosphorus and nitrogen when sludge complies with regulations on heavy metal contents (European Council, 1986). The two main alternatives are incineration and landfilling, which generate waste by-products, and space availability and cost issues respectively. Sewage sludge may be mixed with other toxic wastes such as waste mold sands to increase its silica contents and obtain a basalt-like composition to make a valorized product with potential applications in construction (Tarragó et al., 2018). Like basalt, SS-like melts vitrify easily due to their low viscosity above the liquidus and bind the toxic metals (Hannant et al., 2009, 2008). Moreover, basic melts may host phosphorus up to the wt% range. However, high concentrations of phosphorus have strong effects on glass structure (polymerization, immiscibility, redox ratio, and macroscopic properties (Mysen and Richet, 2005; Ryerson and Hess, 1980; Toplis et al., 1994a)).

P_2O_5 may alter the ratio of ferric to ferrous iron (Mysen, 1992) Phosphorus has the highest reducing power of all major cations in a ferrobasalt bearing up to 9.45 wt% P_2O_5 (Toplis et al., 1994a). Variations in the ferric-ferrous ratio significantly change both density and viscosity of iron-bearing silicate melts. Iron is generally assumed to have a dual role in glasses according to its oxidation state. In silicate glasses, Fe^{3+} is in tetrahedral coordination, acting as a network former, whereas Fe^{2+} is generally in octahedral coordination and plays the role of a network modifier (Mysen and Richet, 2005). In phosphate glasses, it is commonly found in distorted octahedral sites regardless of the oxidation state (Bingham et al., 2009).

The objective of this paper is to determine the effect of increasing phosphorus concentrations on the Fe environment and redox state of a series of P-doped basaltic glasses simulating environmentally-friendly glasses for the inertization of sewage sludge.

5.2 Materials and Methods

The P-doped basaltic glasses have been prepared from 100 g mixtures of basalt from Sant Joan les Fonts (Catalonia) and up to 32% of reagent grade $NH_4H_2PO_4$ (ADHP, Reag-Ph.Eur, PA-ACS 131126.1211). The samples are named BXP, where X stands for P_2O_5 concentration in wt%. Each sample has been heated at 200 ºC during 2 h to decompose ADHP and then at 1450 ºC for 4h in SuperKanthal® furnaces, using Pt-Rh crucibles, and under air atmosphere. All the melts have been cast in a Cu plate except B32P, which has been quenched by immersing the bottom of the crucible in water due to its inability to flow.

The chemical composition of the basalt has been analyzed by X-Ray Fluorescence as lithium tetraborate pearls, using a sequential X-ray spectrophotometer Phillips PW2400. Powder X-Ray diffraction (XRD) patterns have been acquired in a Bragg-Brentano PANAnalytical X'Pert Diffractometer.

Room temperature Mössbauer spectra have been collected in transmission geometry over the velocity range ±4 mm/s using a constant acceleration spectrometer, with a 25 mCi source of ^{57}Co(Rh). Several sets of paramagnetic doublets have been fitted to the spectra, using a Voigt curve profile with a natural width (half with at half maximum of 0.24 mm/s) (NORMOS programs R.A. Brand, Laboratorium fur Angewandte Physik, Univ. Duisburg) to take into account the Gaussian distribution of hyperfine parameters associated to the variability of sites due to cation substitution in crystalline structures and in disordered and glass structures. The hyperfine parameters fitted for each doublet are the isomer shift (IS), relative to α-Fe, the quadrupole splitting (QS) and the full width at half maximum of the absorption lines (Γ). The Fe^{2+} and Fe^{3+} ratios with respect to total Fe, are based on fitted peak areas.

5.3 Results and Discussion

The fitted Mössbauer spectra of the glasses are shown in Figure 5.1. The wide bands are consistent with the amorphous nature of the samples. The estimated Mössbauer parameters IS, QS and Γ are summarized in Table 5.1. The spectra corresponding to glasses B0-B4P show the overlapping of two doublets corresponding to Fe^{3+} and Fe^{2+} in the glass structure. The doublet with IS values between 1.04-1.05 mm/s and QS between 1.91-1.94 mm/s is assigned to Fe^{2+} in octahedral coordination. Besides, the doublet with IS of 0.19 mm/s and QS between 1.25-1.27 mm/s is assigned to Fe^{3+} in tetrahedral coordination. Iron is mainly present as Fe^{3+} and the total $Fe^{3+}/\Sigma Fe$ slightly increases (from 74 to 80 %) with the addition of P. The hyperfine parameters correspond well to Fe in a basaltic glass structure. Fe^{2+} in octahedral coordination is consistent with a network-modifying role. Fe^{3+} in a tetrahedral environment may be replacing Si^{4+} as a network modifier.

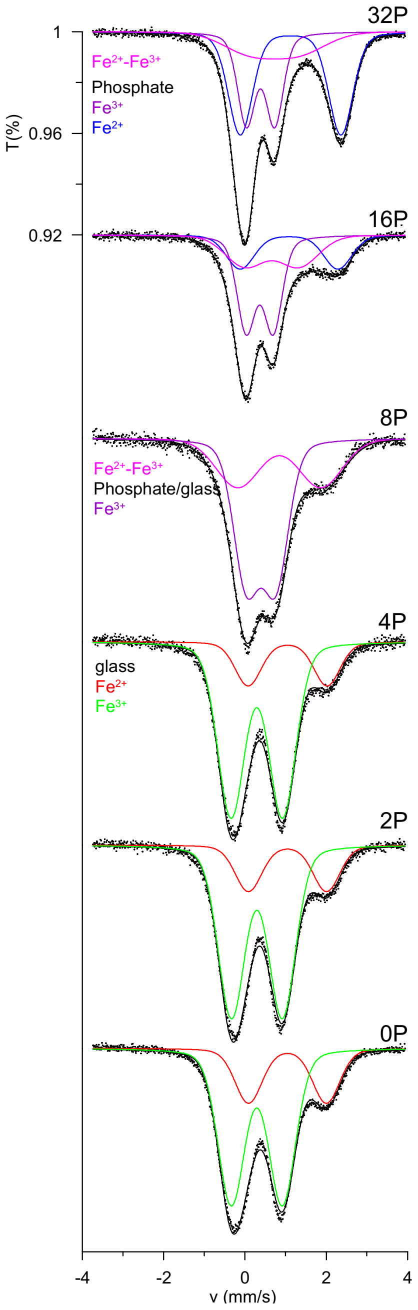

Figure 5.1. ^{57}Fe Mössbauer spectra of the glasses.

Increasing the P content up to 8% (B8P), two broad doublets can be observed. The first, with an IS of 0.40 mm/s and a QS of 0.72 mm/s is assigned to Fe^{3+} in octahedral coordination. The second, with an IS of 0.85 mm/s and a QS of 2.0 mm/s corresponds to a site where both Fe^{3+} and $Fe^{2+}$are present and consequently the hyperfine parameters show intermediate values corresponding to the phenomenon known as valence exchange. Similar parameters are often seen in oxide disordered and nano-sized structures. In the spectra corresponding to samples B16P and B32P, three doublets can be clearly identified (Figure 5.1). The first has an IS of 0.7 mm/s and a QS of 1.2-1.3; the second has an IS of 0.36-0-38 mm/s and a QS of 0.66-0-69 mm/s and the third has an IS of 1.08-1.12 mm/s and a QS of 2.40-2.48 mm/s. The last two correspond to Fe^{3+} and Fe^{2+} in octahedral coordination consistent with a crystalline phosphate with Mössbauer parameters similar to those of the alluaudite group -$NaCaFe^{2+}(Mn,Fe^{2+},Fe^{3+},Mg)_2(PO_4)_3$ (Dyar et al., 2014). In this case, the broadness of the peaks is due to Fe sharing its position with the other cations in the alluaudite structure. The first doublet showing intermediate $Fe^{3+}Fe^{2+}$ values correspond most probably to a disordered or nano-size oxide. The presence of a phase of this nature has been suggested in vitrified SS ash (Hannant et al., 2008).

a) wt%	Al_2O_3	SiO_2	CaO	TiO_2	Na_2O	MgO	MnO	FeO	K_2O	P_2O_5
Basalt	14.37	44.63	10.26	2.55	3.36	10.20	0.17	11.88	2.01	0.56

b)			B0	B2P	B4P	B8P	B16P	B32P
glass	Fe^{2+}	Γ	0.68(0.04)	0.67(0.03)	0.65(0.07)			
		IS	1.01(0.02)	1.05(0.02)	1.05(0.03)			
	(o)	QS	1.91(0.03)	1.92(0.04)	1.94(0.05)			
		%	26(1)	21(1)	20(1)			
	Fe^{3+}	Γ	0.67(0.01)	0.67(0.02)	0.68(0.02)			
		IS	0.19(0.01)	0.19(0.01)	0.19(0.01)			
	(t)	QS	1.25(0.01)	1.25(0.01)	1.27(0.02)			
		%	74(1)	79(1)	80(1)			
	Fe^{2+}-Fe^{3+}	Γ				1.2(0.2)	1.1(0.2)	1.5(0.2)
		IS				0.85(0.05)	0.7(0.1)	0.7(0.2)
		QS				2.0(0.2)	1.3(0.3)	1.2(0.6)
		%				36(5)	30(8)	20(5)
Phosphate	Fe^{3+}	Γ				0.64(0.04)	0.43(0.05)	0.40(0.04)
		IS				0.40(0.03)	0.36(0.04)	0.38(0.01)
	(o)	QS				0.72(0.03)	0.66(0.09)	0.69(0.03)
		%				64(4)	46(6)	32(4)
	Fe^{2+}	Γ					0.71(0.05)	0.60(0.04)
		IS					1.08(0.04)	1.12(0.01)
	(o)	QS					2.40(0.09)	2.48(0.03)
		%					24(6)	48(3)

Table 5.1.a) Chemical composition of the basalt. b) Hyperfine parameters of the fitted spectra. The statistical error is given as the standard deviation in brackets.

The formation of crystalline Ca-Mg-Fe anhydrous phosphates in B16P and B32P is consistent with the XRD spectra of the as-quenched glasses (Figure 5.2). Stanfieldite, $Ca_4(Mg,Fe,Mn)_5(PO_4)_6$ and Powder Diffraction File (PDF) 73-1182, is a phosphate found in stony-iron meteorites; unfortunately, there is no Mössbauer spectroscopy data in the literature. The composition of stanfieldite matches very well our basalts (~10% MgO, ~10% CaO and

~10% FeO). In addition, the broad reflection at 2Theta = 35.522º - the position of the 100% intensity peak of magnetite - consistent with a low crystallinity or nano-size phase.

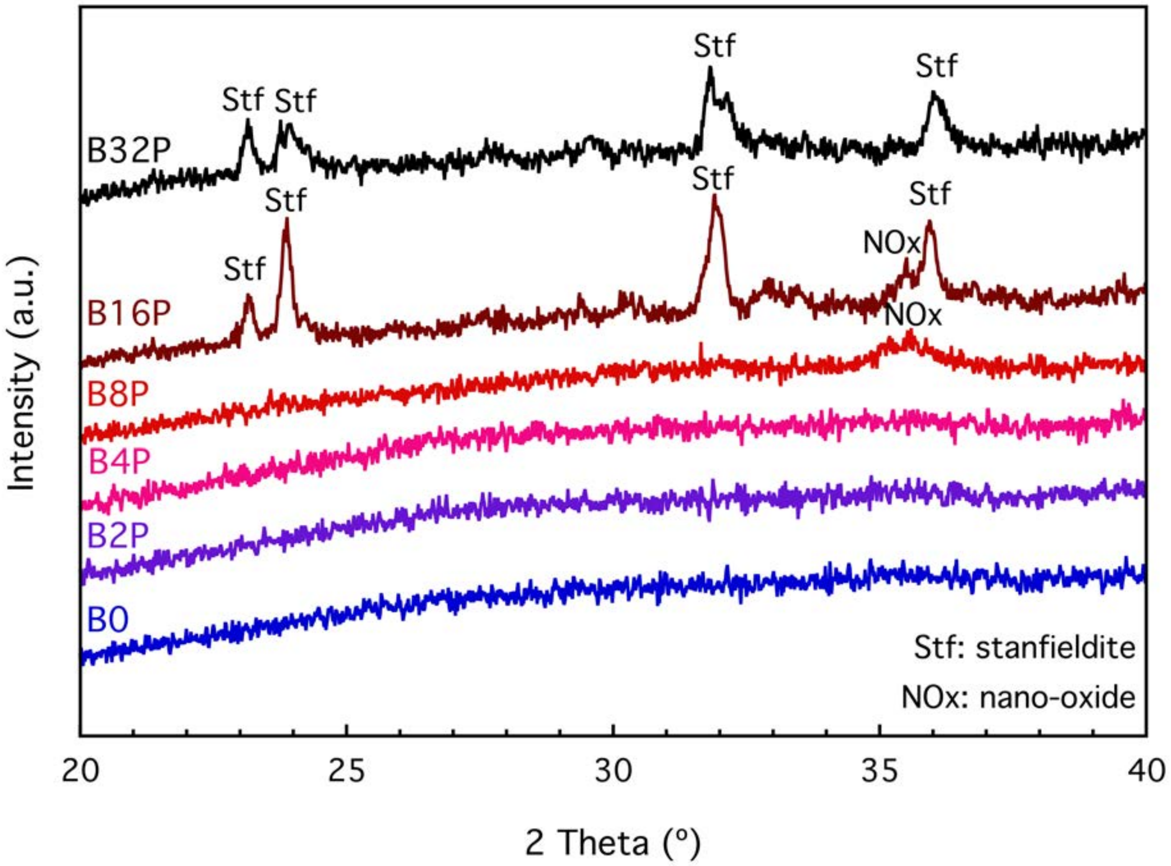

Figure 5.2. XRD spectra of the as-quenched glasses.

The abrupt change on Fe environment – including the formation of the $Fe^{3+}Fe^{2+}$ nano-size oxide phase (Figure 5.3) – and the structural collapse at 8 wt% P_2O_5 (Figure 5.1) are correlated with the nucleation of a spinel-like oxide structure and the onset of a phase separation process in P-doped ferrosilicate systems (Ryerson and Hess, 1980; Toplis et al., 1994a). Although this phase cannot be precisely identified by Mössbauer spectroscopy, it is consistent with the presence of a spinel-like oxide with mixed Fe^{2+}-Fe^{3+} sites – $(X,Fe^{2+})(Y,Fe^{3+})_2O_4$ with X=Mg,Mn and Y=Al^-, such as magnetite-hercynite – $Fe^{2+}(Al,Fe^{3+})_2O_4$ – nanolites observed in iron aluminosilicate melts by Transmission Electron Microscopy (Neuville et al., 1996). Moreover, the addition of phosphorus to ferrobasalt is known to cause the formation of stable Fe^{3+}-PO_4^{3-} complexes in the melt that inhibit the crystallization of magnetite, probably by reducing the activity coefficient of Fe^{3+} (Toplis et al., 1994b). Fe^{3+}-PO_4^{3-}

complexing enhances the formation of the disordered spinel-like oxide and triggers the crystallization of the phosphate phase. If these complexes exist in the liquidus region, they may explain the increase of viscosity that prevented the casting of sample B32P, in good agreement with research on calcium aluminosilicate melts (Mysen, 1992). At low P contents, Fe^{3+}/Fe^{2+} increases due to phosphate complexing as the balance of network formers to network modifiers varies only slightly. At high P contents this balance is much in favor of the network formers, enhancing crystallization. The formation of crystalline phosphates also accounts for the increase of Fe^{2+}.

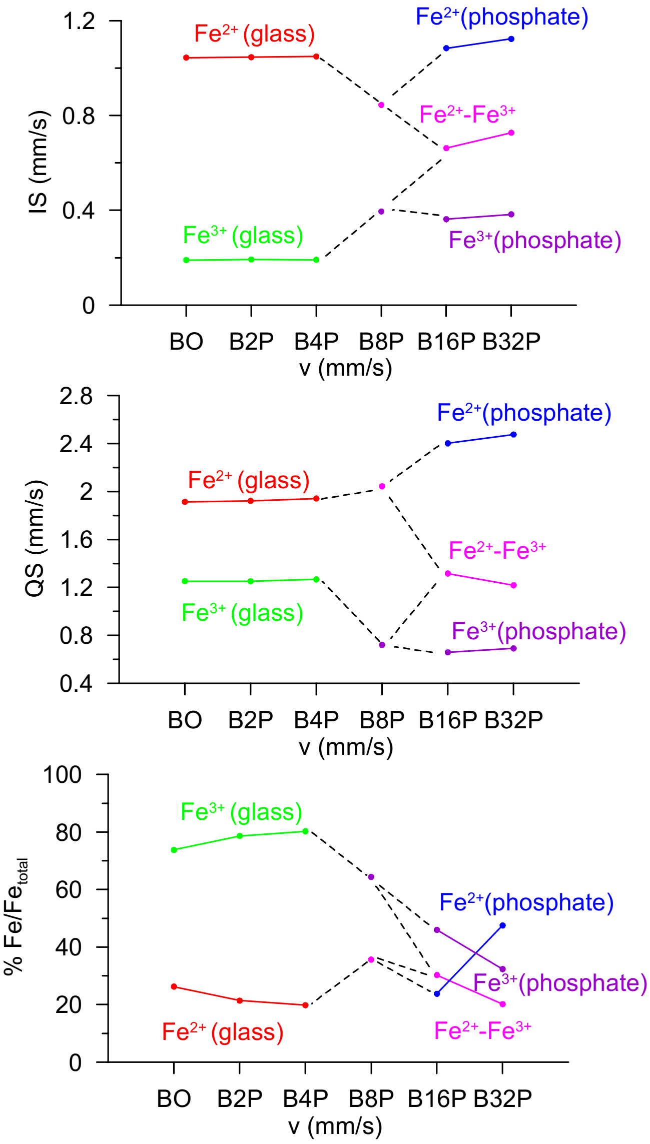

Figure 5.3. Isomer shift, quadrupole splitting and concentration of Fe species.

5.4 Conclusions

The addition of phosphorus to a basaltic melt causes the oxidation of the resulting glass as long as there is no significant increase of the concentration of network-forming cations (Si^{4+}+Al^{3+}+P^{5+}). Fe is located in the glass structure. Further addition of P triggers a structural collapse related to the unmixing of the melt into a silicate and a phosphate phases together with the formation of a $Fe^{3+}Fe^{2+}$-containing disordered/nano-sized oxide phase. An anhydrous phosphate mineral then crystallizes with a structure similar to that of stanfieldite and Mössbauer parameters similar to the alluaudite group, increasing the viscosity of the melt and preventing its casting. The $Fe^{3+/}Fe_T$ ratio decreases due to Fe being mostly in the reduced form in minerals.

CHAPTER 6 Effect of Ca concentration in the vitrification of basalt and case study of glass-ceramics production

I was going to sip on a diet soda, but a little voice convinced me I needed the extra calcium from a cup of hot chocolate.

Cathy Guisewite

6.1 Introduction

Alkaline earth aluminosilicate systems are at the base of a large range of commercial applications; they also represent basaltic natural melts (Mysen and Richet, 2005). Ca plays the role of a network modifier in silicate glasses, causing the formation of non-bridging oxygens (Kalampounias et al., 2003). However, its addition may enhance bot the chemical and mechanical stability of the glass, although an excess of Ca might trigger vitrification (Fernandez Navarro, 1991). In studies on calcium silicate glasses, the configuration of calcium cations changes around a threshold of 45 mol% CaO forming Ca-O-Ca bonds that increase the connectivity of the structure (De Sousa Meneses et al., 2006). There is a certain phase separation in the Ca-rich end of the Al_2O_3-CaO-SiO_2 system (Huang and Behrman, 1991). As shown in the chapter devoted to P, immiscibility processes influence the homogeneity of the glasses at the microscale, thus heavily influencing both the macroscopic properties and crystallization.

Wastes with bulk compositions in the CaO-MgO-Al_2O_3-SiO_2 system offer large possibilities for the inertization by vitrification and glass-ceramic processing (Barbieri et al., 2000; Franus et al., 2016; Park and Heo, 2002). In general, it is possible to obtain large monolithic blocks of glass that crystallize upon a thermal treatment. The typical glass-ceramics include minerals such as wollastonite ($CaSiO_3$), diopside ($CaMgSi_2O_6$), anorthite ($CaAl(AlSiO_6)$, and Fe oxides like magnetite (Fe_3O_4) and maghemite (Fe_2O_3). These materials may commonly be used as coating materials with high chemical and mechanical properties in the building industry or in thermochemical applications (Park and Heo, 2002).

A glass-ceramic process provides a sometimes partially crystallized material from a glass The strengths of glass-ceramics as performing materials arise from their chemical composition and unique microstructure. Controlling the composition of the parent glass, the nucleation and crystallization processes and their effect on the rheological behavior is essential to achieve desirable properties such as low viscosity at high temperature, and to optimize the resistance to abrasion and chemical alteration. Other interesting properties of glass-ceramics are the lack of porosity and high strength and toughness (Holand and Beall, 2012).

Xu and coworkers (Xu et al., 1991) proposed a method to obtain the temperatures of maximum nucleation rate in order to establish the appropriate processing to obtain glass-ceramics with a fine and homogeneous microstructure. Glass-ceramics processing has been shown to have potential to enhance the physicochemical properties of sewage sludge or sewage sludge-like glasses (Garcia-Valles et al., 2007; Tarrago et al., 2017; Tarragó et al., 2018). Examples of the vitrification and production of glass-ceramics from Ca-rich wastes in the literature include sital slag from the steel and copper industries of Russia (Pavluskin, 1986), cupola slag blast (Agarwal and Speyer, 1991), blast furnace slag (Fredericci et al., 2000), and molybdenum tailings (Shi et al., 2017).

The aim of this chapter is to analyze the effect of the addition of Ca to the glass formation ability, the macroscopic properties and the chemical stability of a series of basaltic glass. The range of Ca concentrations of interest is between 10-53 wt% CaO, the concentration in the basalt and the maximum concentration of CaO in sewage sludge (as explained in the Introduction). The most suitable composition is then selected for a more detailed study of the nucleation process, its effect on viscosity and the design of a glass-ceramics process to further improve the performance of the chosen glass.

6.2 Results

6.2.1 Chemical composition, texture and density

The chemical compositions of the glasses are reported in Table 6.1. Glass formation is limited by the crystallization of large, pink merwinite crystals in sample B32Ca (Figure 6.1), hence the solubility of CaO is about 30 wt%. The whole range of CaO concentration in sewage sludge reported in the Introduction cannot be vitrified. All the studied compositions lie in the metaluminous field ($[Na_2O]+[K_2O] < [Al_2O_3] < [Na_2O] + [K_2O] + [CaO]$). The glasses can be described as a calcium aluminosilicates with high Fe contents, which cause their dark brown color in thin section that becomes black in bulk.

	SiO_2	Al_2O_3	CaO	MgO	TiO_2	Na_2O	MnO	FeO	K_2O	P_2O_5
B0	43.89	17.45	9.16	9.85	2.50	2.97	0.19	11.16	1.53	0.60
	(0.40)	(1.01)	(0.19)	(0.29)	(0.35)	(0.11)	(0.03)	(0.27)	(0.03)	(0.08)
B1Ca	43.18	14.44	10.58	10.26	2.47	3.26	0.20	11.53	1.60	0.54
	(0.24)	(0.24)	(0.16)	(0.16)	(0.11)	(0.09)	(0.03)	(0.11)	(0.07)	(0.09)
B2Ca	42.74	13.77	11.73	10.45	2.38	3.39	0.19	11.49	1.63	0.54
	(0.34)	(0.13)	(0.19)	(0.15)	(0.07)	(0.12)	(0.03)	(0.13)	(0.09)	(0.08)
B4Ca	41.69	14.03	13.44	10.24	2.36	3.05	0.18	11.21	1.44	0.52
	(0.31)	(0.62)	(0.17)	(0.35)	(0.08)	(0.21)	(0.03)	(0.28)	(0.07)	(0.08)
B8Ca	39.95	13.41	16.52	9.86	2.28	3.13	0.18	10.73	1.49	0.47
	(0.34)	(1.26)	(0.33)	(0.56)	(0.08)	(0.10)	(0.03)	(0.29)	(0.07)	(0.10)
B16Ca	36.11	12.19	24.44	9.19	2.02	2.28	0.15	10.06	1.12	0.46
	(0.34)	(0.17)	(0.33)	(0.56)	(0.08)	(0.10)	(0.03)	(0.29)	(0.07)	(0.10)
B24Ca	32.74	14.26	28.84	8.04	1.77	2.38	0.13	8.59	1.07	0.41
	(0.37)	(1.26)	(0.45)	(0.18)	(0.10)	(0.13)	(0.03)	(0.15)	(0.08)	(0.09)
B32Ca	29.46	9.98	36.56	7.89	1.70	1.95	0.15	8.28	0.84	0.39
	(0.42)	(0.47)	(0.57)	(0.29)	(0.08)	(0.11)	(0.03)	(0.21)	(0.05)	(0.04)

Table 6.1. Average chemical compositions (wt%) of glass from the original basalt and glasses doped with Ca. Standard deviation of measurements is in brackets.

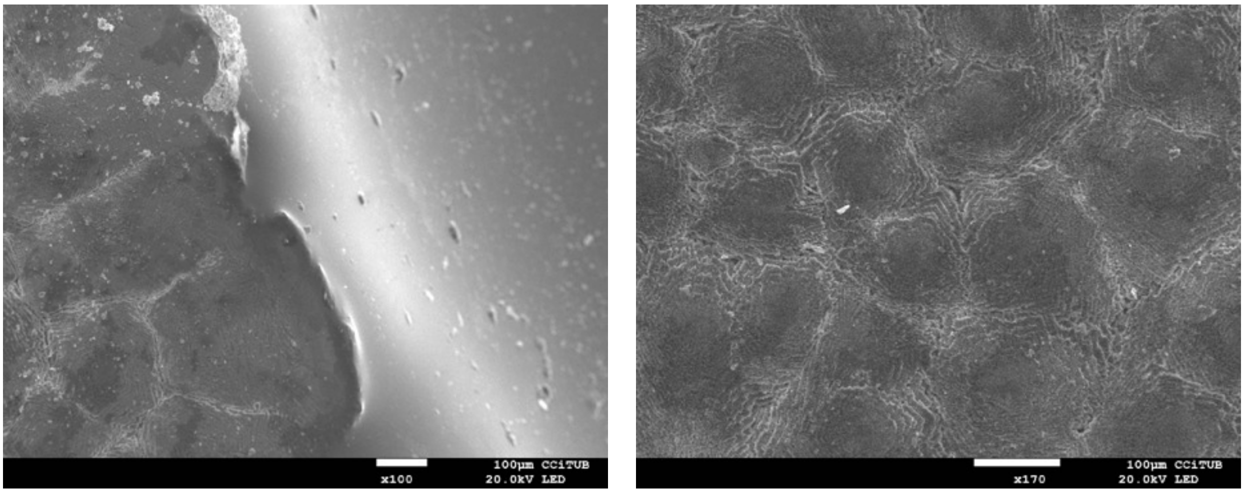

Figure 6.1. SEM micrographs of sample B32Ca, crystallized during quenching. The left image shows the interface between the crystals and the glass. The image on the right pictures a detail of merwinite crystals.

Density grows from 2.845 to 2.975 g/cm^3 with Ca addition (Figure 6.2). The addition of network modifiers rises the density of glasses because the cations occupy free space between tetrahedra and polarize the non-bridging oxygens, contracting the network (Fernandez Navarro, 1991). The increase is roughly linear at first, and then the slope of the curve decreases along with the diminishing availability of space for the emplacement of the additional Ca cations.

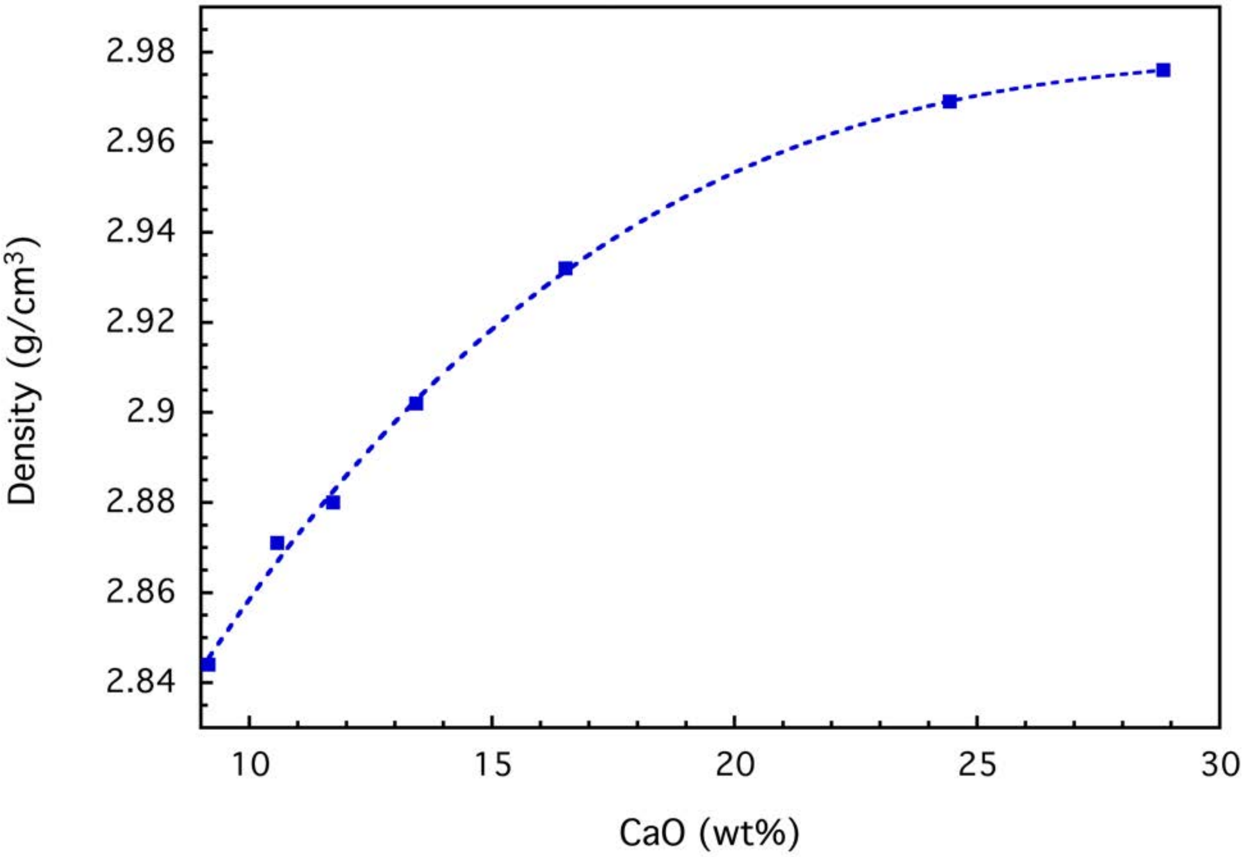

Figure 6.2. Density as a function of Ca contents. The discontinuous line is a guide for the eye.

6.2.2 Raman spectroscopy and structure

The Raman spectra of the Ca-doped basaltic glasses (Figure 6.3) are divided in three main regions: the low frequency (LF), middle frequency (MF) and high frequency (HF) envelopes. The LF covers the area between 200-600 cm^{-1}, the MF range is between 600 and 820 cm^{-1} and the HF goes from 820 to 1250 cm^{-1}. As in the case of P-doped glasses, the signal is quite noisy, probably due to the presence of nanolites such as hercynite-magnetite (Neuville et al., 1996). The intensity of the HF envelope increases and its position shifts to lower frequencies, signaling a depolymerization of the system which is consistent with the addition of Ca in a network-modifying role.

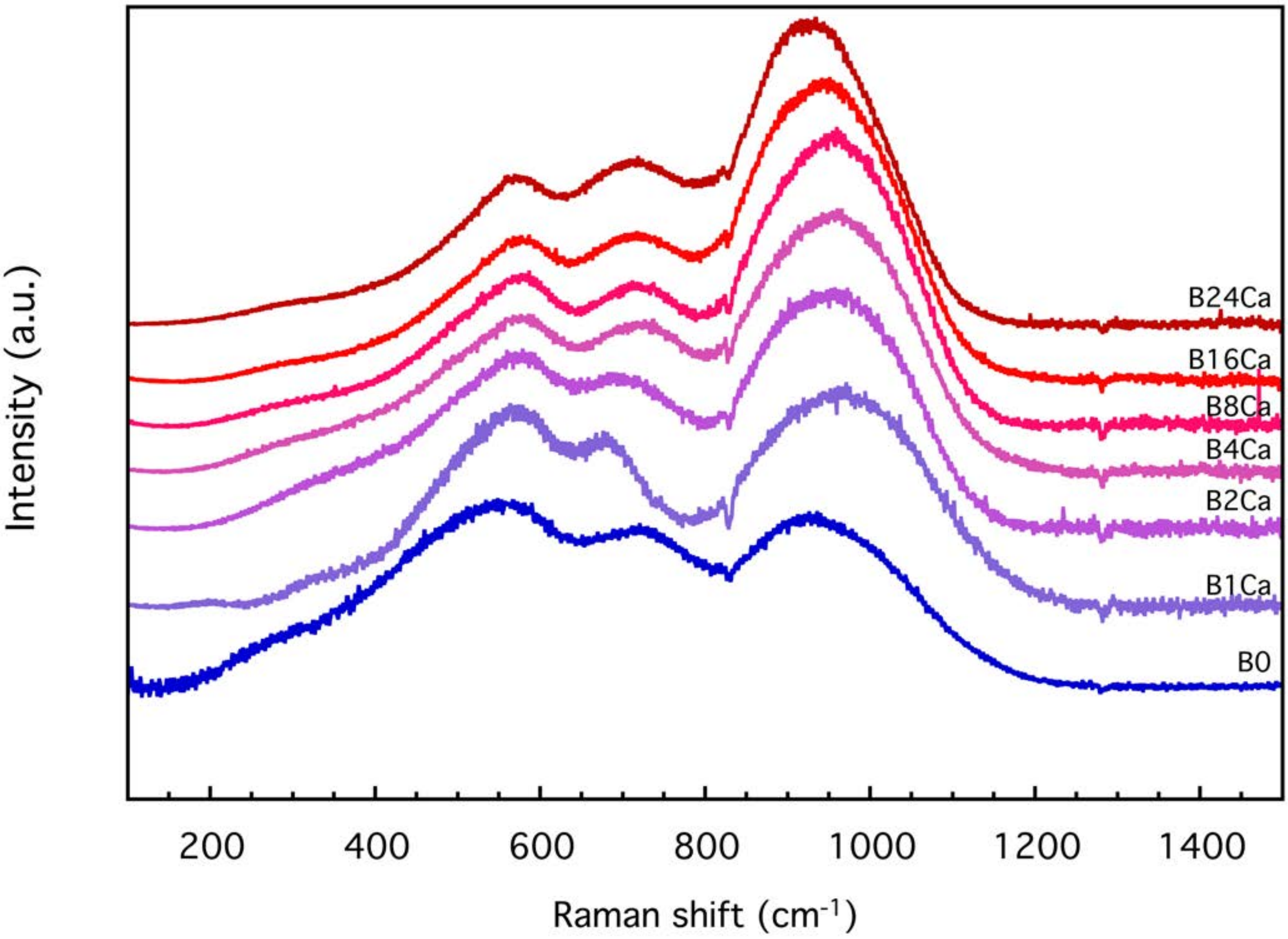

Figure 6.3. Raman spectra of the Ca-doped basalt series.

The attribution of the main envelopes is similar to those of the basalt glass (sample B0) explained in chapter 4. The LF corresponds to rings of 3 or more Si^{4+} tetrahedra linked by bridging oxygens, BO (Bell et al., 1968; McMillan and Piriou, 1982; B. O. Mysen et al., 1980; Mysen, 2003; Neuville et al., 2014a; Neuville and Mysen, 1996; Pasquarello and Car, 1998; Seifert et al., 1982; Umari et al., 2003). The MF is linked to the intertetrahedral mode of polymerized species. Its intensity decreases with silica content (Matson et al., 1983; McMillan, 1984a; Mysen and Toplis, 2007). The HF is attributed to the vibrations of structural elements bearing non-bridging oxygens (NBO). These elements include tetrahedrally coordinated cations (Si^{4+}, Al^{3+}, Fe^{3+}), NBO's and the network-modifying or charge-balancing cations (Bell and Dean, 1972; Cicconi et al., 2016, 2015; Cochain et al., 2012; Furukawa et al., 2011;

Hehlen and Neuville, 2015; Magnien et al., 2008, 2006; McMillan, 1984a; Mysen, 2003; Neuville et al., 2014a). As all the shifts in the positions of the main envelopes are gradual, there is no evidence of any abrupt change in the structure.

6.2.3 Evolution of the crystallization process with Ca contents

DTA profiles (Figure 6.4) show endothermic events between 650 and 750 ºC corresponding to the glass transition (T_g) range. T_g is followed by an exothermal event that oscillates around 850 ºC up to 16.52 wt% CaO and then shifts to higher temperatures. At 24.44 wt% CaO it consists in the convolution of two events, at 856 ºC and 872 ºC, whereas at 28.84% CaO a single event is registered again. These events are assigned to the crystallization of an assemblage containing magnetite (Fe_3O_4), diopside ($CaMgSi_2O_6$) in all the studied samples (Figure 6.5). At CaO contents between 10.58-16.52% rhönite is detected. On the Ca-rich region, akermanite crystallizes starting at 24.44 wt% CaO. Moreover, some nepheline crystallizes in at 24.44 wt% CaO, in sample B16Ca. The endothermal events above 1100 ºC correspond to the melting of the system. Their large areas are an indicator of the good fusibility of the compositions, which is appropriate for glass production. The increase of the melting temperature is related to the rise of the temperature of the liquidus from the pyroxene towards the melilite stability field (Morse, 1980). This effect also reduces the effectivity of supercooling and favors nucleation.

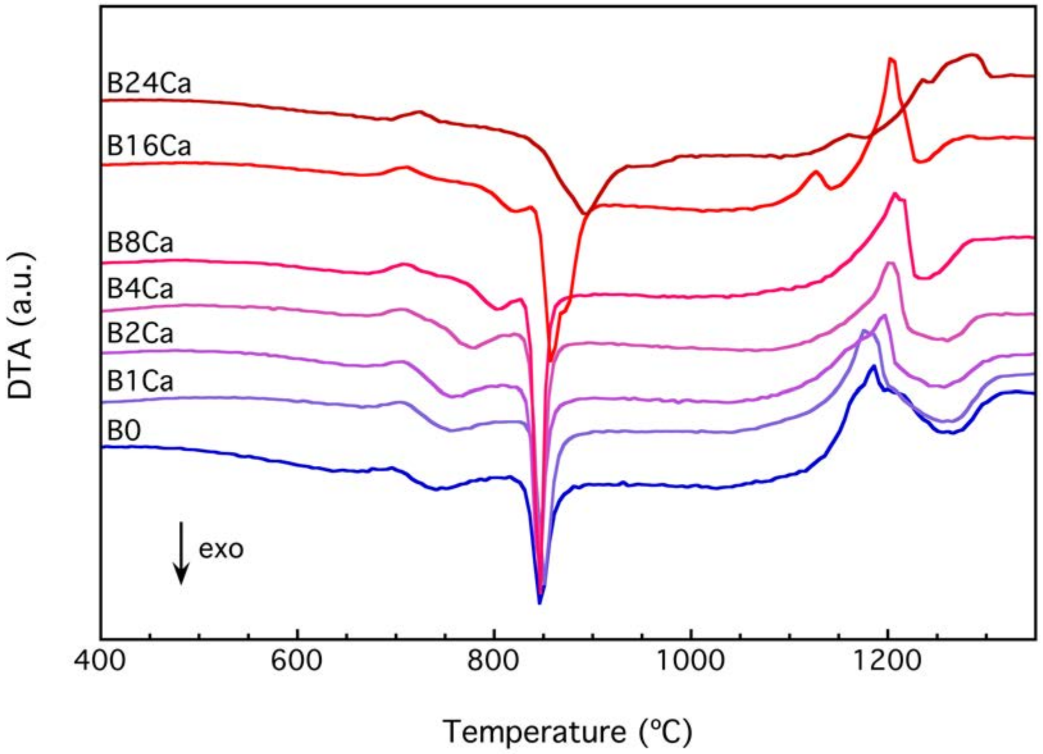

Figure 6.4. DTA analyses of the Ca-basalt compositions performed at a heating rate of 10 ºC/min.

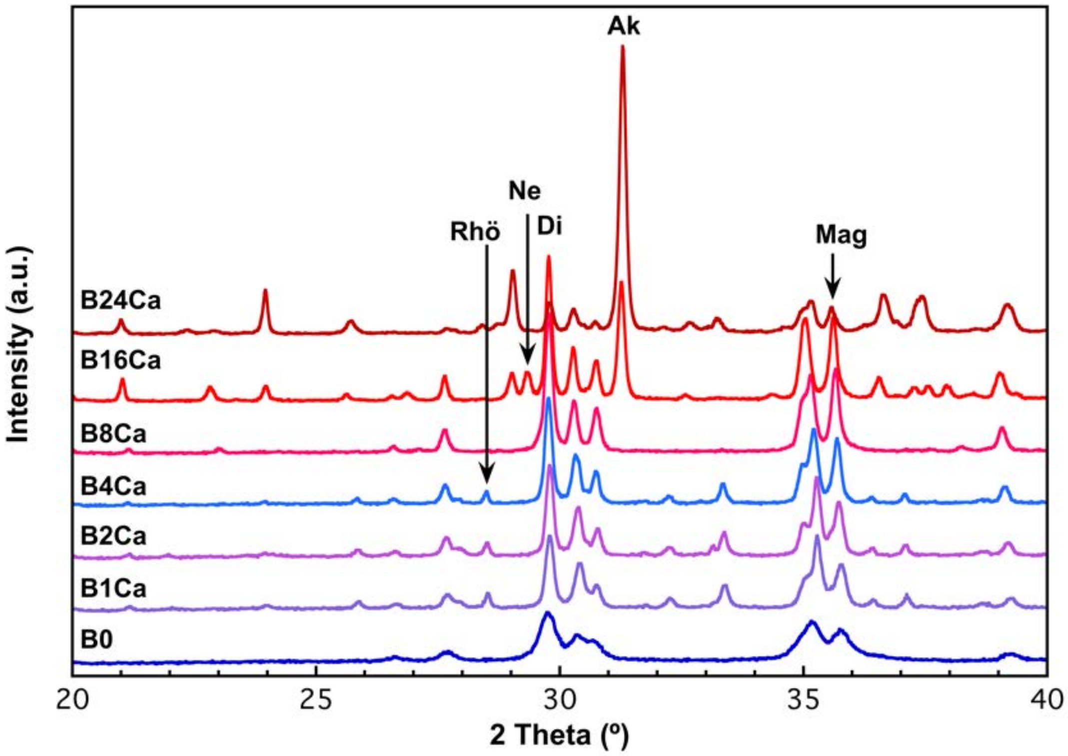

Figure 6.5. XRD diffractograms of the glasses treated at the crystallization temperatures.

The mineralogical evolution is in good agreement with the position of the samples in the CMAS diagram (Figure 6.6 and Figure 6.7). Samples B0 to B8Ca are located well within the stability field of pyroxene, and thus it is the main crystalline phase. Rhönite – a 4-chained inosilicate – may be a precursor of pyroxene and small amounts of it remain in samples B1Ca, B2Ca, and B4Ca. Sample B16Ca is at the border between the stability field of pyroxene and melilite, and thus bears similar amounts of the two species; in addition to some nepheline ((Na,K)$AlSiO_4$). Sample B24Ca is located in the melilite field, hence it crystallizes mostly into akermanite and pyroxene becomes less abundant. Inside the melilite group, the abundance of Ca compared to Al causes the crystallization of akermanite ($Ca_2Mg[Si_2O_7]$). In all cases, magnetite probably nucleates during quenching due to the high Fe contents of the basalt and in agreement with Raman results; hence, these crystals grow in the early stages of the exothermic event.

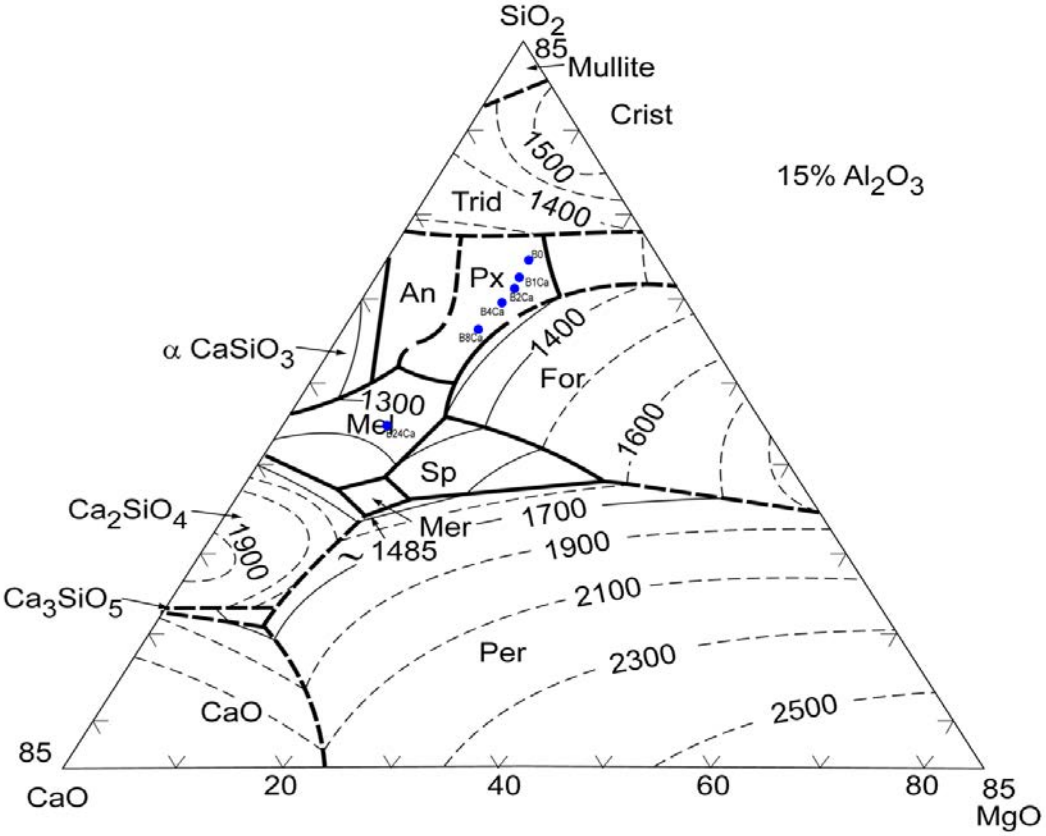

Figure 6.6. Phase diagram of the system CaO-Al_2O_3-MgO-SiO_2; section at 15 wt% Al_2O_3 (Levin and McMurdie, 1975)*. The dots mark the chemical composition of the glasses of this study.*

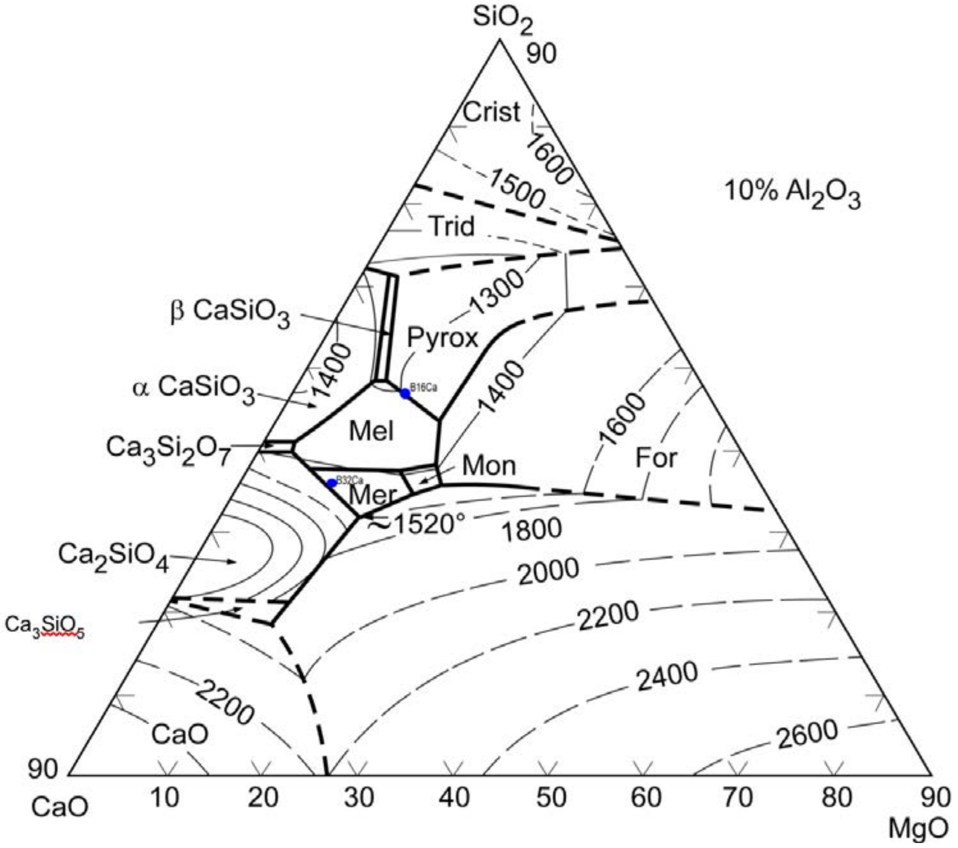

Figure 6.7. Phase diagram of the system CaO-Al_2O_3-MgO-SiO_2; section at 10 wt% Al_2O_3 (Levin and McMurdie, 1975)*. The dots mark the chemical composition of the glasses of this study.*

6.2.4 Dependence of viscosity on Ca contents and temperature

The viscosity-temperature curves of the glasses are shown in Figure 6.8. and compared to a natural basalt from Piton de la Fournaise volcano (Villeneuve et al., 2008). The curves of the Ca-doped glasses have an anomalous convex shape and viscosity decreases more slowly than expected. This effect is caused by the crystallization reflected on the exothermic event registered in DTA plots between 850 and 895 ºC. In viscous melts, the formation of crystalline phases causes an increase of viscosity due to crystals hampering the flow.

The variation of viscosity with Ca addition is influenced by two conflicting processes: the depolymerization related to the increase of network modifiers and crystallization. The first process reduces viscosity, whereas the second increases it. Three main regions can be distinguished (Figure 6.8). From T_g to $10^{7.9}$ Pa·s, the slope of the curve is somewhat similar to that of GBa93, hence crystallization has not started or it is of small importance. The driving force of the deformation is the viscous flow of basalt. Between $10^{7.9\text{-}5.6}$ Pa·s the gradient decreases as the viscosity is increasingly controlled by the crystallization process. In general, viscosity increases as long as the diopside is the phase that crystallizes, and decreases with the appearance of akermanite – although there is significant overlap between the curves. This could be attributed to a decrease in diopside formation and crystallinity at low temperatures which is consistent with the variation of the intensity of the DTA peak of diopside. Below $10^{5.6}$ Pa·s the slope of the curve increases again when melting takes over the flow process. Moreover, the temperatures of the fixed viscosity points of all the samples converge near 7.2-7.4 °C^{-1} (1351-1389 °C) apart from B24Ca, which is significantly higher – its flow point is at 6.6 °C^{-1} (1501 °C).

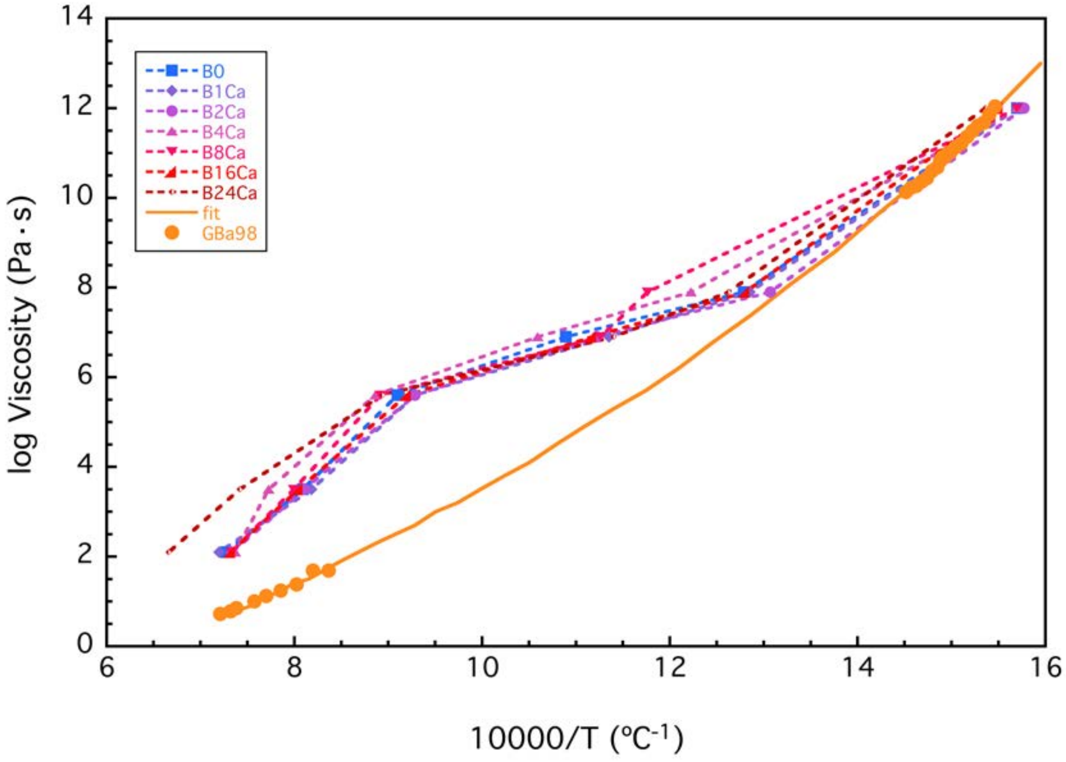

Figure 6.8. Viscosity-temperature curves of the studied compositions compared to a natural basalt (Villeneuve et al., 2008).

6.2.5 Nucleation process

Sample B16Ca has been selected for a detailed study of the nucleation process as explained in the methods section. This sample has been chosen because it admits the highest addition of CaO without it increasing the viscosity of the glass at high temperatures (Figure 6.8). This approach should supply T_N for each of the mineral phases that crystallize from the original glass. Two different events have been isolated. The first is a broad peak centered at 650 ºC from the shift of the exothermic peak at 874 ºC (Figure 6.9a), which appears in all the analyses. The second is a narrower peak centered at 675 ºC, which is only detected for T_N below 750 ºC, corresponding to the variation of the shoulder at 871 ºC (Figure 6.9b).

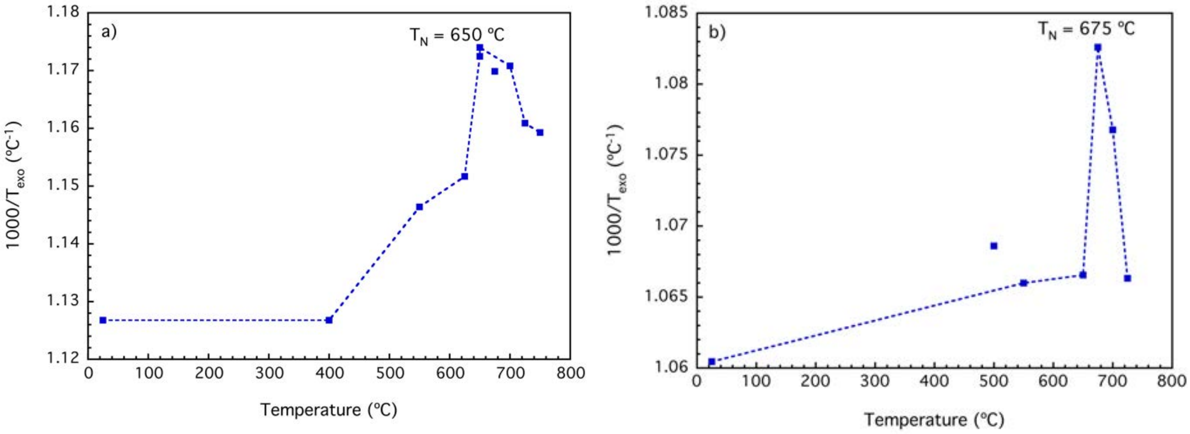

Figure 6.9. Plots representing the shift of the inverse of the temperature of the exothermic peak as a function of temperature corresponding to the first (a) and second (b) exothermic events.

The sequence of nucleation of the newly-formed minerals and the attribution of the T_{MNR} are studied from the evolution of the intensity of the main diffraction peak after a sudden heating at T_N and further heating up to the temperature of the exothermic event (T_{exo}) from DTA to induce crystal growth (Figure 6.10 and Table 6.2). The first T_{MNR} is attributed to the nucleation of magnetite (Fe_3O_4), as it has the most intense XRD peaks at 650 ºC; its peak height later diminishes and becomes undetectable at 700 ºC. Nepheline ($NaAlSiO_4$) starts nucleating at 650 ºC and its nucleation rate is larger at 700 ºC, but cannot be proved to be at its maximum at this temperature. The nucleation of diopside ($CaMgSi_2O_6$) and merwinite

($Ca_3MgSi_2O_8$) is fast and at about the same temperature range: between 650 ºC and 700 ºC. The proximity between all these nucleation events makes it difficult to attribute the T_{MNR} linked to the second event at 675 ºC to a single phase with the available data, as they are probably overlapped.

T_N (ºC)	**Newly-formed minerals (cps)**				
	Magnetite	**Nepheline**	**Diopside**	**Merwinite**	**Akermanite**
600	113	-	-	-	-
650	301	63	431	-	-
700	165	167	265	-	-
750	-	1726	6001	2697	33
800	-	1450	5892	2218	1893

Table 6.2.Intensities of the main diffraction peaks of the newly-formed mineral phases after sudden thermal treatments at the T_N followed by growth at the temperature of the first exothermic.

The intensities and narrowness of the XRD peaks at 750 and 800 ºC, coupled with the apparent scarcity of residual glass, show that the nucleation stage has finished and crystal growth is the ongoing process. A new mineral phase, akermanite ($Ca_2Mg[Si_2O_7]$) is detected at 750 ºC.

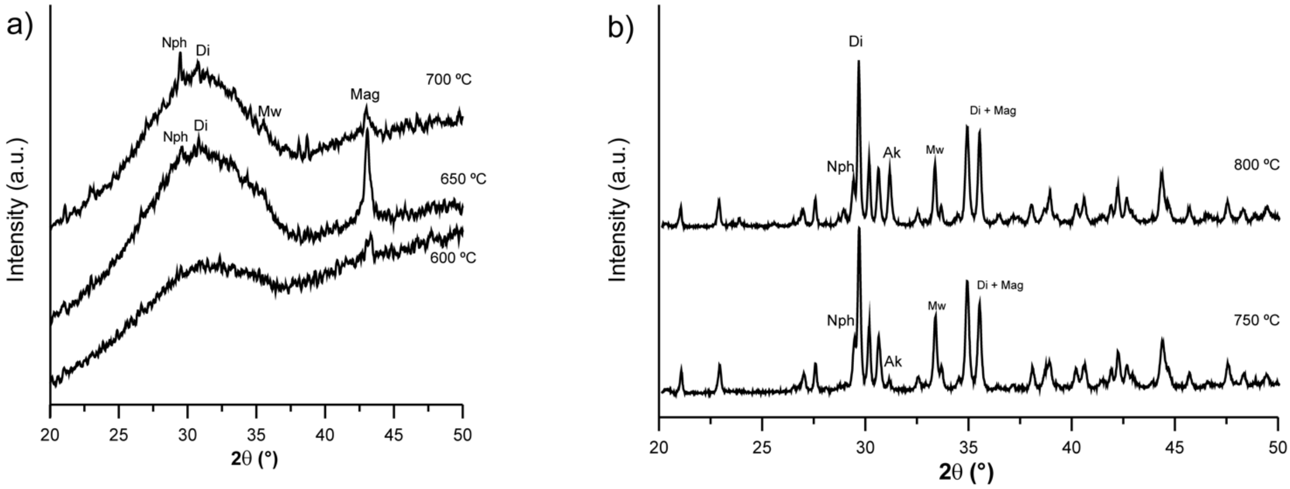

Figure 6.10. Sequence of XRD patterns obtained after a sudden heating of glass samples at a) T_{MNR} and b) T_{GR} for each phase. The temperatures in the plot correspond to the T_N of each treatment.

6.2.6 Evolution of the crystalline phases in the devitrification process

XRD spectra show the evolution of the newly-formed mineral phases between 770–1200 ºC during devitrification of the original glass in *in-situ* HT-XRD (Figure 6.11). The sample stays amorphous up to 760 ºC and the first diffraction peaks can be detected at 770 ºC. The nucleation process is not controlled in this experiment, hence the series of XRD patterns show both nucleation and growth of the minerals with increasing temperature.

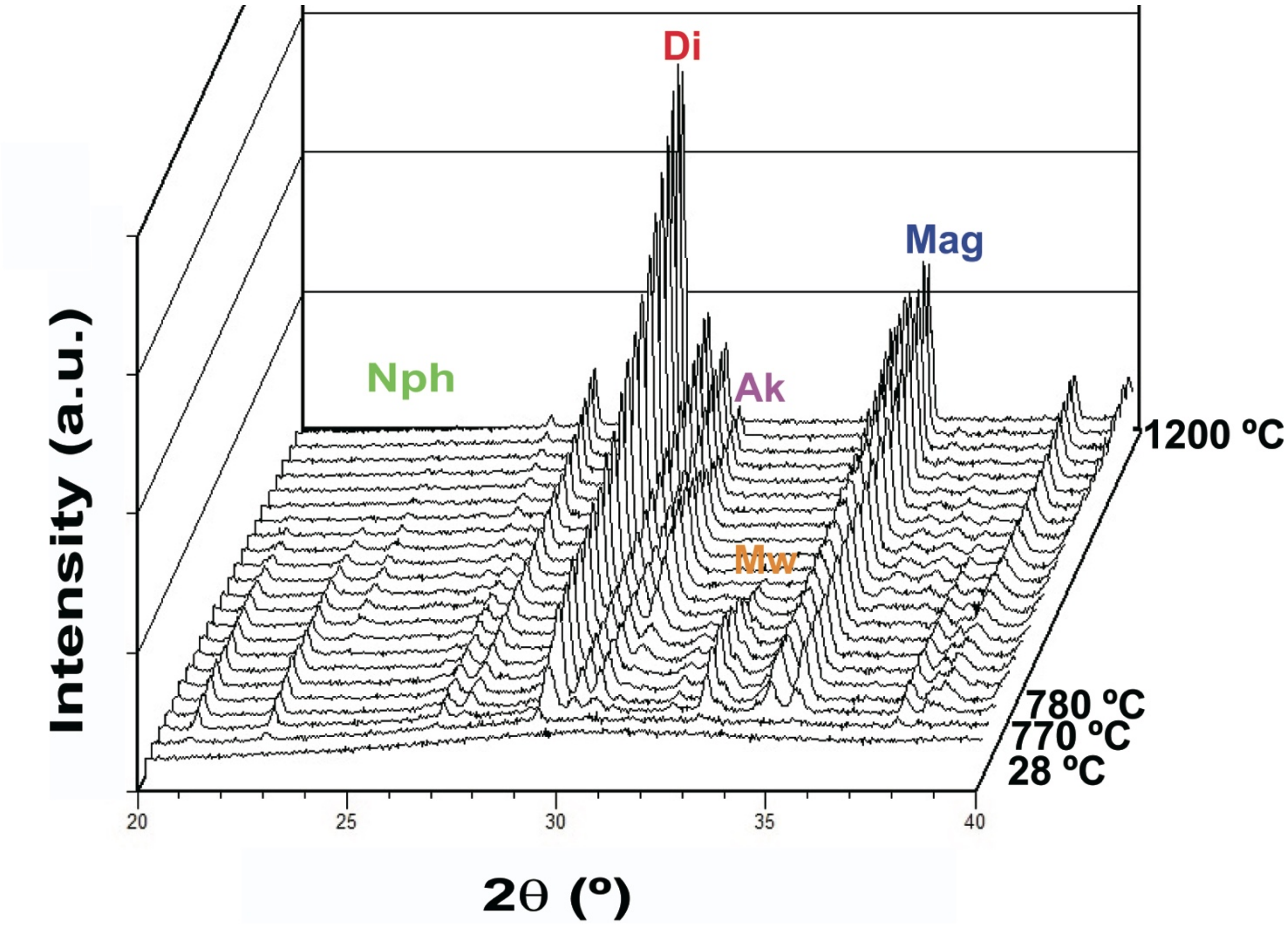

Figure 6.11. HT-XRD spectra in the range 2θ between 20 and 40 º.

Diopside, nepheline and merwinite can be seen in the HT-XRD spectrum at 770 ºC, whereas akermanite is detected from 800 ºC (Figure 6.11). The evolution of the intensity of each of the mineral phases has been tracked using the following diffraction peaks: d_{201} for nepheline, d_{310} for merwinite, d_{310} for diopside and d_{211} for akermanite (Figure 6.12). They are the most intense that did not overlap with peaks from coexistent phases. The evolution of magnetite could not be tracked in this experiment because its main diffraction peak overlaps with a major peak of diopside and the rest of reflections are not intense enough.

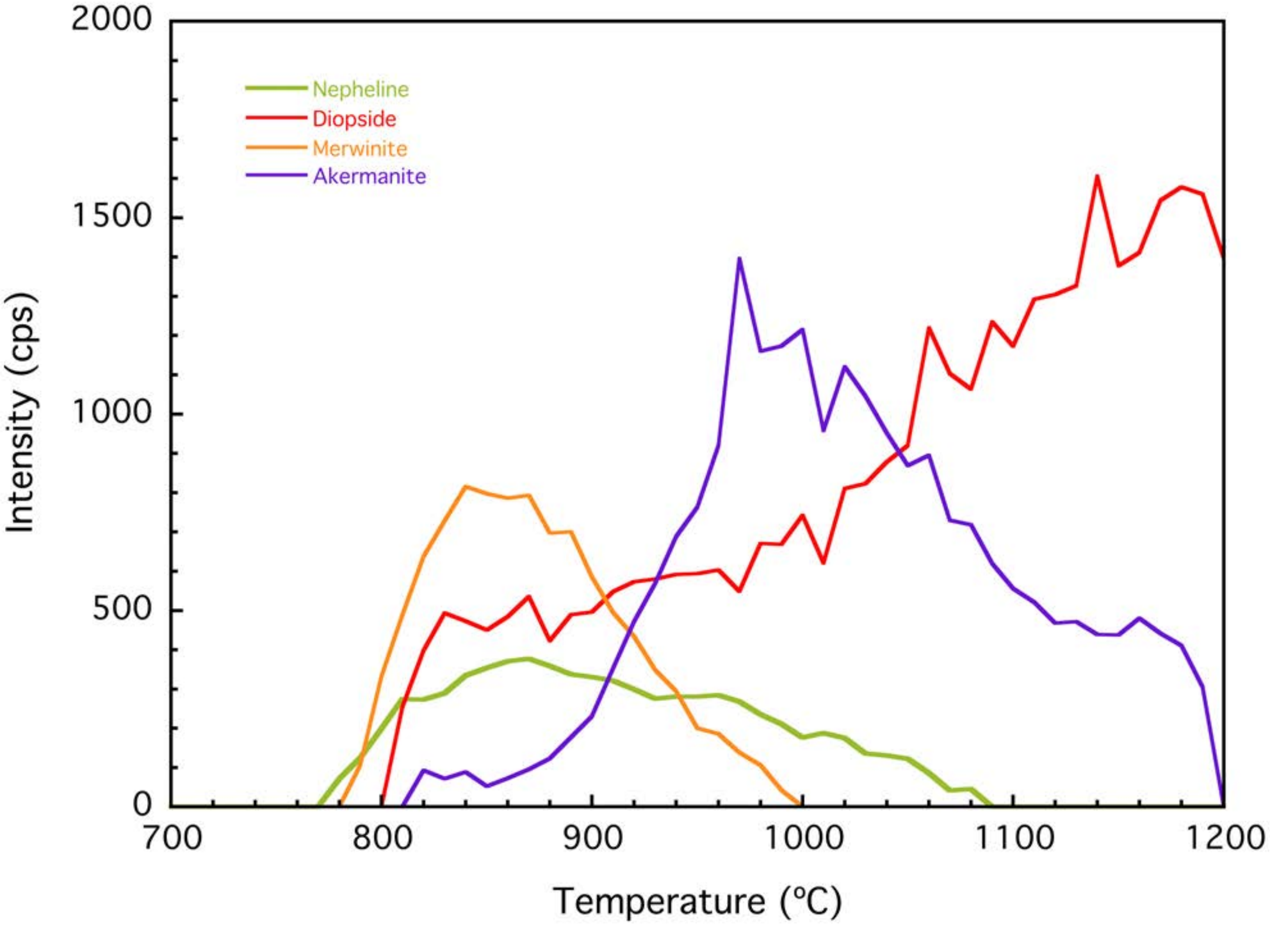

Figure 6.12. Evolution of the intensities of selected XRD peaks during the crystallization of sample B16Ca (d_{201} for nepheline, d_{310} for merwinite, d_{310} for diopside and d_{211} for akermanite) as a function of temperature.

Nepheline is stable between 760 ºC and 1080 ºC, with a maximum intensity at 860 ºC. Merwinite has a similar behavior: it also reaches a maximum at 860 ºC and becomes undetectable over 980 ºC. The intensity of akermanite increases during the decrease of these two phases, reaches its maximum at 970 ºC and becomes undetectable at 1190 ºC. The intensity of diopside reflections increases along the whole temperature range, alongside with the crystallization and melting reactions of merwinite and akermanite (Figure 6.11 and Figure 6.12). The sample does not undergo additional changes during cooling.

The sizes of coherent crystals at each temperature can be calculated using Scherrer’s equation to establish the growth of each phase. The maximum crystal size reached in HT-XRD for all the minerals is between 40 – 70 nm. This can be due to the fact that all phases nucleate in a narrow temperature range, hence forming a large number of nuclei before reaching the crystal growth temperature (T_{GR}) and constraining crystal growth. Magnetite crystals are still smaller, reaching a maximum of 18 nm. Their role is to act as a nucleus for the growth of diopside and it is absorbed inside its structure to approach the Fe-rich end-member.

In agreement with the reported results, the thermal treatment of the parent glass to obtain the glass-ceramic included the following steps:

- Heating up to 650 ºC at 2 ºC/min for 6 h (T_{MNR} of magnetite),
- Heating at 675 ºC at 2 ºC/min for 6 h (2nd T_{MNR}, discussed further in the manuscript)
- Heating up to 874 ºC at 10 ºC/min for 6 (the temperature of the exothermic DTA peak)
- Heating to 1000 ºC at 2 ºC/min for 6 h (at this temperature merwinite has been exhausted by reacting with diopside to form akermanite)
- Free cooling

6.2.7 Degree of crystallization of thermally treated glasses

HSM is a comparative technique that provides an estimation of the evolution of viscosity of glasses during a heating process. However, it must be pointed that by default this technique cannot avoid the crystallization range. Hence, it is reasonable to question the amount of amorphous phase remaining in the crystallization range. This issue is addressed by XRD experiments and Rietveld refinement of the profile to quantify the ratio between the minerals and the amorphous phase on sample B16Ca treated at 900 (Figure 6.13) and 1100 ºC (Figure 6.14) in the HSM conditions. These tests prove that there is barely any amorphous material remaining at either 900 ºC or 1100 ºC, 2.60 and 2.04 wt% respectively (Table 6.3).

Mineral phase/T (ºC)	900	1100
Akermanite	25.97 (0.90)	32.32 (0.65)
Diopside	27.12 (0.51)	22.37 (0.46)
Nepheline	7.91 (0.64)	–
ZnO (internal standard)	39.01 (0.52)	45.31 (0.48)
Amorphous matter	2.60	2.04

Table 6.3. Results of the quantification of the mineral and amorphous components in the HSM-treated samples. The error of the measurements is in brackets.

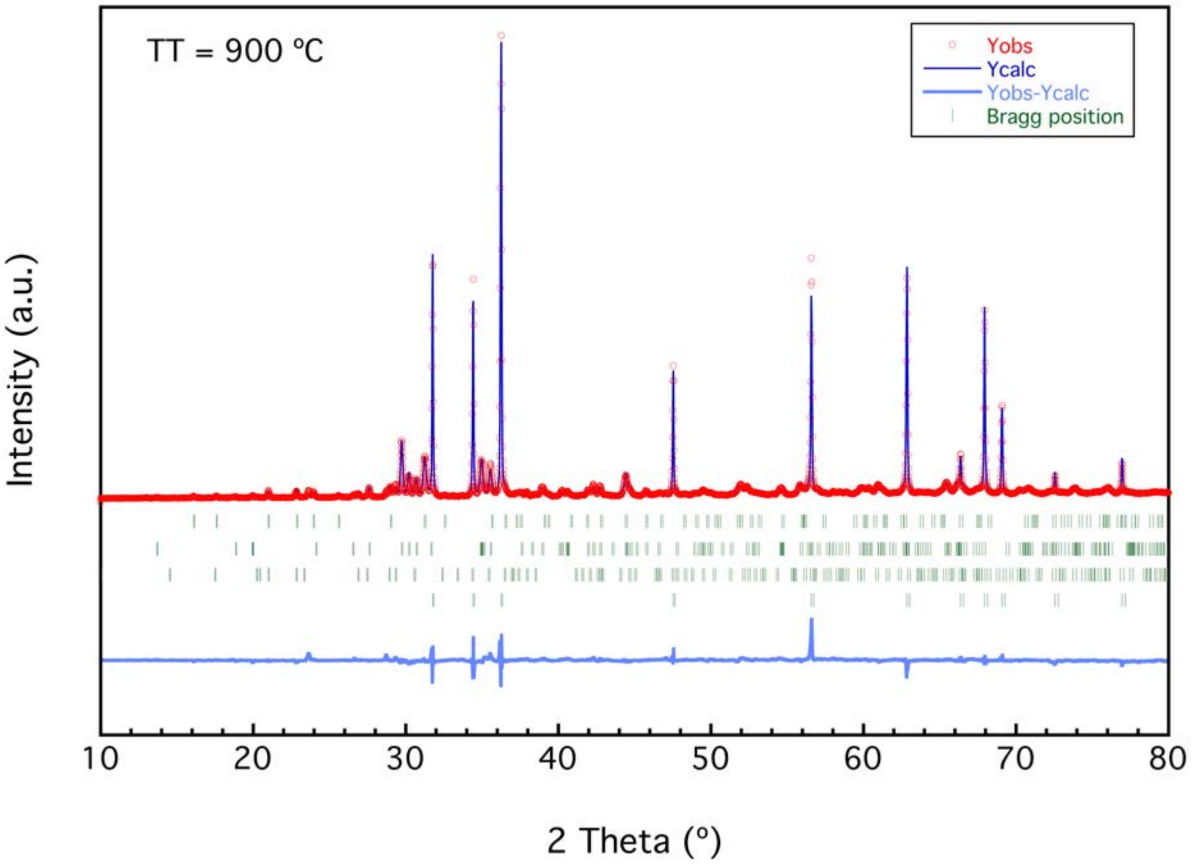

Figure 6.13. Rietveld refinement of the XRD profile of sample B16Ca treated at 900 ºC and mixed with ZnO as internal standard.

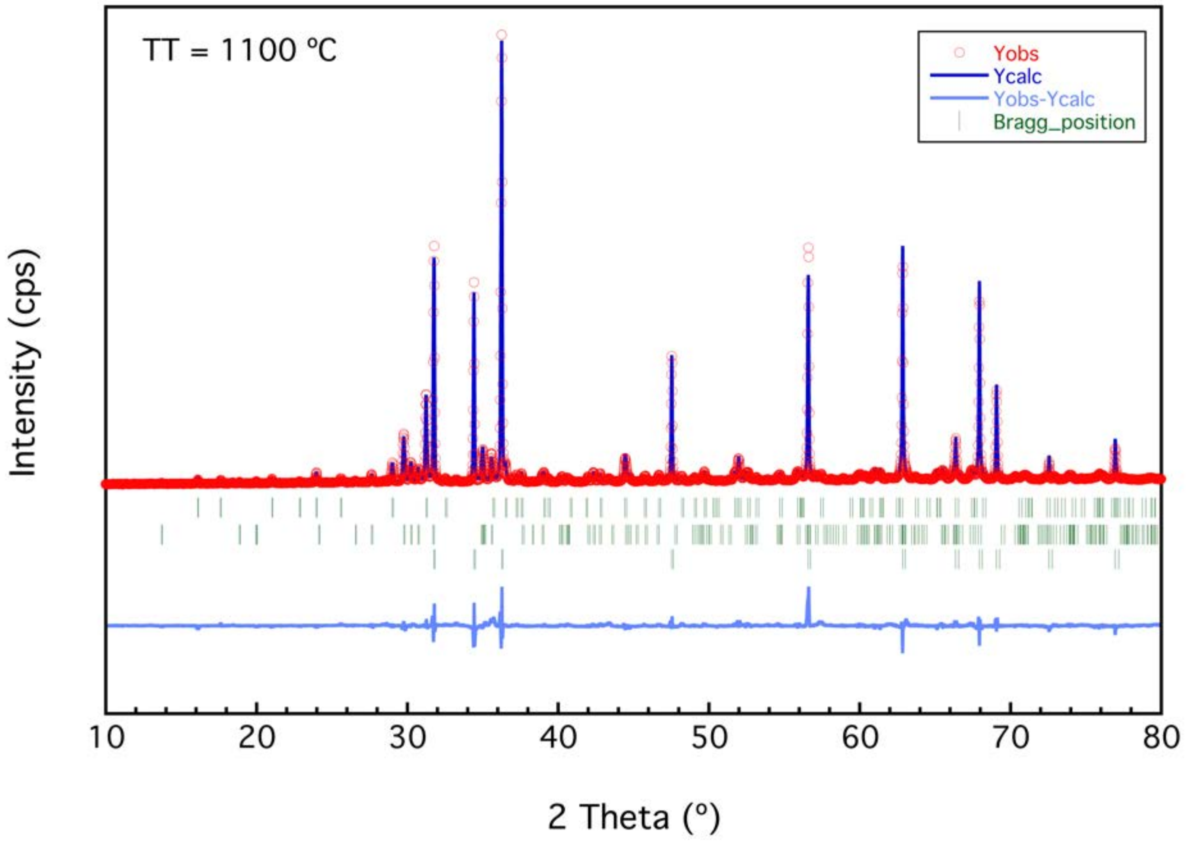

Figure 6.14. Rietveld refinement of the XRD profile of sample B16Ca treated at 1100 ºC and mixed with ZnO as internal standard.

6.2.8 Evolution of the viscosity of sample B16Ca as a function of nucleation time

The viscosity-temperature curves of glasses of B16Ca composition treated at a nucleation temperature of 650 ºC during different periods of time (between 0 and 8 h) are traced using the fixed viscosity points from HSM (Pascual et al., 2001) (Figure 6.15). In general, a longer nucleation time increases the viscosity (for a nucleation period between 0 and 4h), in the high viscosity range (between $10^{7.9–6.9}$ Pa·s). However, the sample treated during 8 h is very similar to the sample nucleated for 2 h as the system becomes multiphasic with the separation between two solid phases, one crystalline and one amorphous. However, increasing nucleation time reduces the viscosity in the low viscosity range (between $10^{5.6–2.1}$ Pa·s). At 650 ºC the phases that will nucleate are magnetite and nepheline. The nucleation of nepheline will extract Na and K from the glass, thus increasing the viscosity according to longer nucleation times. The variation of viscosity is also conditioned by the effect of nucleation on the sintering process. Between the first shrinkage ($10^{7.9}$ Pa·s) and the softening points ($10^{5.6}$ Pa·s), all matter will be in the solid state, either as a crystalline or an amorphous phase. The shrinkage of the probe at this stage is controlled by an evaporation-condensation process depending on vapor pressure. Increasing the amount of nuclei will reduce vapor pressure because crystals have lower vapor pressure than amorphous materials. The formation of nuclei requires increasing the vapor pressure by means of a temperature rise for the sintering process to occur, which is in good agreement with the temperature at which each samples reaches the maximum shrinkage point ($10^{6.9}$ Pa·s) increasing with nucleation time.

For viscosities below the softening point, matter will be a mixture of solid crystals and a melt. In these conditions, the main agent controlling viscosity is capillarity, defined as the interstitial energy between solid and liquid (Kingery, 1960). In addition, a larger number of nepheline crystals will cause a more sudden decrease in viscosity upon its melting between 897 and 1080 ºC. In the viscosity-temperature curves this corresponds to a drop between first shrinkage and softening, which can be correlated to the decrease in the viscosity of the melt caused by the incorporation of Na and K that have left the nepheline structure. The second, more gradual, viscosity drop is attached to a decrease in the crystal/liquid ratio, which is independent of nucleation time, as the curves are approximately parallel in this range (Figure 7).

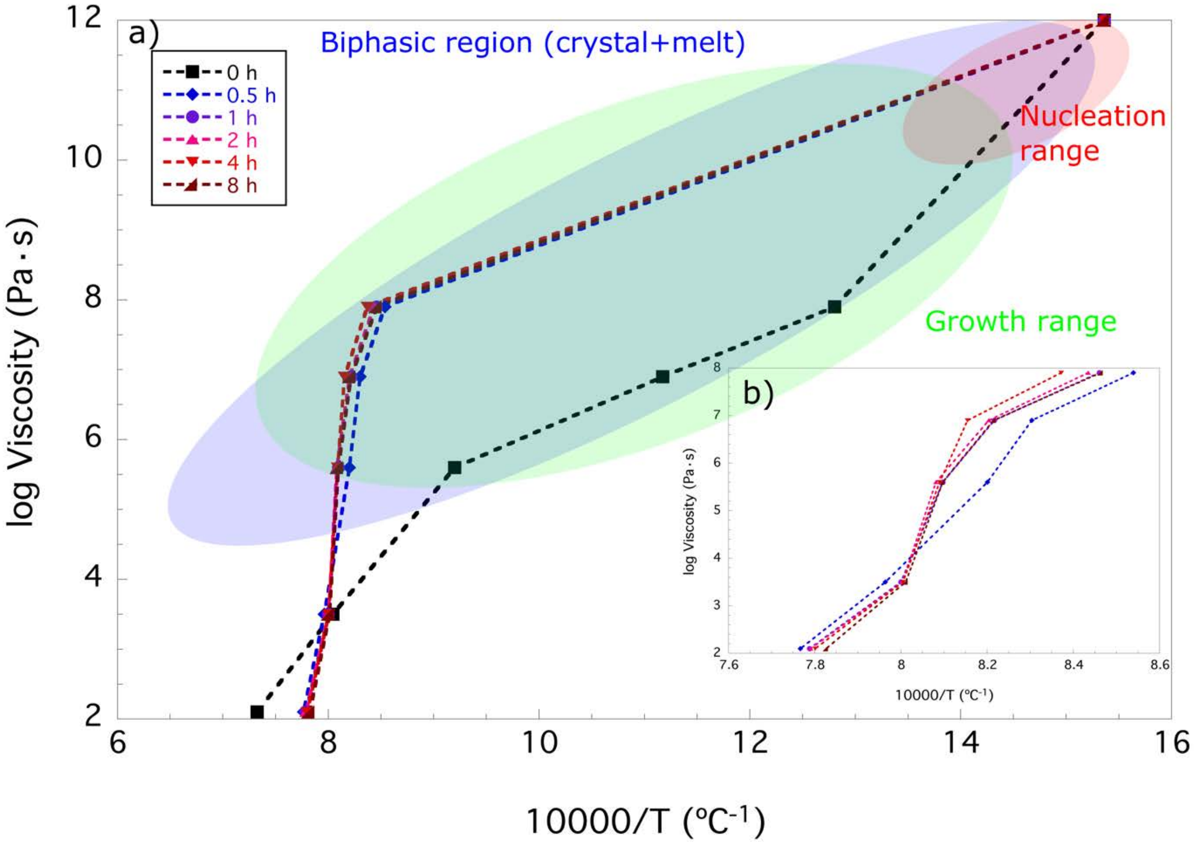

Figure 6.15. Viscosity-temperature curves for glasses with a) different nucleation times b) magnification focusing on the samples nucleated before the HSM experiments. The highlighted areas represent the biphasic region, where a crystal and a glass/melted phase coexist (blue), the nucleation range, which are XRD-amorphous (red) and the growth range, where crystallization increases viscosity as a function of the nucleation time (green).

6.2.9 Glass-ceramic characterization

The glass-ceramic has been obtained through the thermal treatment of the original B16Ca glass based on the T_N and T_{GR} exposed in the nucleation section. It is formed by nepheline (12.15 wt%), magnetite (6.03 wt%), diopside (41.32 wt%) and akermanite (40.50 wt%) (Figure 6.16).

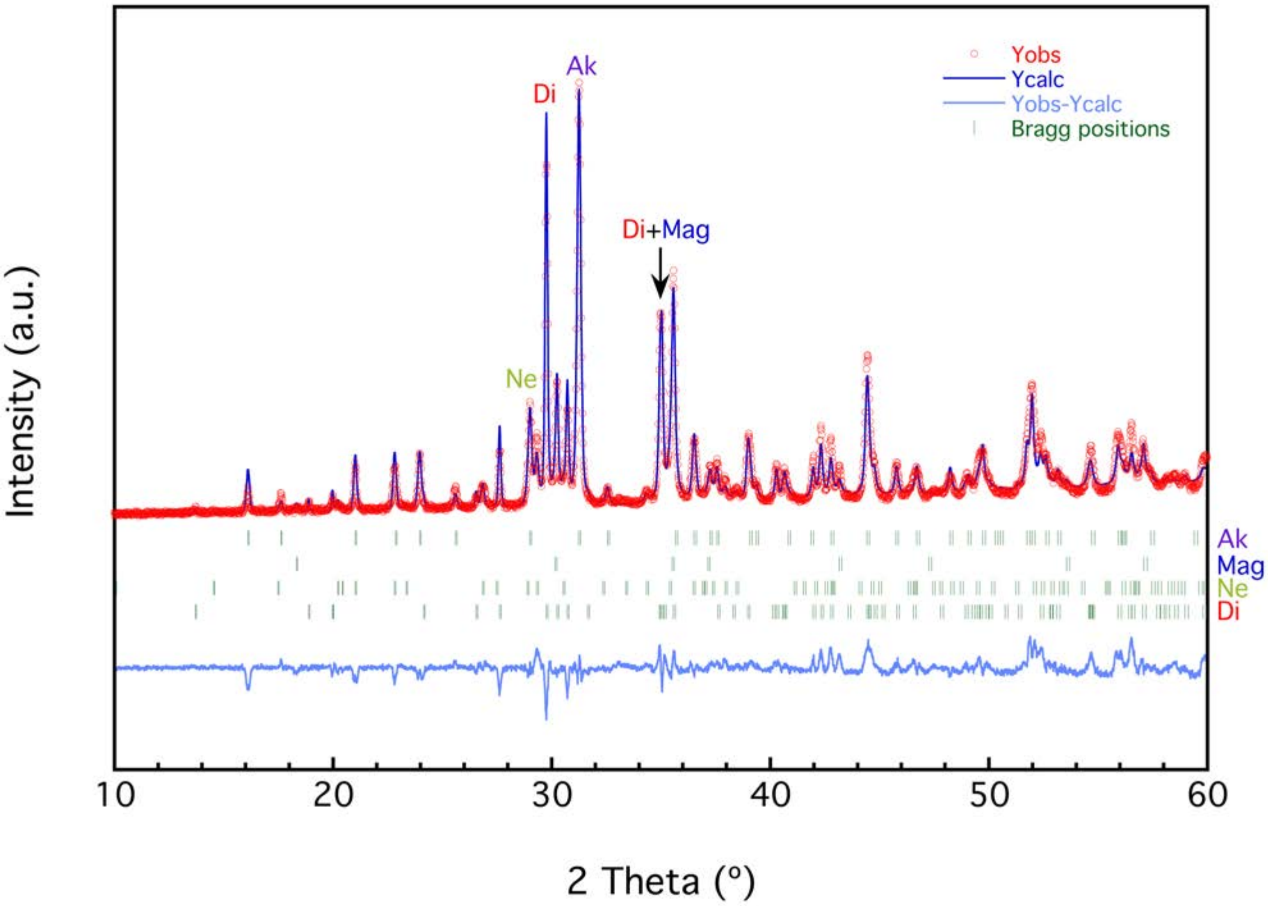

Figure 6.16. XRD pattern of the glass-ceramic showing the observed intensity (Yobs) of the experiment, the calculated intensity of the Rietveld refinement (Ycalc), the difference curve and the Bragg positions of the diffraction for each mineral phase. The labels identify the 100% intensity diffraction peak of each crystalline phase.

Treating the parent glass at the T_{MNR} generates a large number of nuclei, which grow upon further heating. Between each T_N the heating is fast to minimize the growth of the phases that were nucleated in previous steps, ensuring a homogeneous crystal size. The bulk microstructure of the glass-ceramic observed on SEM consists on idiomorphic crystals ranging between 60 and 120 nm (Figure 9). Diopside, akermanite and nepheline form a homogeneous grain microstructure. Akermanite and diopside crystals have been tentatively distinguished by their Si/Ca ratio (higher in diopside than in akermanite). The observed sizes of the crystals are larger than 40–70 nm obtained from Scherrer's equation for diopside, nepheline and akermanite and 18 nm for magnetite. This difference arises from the steps for crystallization during glass-ceramic production being much longer than for *in-situ* HT-XRD.

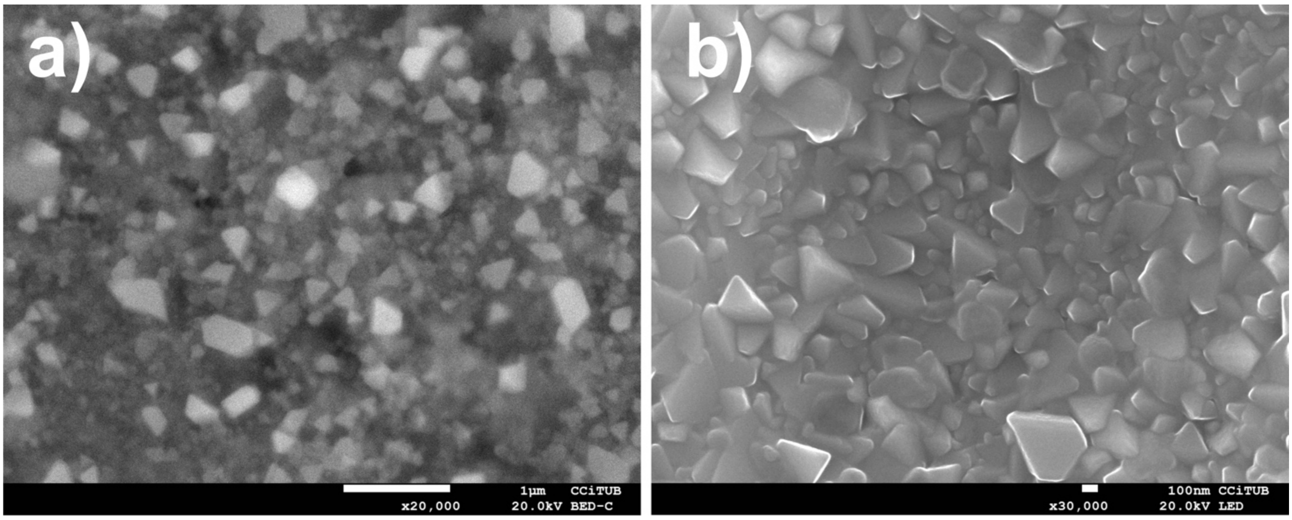

Figure 6.17. SEM micrographs showing the texture of the glass-ceramic. a) a BDS image of the mass of the crystals where dense magnetite crystals stand out b) a detail of the mixture of fine grained idiomorphic diopside, akermanite and nepheline.

6.2.10 Microhardness Vickers

The microhardness Vickers of the glasses decreases with the first Ca addition then starts rising near 13 wt% up to 28 wt% CaO (Figure 6.18). A decrease of the same order of magnitude than the whole increase then happens between 28 and 36 wt% CaO. The first decrease can be attributed to the increase of the bulk proportion of network-modifiers that fragilizes the network. The increase may be linked to the rise of the liquidus temperature due to the bulk composition of the system moving from the diopside to the melilite stability field Figure 6.7. This change may be causing more extensive nucleation in the glasses during quenching. Finally, the microhardness of the glassy portion greatly decreases with the onset of the crystallization of merwinite. This can be attributed to the depletion in nuclei that have integrated the crystal phase.

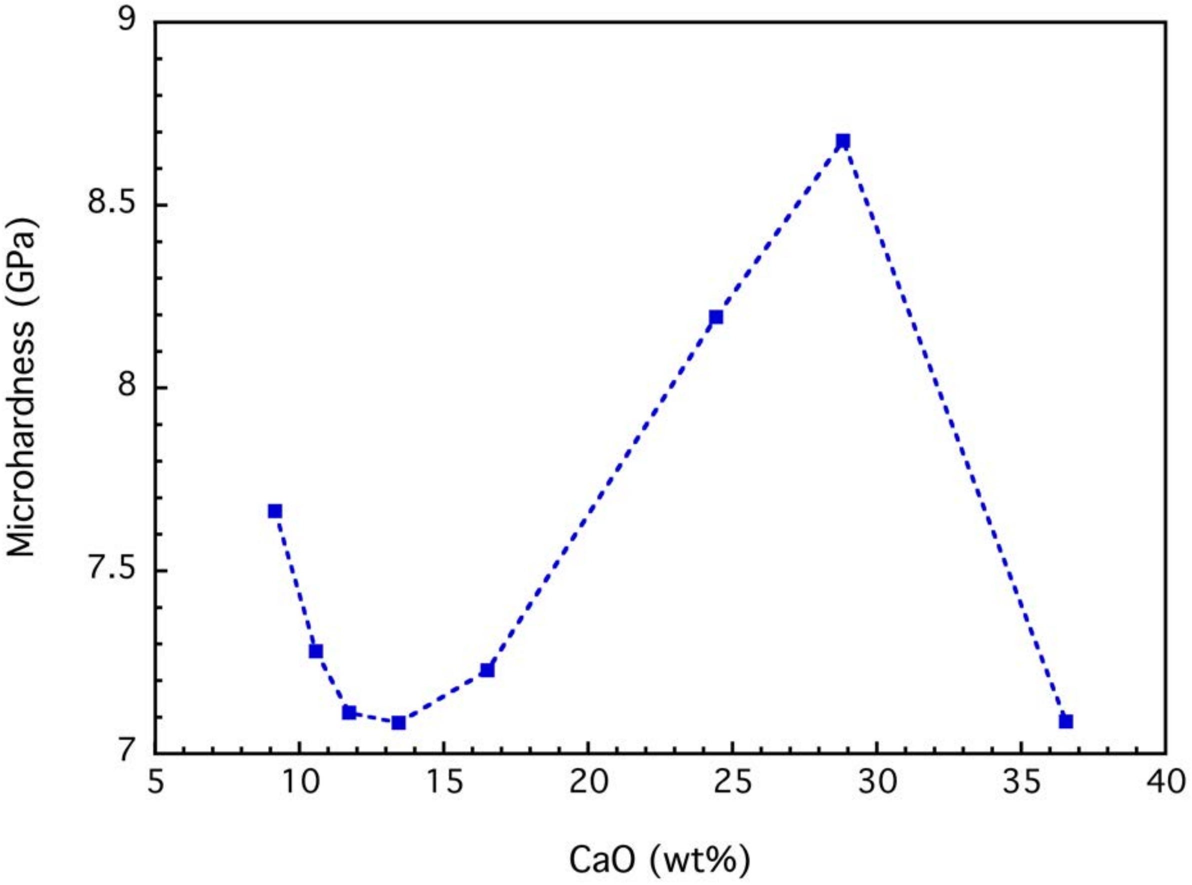

Figure 6.18. Microhardness Vickers measurements as a function of CaO concentration. The discontinuous line is intended as a guide for the eye.

Considering composition B16Ca, the microhardness of the parent glass equals 8.2 GPa, which increases up to 8.6 GPa for the glass-ceramic. These values – and those on all the glasses – lie in the hardness range of the diopside-hedenbergite series (from 7.7 to 9.8 GPa), are higher than the augite series (from 6.6 to 8.0 GPa), and considerably higher than the hardness of akermanite (5.2 to 6.6 GPa). The abundance of diopside and the development of a fine microstructure are the main contributors to the increase of the microhardness, which leads to an improvement on the mechanical properties of the obtained material.

6.2.11 Chemical resistance

The chemical stability and the inertization of the potentially toxic elements of the studied glasses is proven by their resistance to leaching (Table 6.4 and Table 6.5). For all the analyzed elements, the concentrations in the leachate are at least 6 orders of magnitude below the initial concentration in the glass for the major elements and at least 3 orders of magnitude for the minor elements. Apart from the elements summarized in the table, the measurements on As, Hg, and W are not reported due to being below the detection limit.

ppm sol	Si	Al	Ca	Mg	Na	K	Fe	P
B0	1.71	BDL	BDL	0.96	0.20	0.23	BDL	BDL
B1Ca	2.15	0.33	9.00	3.46	39.32	5.42	0.18	BDL
B2Ca	2.44	0.37	9.68	4.06	36.03	5.07	0.20	0.09
B4Ca	2.39	0.41	9.67	3.65	34.62	5.21	0.20	0.04
B8Ca	2.39	0.39	10.53	3.62	37.19	5.13	0.20	BDL
B16Ca	2.58	0.53	10.64	3.59	36.68	4.78	0.16	BDL
GC16Ca	4.79	0.88	4.43	2.45	8.31	1.88	0.11	BB
B24Ca	2.68	1.04	13.07	3.73	34.89	4.85	0.11	BDL

Table 6.4. Concentration of the major elements on the leachates after blank subtraction. BB stands for "below blank concentration" and BDL for "below detection limit".

ppb sol	Ba	Cd	Cr	Cu	Mn	Ni	Pb	Ti	Zn
B0	3.09	0.05	4.27	0.44	BDL	<0.6	BDL	BDL	1.35
B1Ca	196.48	BDL	5.94	7.38	7.49	8.99	0.37	30.13	1.49
B2Ca	182.43	BDL	10.80	14.73	8.87	3.76	0.60	35.83	3.30
B4Ca	66.88	BDL	6.60	13.36	7.18	6.90	6.26	33.98	6.52
B8Ca	83.21	BDL	6.27	7.14	7.07	4.03	1.09	33.61	5.63
B16Ca	116.54	BDL	6.35	3.58	5.03	2.64	0.84	25.15	0.83
GC16Ca	40.00	0.18	BDL	10.68	BDL	7.16	1.04	26.73	2.85
B24Ca	104.57	BDL	6.62	5.94	4.13	5.42	0.22	19.51	0.61

Table 6.5. Concentration of the minor elements on the leachates after blank subtraction. BB stands for "below blank concentration" and BDL for "below detection limit".

The glass-ceramic process has increased the overall stability of the glass, as the concentration of most of the major elements are lower in the glass-ceramics than in the glass leachate (Table 6.4 and Table 6.5However, the leachability of elements such as Ca, Si, Zn and Pb, As and Cd is higher from the glass-ceramic than the glass.

6.3 Discussion

The compositions of the glasses plotted in the phase diagram of the CaO-Al_2O_3-MgO-SiO_2 system – the major glass components – lie in the pyroxene, melilite and merwinite stability fields (Figure 6.6 and Figure 6.7). The crystallization of akermanite, the magnesian end-member of the melilite solid solution ($((Ca,Na)(Al,Mg,Fe^{2+})[(Al,Si)SiO_7])$) and its relationship with merwinite is a controversial question in the literature. Kalinina and Filipovich (Fredericci et al., 2000) consider merwinite a metastable phase formed during the thermal treatments of multicomponent glasses in the initial stages of the devitrification process, around T_g. The relaxation of the glass structure upon at higher temperatures will facilitate the diffusion of ions (Erol et al., 2007) causing the destabilization of merwinite, which will react with the other minerals to produce the stable mineral phases according to the phase diagram of the system.

A study of the crystallization of a glass of a composition in the akermanite-gehlenite system ($2CaO\cdot(1-x)\cdot MgO\cdot xAl_2O_3\cdot(2-x)SiO_2$) proved that merwinite is a metastable phase for all x below or equal to 0.6 and attributed this fact to structural reasons (Orsini et al., 1974). In the case of the melilite minerals, corresponding to the sorosilicate group, the structure consists in a fragmented network of silica tetrahedra and modifier cations are stabilized by the ionic bonds between the tetrahedra and the cations (Fredericci et al., 2000). Merwinite is a nesosilicate and thus presents a lower concentration of silica tetrahedra, creating a less strong network that melts at lower temperature (Orsini et al., 1974). The formation of akermanite may then be explained from the diffusion of Ca from merwinite to diopside described by the following reaction:

Merwinite + Diopside → Akermanite

$3CaO\cdot MgO\cdot 2SiO_2 + CaO\cdot(MgO,FeO)\cdot 2SiO_2 \rightarrow 2CaO\cdot(MgO,FeO)\cdot 2SiO_2$

Taking the melilite formula into account, the bulk composition of B16Ca can be expressed as $2CaO\cdot 1.05MgO\cdot 0.55Al_2O_3\cdot 2.76SiO_2$. In this case, x is effectively below 0.6 and then merwinite is metastable. Moreover, the already insufficient concentration of Al in the system is also influenced by the formation of nepheline during the devitrification process. Nepheline is the phase with a higher Al concentration between those formed during the devitrification process hence its formation extracts Al from the system, destabilizing merwinite and enhancing the crystallization of akermanite. Even the melting of nepheline over 860 ºC does not reenter enough Al in the system to allow the formation of merwinite, and thus it is not present the glass-ceramic. The relationship between diopside, akermanite and merwinite is in good agreement with the diagram in Figure 6.7. As this transformation occurs in the solid state, the diffusion of the components of the system is heterogeneous along the sample.

Nucleation and crystallization influence macroscopic properties of the melt such as viscosity (Kim et al., 2004), which are essential in the production of the glass and the glass-ceramic. The disproportionate increase of viscosity in sample B24Ca may be influenced by two factors: first, the formation of Ca-O-Ca bonds as it happens in calcium silicate glasses (De Sousa Meneses et al., 2006), and second, a possible phase separation (Huang and Behrman, 1991) that in sample B32Ca evolves into the crystallization of merwinite. Concerning the effect of the nucleation on viscosity, the large increase in viscosity between the parent and the nucleated glasses is attributed to the formation of a biphasic system consisting in a crystalline and an amorphous phase. The crystals facilitate the formation of the fine-grained glass-ceramic by hampering the viscous flow at the nucleation range, limiting the reactivity between the different phases (Figure 7) in a similar manner. A further temperature rise decreases the bulk viscosity of the material permitting reactions between minerals but preserving the fine microstructure until the melting range (around 10^3 Pa·s), where the system becomes monophasic again.

The production process of the glass-ceramic based on the determination of the temperatures of maximum nucleation rates and the study of crystal growth has provided a crystalline material with a fine microstructure. Obtaining extensive nucleation on a glass-ceramic based on basalt usually requires a Fe_2O_3/FeO ratio over 0.5 (Beall and Rittler, 1976). The raw basalt Fe_2O_3 /FeO equals 0.501 (Alfonso, 1985) and supplementary oxidation is provided by melting the ground basalt under air atmosphere (Beall and Rittler, 1976). This fine microstructure is a direct result of the treatment of the glass at the temperatures of maximum nucleation rate for an extended period (in this case, 6 h) followed by a fast heating of the sample up to the growth temperature to avoid the formation of metastable phases such as merwinite. An additional factor that may help in developing this microstructure is the presence of pre-structured domains as hinted by the noisy Raman signal. The presence of magnetite and diopside in the mineralogy of the glass-ceramic shows a good potential for the inertization of PTE such as Cr or Zn present in sludge (Hossain et al., 2009; Rawlings et al., 2006; Tervahauta et al., 2014) because they could be hosted in the spinel structure or in the pyroxene lattice.

The microhardness of the glasses and the glass-ceramic lie on the same range, and near the higher limit, of the reported values for basalt glasses and glass-ceramics in the literature (Table 6.6). The extensive nucleation of the parent glass creates a fine microstructure and limits the eventual formation of porosity due to crystal growth (Figure 6.17), making the glass-ceramic harder than the glass in spite of bearing approximately 40 wt% of the softer mineral akermanite (5.2-6.6 GPa). These results have to be taken with certain reserve because the difference in hardness between B16Ca glass and glass-ceramic is within the experimental error. However, the trend of increasing hardness is a promising advocate for the glass-ceramic process as a means for improving the mechanical properties of multicomponent glass.

Material	Vickers microhardness (GPa)
Sant Joan les Fonts Basalt glass (B0)	7.7 ± 0.3
B16Ca glass	7.08-8.67 ± 0.5
B16Ca glass-ceramic	8.6 ± 0.5
Canary Island Basalt glass	5.16-6.28 (De Vicente Mingarro, 1992)
Canary Island Basalt glass-ceramic	6.62-8.66 (De Vicente Mingarro, 1992)
Basalt rock fiber glass	7.7 (Jensen et al., 2009)
Basalt glass/crystal mixtures	6.8-8.9 (Jensen et al., 2009)
Holyoke basalt glass	8.9 (El-Shennawi et al., 1999)

Table 6.6. Microhardness results of this study compared to Vickers microhardness values for basaltic glasses and glass-ceramics in the literature.

Glass-ceramics are generally characterized by a good chemical resistance, comparable to other ceramic materials (McMillan and Piriou, 1975). In this study, the leachability tests provided complex results. The decrease in the concentrations of most of the main components between the leachates of the glass and the glass-ceramic point to an overall better inertization potential. However, the leachability of Si, Ca, Cu, Ni, Pb and Zn is lower in the glass than in the glass-ceramic. The trace metals As, Cd, Pb and Zn may be partitioning to a Fredericci and coworkers observed a similar situation in the increase of weight loss between a blast furnace slag glass and glass-ceramics (Fredericci et al., 2000). This situation might be caused by the high amount of akermanite, which is the phase with higher Si contents of the glass-ceramic. Karamanov and coworkers (Karamanov et al., 1994) produced a diopside glass-ceramic which underwent a weight loss as low as 0.3 wt%, whereas the experiments of Kruchnin (Fredericci et al., 2000) found a weight loss of 1.2 wt% for acid-resistant melilite glass-ceramics. Future research could be based on decreasing the amount of Ca to increase the proportion of pyroxene and maximize the chemical resistance.

6.4 Conclusions

Basalt glasses may be enriched up to 28.84 wt% CaO until the system crystallizes into merwinite during quenching. Increasing the amount of Ca controls the devitrification process: at low Ca concentrations, the main phase is diopside, changing to akermanite at higher Ca contents. The relationship between crystallization and viscosity is complex; however, it seems that a larger DTA peak and intensity of the XRD reflections of diopside are correlated with a higher viscosity.

The glass-ceramics processing of sample B16Ca based on the determination of the temperatures of maximum nucleation rate and crystal growth of the newly-formed phases (magnetite, nepheline, pyroxene, merwinite and melilite) has provided a material with improved mechanical resistance and chemical stability compared to its parent glass Nucleation and crystallization condition the rheology of the glass because the system becomes biphasic, hence its apparent viscosity increases. This confers a certain rigidity to the material, hampering the reactions between formed nuclei and the residual liquid phase until crystallization is finished. The final result is a nanometric homogeneous microstructure that enhances the mechanical properties of the glass-ceramic.

Both the glasses and the glass-ceramic have a high hardness, in the range of ceramic tiles used in the building industry. Moreover, the leaching tests prove the binding of the PTE inside the glass structure and in the lattices of the minerals forming the glass-ceramic (spinel group magnetite and pyroxene). Optimizing the leachability may require adjusting the concentration of calcium to control the crystallization of akermanite.

CHAPTER 7 Effect of Ca in P-doped basaltic glass-ceramics: application to waste inertization

With you I can imagine a place where to be phosphate of calcium is enough.

John Berger

7.1 Introduction, Materials and Methods

This chapter discusses the effect of the calcium concentration in a P-doped basalt achieving a bulk compositions analogous to that of sewage sludge. The more significant results of chapters 4 and 6 concerning glass formation and viscosity may be summarized as:

- Concentrations over 4 wt% P_2O_5 cause a phase separation between a silicate and a phosphate liquids that result in crystallization during quenching above 16 wt% P_2O_5.
- Viscosity at high temperatures is boosted between 24 and 28 wt% CaO when the bulk composition of the glass enters the melilite stability field.

The glasses studied in this chapter are made from basalt mixed with about 5 wt% P2O5 and a concentration of Ca ranging from 9.73 to 30.21 wt% CaO. They have been analyzed in using EMPA, Raman spectroscopy, DTA, dilatometry, XRD, HSM, Vickers microhardness, and leaching tests in the conditions explained in chapter 3 (Materials and Methods). It must be noted that the acquisition time of the Raman spectra was reduced to 300 s per frame to optimize the duration of the analyses.

The study of the nucleation process of sample M23Ca has been done on glasses treated to maximize the formation of nuclei.

- The glass fragments are placed straight from room temperature to the furnace at Tn = 675ºC to ensure the nucleation of all minerals.
- The fragments are removed from the furnace back to room temperature.
- The fragments are placed in the furnace from room temperature to Texo (either 873 or 975 ºC), and left for 40 min. They are then removed to cool straight down to room temperature.
- The treated glasses are analyzed by XRD.

7.2 Results and discussion

7.2.1 Chemical composition and density

The chemical composition of the glasses made from mixtures of P, Ca and basalt is reported in Table 7.1. The P-Ca-basalt glass series of this chapter is compared to sample B4P commented in chapter 4.

	Major elements (wt%)									
	SiO_2	**Al_2O_3**	**CaO**	**MgO**	**Na_2O**	**K_2O**	**MnO**	**FeO**	**TiO_2**	**P_2O_5**
B4P	42.31	13.63	9.73	9.67	3.19	1.91	0.16	12.52	2.42	4.48
M14Ca	40.63	13.26	14.04	8.90	3.30	1.72	0.16	11.47	2.30	4.23
	0.18	0.08	0.14	0.06	0.07	0.04	0.02	0.09	0.03	0.18
M23Ca	35.58	11.44	22.10	8.07	2.99	1.48	0.14	10.34	2.01	5.85
	0.23	0.12	0.19	0.06	0.09	0.03	0.06	0.14	0.02	0.25
M30Ca	31.43	10.12	30.21	7.17	2.69	1.28	0.13	9.19	1.77	6.01
	0.27	0.06	0.21	0.05	0.07	0.21	0.02	0.09	0.10	

Table 7.1. Chemical composition of the glasses and error expressed as the standard deviation of the measurements.

The density of the glasses grows linearly from 2.83 to 2.98 g/cm3 with Ca addition (Figure 7.1). Its low standard deviation (below 0.006) and the low standard deviation of the EMPA measurements verify the homogeneity of the glasses. The addition of network modifiers rises the density of glasses because the cations occupy free space between tetrahedra and polarize the non-bridging oxygens, contracting the network (Fernandez Navarro, 1991).

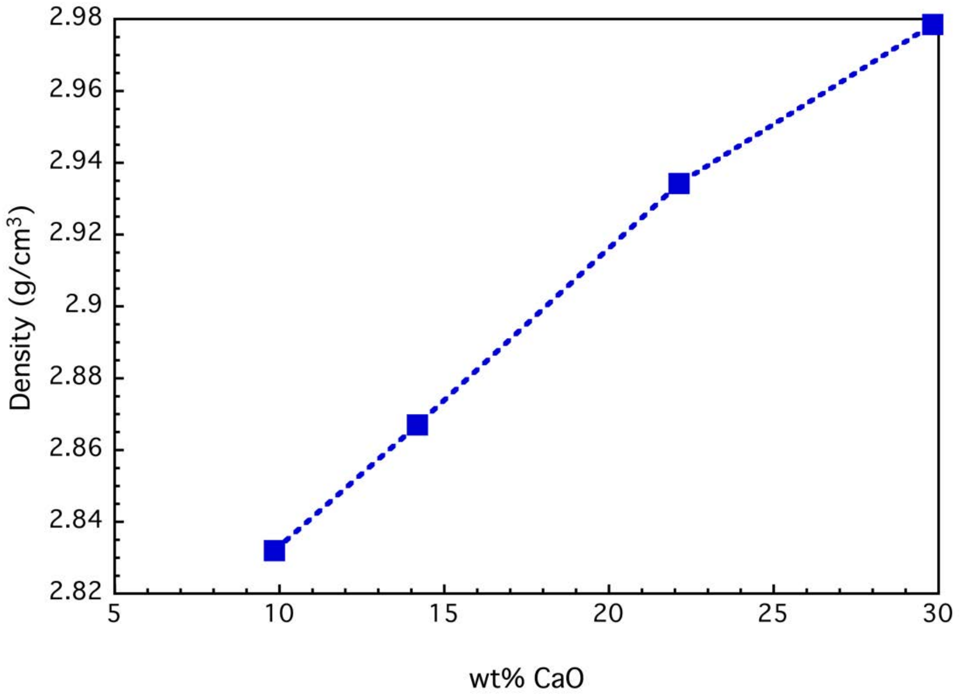

Figure 7.1. Density of the glasses as a function of the bulk concentration of calcium. The error of the measurements is smaller than the symbol.

7.2.2 Effect of calcium on the glass structure

The effect of the Ca concentration on structure of the glasses is determined from Raman spectra, divided in three regions (Figure 7.2). The Low Frequency, LF, is linked to the vibrations of the bridging oxygen in ring structures. The Middle Frequency, MF, is attributed to the intertetrahedral bending mode of polymerized species. It shifts to lower frequencies with the decrease in silica concentration due to Ca addition (Matson et al., 1983; McMillan, 1984b). The High Frequency, HF, is the region of the vibration of depolymerized species bearing non-bridging oxygens. The most intense band of the spectra is located between 953 and 978 cm^{-1}. It shifts to lower frequencies due to depolymerization caused by Ca addition. In Ca-Mg silicate glasses, this band between 950-1000 cm^{-1} and has been attributed to the vibration of Q^2 silicate groups (McMillan, 1984b). A shoulder of this band is visible at 877 cm^{-1} at 23 wt% CaO. It becomes stronger and shifts to 862 cm^{-1} at 30 wt% CaO. In Ca-Mg silicate glasses, this band is linked to Q^0 silicate groups (McMillan, 1984b). Its growth is consistent with the depolymerization trend caused by Ca addition in a network-modifying role. The rise of defined bands must also be influenced by the P contents, as they do not appear in the glasses that are only doped with Ca. As the free volume of the PO_4 tetrahedra is larger than that of SiO_4 (Mysen and Richet, 2005), it is possible that it promotes an arrangement of the tetrahedra in linear-based structures (Q^2) instead of in more polymerized arrangements. Moreover, the regions near P tetrahedra probably have a short range ordering different that the rest of the glass even though it is not likely that a full phase separation has developed according to the EMPA and density results. . The noise of the Raman signal points to the presence of nanolites, probably magnetite (Neuville et al., 1996).

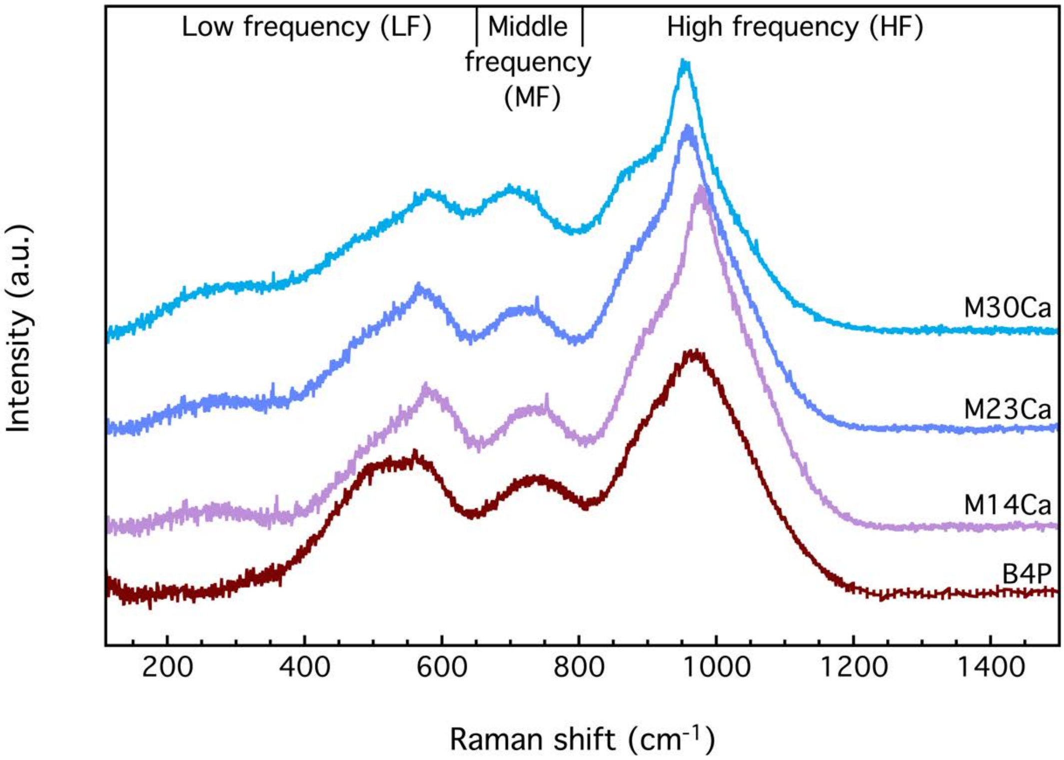

Figure 7.2. Raman spectra of the P-doped basalt (B4P) and the derived compositions with increasing concentrations of Ca.

7.2.3 Thermal analysis and crystallization process

DTA profiles (Figure 7.3) show endothermic events between 650 and 720 ºC corresponding to the glass transition range (T_g). The addition of Ca first increases DTA T_g due to the formation of the differentiated environment but then decreases in agreement with the depolymerization observed on the Raman spectra (Figure 1). The wide exothermal events bserved between 710 and 1000 ºC are due to the overlap of the crystallization of more than one crystalline phase at a time. In general, they shift to higher temperatures with Ca addition

(Table 7.2). The lack of consistency between of the evolution of Tg (specially the dilatometric Tg) with composition is related to the overlap of the glass transition and the crystallization peaks.

	Tg (DTA)	Tg (DIL)
B4P	661	638
M14Ca	698	620
M23Ca	687	636
M30Ca	684	648

Table 7.2. Temperatures of the exothermic events observed during the heating of the glasses.

The large endothermal events over 1070 ºC correspond to the melting of the system and are an indicator of the good fusibility of the compositions apart from the remaining magnetite nanolites. Their temperatures increase with the addition of calcium.

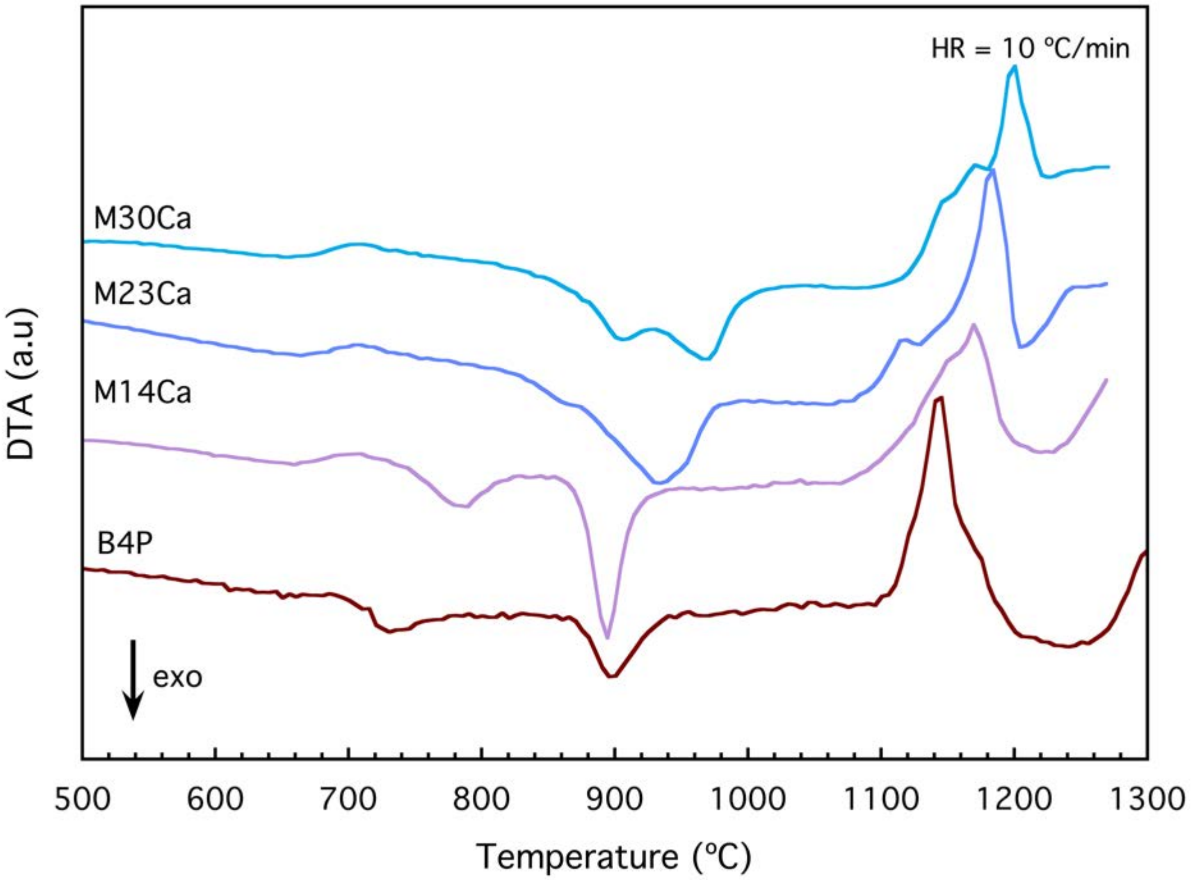

Figure 7.3. DTA of the effect of the calcium concentration on the thermal behavior.

The study of the devitrification of the glasses by means of XRD shows the crystallization of magnetite (Fe_3O_4), diopside ($CaMgSi_2O_6$), and also akermanite ($Ca_2MgSi_2O_7$), nepheline ($(Na,K)AlSiO_4$) and merwinite ($Ca_3MgAlSiO_4$) in sample M30Ca (Figure 7.4). The crystallization and relative importance of diopside appears to be correlated with the presence of chain-like Q^2 groups – in the fashion of inosilicates – whereas the formation of akermanite, a sorosilicate, happens when the melt is less polymerized. Hence, it is possible that the ordering in the glass precedes and conditions the crystallization process of the main minerals. The addition of Ca compensates the role of P inhibiting the crystallization of diopside and magnetite.

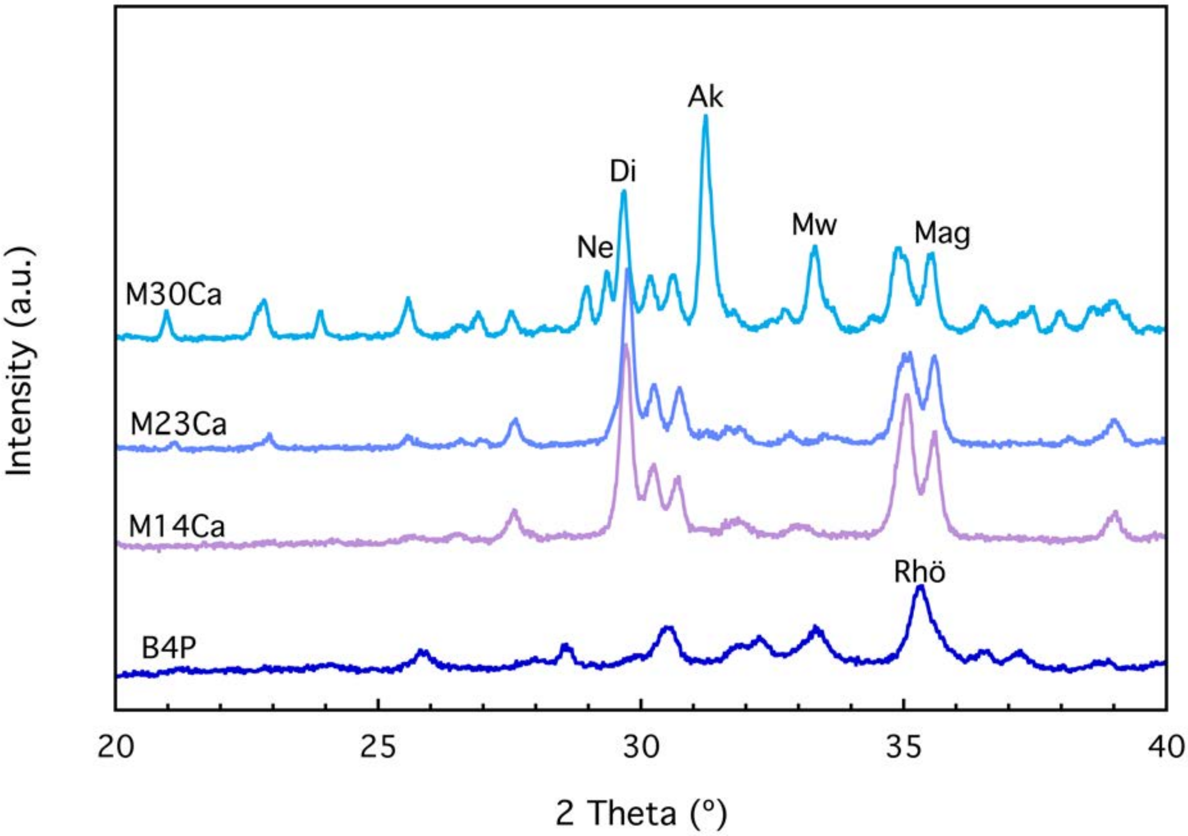

Figure 7.4. XRD profiles of the glasses treated at the temperatures of the DTA exothermal events.

The increase of the melting temperature is consistent with the liquidus rising from the pyroxene towards the melilite and merwinite stability fields (Morse, 1980). However, the increase of the liquidus temperature also affects the quenching, as the supercooling is more effective when the melting temperatures are lower. This produces an increase in nucleation with Ca addition.

7.2.4 Viscosity-temperature curves

The study of the viscous flow offers some insight on glass production and crystallization by comparison to a natural basalt glass from Piton de la Fournaise volcano (Villeneuve et al., 2008) (Figure 7.5). At the low temperature interval (during shrinkage), the deformation is dominated by the amorphous phase and the temperature of the fixed viscosity points decreases with Ca addition, in agreement with the depolymerization. In the softening range the material crystallized extensively, hampering the viscous flow (Fig. 3). The bump of viscosity is larger in the samples with less Ca because they were less nucleated during quenching. The high temperature range is dominated by the liquid phase. The viscosity decreases with Ca addition because of the depolymerization of the network. However, the increase of the melting temperature of the remaining crystals delays the flow stage (Figure 7.5).

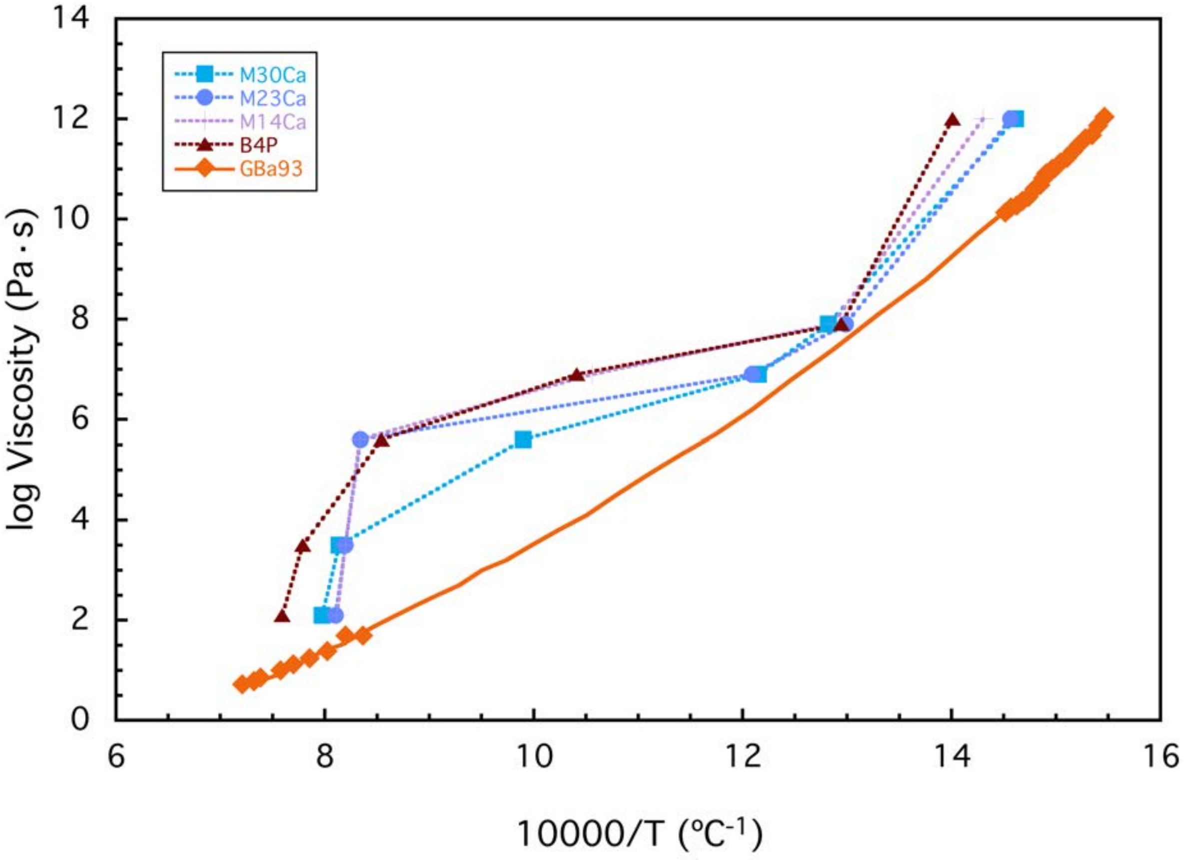

Figure 7.5. Temperatures of the fixed viscosity points of HSM on solid-liquid mixtures compared to the viscosity of GBa93 (Villeneuve et al., 2008).

7.2.5 Microhardness

The addition of Ca increases the microhardness Vickers of the annealed materials from 6.7 to 7.3 GPa (Figure 7.6). All the values are inside the range of basalt glasses (5.16-8.9 GPa (De Vicente Mingarro et al., 1991; Jensen et al., 2009)). This rise of microhardness is correlated with more extensive nucleation at higher Ca concentrations, as crystals are generally harder than the amorphous phases of the same composition.

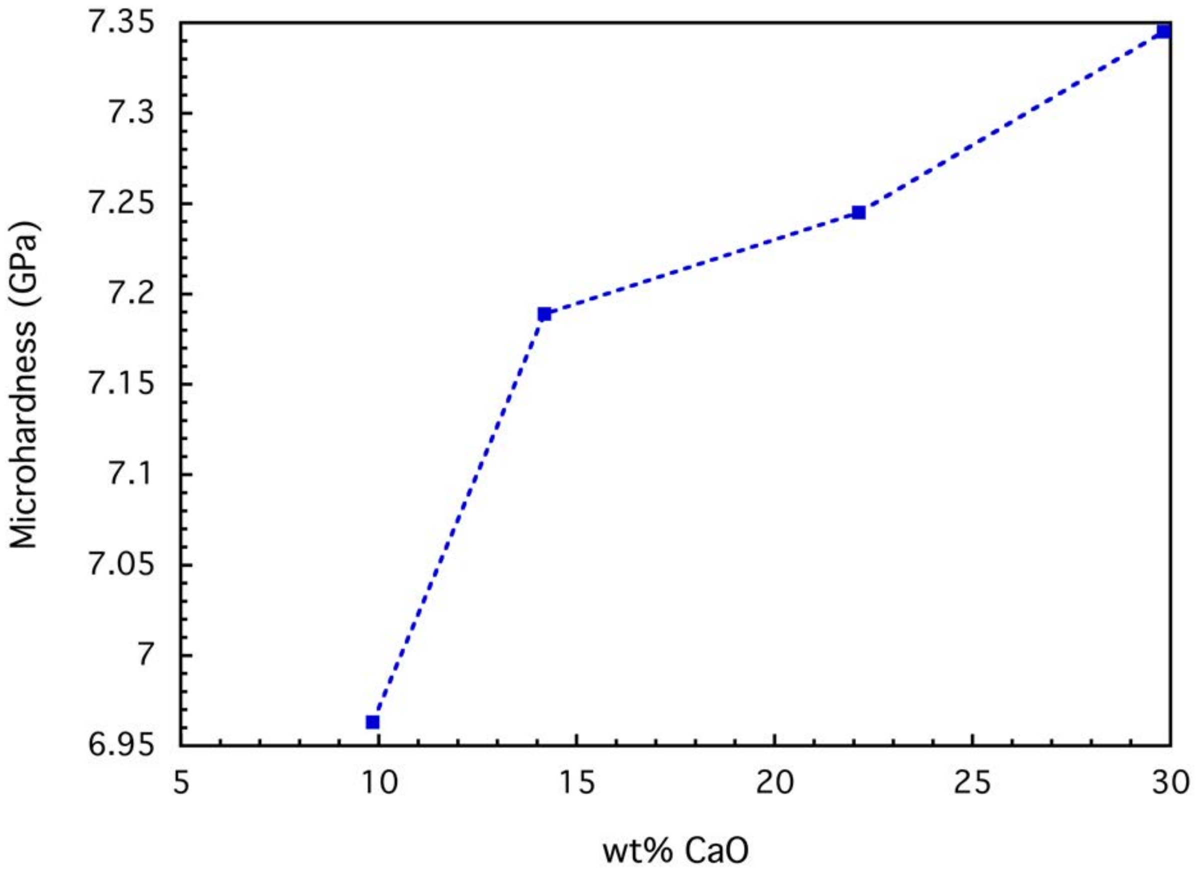

Figure 7.6. Microhardness Vickers as a function of Ca contents. The error of the measurements is about 0.5 GPa.

7.2.6 Nucleation process and glass-ceramics production

Composition M23Ca has been chosen for an extended study of its nucleation process because it bears the highest concentration of Ca while still crystallizing into pyroxene and magnetite. The T_{MNR}s are determined using the shift of the exothermic peaks at 873 and 935 ºC for the glasses treated at different nucleation temperatures (Figure 7.7). According to the maxima of the plots of the inverse of the temperature of the exothermic as a function of nucleation temperature, the T_{MNR} are 660 and 648 ºC.

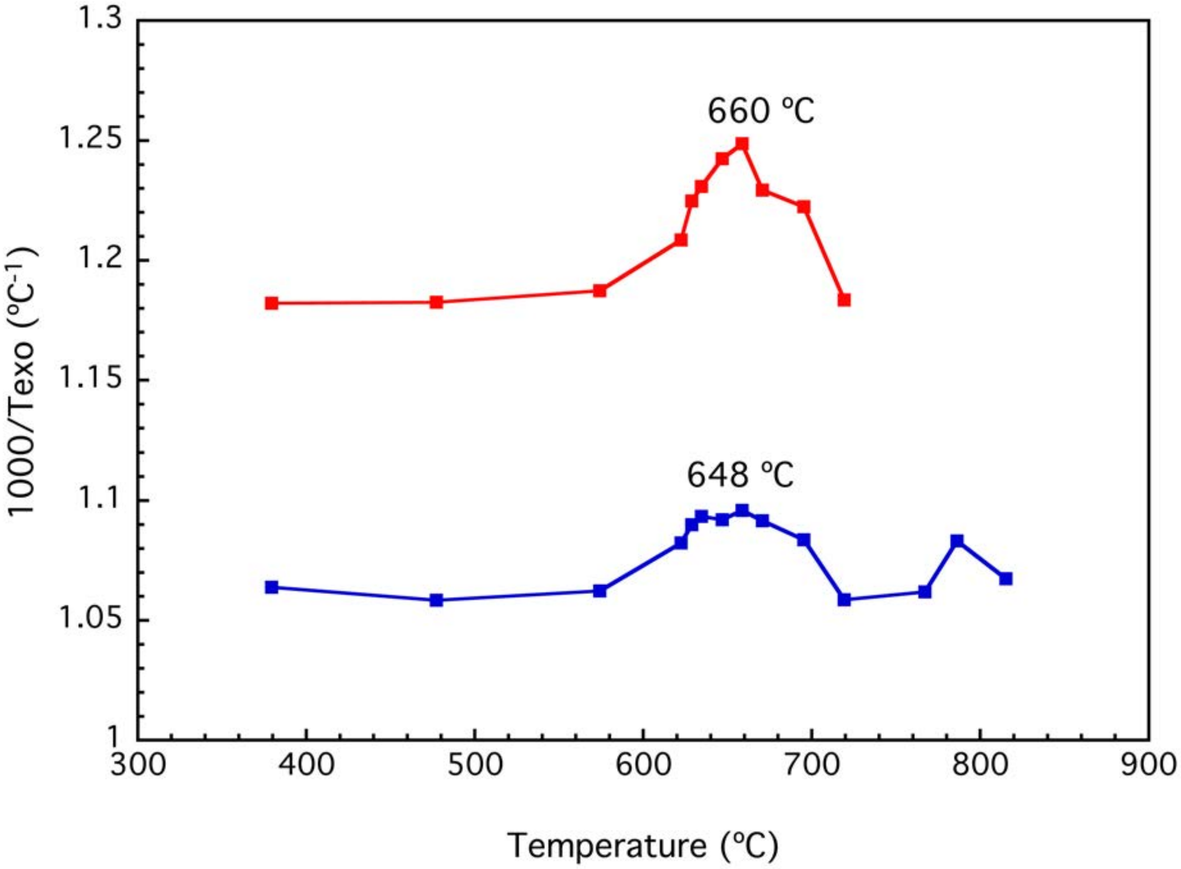

Figure 7.7. Variation of the inverse of the peak temperature as a function of nucleation temperature.

The first T_{MNR} corresponds to the nucleation of magnetite (Figure 7.8). The reduced amount of reflections is consistent with a cubic phase, and their limited height is due to the bulk concentration of Fe being below 10 wt%. The treatment at the second T_{MNR} has caused the crystallization of diopside together with minor amounts of nepheline and akermanite. This means that all their T_{MNR}s must be very close and thus they cannot be isolated. However, it is likely that T_{MNR}=660 ºC corresponds to diopside since its intensity is 6 and 13 times higher than those of nepheline and akermanite, respectively (Figure 7.8).

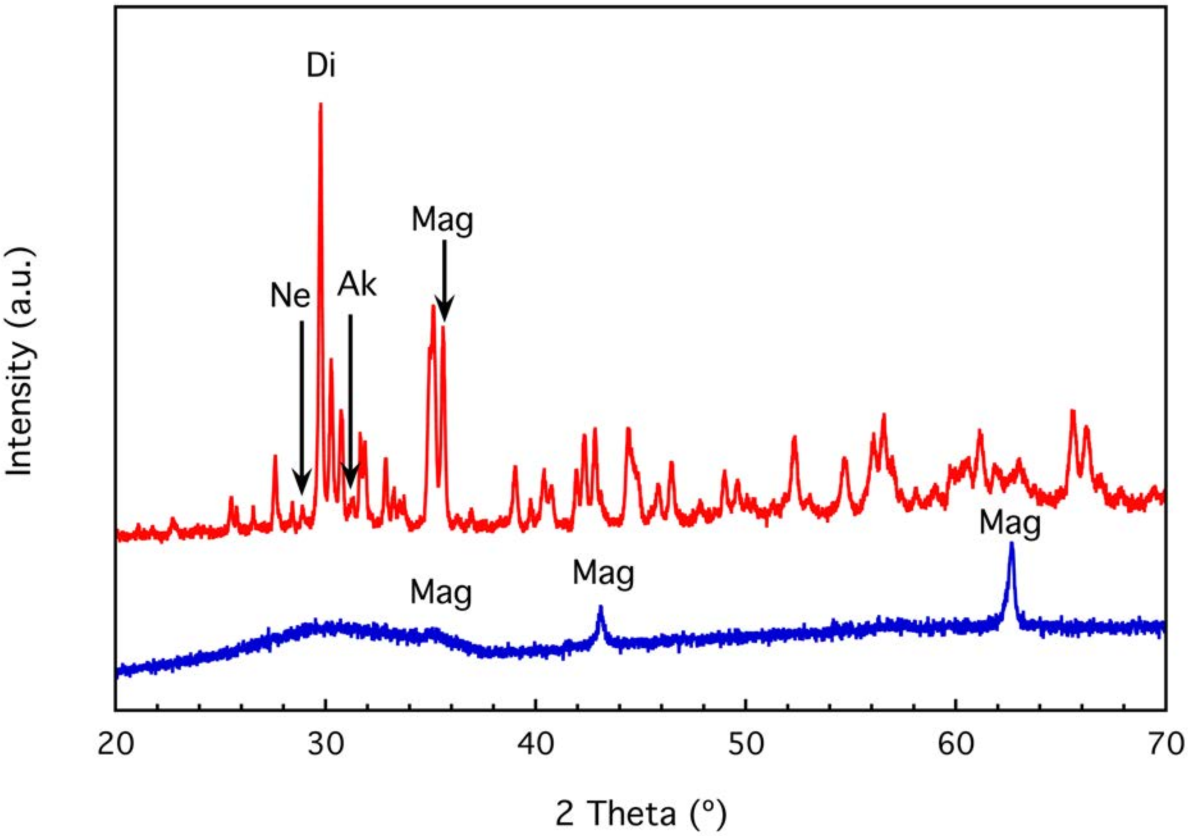

Figure 7.8. XRD spectra of glasses of M23Ca composition treated at the corresponding nucleation temperatures for 40 min.

The thermal treatment to produce the glass-ceramics has been designed in agreement with the results of the study of the nucleation. It includes the following heating steps:

- From room temperature to 648 ºC (T_{MNR} of magnetite) at 15ºC/min for 8h.
- From 649 to 661 ºC (T_{MNR} of diopside) at 15ºC/min for 8h.
- From 661 to 873 ºC (peak of the 1st exothermic event) at 15ºC/min for 8h.
- From 873 to 940 ºC (peak of the 2nd exothermic event) at 15ºC/min for 8h.
- Free cooling.

The glass-ceramics has been characterized both from the microstructural and the mineralogical points of view. The SEM image shows the crystal grains of a diameter about 100-200 nm formed during the glass-ceramics processing (Figure 7.9). It is not possible to distinguish the composition of the crystals by EDS due to their small size, about 100-200 nm.

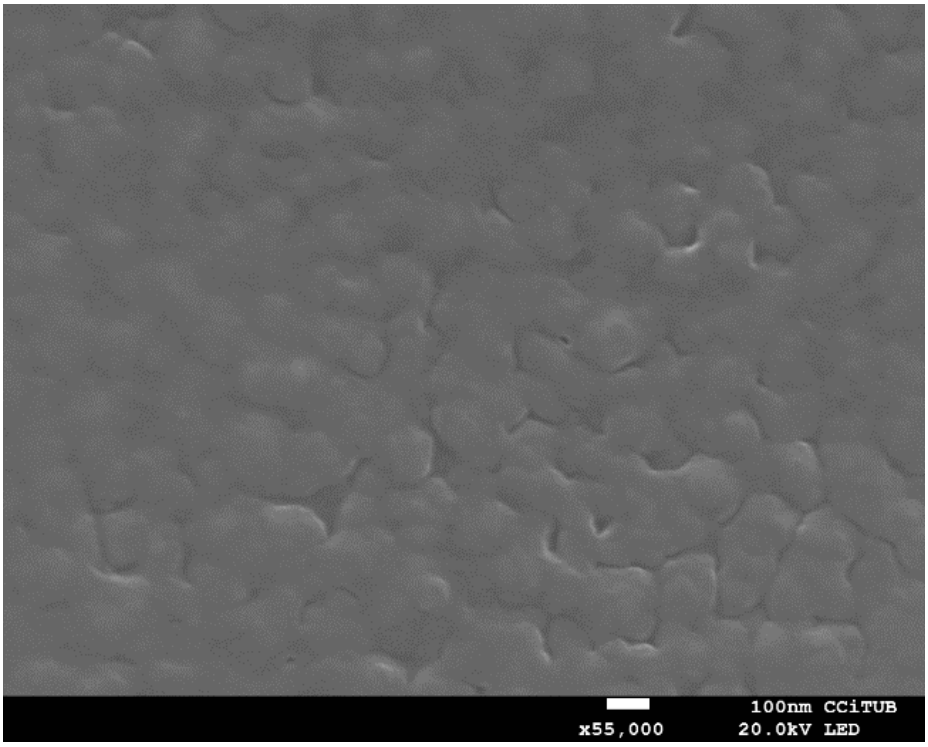

Figure 7.9. SEM micrograph of the glass-ceramics of sample M23Ca.

XRD has shown the presence of diopside and magnetite as the main phases together with minor amounts of akermanite and nepheline (Figure 7.10). The presence of nepheline and akermanite is attributed to the larger treatment time of the glass-ceramics process combined with the overlap between their crystallization processes and that of diopside. Individual magnetite crystals cannot be observed in SEM because they have acted as the nuclei for the growth of pyroxene.

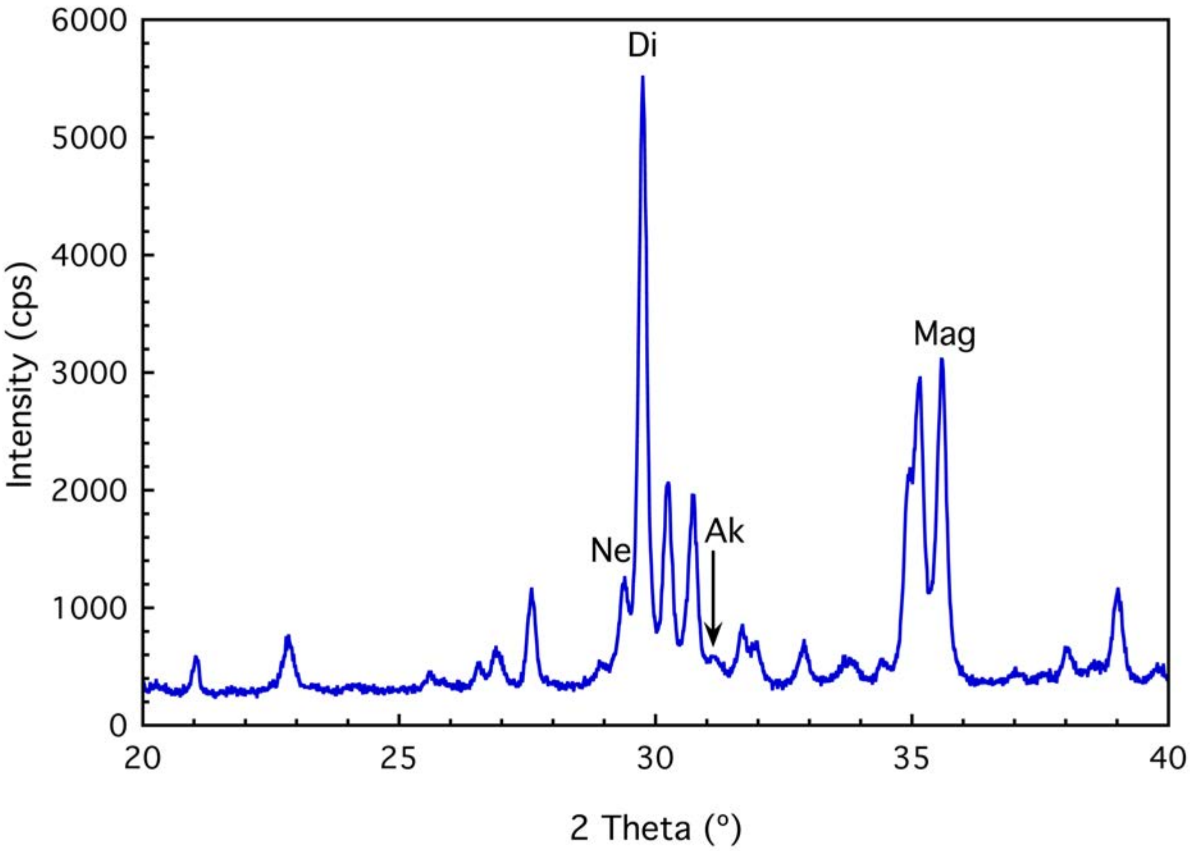

Figure 7.10. XRD profile of the glass-ceramics showing the presence of diopside, magnetite and minor amounts of nepheline and akermanite.

7.2.7 Chemical stability

The leachates of the quenched products contain concentrations of the main elements at least six orders of magnitude below those of the original glasses (Table 7.3), together with concentrations at least 4 times smaller for the minor elements (Table 7.4). Moreover, all the compositions comply with the requirements of DIN38414-S4 for the glasses to be considered inert.

Leaching of the major elements (ppm)										
	Si	Al	Ca	Mg	Na	K	Mn	Fe	Ti	P
B4P	2.19	BDL	BB	1.02	0.99	0.34	$4.2*10^{-4}$	BDL	0.00	BB
M14Ca	2.87	0.53	4.03	2.1	2.41	0.74	3.42	0.15	0.03	BB
M23Ca	3.61	1.01	3.60	2.86	10.30	2.06	3.60	0.23	0.05	BB
GCM23Ca	5.85	0.88	13.03	2.83	9.36	2.11	$3.8*10^{-4}$	0.11	0.03	BDL
M30Ca	4.04	1.18	6.33	2.99	8.49	2.10	1.98	0.17	0.03	BB

Table 7.3. Concentrations of the main elements of the quenched products in the leachates.

Trace elements leached (ppb)							
	As	Ba	Cd	Cu	Ni	Pb	Zn
B4P	BDL	BB	BDL	BDL	BDL	BB	BB
M14Ca	0.09	29.15	1.47	2.85	3.45	0.68	5.33
M23Ca	BDL	BB	0.77	15.92	5.12	0.77	7.15
GC M23Ca	0.71	100	0.24	15.79	7.16	1.36	15.37
M30Ca	BDL	BB	0.82	8.34	BDL	0.82	BB
DIN38414-S4	500	-	40	2000	400	500	4000

Table 7.4. Concentrations of the trace elements of the quenched products in the leachates compared to the allowed limits according to DIN38414-S4 (DIN-38414S4, 1984).

7.3 Conclusions

The addition of Ca to P-doped basaltic melts gives nucleated glasses after quenching. The vitreous part is depolymerized with Ca addition in presence of P, leading to a decrease in viscosity and the formation of bands assigned to Q^2 and Q^0 silicate groups. The nucleation becomes more extensive with Ca addition, increasing microhardness. All the products are chemically stable, and have a potential for the inertization of industrial wastes.

After the glass-ceramics processing, sample M23Ca crystallizes mainly into fine-grained pyroxene, magnetite and minor amounts of nepheline and akermanite. The apparent absence of magnetite on SEM may be attributed to its integration in the crystal lattice of pyroxene. The fine microstructure of the glass-ceramics may potentially improve the mechanical properties of the parent glass.

CHAPTER 8 Vitrification of toxic elements

Right now, other frightening imperatives have distracted us so far from the program of benevolence toward our planet that it seems we might just try to burn the whole world for fuel to keep ourselves guarded and cozy. But that is not the expressed will of our people. Most of us do understand, when we can calm down and think clearly, that whether we are at peace or at war, the lives that hang in the balance are not just ours but the millions more that create the support system and biological context for humanity. More and more of us are listening for the silent alarm, stopping in our tracks, wishing to salvage the parts of this earth we haven't yet wrecked.

Barbara Kingsolver, Small Wonder

8.1 Introduction

This chapter focuses on the inertization of potentially toxic elements in sewage sludge-like matrices. The concentrations of PTE have been established according to two factors: their abundance in sewage sludge (as reported on chapter 1) and the determination of their maximum solubility limit. The concentrations of the elements of interest in some examples of sewage sludge from Catalonia are reported in Table 8.1. The focus of this chapter lies in explaining and discussion the specific changes related to the addition of heavy metals.

ppm	Centelles	Vic	Taradell	Torelló	Manlleu	Tona	Prats	Roda
Ba	0.17	BDL	0.18	BDL	0.29	0.14	0.12	0.07
Cu	70.76	52.92	104.97	36.75	33.11	BDL	61.36	50.17
Cr	BDL	742.7	BDL	23.89	BDL	BDL	195.45	265.21
Ni	BDL	BDL	BDL	23.89	BDL	BDL	31.82	BDL
Zn	39.8	58.59	50.89	115.76	46.35	54.28	BDL	77.65

ppm	Centelles	Vic	Taradell	Torelló	Manlleu	Tona	Prats	Roda
Ba	0.17	BDL	0.18	BDL	0.29	0.14	0.12	0.07
Cu	70.76	52.92	104.97	36.75	33.11	BDL	61.36	50.17
Cr	BDL	742.7	BDL	23.89	BDL	BDL	195.45	265.21
Ni	BDL	BDL	BDL	23.89	BDL	BDL	31.82	BDL
Zn	39.8	58.59	50.89	115.76	46.35	54.28	BDL	77.65

Table 8.1. Concentrations of potentially toxic elements in Catalan sewage sludge. BDL stands for below detection limit.

8.2 Barium

8.2.1 Chemical composition and density

The chemical compositions of the Ba-doped glasses are presented in Table 8.2 and compared to the composition of its base matrix M23Ca.

Wt %	**SiO_2**	**Al_2O_3**	**CaO**	**MgO**	**Na_2O**	**K_2O**	**TiO_2**	**FeO**	**MnO**	**P_2O_5**	**BaO**
M1Ba	34.76	13.13	21.86	7.80	2.83	1.47	1.99	9.05	0.15	5.61	1.23
Std dev	0.99	1.93	0.46	0.25	0.08	0.05	0.10	0.18	0.02	0.29	0.08
M5Ba	33.35	10.99	21.10	7.58	2.94	1.42	1.98	8.80	0.15	5.54	6.01
Std dev	0.20	0.05	0.20	0.06	0.07	0.04	0.07	0.10	0.01	0.31	0.29
M10Ba	31.95	10.60	20.28	7.11	2.80	1.37	1.94	8.31	0.14	5.44	12.37
Std dev	0.18	0.08	0.09	0.05	0.03	0.02	0.07	0.07	0.02	0.28	0.38
M23Ca	33.58	11.44	22.10	8.07	2.99	1.48	0.14	10.34	2.01	5.85	0.00
Std dev	0.23	0.12	0.19	0.06	0.09	0.03	0.02	0.14	2.01	0.25	0.00

Table 8.2. Chemical compositions of the matrix glasses doped with barium and error of the measurements expressed by means of the standard deviation (Std dev).

The density of the glasses increases with BaO addition due to the high atomic weight of the Ba atom compared to the average of the rest of the components (Figure 8.1). The low error of these measurements is an indicator of the homogeneity of the glasses.

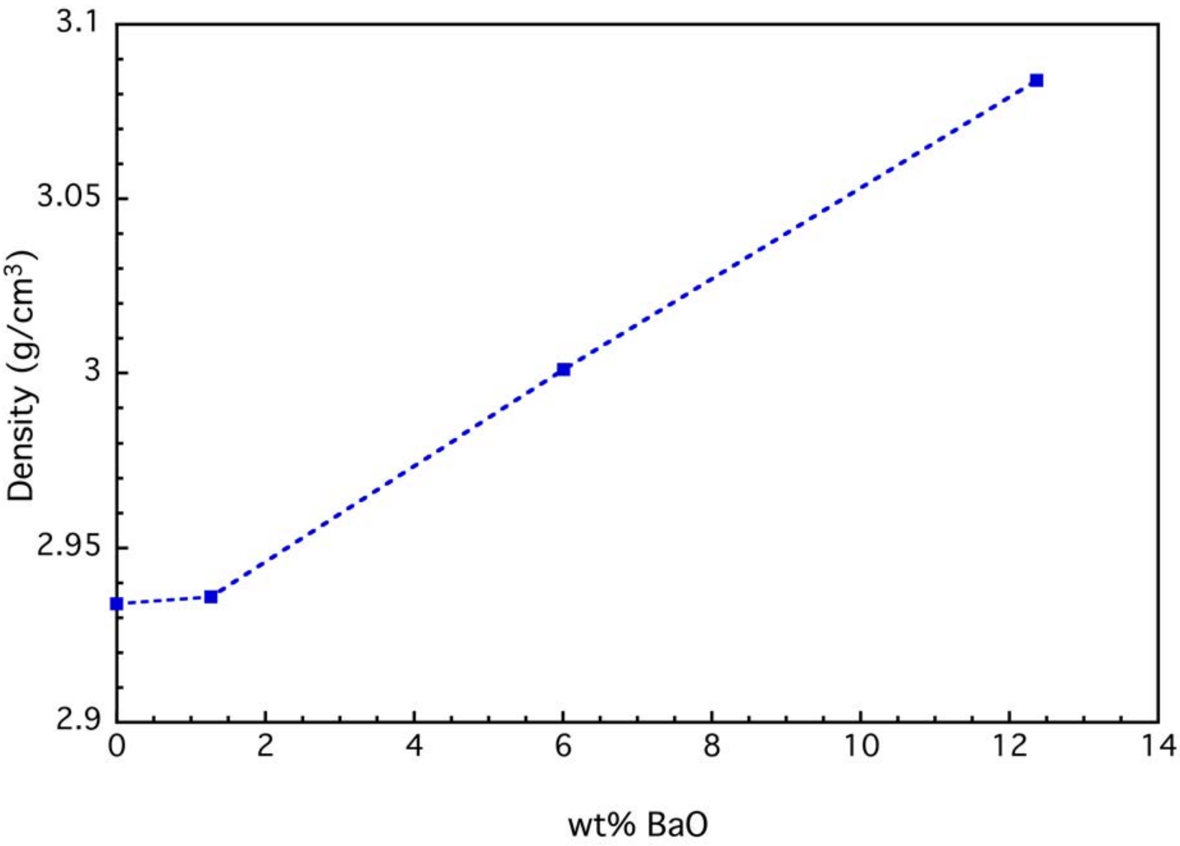

Figure 8.1. Variation of density as a function of the concentration of BaO. The error of the measurements is smaller than the symbol.

8.2.2 Raman spectroscopy

The Raman spectra are divided in three regions (Figure 8.2): the low (LF), middle (MF) and high frequency (HF) spectra described and discussed in previous chapters. The attribution of the bands is similar to that of sample M23Ca (chapter 9). Increasing the concentration of Ba does not seem to have major effects on the shape of the bands: the LF is located centered around 568 cm^{-1} and the MF, centered about 710 cm^{-1} shifts slightly to lower frequencies with the decreasing silica contents. The HF envelope is also very similar to the base composition: the main vibration that oscillates near 950 cm^{-1} is linked to the presence of Q^2 groups and the shoulder at 875 cm^{-1} may be attributed to Q^0 groups (McMillan, 1984a). The reduced effect of barium in the glass structure is consistent with the observations that in alkali and alkaline earth glass Raman spectra, regardless of the metal/silicon ratio, the frequencies assigned to antisymmetric Si-NBO and Si-BO stretch vibrations in the various Q^n-species are nearly independent of glass composition (Mysen and Richet, 2005). In other words, as long as the added metal is an alkali or an alkaline earth, the position of the bands changes with the degree of polymerization but not due to the nature of the element. In consequence, Ba occupies the structural position of Ca. However, the effect on polymerization is less patent because the larger ionic radius of Ba leaves less margin for the aluminosilicate network to accommodate.

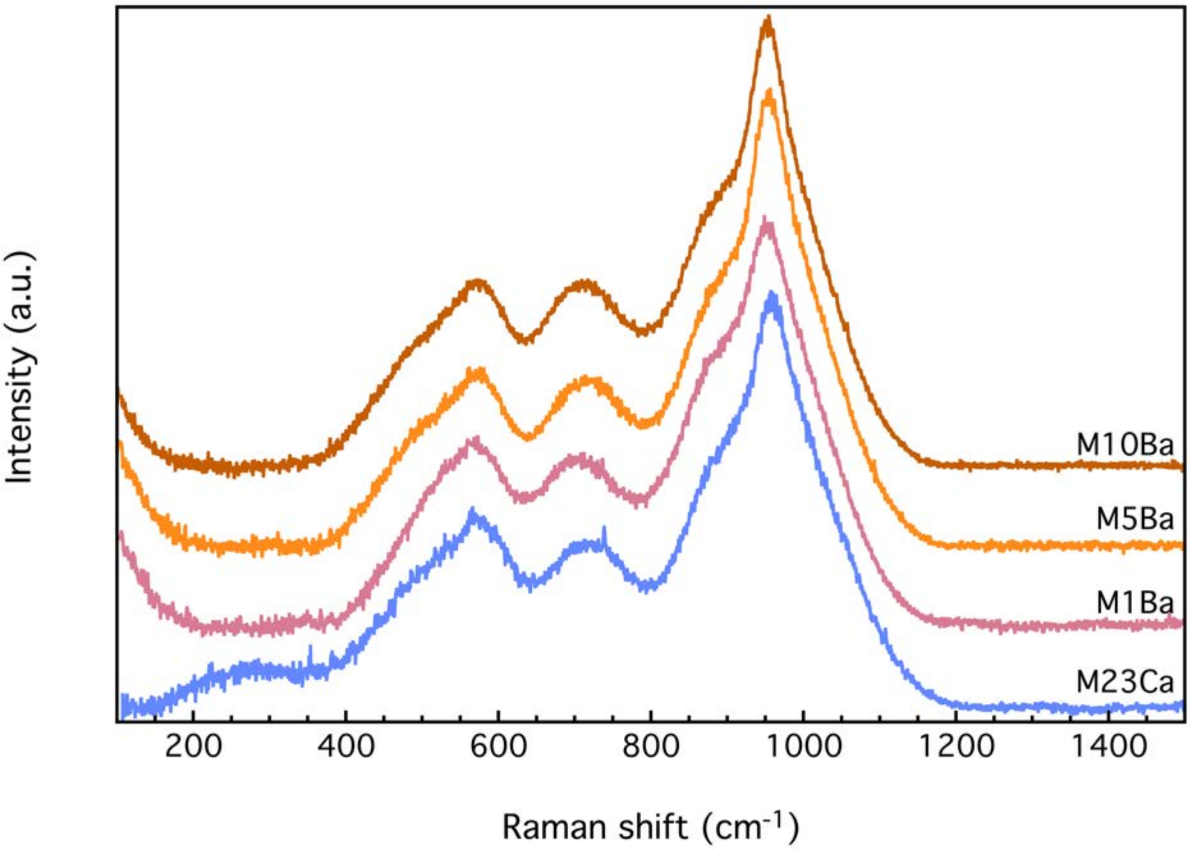

Figure 8.2. Raman spectra of the Ba-doped matrix glasses.

8.2.3 Thermal analysis and crystallization

The DTA of the Ba-doped glasses shows three sets of events: an endothermic near 690 ºC, a wide exothermal event between 860 and 1000 ºC, and one or two endothermal events located between 1100 and 1200 ºC (Figure 8.3). All these events shift to lower temperatures with Ba addition.

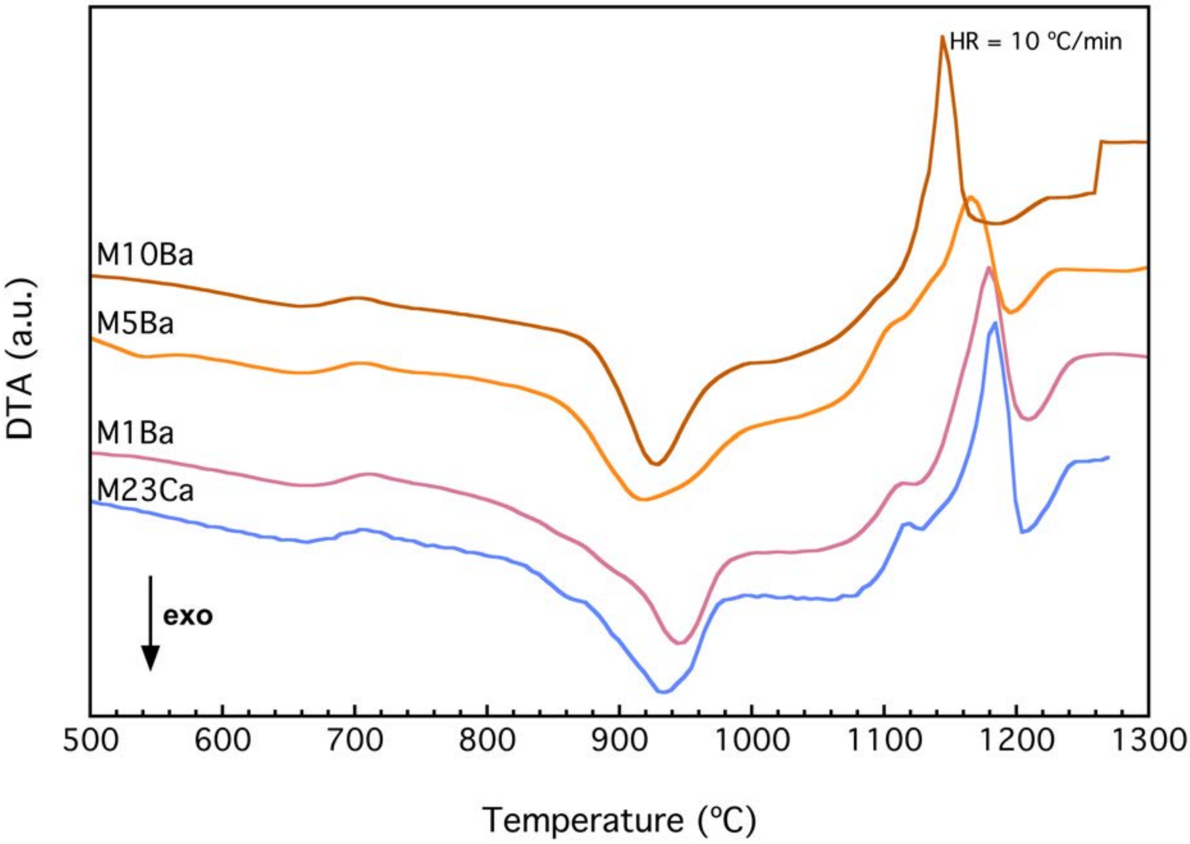

Figure 8.3. DTA profiles of the Ba-doped matrix glasses compared to their base composition M23Ca.

The endothermal event around 690 ºC corresponds to the glass transition. The calculated values of the Tg are presented in Table 8.3. The oscillation of the major band at 950 cm^{-1}, without a specific trend pointing to either polymerization or depolymerization, is particularly consistent with the oscillation of DTA Tg around 690 ºC.

Sample	DTA Tg (ºC)	Dilatometric Tg (ºC)
M23Ca	687	636
M1Ba	691	654
M5Ba	688	656
M10Ba	692	648

Table 8.3. DTA and dilatometric Tg of the Ba-doped glasses.

The wide exothermal events are the convolution of several crystallization peaks attributed to the formation of diopside, nepheline, akermanite, celsian ($BaAl_2Si_2O_8$) and magnetite (Figure 8.4). The onset of these events shifts to higher temperatures with increasing Ba. The concentrations of akermanite and celsian increase with Ba addition, whereas the abundance of diopside diminishes. This may be attributed to the removal of Al from the system during the crystallization of celsian, thus leaving an excess SiO_2 and specially CaO that integrate the akermanite lattice instead of that of diopside. The last endothermal events are linked to the melting of the system; their large area is an indicator of the good fusibility of the compositions. The first peak near 1100 ºC is attributed to the melting of akermanite – in agreement with the in-situ HT-XRD studies of composition B16Ca. The second peak corresponds mostly to the melting of diopside, which is the most abundant mineral phase. The melting peaks of Ak and Di get closer with increasing Ba addition. Celsian is a very refractory material and has a melting temperature of 1760 ºC after transforming into hexacelsian at 1590 ºC (Lin and Foster, 1968).

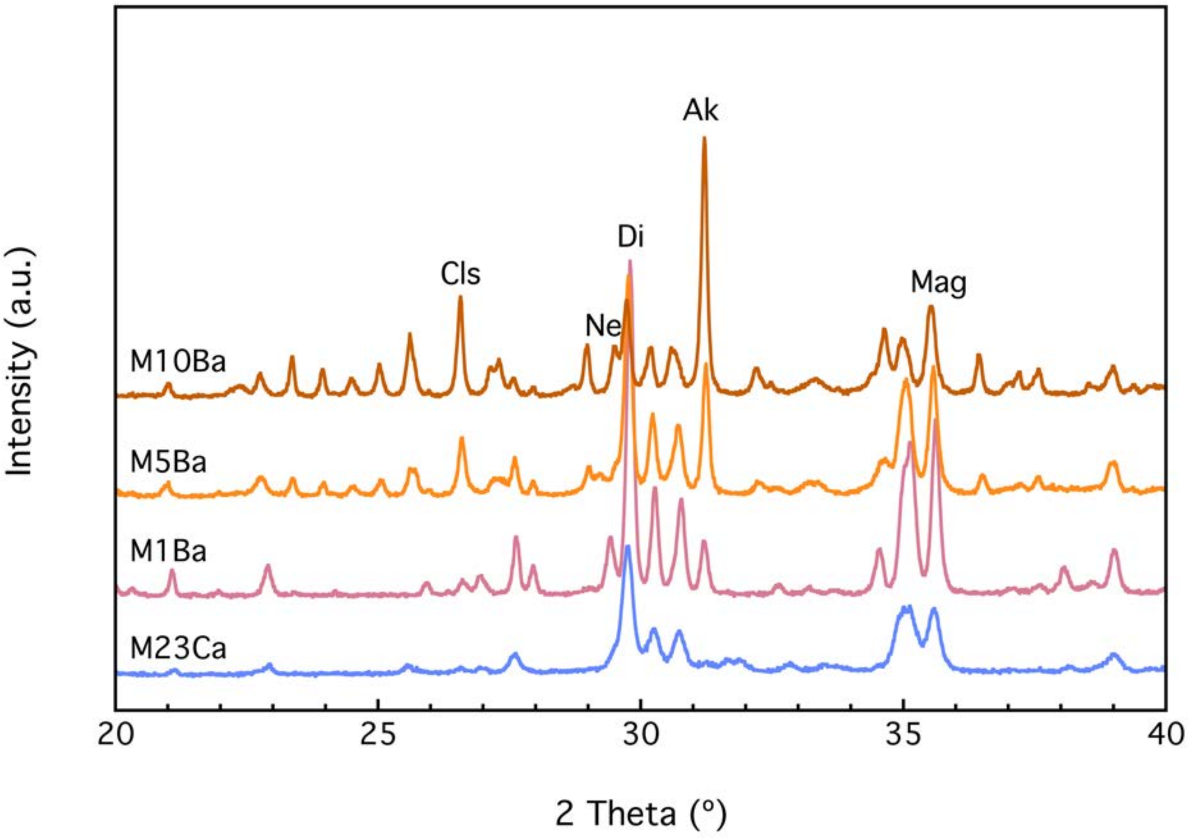

Figure 8.4. Crystallization of the matrix composition as a function of the Ba concentration.

8.2.4 Viscosity-temperature curves

The effect of the addition of Ba on viscosity is presented in Figure 8.5. As explained in the previous chapters, crystallization causes an anomalous bump in the middle range (especially between $10^{7.9}$ and $10^{5.4}$ Pa·s) and then decreases at high temperatures where it is controlled by the liquid phase. Concerning the specific effect of Ba, in the low temperature range it increases the viscosity; in the mid-temperature range it is controlled by the relationship between the crystallization of diopside and akermanite. In the high temperature range, the viscosity of the liquid phase decreases with Ba concentration, which is consistent with its role as a network modifier.

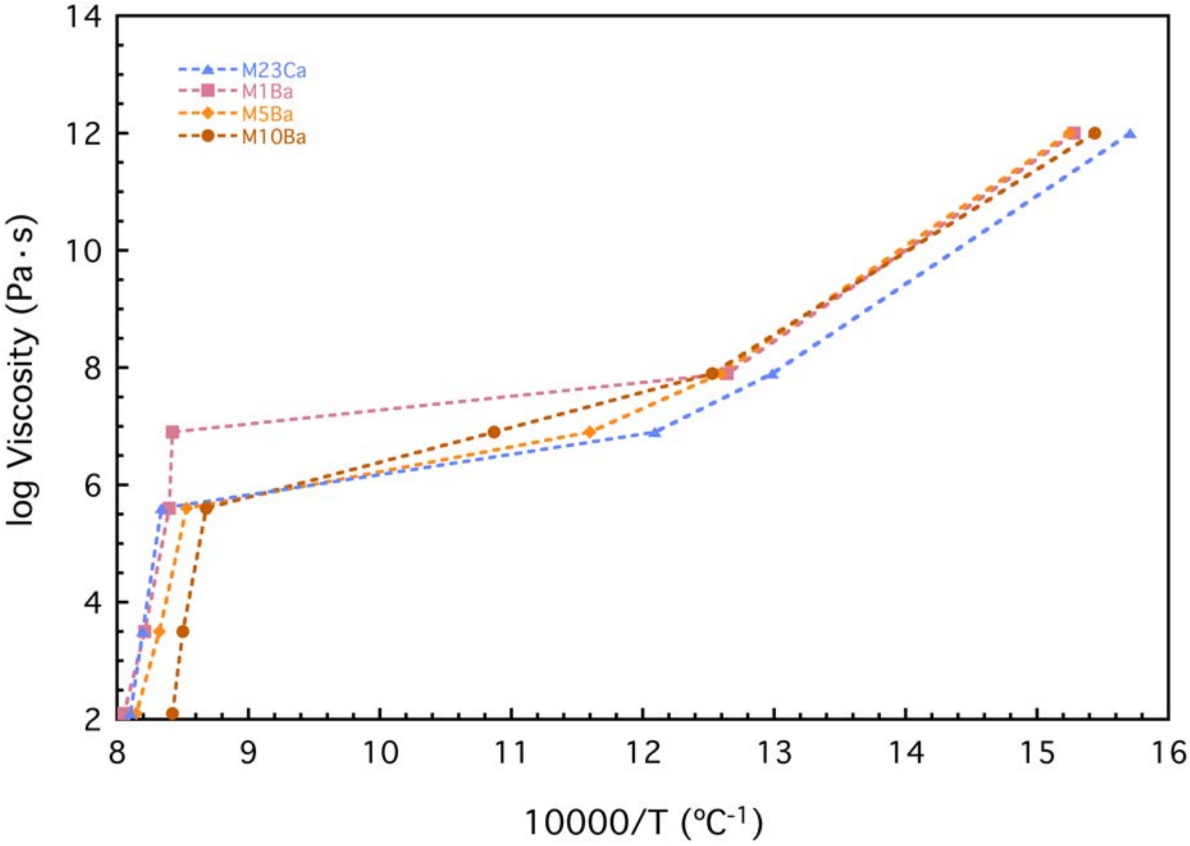

Figure 8.5. Viscosity-temperature curves of the glasses with different barium concentration.

The microhardness Vickers of the Ba-doped glasses increases from 7.249 to 8.908 GPa up to 6 wt% BaO and then decreases to 7.751 at 12.4 wt% BaO. In a similar way as in the matrix glasses, this evolution may be explained by the extent of nucleation during quenching and the fact that Ba plays the same role as Ca. In the CMAS diagram – presented in chapter 6 – if the concentration of Ba is added to that of Ca, the bulk compositions of the system move from the melilite through the merwinite and to the Ca_2SiO_4 stability fields. During this process, the liquidus temperature first increases and then decreases. When the liquidus temperature is higher nucleation is more extensive, whereas it will be reduced when the liquidus temperature is lower. This causes the oscillation of microhardness.

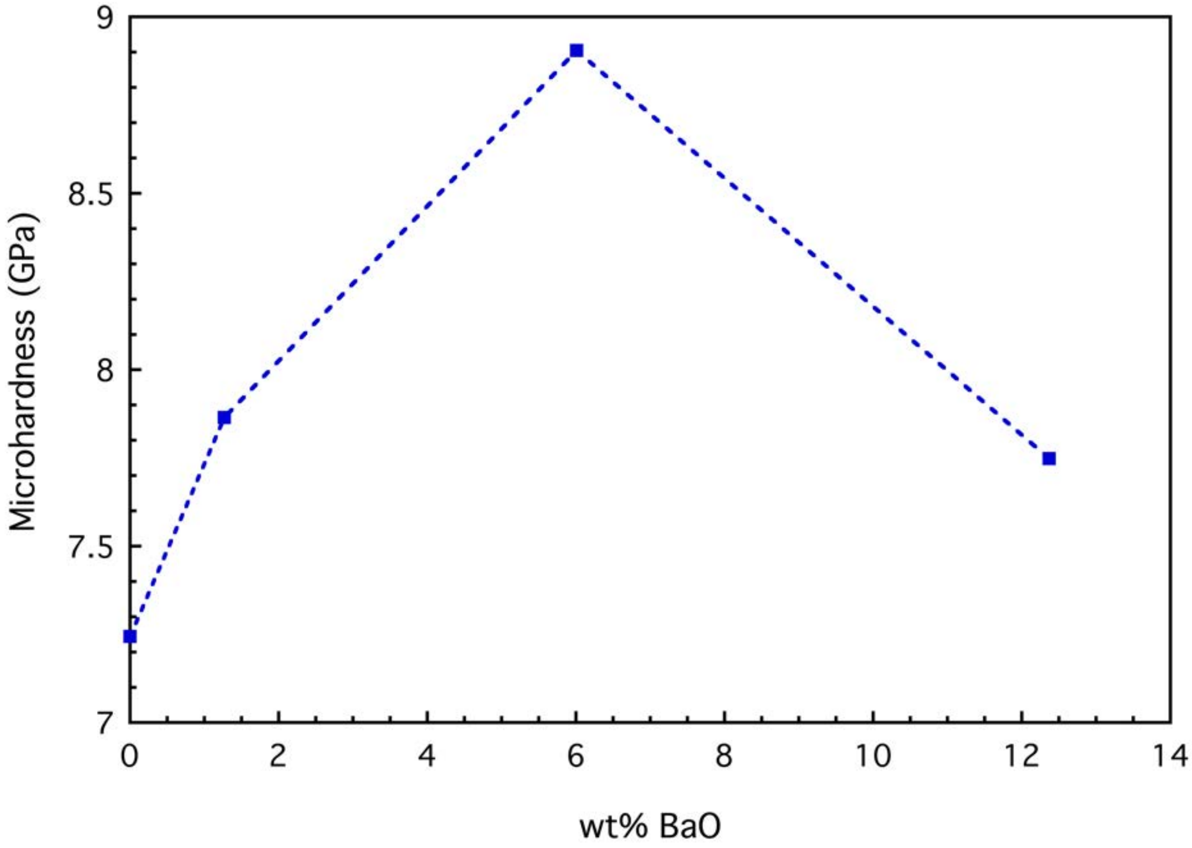

Figure 8.6. Microhardness Vickers as a function of the concentration of BaO.

8.2.5 Leaching

The concentrations of the main elements of the glass are generally low in the leachate, at least 3 orders of magnitude below their concentration in the glass (Table 8.4 and Table 8.5). The evolution of the concentration of Ba in the leachate mimics that of the microhardness: it increases in M5Ba and then decreases again. Although nuclei are expected to be more stable than glass, they also have a larger surface area. Moreover, the Ba-containing phase that crystallizes in the glasses is the feldspar celsian. Feldspars tend to be easily weatherable in comparison to the other silicate minerals (Deer et al., 1992), and might explain the evolution of leaching if it is the phase that has nucleated. In any case, the concentration of Ba in the leachates is low enough for the glasses to be considered inert (Council of the European Union and 2003/33/EC, 2003).

	Si	Al	Ca	Mg	Na	K	Fe	P
M1Ba	6.82	1.96	12.78	3.63	10.74	2.65	1.22	1.08
M5Ba	12.26	3.28	21.10	6.47	28.14	5.93	2.84	1.47
M10Ba	4.78	1.12	9.95	2.78	8.67	2.03	0.31	0.81
M23Ca	3.61	1.01	3.6	2.86	10.3	2.06	0.23	BB

Table 8.4. Chemical composition of the leachates of the Ba-doped glasses (major components).

	As	Ba	Cd	Cr	Cu	Mn	Ni	Pb	Ti	Zn
M1Ba	< 0.3	507.76	0.14	3.65	15.73	22.78	6.78	14.56	234.33	24.80
M5Ba	< 0.5	2359.42	0.16	8.05	30.10	59.11	12.00	5.89	506.36	28.72
M10Ba	0.18	1931.56	0.14	BDL	6.69	6.68	3.02	2.96	79.14	9.15
M23Ca	BDL	BB	0.77	BDL	15.92	0.36	5.12	0.77	47.9	7.15
DIN	500	20000	40	500	2000	-	400	500	-	4000

Table 8.5. Chemical composition of the leachates of the Ba-doped glasses (trace components) compared to the limits to the PTE established by (DIN-38414S4, 1984) *and* (Council of the European Union and 2003/33/EC, 2003).

8.2.6 Conclusions

- Ba increases the density of the glasses due to its high molecular weight.
- Ba shares the position of Ca in basaltic glasses
- The glasses crystallize into diopside, akermanite, celsian, magnetite and merwinite.
- The addition of Ba changes the nucleation according to the increase-decrease of the liquidus temperature. In its turn, it increases and then decreases both microhardness and leachability of Ba.

8.3 Chromium

8.3.7 Chemical composition, texture and density

The calculated chemical compositions of the Cr-doped glasses and the chromite of sample M15Cr (measured on EDS) are reported in Table 8.6. The solubility of Cr in the glass is below 1% in good agreement with measurements of about 0.13 wt% Cr_2O_3 in magmatic melts reported in the literature (Roeder and Reynolds, 1991).

	SiO_2	Al_2O_3	CaO	MgO	Na_2O	K_2O	MnO	TiO_2	FeO	P_2O_5	Cr_2O_3
M14Ca	41.06	12.40	14.19	8.99	3.34	1.74	0.16	2.32	10.43	3.88	0.00
M1Cr	38.81	12.50	15.84	8.87	2.92	1.75	0.15	2.21	10.46	3.96	1.00
M5Cr	37.24	11.99	15.20	8.51	2.80	1.68	0.14	2.30	10.03	3.80	5.00
M15Cr	33.32	10.73	13.60	7.61	2.51	1.50	0.13	1.90	8.98	3.40	15.00

Table 8.6. Chemical composition of the matrix glasses doped with Cr. The concentration of chromium reflects the nominal bulk chemical composition of the glasses, as it was too low to be measured precisely in the EMPA equipment.

Sample M1Cr seems homogeneous at the large scale (Figure 8.7a). However, a more detailed observation shows the presence of clusters of nuclei with a diameter about 100 nm in the glass surface (Figure 8.7b). Their EDS analysis corresponds to an aluminosilicate phase. Over 1 wt% Cr_2O_3 the excess Cr of the melts crystallizes extensively into chromite (Chr) (Figure 8.7c, d, e, f). The underlying glassy matrix is homogeneous and it does not contain any Cr. (Figure 8.7c, e). The crystallization of chromite is increasingly pervasive at higher Cr contents. The size of the chromites varies from 5 μm in M5Cr to 10 μm in M15Cr. In both samples the growth of the crystals has strained the glass to create porosity. Additional EDS analyses on the chromite crystals show a zonation where the concentration of Cr is maximal in the center of the crystals and decreases towards the glass. This is consistent with chromite being more refractory than Mg-, Al-, and Fe-rich spinel-like phases (Deer et al., 1992).

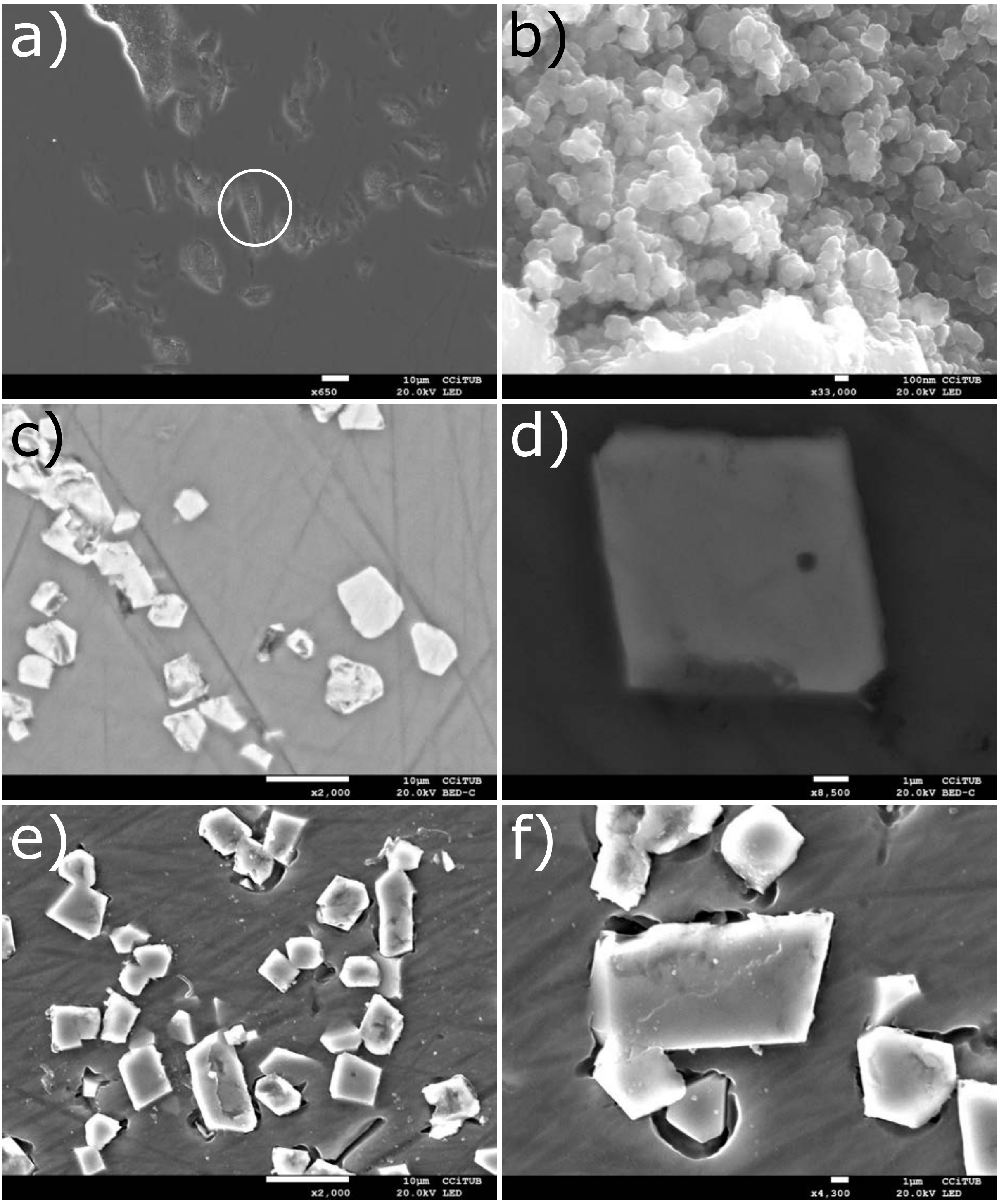

Figure 8.7. FE-SEM images of the crystals formed during quenching. a) general overview of sample M1Cr. b) magnification of the region within the white circle. c) overview of sample M5Cr. d) detail of a chromite crystal. e) overview of sample M15Cr. f) detail of a group of chromite crystals.

The addition of Cr increases the density of the glasses due to the high molecular weight of Cr_2O_3 (Figure 8.8).The density of M1Cr is higher than expected according to the almost linear trend of the other samples. This may be related to the nucleation of an aluminosilicate phase observed on SEM. The large error of the measurements on sample M15Cr is linked to the crystallization of chromite. The same effect should be expected on sample M5Cr. However, the smaller size and lower abundance of the crystals may have enabled obtaining consistent measurements.

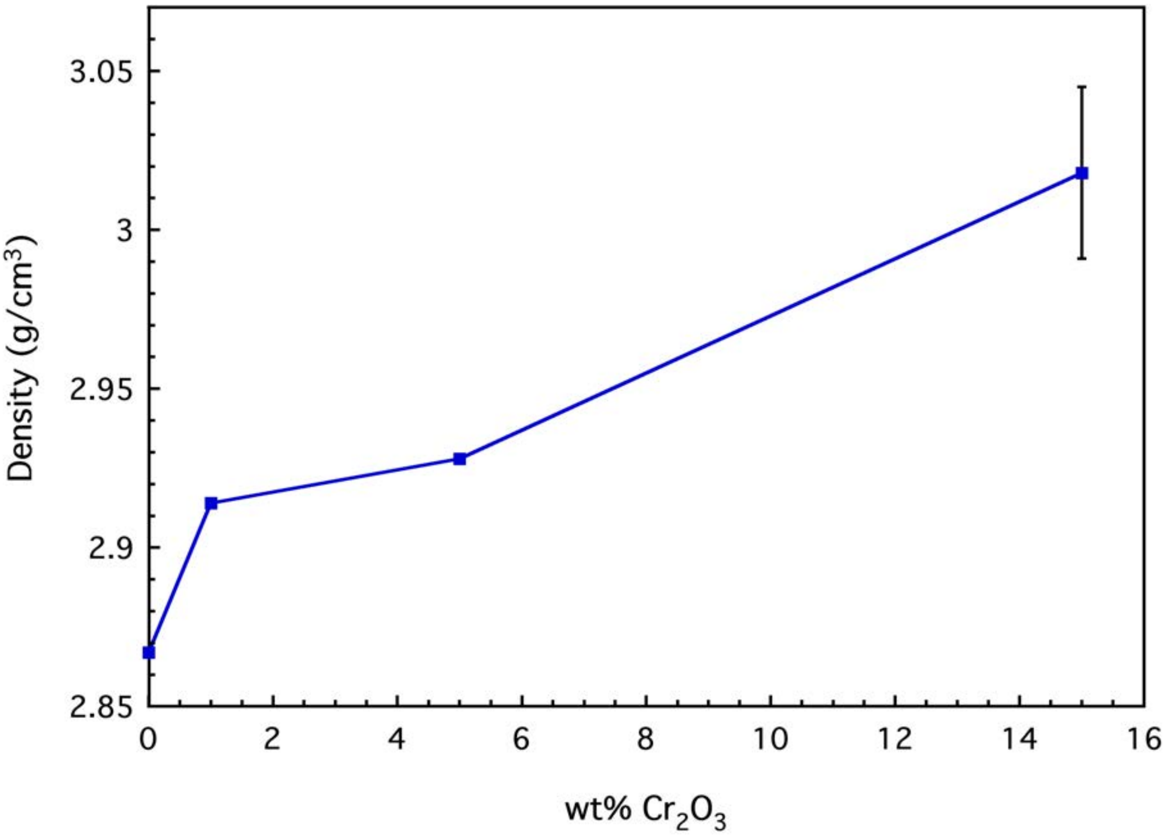

Figure 8.8. Density of the glasses as a function of Cr concentration.

8.3.8 Raman spectroscopy

The Raman spectra of the glasses with low concentration of Cr have a similar structure to that of matrix M14Ca (**Error! Reference source not found.**). They are divided in the LF (400-650 cm^{-1}), MF (650-800 cm^{-1}) and HF (800-1200 cm^{-1}) envelopes (see chapter 6 for attribution and discussion). The LF and MF envelopes do not experience major changes up to 5 wt% Cr_2O_3 apart from the shift of the MF due to the decrease of the concentration of silica.

However, the HF shifts to lower frequencies, from 976 to 954 cm^{-1} with even with small Cr addition, showing a depolymerization of the glass. This is consistent with a pre-ordering of the spinels that removes Al^{3+} and Fe^{3+}, which at low P contents play a network forming role (see chapter 4). The maxima and the shoulder of the HF – around 890 cm^{-1} – are linked to the presence of Q^2 and Q^0 groups (McMillan, 1984b; Neuville et al., 2014a).

In the samples with higher Cr contents, the Raman spectra is made of the signatures of both the glass and the chromite (Figure 8.9). The main band of chromite overlaps the MF, making it increasingly higher and sharper at higher Cr contents. The HF does not undergo further modification showing that the glassy matrix stays unchanged. Another vibration arises in the M15Cr spectrum. Its attribution is uncertain, as it is unusual to find bands in this region either in silicate systems (Yadav and Singh, 2015); most spectra of chromite are only recorded up to 1000 or 1200 cm^{-1} (Chazhengina et al., 2016). The vibration of P-O-Si linkages in phosphosilicate glasses lies near this range (Yadav and Singh, 2015). However, it is unlikely to observe such a large signature in the Raman spectra with only 4 wt% P_2O_5, hence it is assumed that it corresponds to vibrations in the chromite structure.

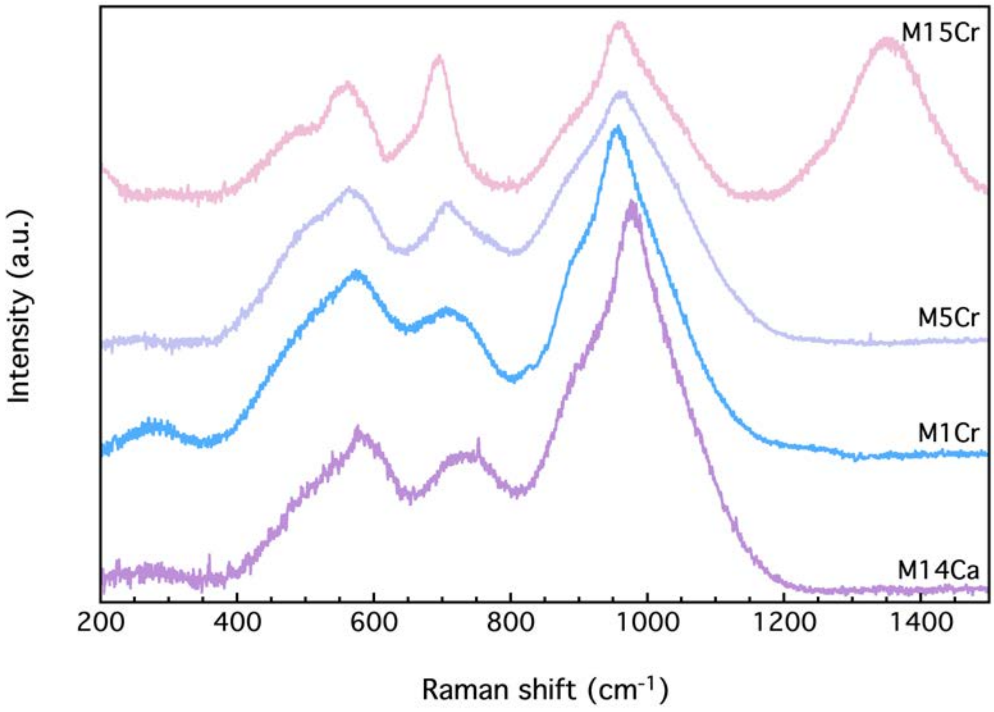

Figure 8.9. Raman spectra of the Cr-doped glasses.

8.3.9 Thermal behavior and crystallization

The thermal behavior of the glasses changes with the addition of Cr (Figure 8.10). The heating causes three main events: an endothermal event near 700 ºC, an exothermal event near 910 ºC and another endothermal event around 1175 ºC. The first endothermal event corresponds to the glass transition, which increases with Cr addition due to nucleation and crystallization upon quenching (Table 8.7).

	DTA Tg (ºC)	Dilatometric Tg (ºC)
M14Ca	698	620
M1Cr	687	636
M5Cr	698	658
M15Cr	705	664

Table 8.7. Tg of the Cr-doped glasses.

At the end of the glass transition there is a minor exothermic event between 788 and 830 ºC corresponding to the crystallization of magnetite. The exothermic peak that oscillates between 895 and 927 ºC corresponds to the crystallization of diopside (Figure 8.11). The endothermal event corresponds to the melting of the aluminosilicate system.

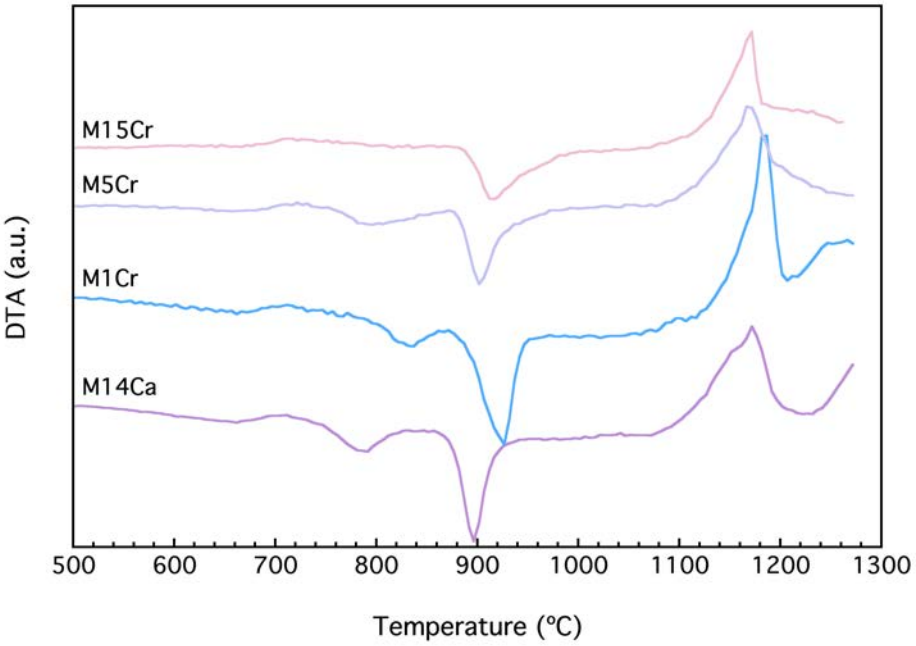

Figure 8.10. DTA plots of the Cr-doped glasses-

The presence of chromite after heating is due to its formation, most likely straight from the liquid phase. The melting point of chromite is between 2160 and 2400 ºC depending on its Mg/Fe ratio (Deer et al., 1992). The decrease of the melting point with Cr addition may be attributed to a removal of Fe and Al. It is also possible that the excess P plays a role. DTA analysis and XRD spectra also reinforce the idea that once chromite has crystallized its behavior is completely independent of the aluminosilicate network.

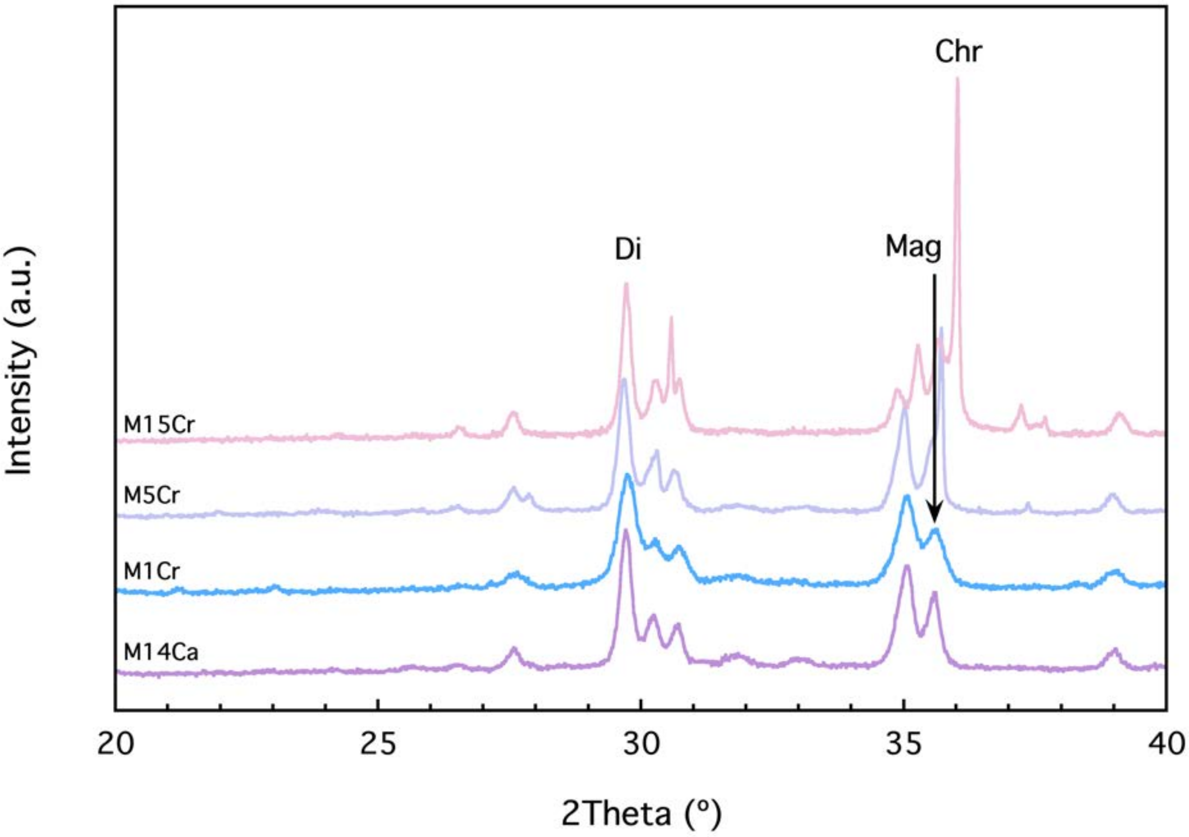

Figure 8.11. XRD profiles of the thermally treated Cr-doped glasses.

8.3.10 Viscosity-temperature curves

The effect of Cr on the viscosity-temperature curves is hard to assess since all the curves overlap throughout most of the studied range (Figure 8.12). Cr_2O_3 concentration has a major effect in dilatometric Tg, which decreases from 698 to 621 ºC. Overall, viscosity is first and foremost influenced by crystallization in the intermediate viscosity range, between 7.9 and 5.6 Pa·s. Crystallization increases the apparent viscosity of the system, causing a bump in the plot due to the reduced gradient of the decrease of viscosity with temperature. The presence of large chromite crystals does not seem to have a significative effect over the bulk viscosity, which is more affected by the formation of diopside. This may be related to the small size of the glass particles used in the HSM experiment. In the low viscosity range – below 5.6 Pa·s – viscosity suddenly drops due to the onset of melting; the behavior becomes then controlled by the liquid phase.

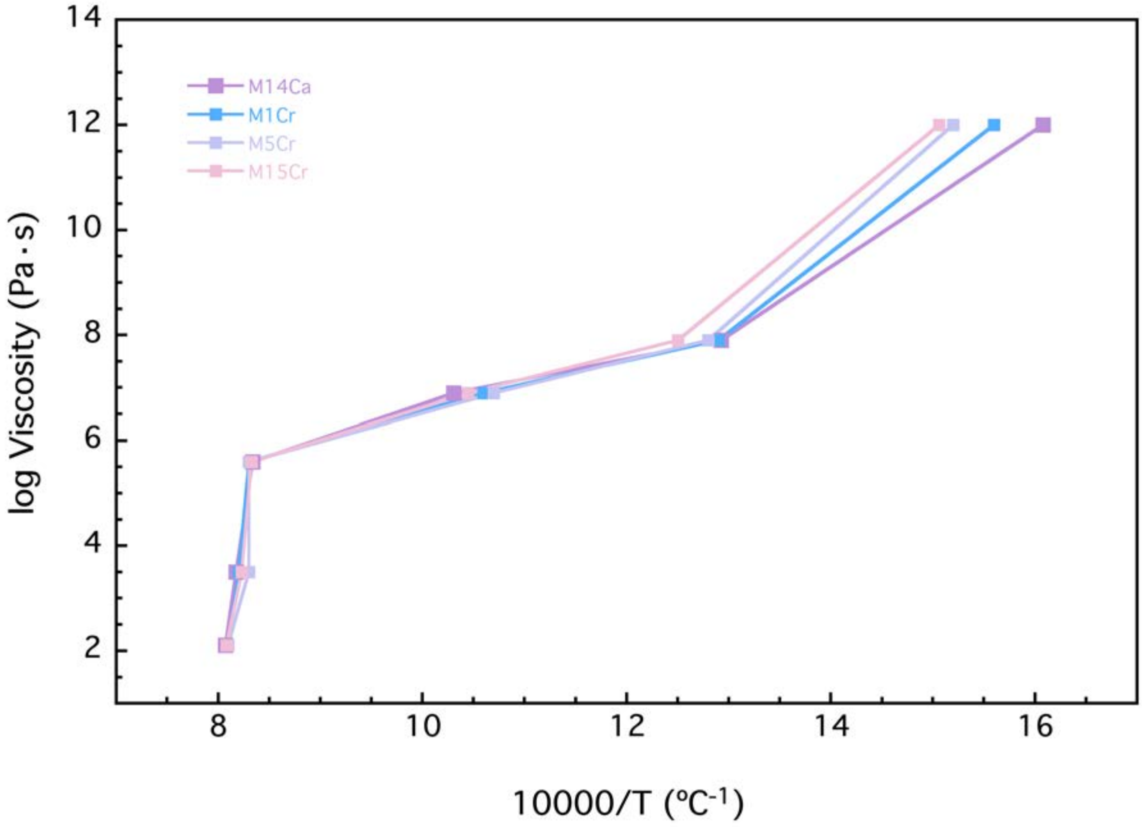

Figure 8.12. Viscosity-temperature curves of the Cr-doped glasses.

8.3.11 Microhardness

The addition of Cr increases the microhardness Vickers of the system up to 5 wt% Cr_2O_3 and then decreases with the extensive formation of chromite and porosity in M15Cr (Figure 8.13).

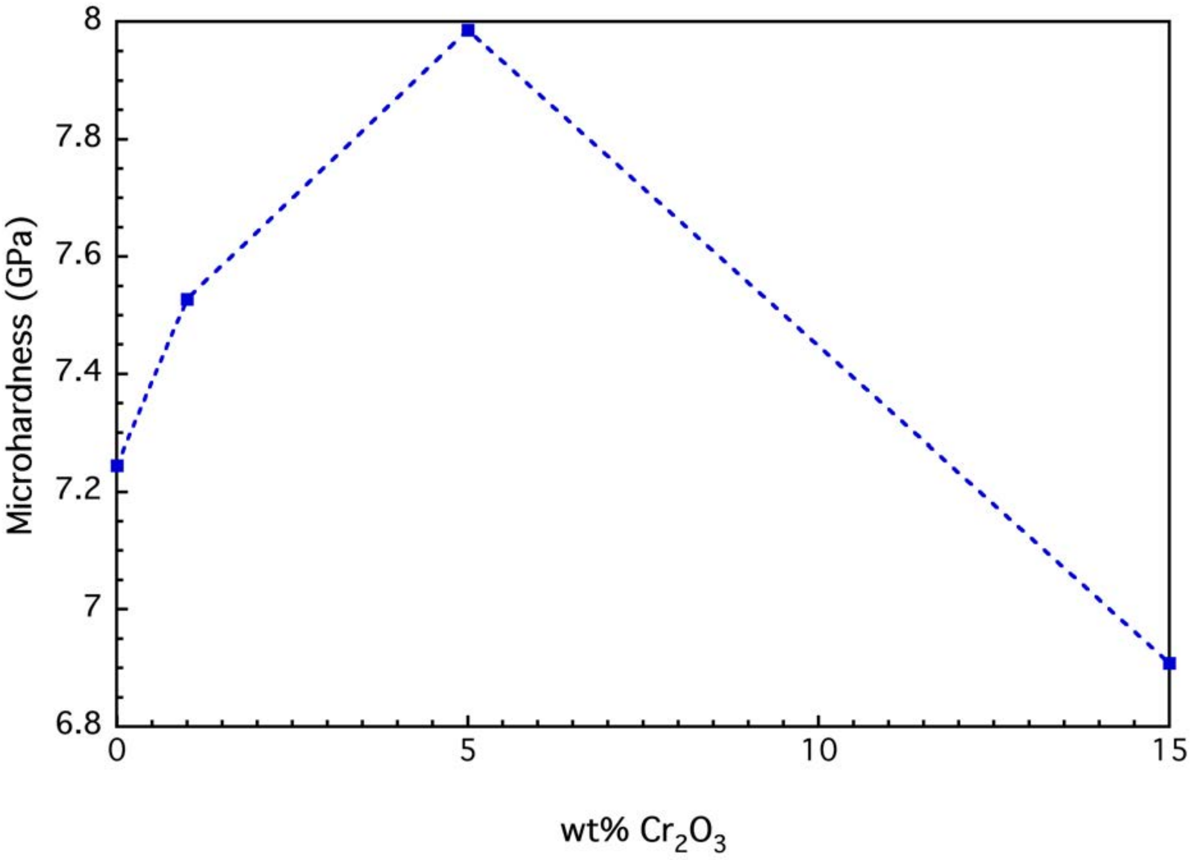

Figure 8.13. Microhardness Vickers as a function of the concentration of Cr_2O_3.

The crystallization of chromite creates two environments with clearly different microhardness in both M5Cr and M15Cr. Although the crystals of M5Cr are too small to be distinguished with the microscope of the equipment, it has been possible to do separate measurements on sample M15Cr (**Error! Reference source not found.**). The presence of chromite is a major factor in increasing the bulk hardness of the material, improving its macroscopic properties. However, it also causes the formation of porosity that decreases the hardness of the glassy fraction.

Phase	**Microhardness Vickers (GPa)**
Glass	6.901
Mixture of chromite and glass	10.230
Chromite crystal	12.950

Figure 8.14. Microhardness measurements on the glas and crystals of M15Cr.

8.3.12 Nucleation and glass-ceramics processing

A study of the nucleation process of sample M1Cr has been made to establish a glass-ceramics process. The shift of the exothermic peaks with the nucleation temperature has provided two T_{MNR} at 685 and 670 ºC, corresponding to the two exothermic events at 830 and 926 ºC (Figure 8.15). The identification of these phases is made from the XRD profiles of the glasses heated at 15 ºC/min, kept at the T_{MNR} for 7 h and then reheated up to the temperatures of the respective exothermic peaks for 2 h. The first T_{MNR} at 669 ºC corresponds to magnetite and the second at 684 ºC, corresponds to diopside (Figure 8.16). It is likely that the formation of the first nuclei of magnetite, around 600 ºC (marked by the onset of the peak) stimulates the start of the nucleation of diopside – around 620 ºC. It must be noted that the nucleation process overlaps the glass transition; this makes the glasses crystallize fast even at low temperatues as seen in the HSM experiments.

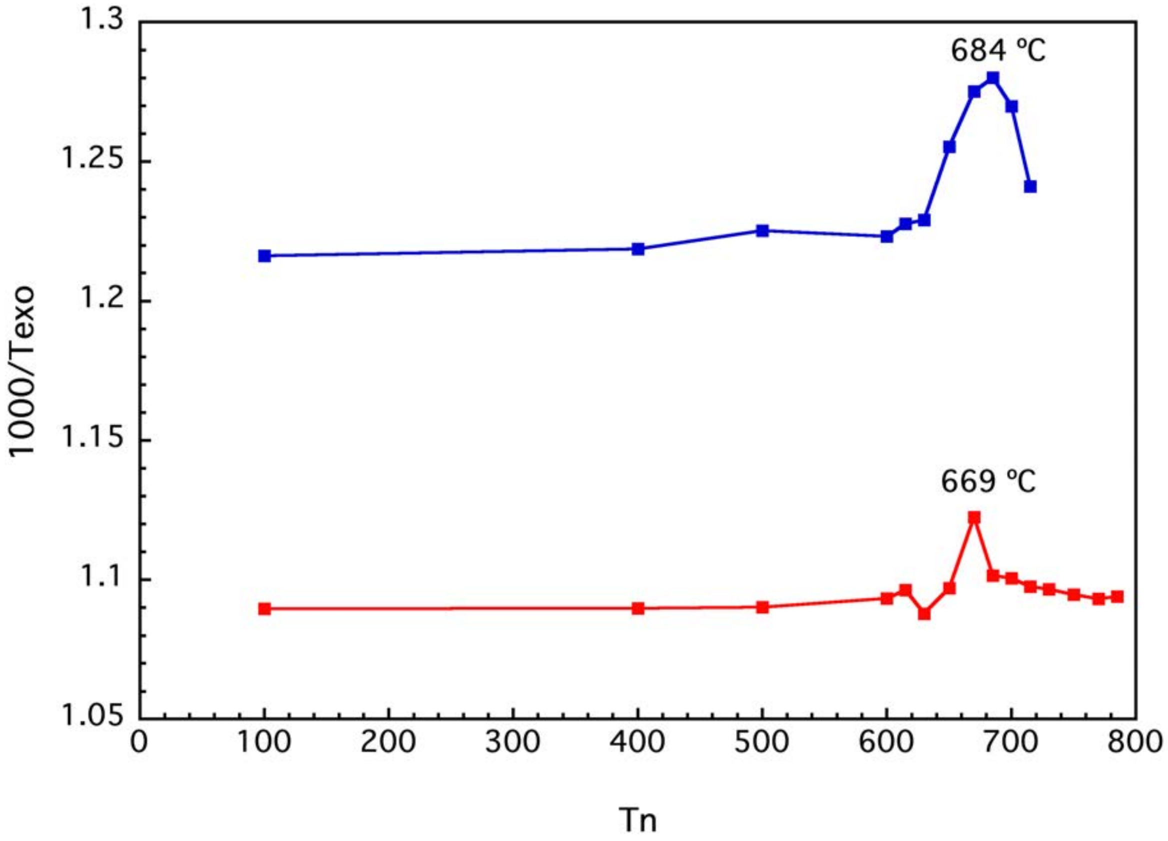

Figure 8.15. Effect of the nucleation temperature on the temperature of the exothermic peaks of M1Cr. The maximum of each plot corresponds to the T_{MNR} of a crystalline phase.

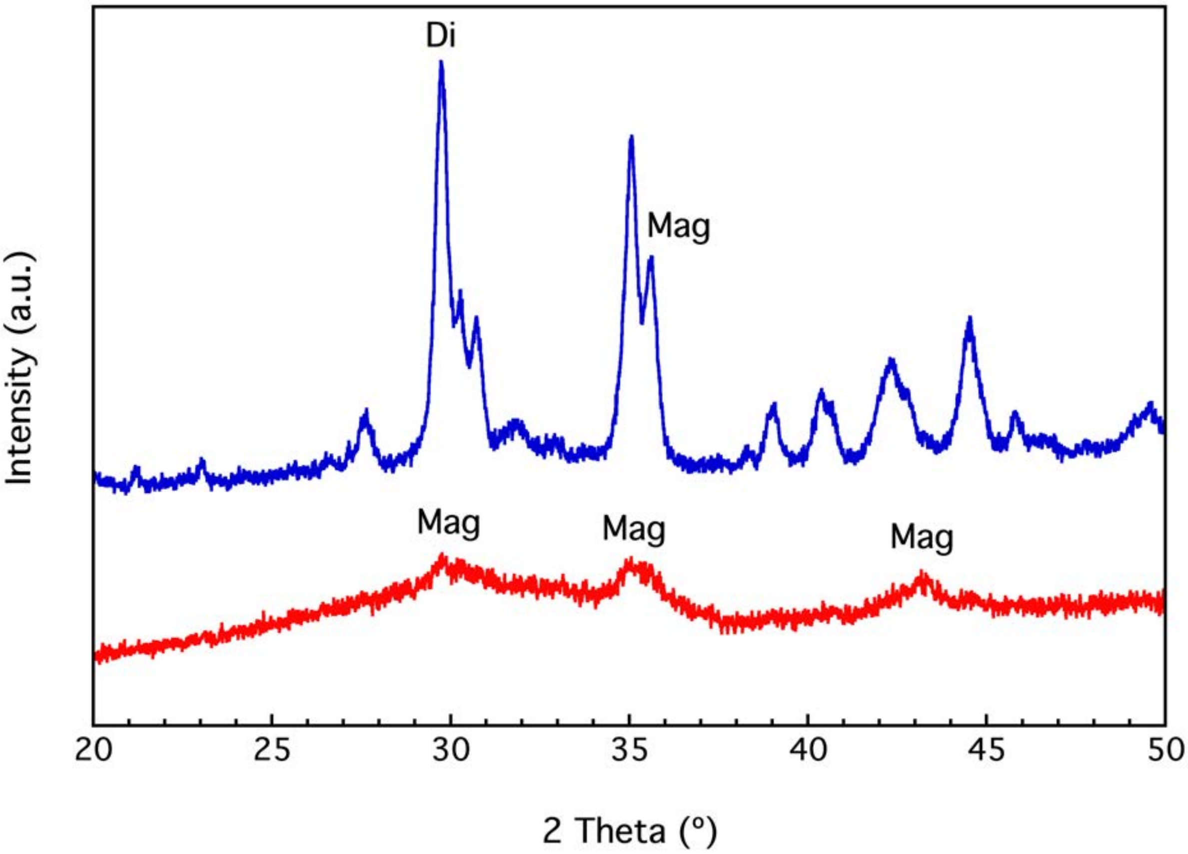

Figure 8.16. XRD profiles for the identification of the nucleated phases..

According to these T_{MNR}, the termal treatment to obtain the glass-ceramics includes the following steps:

- From room temperature to 669 ºC (T_{MNR} of magnetite) at 15ºC/min for 5h.
- From 669 to 684 ºC (T_{MNR} of diopside) at 15ºC/min for 3h.
- From 661 to 873 ºC (peak of the 1st exothermic event) at 15ºC/min for 8h.
- From 873 to 940 ºC (peak of the 2nd exothermic event) at 15ºC/min for 8h.
- Free cooling.

The obtained glass-ceramics has a fine-grained texture consistent with a fast, pervasive nucleation (Figure 8.17a), and some crystals have straight faces (Figure 8.17b). The XRD profile identifies these phases as diopside and magnetite (Figure 8.18). Cr is likely emplaced in the magnetite structure. Comparatively the reflections are more intense than in the samples that were only nucleated because the thermal treatment is longer.

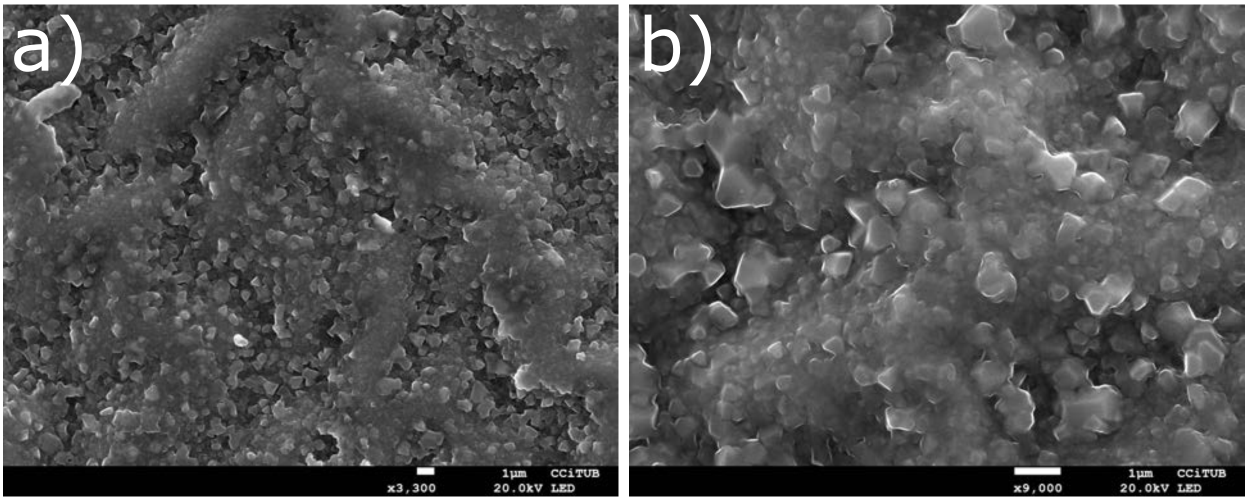

Figure 8.17. SEM micrographs of the glass-ceramics of sample M1Cr. a) general aspect of the glass-ceramics. b) well-formed faces of diopside crystals.

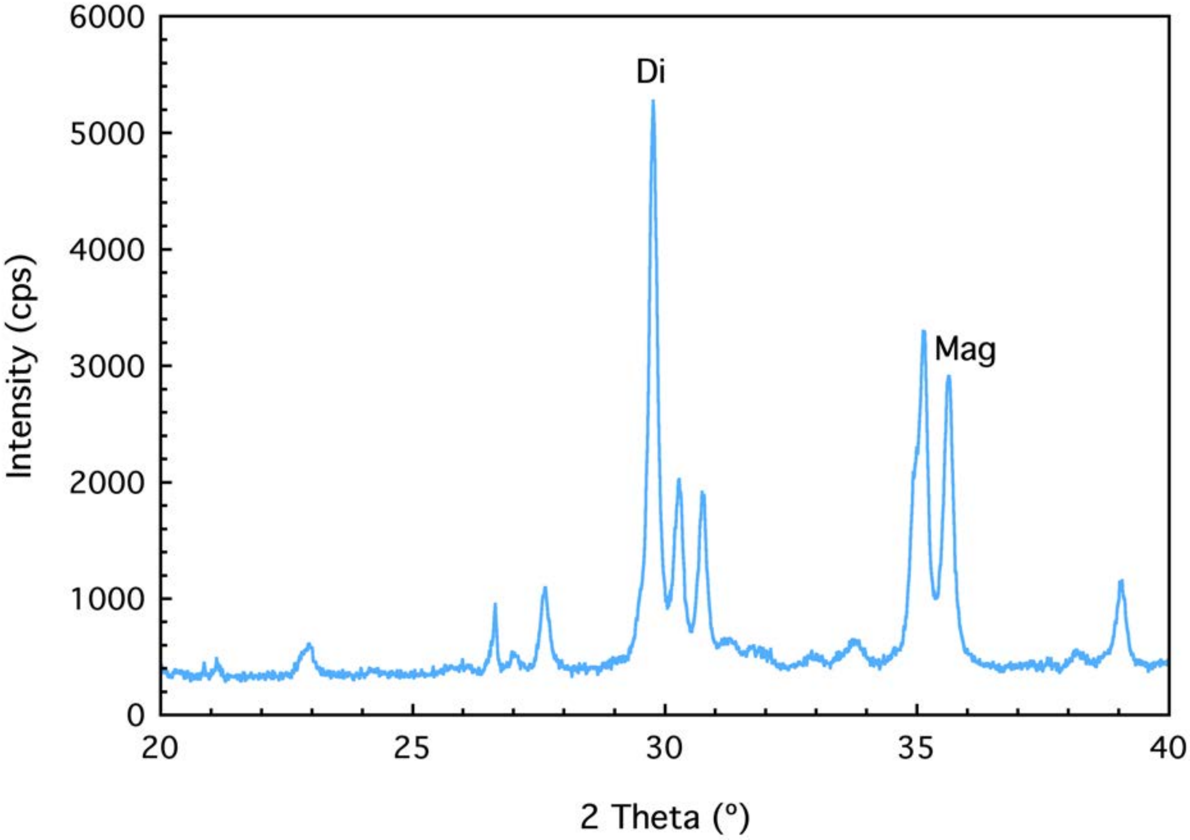

Figure 8.18. XRD profile of the glass-ceramics of sample M1Cr.

8.3.13 Leaching

The concentrations of the constituent elements and specially of the potentially toxic elements are at least 6 orders of magnitude lower in the leachate than its original concentration in the glasses, hence they are generally stable (Table 8.8 and Table 8.9). It must be noted that there is virtually no leaching of Cr until its concentration reaches 5 wt%, and even then, the leaching from the chromite crystals is about tens of ppbs (Table 8.9). The values of the leaching on the glass-ceramics are quite similar to those of its parent composition M1Cr.

[ppm in sol]	**Si**	**Al**	**Ca**	**Mg**	**Na**	**K**	**Fe**	**P**
M14Ca	2.87	0.53	4.03	2.1	2.41	0.74	0.15	BB
M1Cr	3.24	0.72	6.28	2.08	8.21	1.99	0.22	0.50
GC M1Cr	6.57	0.41	15.61	2.50	9.68	1.94	BDL	BDL
M5Cr	2.46	0.55	4.03	1.57	6.80	1.40	0.19	BDL
M15Cr	2.61	0.48	5.03	1.69	7.78	1.62	0.10	0.53

Table 8.8. Chemical composition of the leachates of the Cr-doped glasses (major components).

[ppb in sol]	**As**	**Ba**	**Cd**	**Cr**	**Cu**	**Mn**	**Ni**	**Ti**	**Pb**	**Zn**
M14Ca	0.09	29.15	0.7	BDL	2.85	0.46	3.45	27.35	0.68	5.33
M1Cr	0.17	6.78	BDL	BDL	5.13	4.51	2.92	39.36	0.39	4.69
GC M1Cr	0.29	64.29	0.34	10.92	8.54	0.50	BDL	1.65	0.13	BDL
M5Cr	0.13	5.24	BDL	35.62	1.26	3.28	1.32	30.27	0.29	BDL
M15Cr	0.13	4.50	0.05	62.78	1.78	1.62	1.49	14.81	0.14	BDL
Limits	500	20000	40	500	2000	N/A	400	N/A	500	4000

Table 8.9. Chemical composition of the leachates of the Cr-doped glasses (minor elements). Limits from (Council of the European Union and 2003/33/EC, 2003; DIN-38414S4, 1984)*.*

8.3.14 Conclusions

- Cr has a low solubility in silicate melts. Chromite crystallizes above 1 wt% Cr_2O_3.
- The crystallization of chromite does not influence the structure of the main aluminosilicate glass.
- The glasses crystallize into magnetite and diopside. It is possible to obtain a fine-grained glass-ceramics based on the study of the T_{MNR}.
- The addition of large amounts of Cr and the crystallization of chromite do not compromise the chemical stability of the glasses.

ç

8.4 Copper

8.4.1 Chemical composition, texture and density

The chemical compositions of the Cu-doped glasses are presented in Table 8.10. The solubility limit of Cu in the Ca-P-doped basaltic melt is below 5 wt% CuO as shown by the formation of small clusters of crystals in SEM (Figure 8.19). Although these nuclei do not necessarily bear Cu, they are a marker of the onset of crystallization processes.

	SiO_2	Al_2O_3	CaO	MgO	Na_2O	K_2O	MnO	FeO	TiO_2	P_2O_5	CuO
M23Ca	35.58	11.44	22.10	8.07	2.99	1.48	0.14	10.34	2.01	5.85	0.00
	0.23	0.12	0.19	0.06	0.09	0.03	0.02	0.14	0.06	0.25	0.01
M1Cu	35.24	11.54	22.41	8.07	2.99	1.50	0.15	9.40	2.02	5.77	1.06
	0.17	0.05	0.24	0.06	0.09	0.03	0.01	0.09	0.06	0.25	0.05
M5Cu	33.79	11.00	21.44	7.76	2.85	1.42	0.14	8.99	1.95	5.63	5.23
	0.27	0.06	0.21	0.05	0.07	0.03	0.02	0.09	0.10	0.23	0.07

Table 8.10. Chemical composition of the Cu-doped glasses.

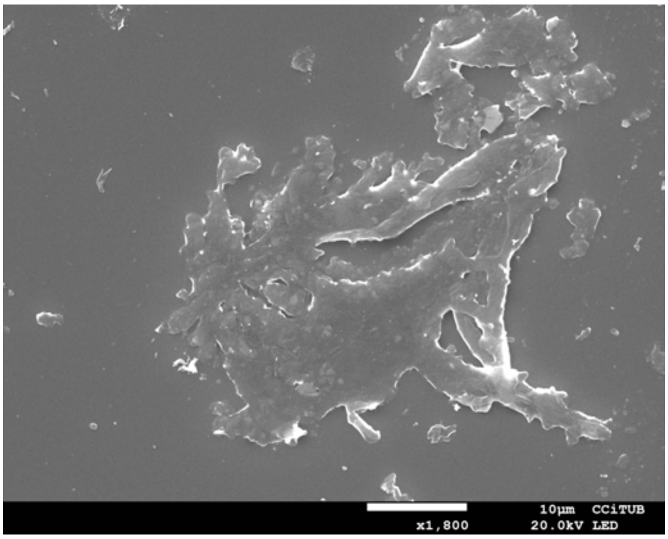

Figure 8.19. SEM micrograph of M5Cu showing the presence of nuclei.

The density of the glasses increases with the addition of Cu due to its high atomic weight. The low error and consistency of the density measurements shows that the glasses are homogeneous.

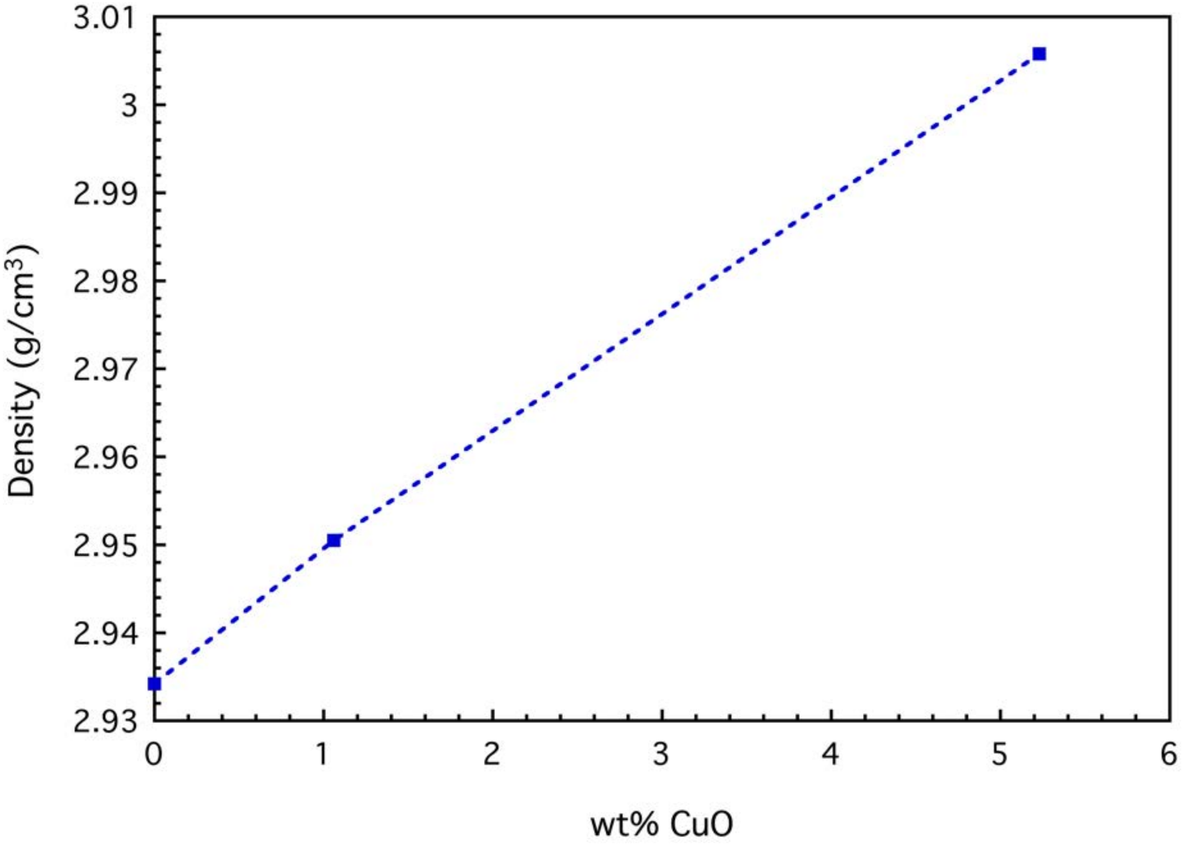

Figure 8.20. Density of the glasses as a function of the concentration of CuO. The error of the measurements is smaller than the symbols.

8.4.2 Raman spectroscopy

The Raman spectrum of sample M1Cu (Figure 8.21) is divided in the three regions as explained in previous chapters: the LF, MF and HF that are attributed to the same vibrations of sample M23Ca. In comparison, only the MF shifts to lower frequencies due to the decrease of the concentration of SiO_2. The band centered at 956 cm^{-1} and corresponding to the Q^2 groups (Matson et al., 1983; McMillan, 1984b) becomes slightly less well defined. The same happens with the shoulder near 875-900 cm^{-1} that is assigned to Q^0 groups (chapter 7 and (McMillan, 1984b)). The spectrum of sample M5Cu is divided in two regions: the LF between 400-800 cm^{-1} and the HF between 800-1200 cm^{-1}. The LF has become broader and as intense as the HF. The vibration at 625 cm^{-1} is linked to the presence of Cu^0 (Colomban and Schreiber, 2005). The increase of the intensity of the LF may be linked to the formation of a silica-rich environment, as it corresponds to the convolution of delocalized modes principally related to the symmetric stretching of bridging oxygen relative to 4-fold coordinated cations such as Si^{4+} and Al^{3+} (T) in TO_4 rings (Bjørn O. Mysen et al., 1980).

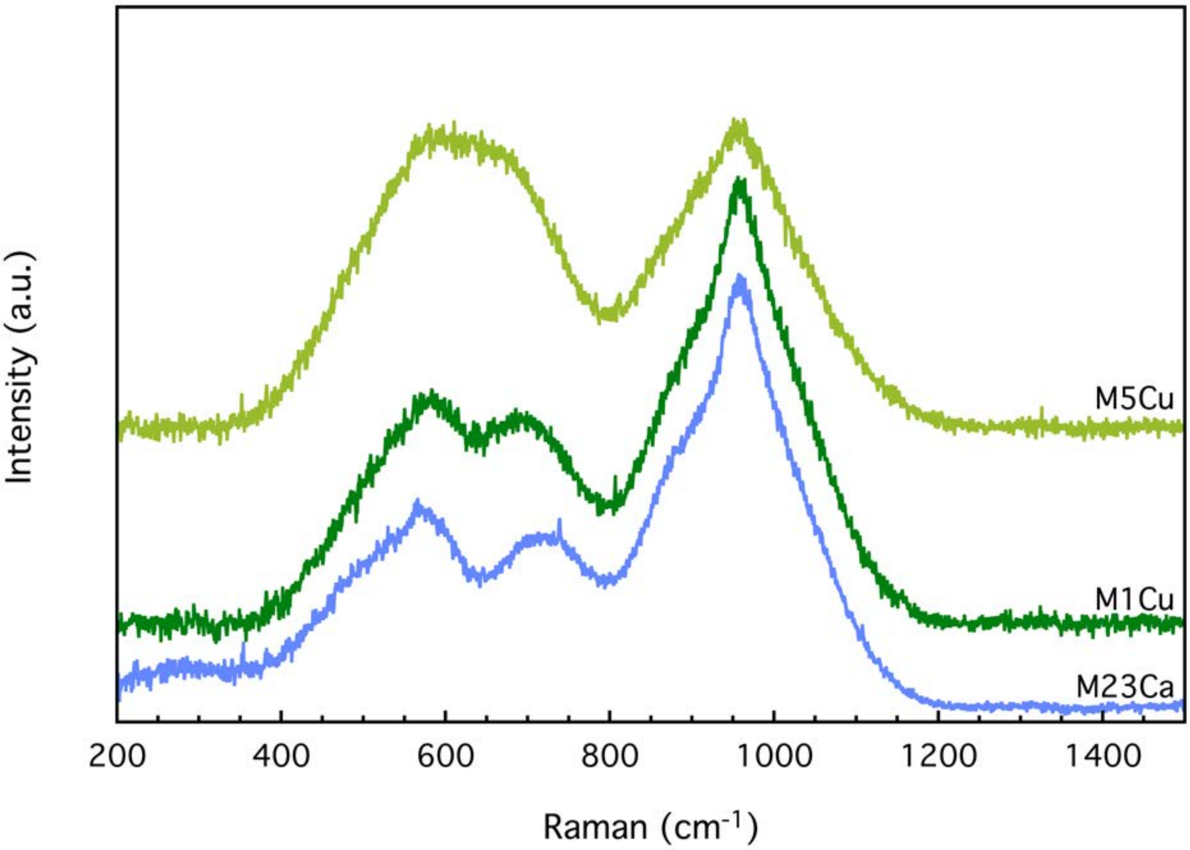

Figure 8.21. Raman spectra of glasses with increasing CuO concentrations.

8.4.3 Thermal analysis and crystallization

The DTA analyses of the Cu-doped glasses show three groups of phenomena: endothermal events between 600-730 ºC, exothermal events between 800-1000 ºC, and endothermal events between 1000-1200ºC (Figure 8.22).

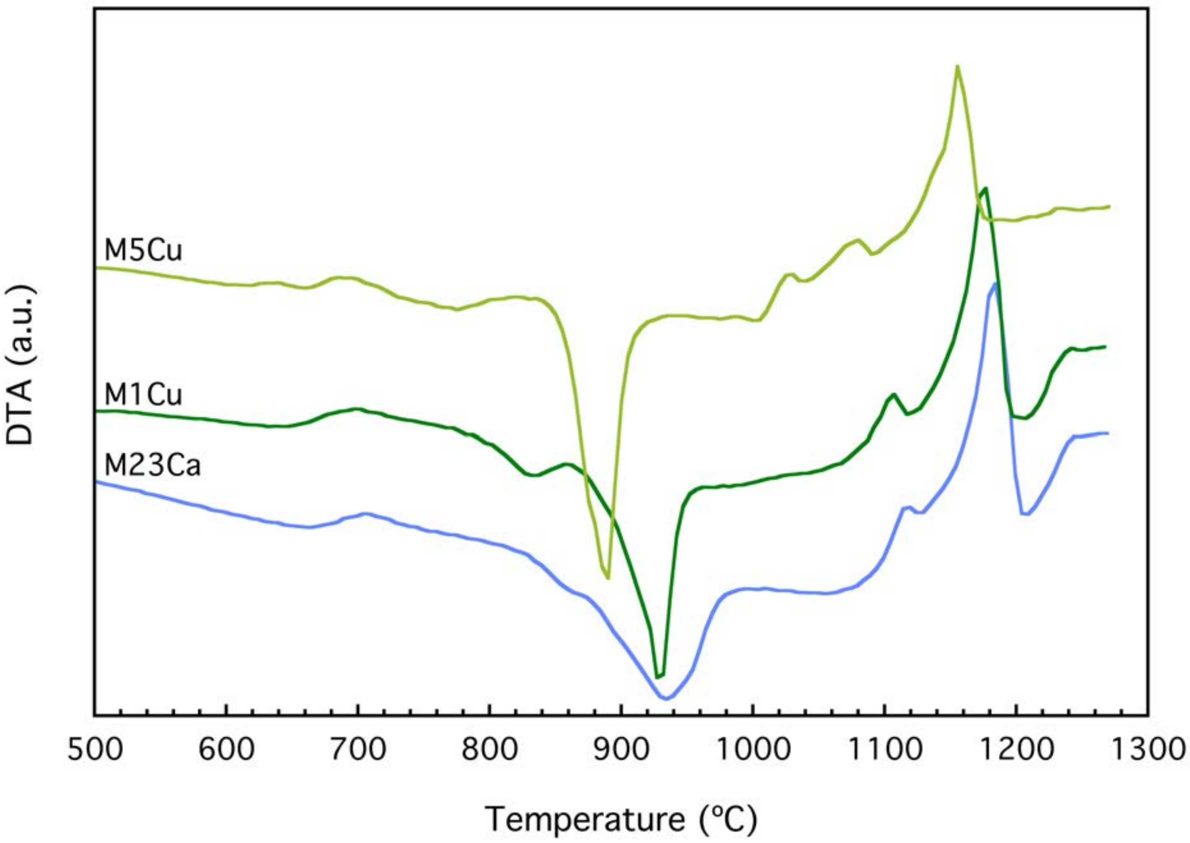

Figure 8.22. DTA plots of the Cu-doped glasses.

The first group of endothermal events are attributed to the glass transition that shifts to lower temperatures at higher concentrations of Cu (Table 8.11). It must be noted that sample M5Cu undergoes two different glass transition events, attributed to the presence of two separated glassy networks that correspond to the silica-rich and the silica-poor environments seen in the Raman spectrum.

	DTA Tg (ºC)	DIL Tg (ºC)
M23Ca	687	636
M1Cu	682	604
M5Cu	638/683	575

Table 8.11. Tg of the Cu-doped glasses.

The exothermal events between 800-1000 ºC correspond to the crystallization of magnetite, diopside, nepheline, and merwinite in sample M1Cu and magnetite, diopside, and minor amounts of akermanite in sample M1Cu and merwinite in sample M5Cu (Figure 8.23).

In both cases magnetite incorporates tenorite (CuO) in solid solution. The endothermal events above 1000 ºC correspond to the melting of these crystalline phases, probably first nepheline, then akermanite and finally diopside as seen in the *in-situ* HT-XRD measurements of chapter 7. Neither magnetite (which melts at 1594 ºC (Deer et al., 1992)) nor tenorite (which melts at 1446 ºC) melt in the temperature range of the DTA experiment.

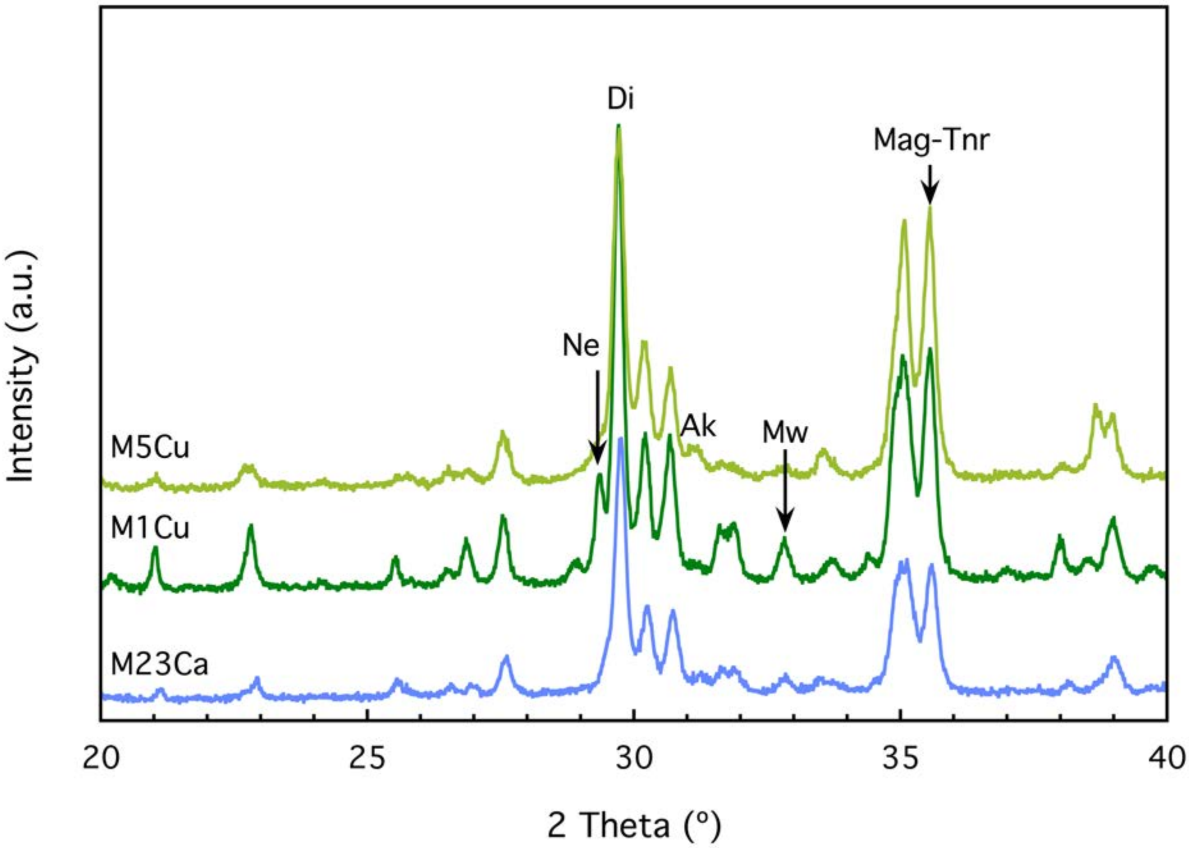

Figure 8.23. XRD profiles of the Cu-doped glasses

8.4.4 Dependence of viscosity on temperature and composition

The effect of Cu in the viscosity is presented in Figure 8.24. The curves can be divided in three sections of different slope. In the first section, between $10^{6.9}$-10^{12} Pa·s, viscosity is controlled by the sintering of the glass particles and their transition from the rigid to the plastic behavior. It must be noted that Tg remarkably decreases with the addition of Cu. This is consistent with the role of Cu^{2+} as a network modifier. In the second zone, between $10^{5.6}$-$10^{6.9}$ Pa·s, the slope is greatly reduced as viscosity increases due to the crystallization of the mineral assemblages explained in the thermal analysis and crystallization section. The presence of Cu^0 nanoparticles makes M5Cu more viscous than the rest at this stage. The last section, between $10^{2.1}$-$10^{5.6}$ Pa·s, has a much steeper slope as the behavior is controlled by the liquid resulting from the melting of these crystalline phases. Viscosity decreases proportionately to CuO because the effect of Cu^{2+} as a network modifier predominates again.

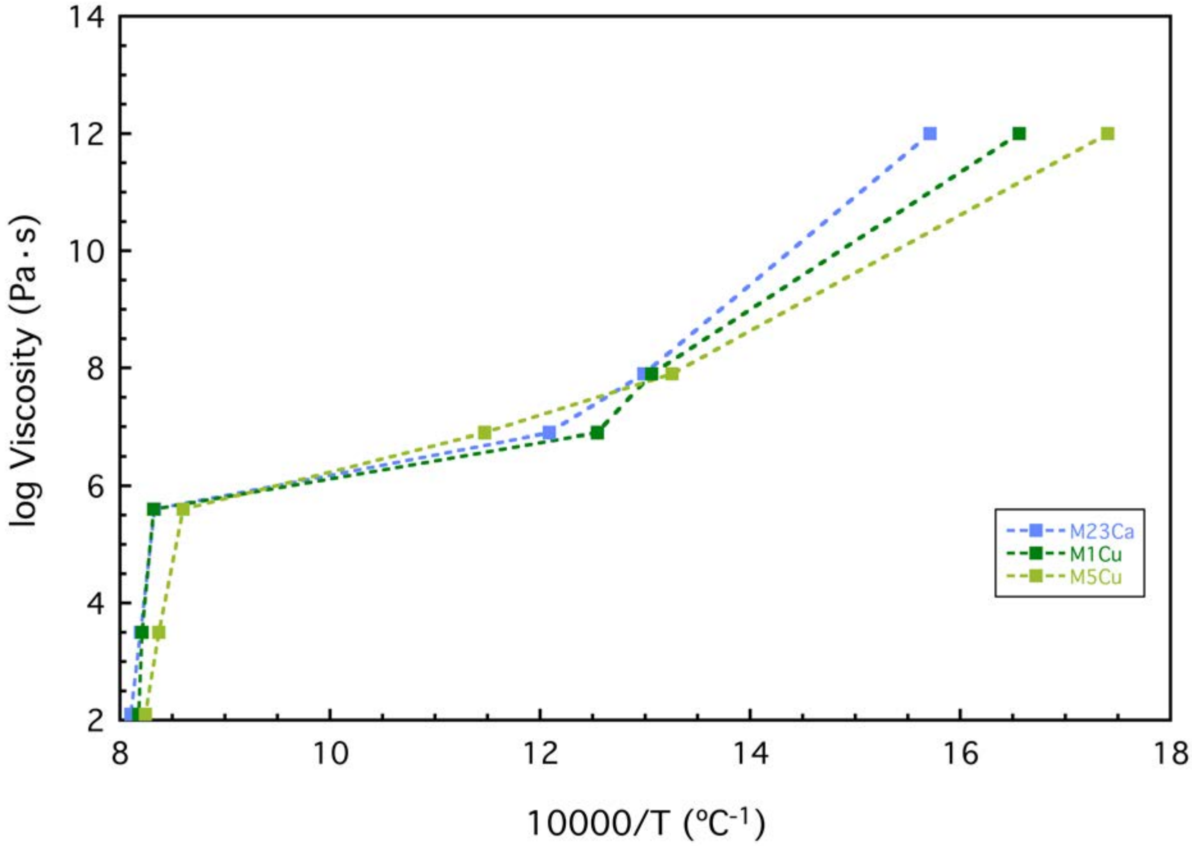

Figure 8.24. Viscosity-temperature plots of the Cu-doped glasses.

8.4.5 Microhardness Vickers

The microhardness Vickers of the glasses first decreases and then increases with Cu addition (Figure 8.25). The decrease between M23Ca and M1Cu may be attributed to the fragilization of the network due to the increase in the concentration of Cu^{2+} in a network-modifying role. The increase between M1Cu and M5Cu is likely linked to the presence of nanocrystalline Cu^0 particles as explained in the Raman section.

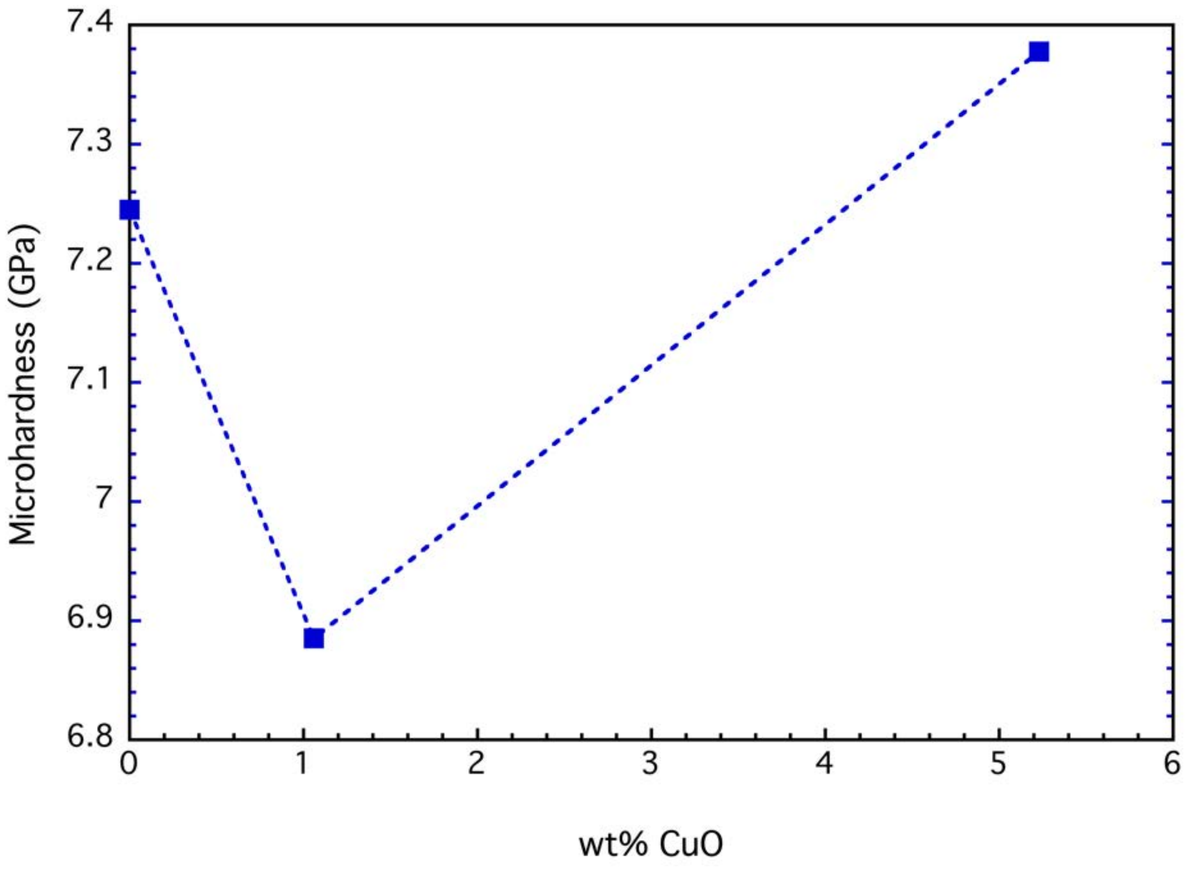

Figure 8.25. Microhardness Vickers as a function of the concentration of CuO.

8.4.6 Leaching

The leaching tests have shown that the glasses can be considered stable because the concentrations of their main components in the leachates apart from Cu are at least five orders of magnitude below the original concentration in the corresponding glasses. The concentration of Cu and the minor, potentially toxic elements comply with the limits established by DIN38414-S4 for wastes to be considered inert (DIN-38414S4, 1984).

[ppm] sol	Si	Al	Ca	Mg	Na	K	Fe	P	Cu
M1Cu	3.92	0.86	12.62	3.10	12.97	2.48	0.19	0.68	0.04
M5Cu	5.99	1.46	9.61	3.00	25.89	2.60	1.10	0.69	0.52
M23Ca	3.61	1.01	3.6	2.86	10.3	2.06	0.23	BB	0.01
DIN	N/A	N/A	N/A	N/A	N/A	N/A	N/A	N/A	2

Table 8.12. Concentrations of the major components of the glass in the leachate. N/A stands for not applicable.

[ppb] sol	As	Ba	Cd	Cr	Hg	Mn	Ni	Pb	Ti	Zn
M1Cu	BDL	92.86	0.12	BDL	0.21	4.00	BDL	2.91	36.23	16.23
M5Cu	BDL	385.71	0.11	4.39	0.66	26.26	6.37	3.64	668.12	34.16
M23Ca	BDL	BB	0.77	BDL	BDL	0.36	5.12	0.77	47.90	7.15
Limits	500	20000	40	500	1	N/A	400	500	N/A	4000

Table 8.13. Concentrations of the minor components of the glass in the leachate. Limits from (Council of the European Union and 2003/33/EC, 2003; DIN-38414S4, 1984).

8.4.7 Conclusions:

- The addition of Cu facilitates the crystallization of the glasses upon quenching and causes an increase in density due to the high atomic weight of the element.
- The addition of Cu decreases Tg as Cu^{2+} plays a network-modifying role.
- At low concentrations copper is incorporated to the glass as Cu^{2+} form, causing a reduction in microhardness. Increasing the amount of added CuO causes the formation of Cu^0 probably in the form of nanoparticles that increase microhardness.
- The glasses are chemically stable due to the at least partial incorporation of Cu2+ to the glass structure and comply with the límits to be considered inert.

8.5 Nickel

8.5.1 Chemical composition, texture and density

The chemical compositions of the NiO-doped glasses are summarized in Table 8.14. The solubility of Ni is below 0.5 wt% as shown quenching. The measured concentrations of NiO agree with the order of magnitude of the nominal concentrations. The difference between the intended concentration of 15 wt% and the actual concentration of 10.91 wt% NiO, together with the large standard deviation of the measurements is due to the formation of dendritic crystals during quenching (Figure 8.26). The dimensions of the crystals fall short of the size of the electron beam.

	SiO_2	**Al_2O_3**	**MgO**	**P_2O_5**	**TiO_2**	**CaO**	**K_2O**	**Na_2O**	**FeO**	**MnO**	**NiO**
M14Ca											
M05Ni	40.20	13.23	9.05	3.95	2.31	14.39	1.74	3.39	10.62	0.17	0.46
	0.21	0.07	0.07	0.21	0.07	0.10	0.03	0.10	0.12	0.01	0.01
M1Ni	40.70	13.38	8.95	3.80	2.29	14.37	1.74	3.40	10.59	0.17	1.02
	0.17	0.06	0.09	0.21	0.06	0.15	0.03	0.07	0.09	0.02	0.01
M15Ni	37.69	11.52	8.55	3.65	1.95	13.30	1.57	3.20	8.13	0.16	10.91
	0.41	0.13	0.28	0.16	0.08	1.00	0.12	0.11	0.28	0.02	1.98

Table 8.14. Chemical composition of the matrix glasses doped with NiO. The error of the measurements is expressed using the standard deviantion.

The two glasses with lower Ni concentration look homogeneous apart from the formation of a certain amount of nuclei (Figure 8.26a and c). In sample M15Ni the excess nickel causes the crystallization of dendritic trevorite ($Ni(Fe^{3+})_2O_4$) crystals.

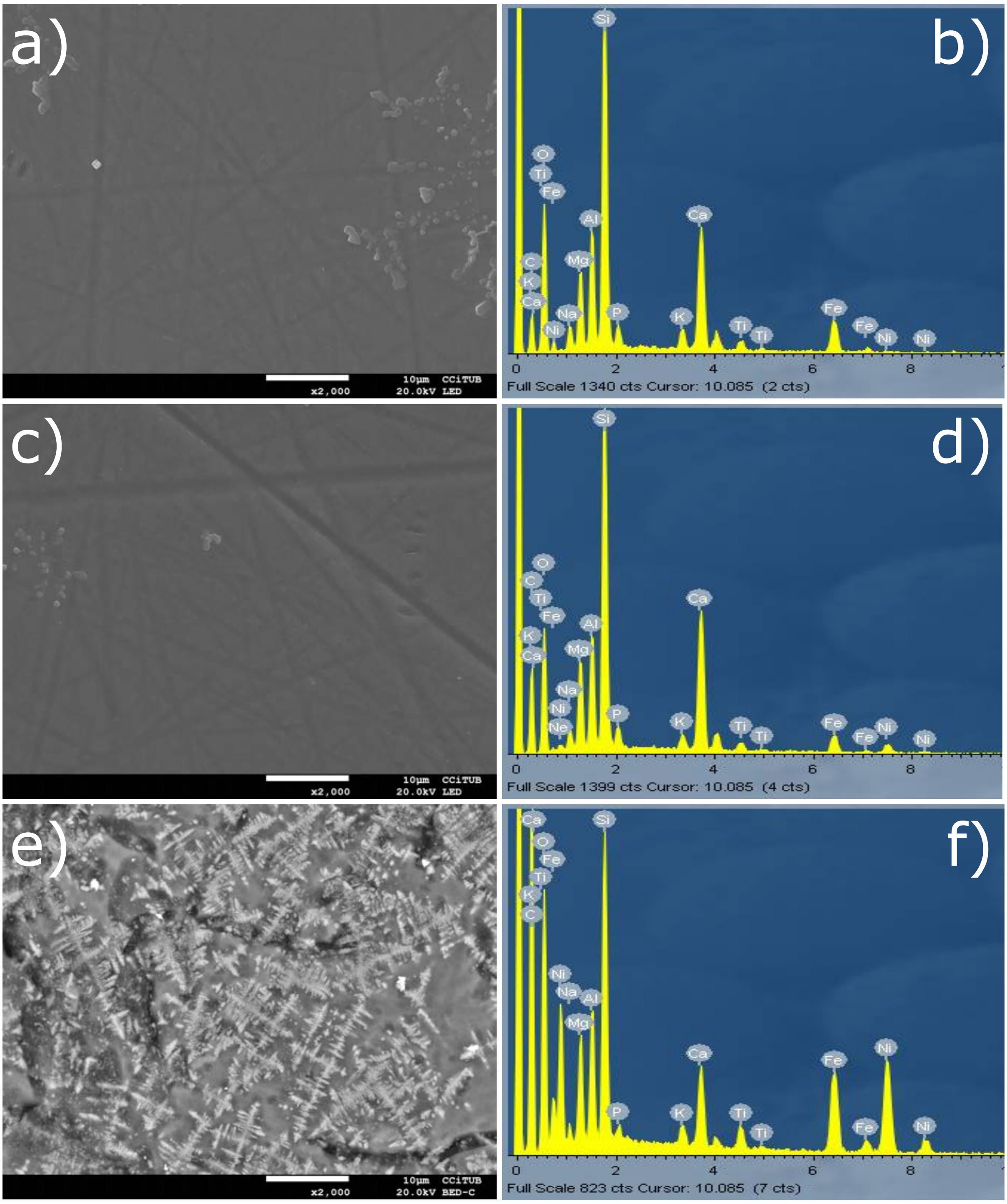

Figure 8.26. SEM micrographs and corresponding EDS spectra of the Ni doped glasses. a) micrograph of sample M05Ni b) EDS spectra of sample M05Ni c) micrograph of sample M1Ni d) EDS spectra of sample M1Ni e) micrograph of sample M15Ni showing the growth of trevorite crystals on glass f) EDS spectra of sample M15Ni.

The density of the glasses increases with Ni addition due to the high atomic weight of this element in comparison to the silicate matrix (Figure 8.27). Up to 1 wt% NiO, the individual density measurements do not differ within the experimental error, hence even the glasses are homogeneous. However, in sample M15Ni the crystallization of trevorite results in a large error of both the of the measurements, showing the heterogeneity of the sample.

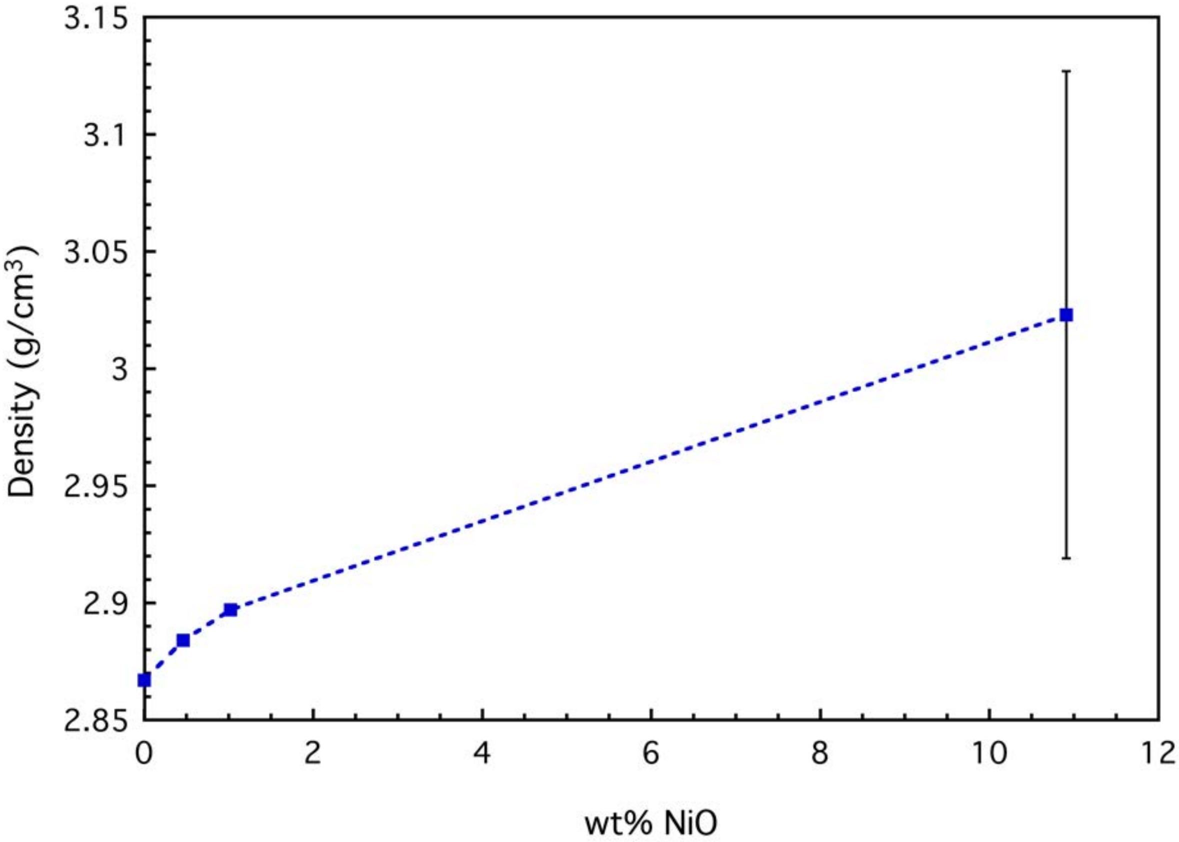

Figure 8.27. Density of the glasses as a function of the concentration of NiO.

8.5.2 Raman spectroscopy

The Raman spectra of the Ni-doped glasses show three main features at low concentrations of Ni: the previously described low (LF), middle (MF) and high frequency (HF) envelopes (Figure 8.28). The MF shifts to lower frequencies due to the reduction of the concentration of silica with Ni addition. In the HF, the prominent band of M23Ca attributed to the Q^2 groups is less intense and well-resolved; the bulk of the envelope shifts to lower frequencies. The first effect may be due to Ni being a worse Raman scatterer than Ca or to the fact that Ni replaces Fe – which may be playing the role of a network modifier as Fe^{2+} –

whereas Ni^{2+} is likely a network former (Calas et al., 1997). The bulk shift is consistent with Ni^{2+} playing the role of a network modifier. In the case of sample M15Ni, the most intense feature in the spectrum is the wide band centered at 690 cm^{-1} that corresponds to the crystallization of the spinel-like phase trevorite. The HF envelope is greatly reduced although its position is essentially the same. The LF and MF envelopes have shifted to lower frequencies due to the influence of the trevorite band. They may be attributed to the presence of a polymerized region alongside the trevorite crystals similar to the case of Cu.

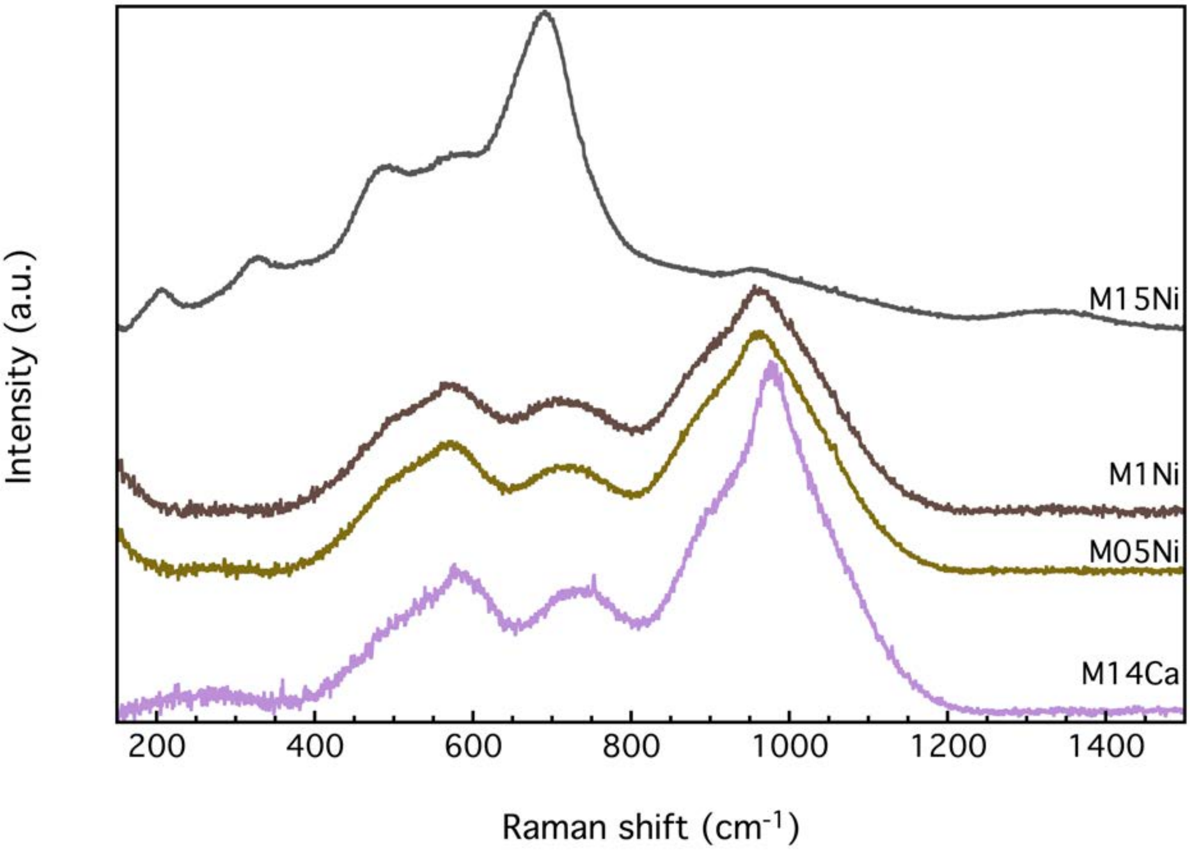

Figure 8.28. Raman spectra of the Ni-doped glasses.

8.5.3 Thermal analysis and crystallization

The DTA plots show three sets of events during the heating cycle (Figure 8.29): the first set, an endothermal event between 650 and 740 ºC, corresponds to the glass transition range (Table 8.15).

	DTA Tg (ºC)	DIL Tg (ºC)
M14Ca	698	620
M05Ni	672	645
M1Ni	679	647
M15Ni	702	667

Table 8.15. Tg of the Ni-doped glasses.

The second set, between 720-990 ºC, are exothermal events corresponding to crystallization of magnetite – around 740 ºC – and diopside – from 872 to 922 ºC – (Figure 8.30). It must be noted that the first exothermic seems to overlap the glass transition. It is likely that in this step Ni is hosted in the magnetite structure, as this mineral forms a solid solution with trevorite. The third set, between 1080-1200 ºC, is linked to the melting of the phases that have formed during the heating process. Tg increases with Ni addition in agreement with its network forming role. In the case of M15Ni, the crystallization peak is less intense because there is a lower fraction of glass.

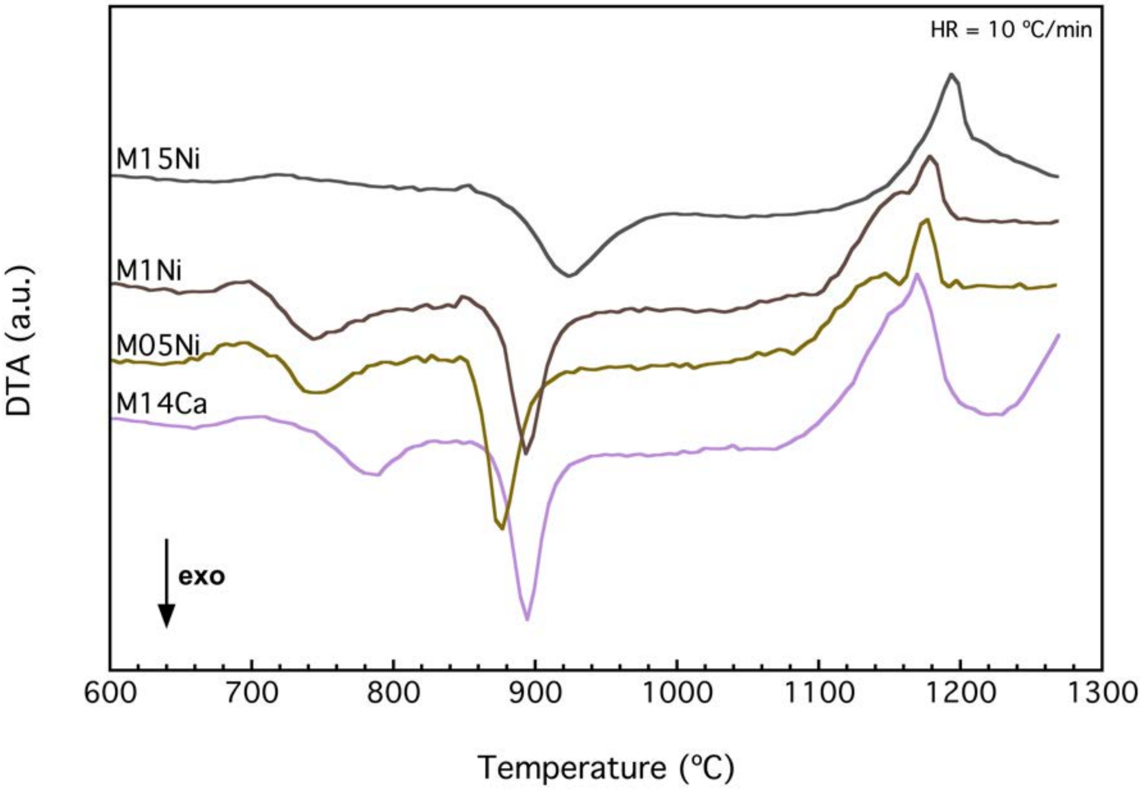

Figure 8.29. DTA plots of the Ni-doped glasses.

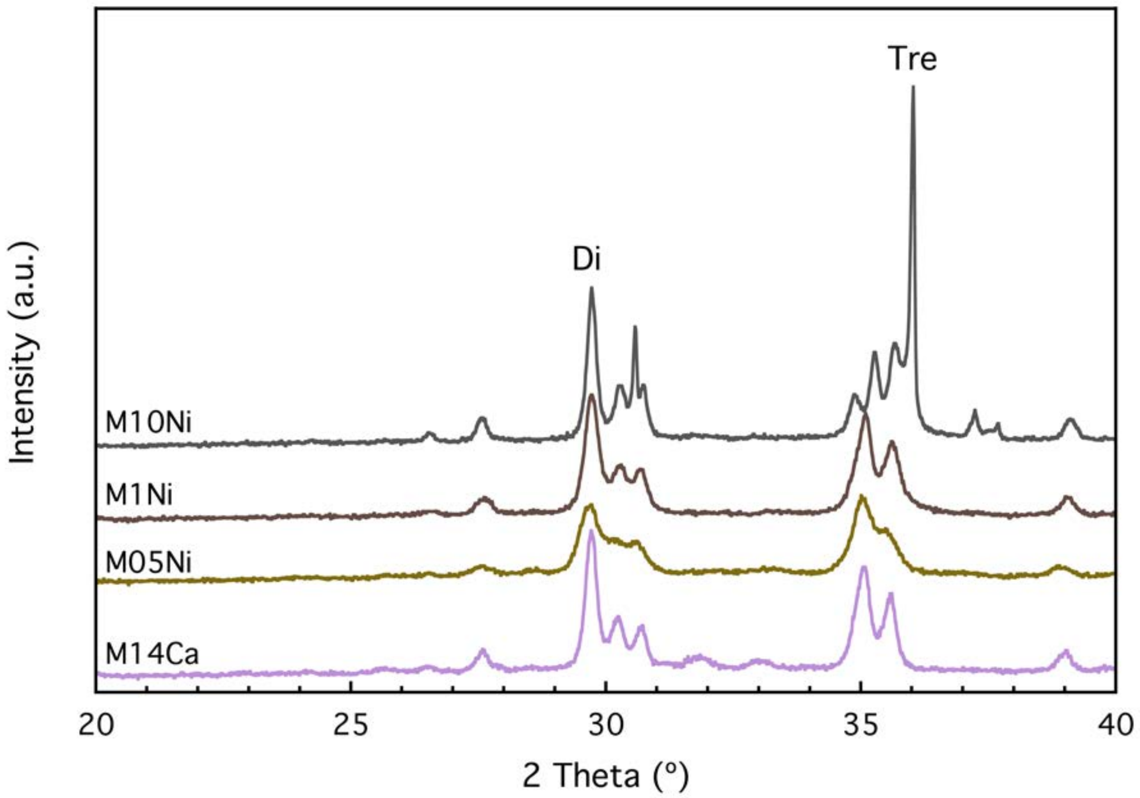

Figure 8.30. XRD profiles of the thermally treated Ni-doped glasses.

8.5.4 Nucleation and glass-ceramics production

The study of the shift of the exothermic peaks of the crystallization events has provided the temperatures of maximum nucleation rate of each phase. The shift of the peak at 744 ºC provides a T_{MNR} of 649 ºC (

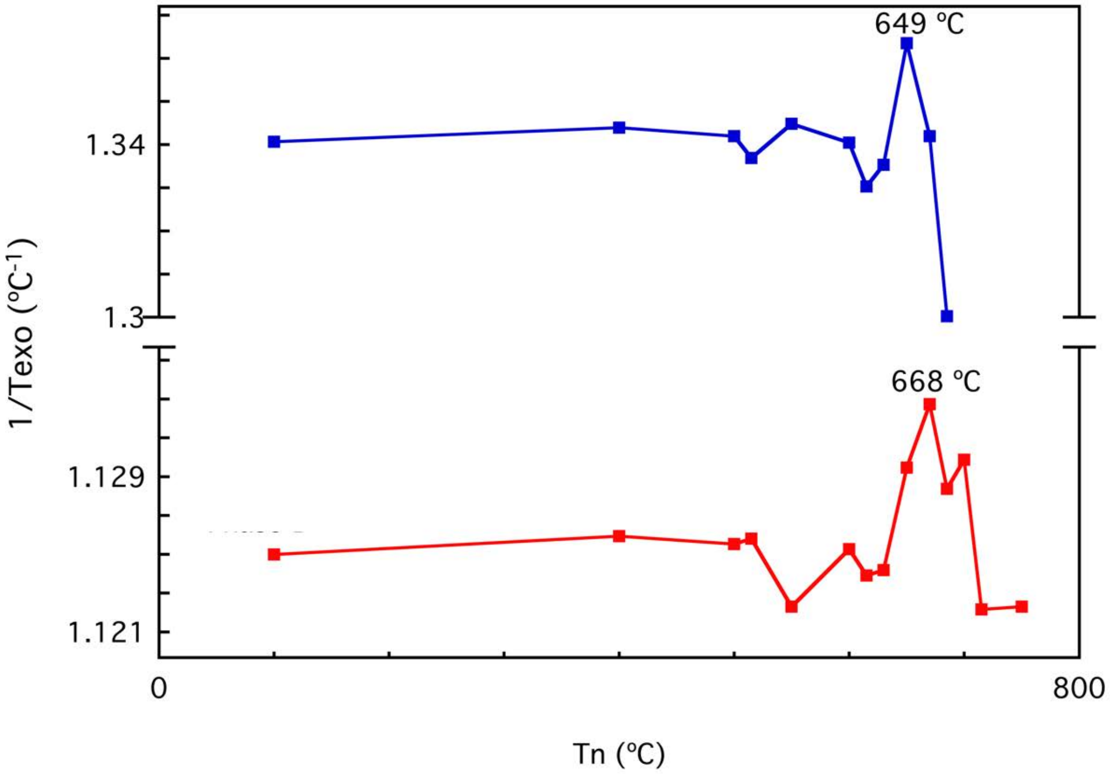

Figure 8.31) for a spinel-like phase, most likely magnetite (Figure 8.32). The shift of the second peak at 894 ºC results in a T_{MNR} of 668 ºC(

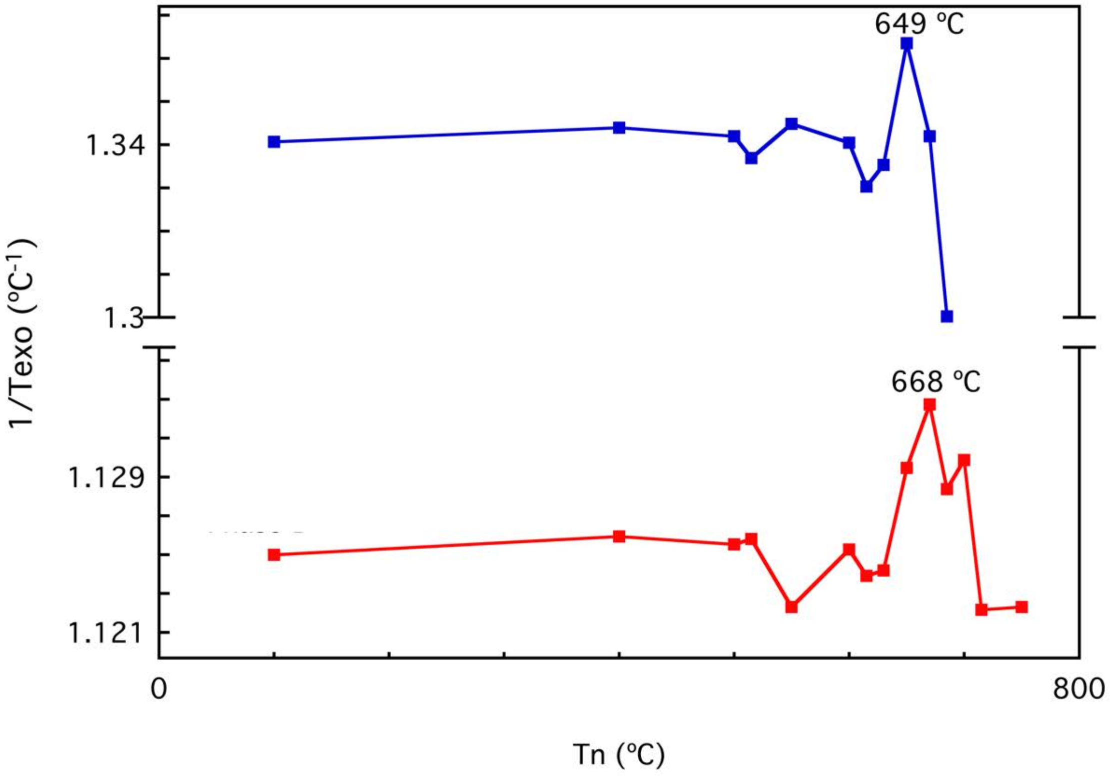

Figure 8.31) for diopside. According to these results, the treatment to produce the glass-ceramics includes the following steps:

- From room temperature to 649 ºC (T_{MNR} of magnetite) at 15ºC/min for 5h.
- From 449 to 668 ºC (T_{MNR} of diopside) at 15ºC/min for 3h.
- From 668 to 743 ºC (peak of the 1st exothermic event) at 15ºC/min for 8h.
- From 873 to 894 ºC (peak of the 2nd exothermic event) at 15ºC/min for 8h.
- Free cooling.

-

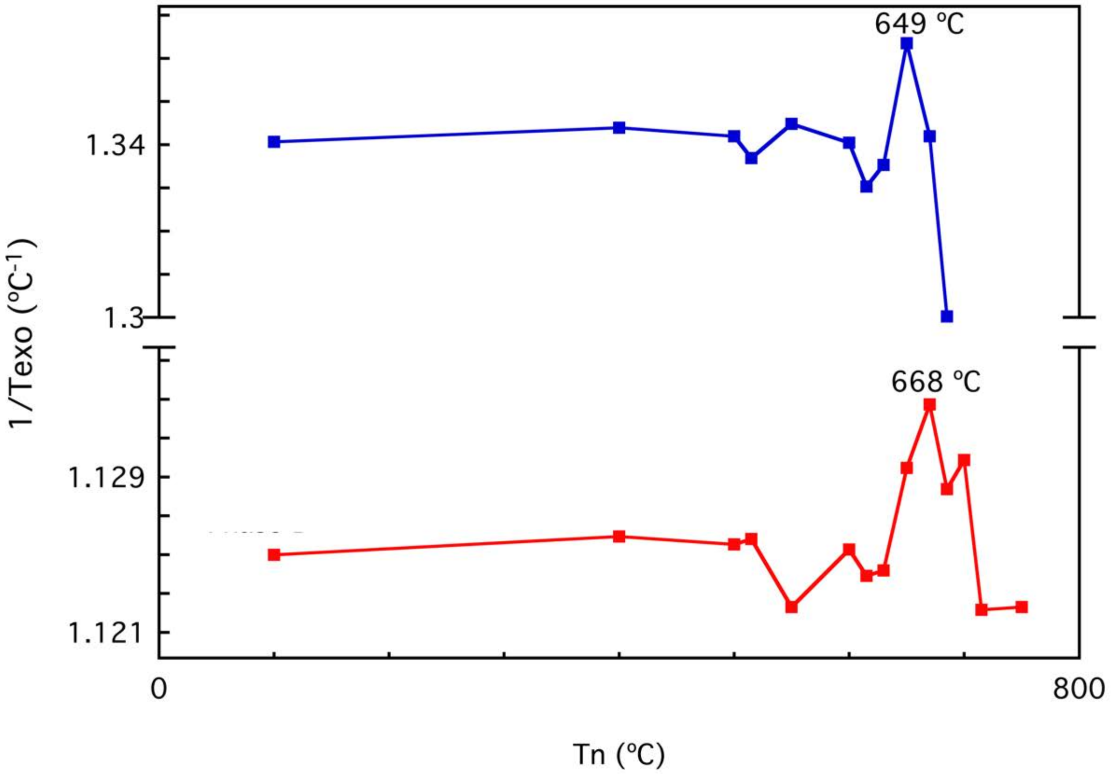

Figure 8.31. Shift of the DTA exothermic peaks of sample M1Ni.

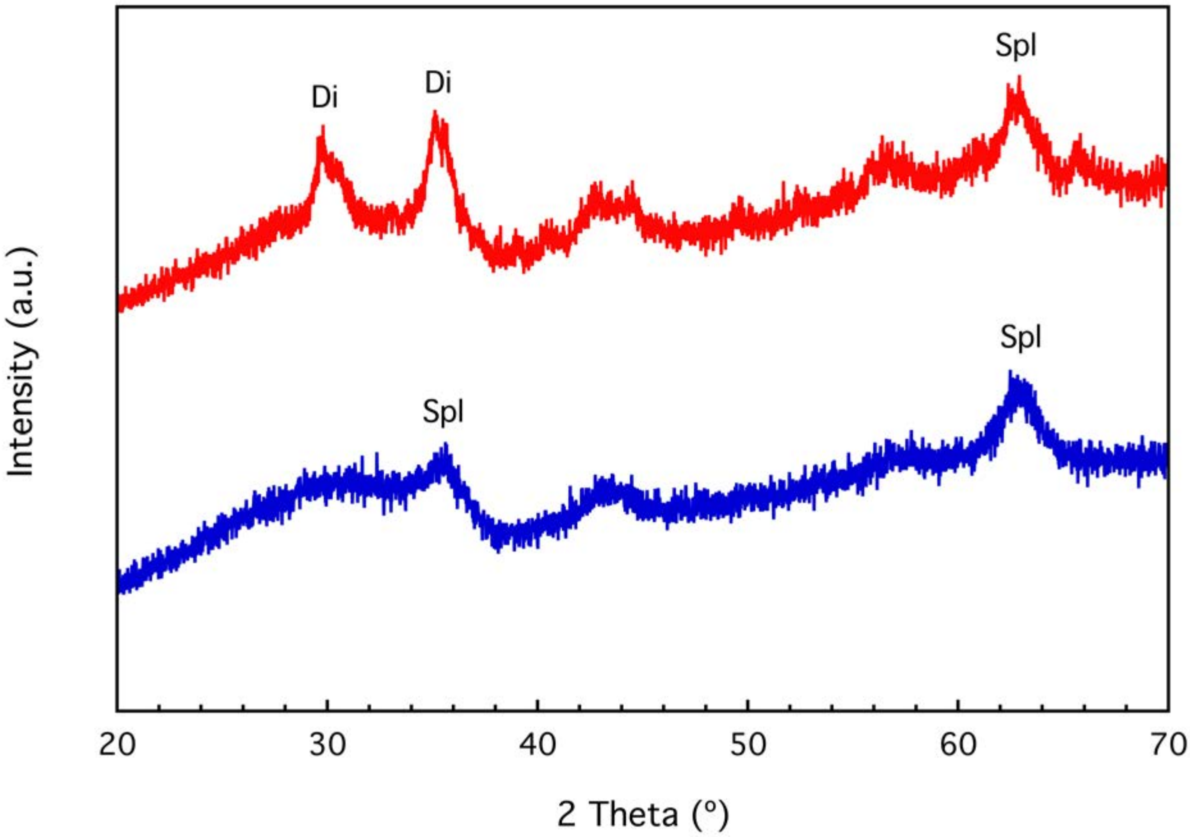

Figure 8.32. XRD profiles of the glasses treated at the T_{MNR}.

The treatment of the glass at these temperatures resulted in the formation of a highly crystalline glass-ceramics with a fine microstructure made up mostly of diopside crystals Figure 8.33). The glass-ceramics also contains trevorite even though it has not been possible to identify individual crystals (Figure 8.34). Trevorite forms during the glass-ceramics treatment although it did not crystallize in the initial thermal treatments because the longer heating process allows for a better rearrangement of the formation of the mineral structure of the solid solution magnetite-trevorite.

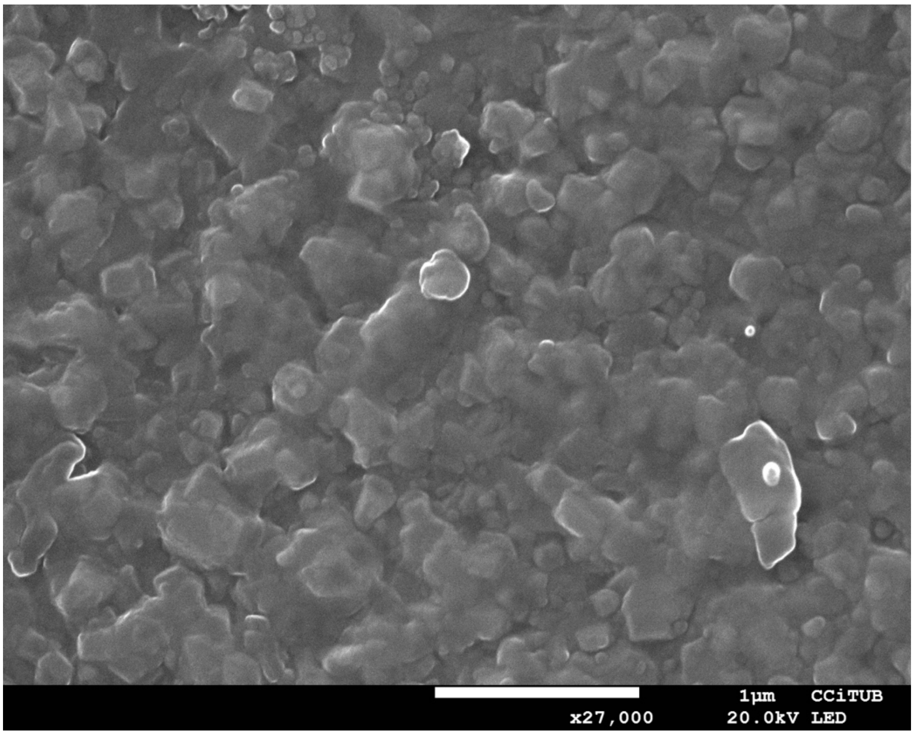

Figure 8.33. SEM micrograph of the glass-ceramics of sample M1Ni.

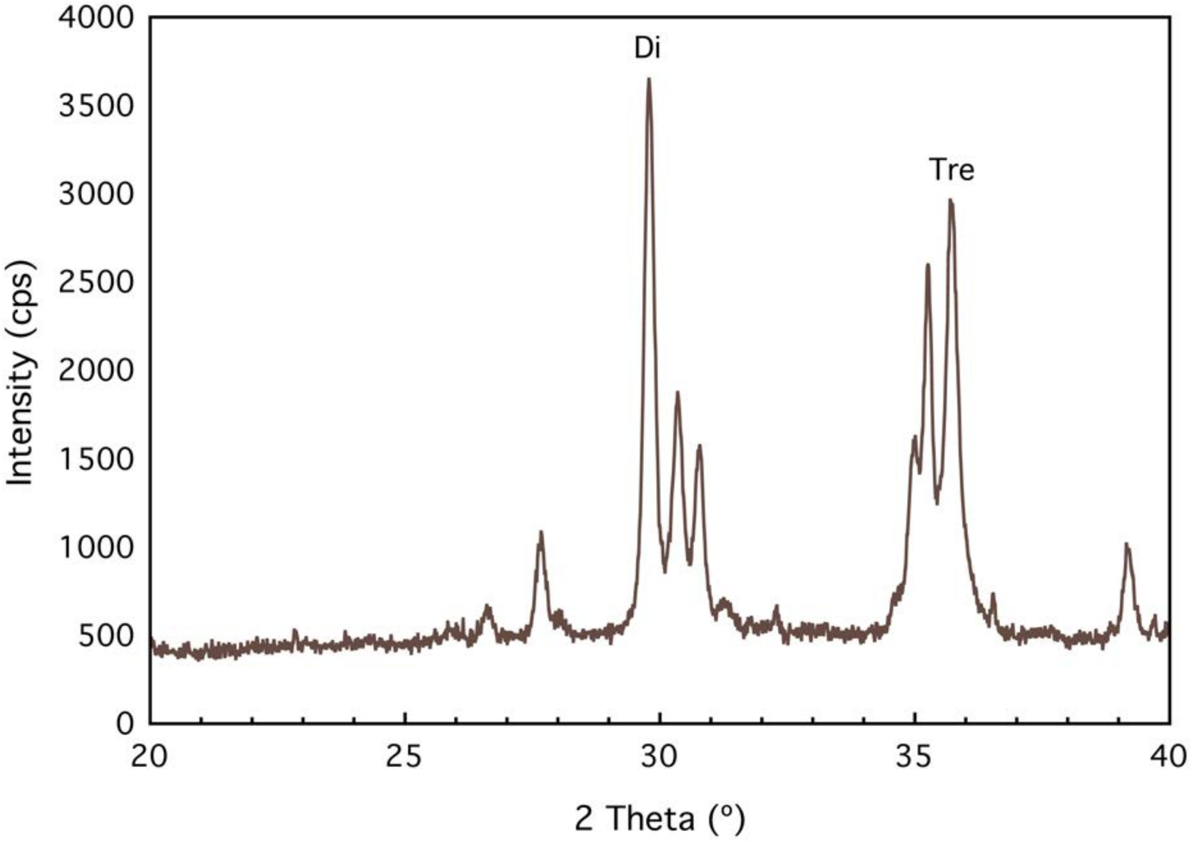

Figure 8.34. XRD profile of the glass-ceramics of M1Ni.

8.5.5 Viscosity-temperature curves

The viscosity-temperature curves of the Ni-doped series are presented in Figure 8.35. As in the previous cases, the curves are divided in three parts. Between $10^{7.9}$-10^{12} Pa·s, the domain of the rigid-to-plastic transition, the viscosity increases with Ni addition in agreement with its role as a nucleating agent. In the $10^{7.9}$-$10^{5.6}$ Pa·s range, the flow is controlled by crystallization and the apparent viscosity increases inversely to the concentration of Ni, as the amount of crystals increases more. Finally, between $10^{5.6}$-$10^{2.1}$ the formation liquid phase causes viscosity to increase again with the concentration of Ni. The viscosity of M15Ni is significantly higher than the others due to the permanence of trevorite crystals, that do not melt in the range of the HSM experiment.

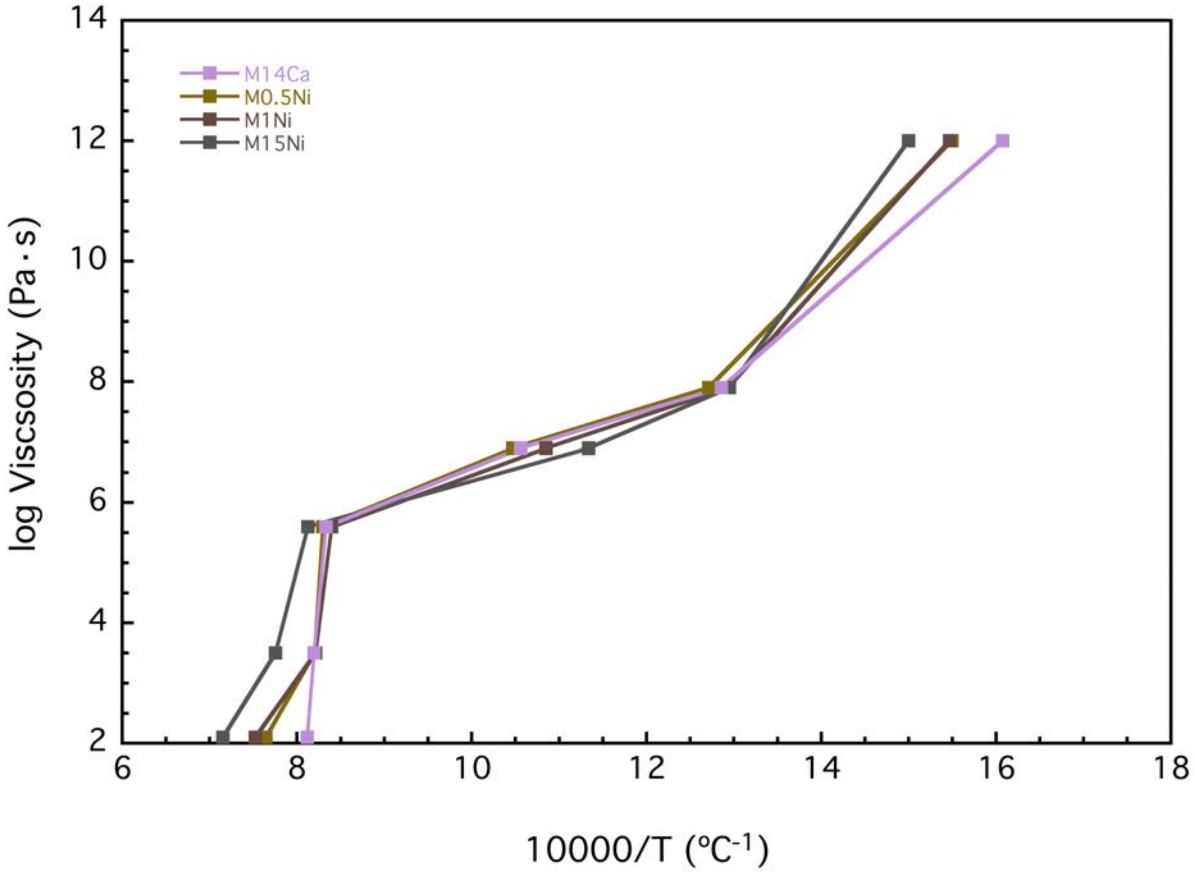

Figure 8.35. Viscosity-temperature curves of the Ni-doped glasses.

8.5.6 Microhardness

The microhardness of the Ni-doped glasses is higher than that of the matrix, although its evolution is complex as it decreases between M05Ni and M1Ni but increases in the rest of intervals. The increase between the matrix and M05Ni is due to Ni stimulating nucleation. M15Ni is the hardest due to the trevorite crystals; however, they are not large enough to be distinguished in the microdurometer.

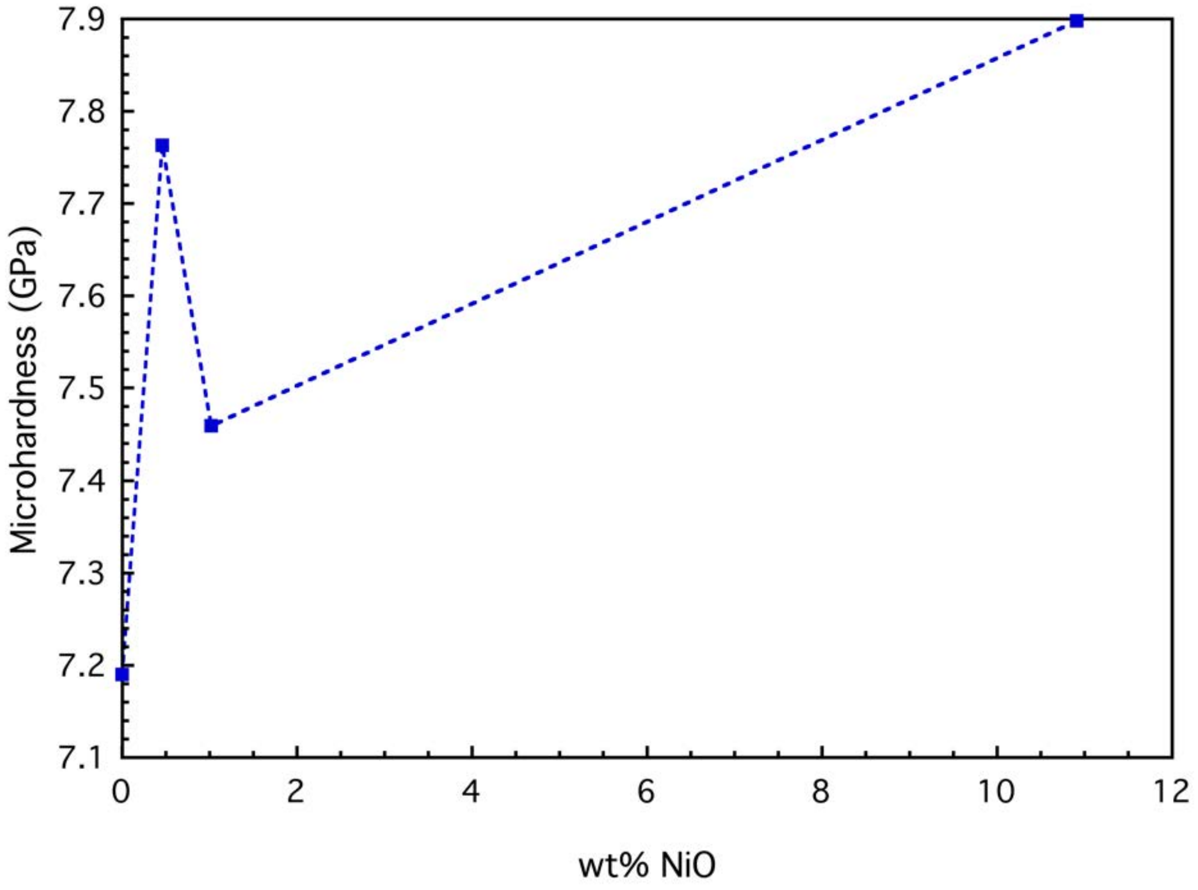

Figure 8.36. Microhardness Vickers of the Ni-doped glasses.

8.5.7 Leaching

The leaching tests show that the glasses are stable because the concentrations of the main components in the leachates are at least 6 degrees of magnitude below those of their concentrations in the glasses (Table 8.16). Moreover, the toxic elements are properly bound in concentrations at least 3 orders of magnitude below those of the glasses (Table 8.17). Ni has been properly isolated in all cases, either in the glasses or in trevorite. In general, the leaching has affected the glass-ceramics of M1Ni more than its parent glass. However, it must be noted that Ni is actually more strongly bound in the glass-ceramics. All the studied materials comply with the requirements of DIN38414-S4 to be considered inert (DIN-38414S4, 1984).

	Si	Al	Ca	Mg	Na	K	Fe	P
M05Ni	1.88	0.40	3.26	1.44	6.62	1.30	0.13	0.51
M1Ni	2.39	0.53	5.27	2.10	8.74	1.57	0.15	BDL
GC M1Ni	4.84	0.55	9.38	2.85	8.21	1.32	0.06	BDL
M15Ni	2.85	0.48	4.01	1.82	6.65	1.32	0.09	BDL

Table 8.16. Concentrations of the main elements of the Ni-doped glasses in the leachates.

	As	Ba	Cd	Cr	Cu	Hg	Mn	Ni	Ti	Pb	Zn
M05Ni	0,09	3,88	0,18	BDL	0,53	BDL	2,96	10,34	24,34	0,31	BDL
M1Ni	BDL	4,84	0,07	BDL	1,10	BDL	3,22	23,95	26,27	0,17	BDL
GC M1Ni	0,15	41,09	0,10	BDL	9,91	BDL	5,45	13,56	6,51	0,15	BDL
M15Ni	BDL	2,79	0,07	BDL	BDL	BDL	1,97	93,46	15,00	0,09	BDL
M14Ca	0.09	29.15	1.47	BDL	2.85	BDL	0.46	3.45	27.35	0.68	5.33
Limits	500	20000	40	N/A	2000	1	N/A	400	N/A	500	4000

Table 8.17. Concentrations of the trace elements of the Ni-doped glasses in the leachates. Limits from (Council of the European Union and 2003/33/EC, 2003; DIN-38414S4, 1984).

8.5.8 Conclusions

- The density of the glasses increases with Ni addition
- At low concentrations, Ni is emplaced in the glass structure, whereas at higher concentrations it forms the spinel phase trevorite.

- The glasses crystallize into diopside and magnetite. The glass-ceramic processing allows the formation of trevorite because its extended length permits a better rearrangement.
- Viscosity increases with Ni addition because it facilitates nucleation.
- The microhardness increases with Ni addition.

8.6 Zinc

8.6.1 Conclusions

The chemical composition of the Zn-doped glasses is reported in Table 8.18. The solubility of ZnO in the Ca-P-doped basalt is between 5 and 10 wt%. The concentration of Zn in the glasses are in good agreement with its nominal composition apart from sample M10Zn. This is due to the crystallization of a spinel-like phase during quenching, as seen in Figure 8.37.

	SiO_2	Al_2O_3	CaO	MgO	Na_2O	K_2O	MnO	FeO	TiO_2	P_2O_5	ZnO
M23Ca	35.58	11.44	22.10	8.07	2.99	1.48	0.14	10.34	2.01	5.85	0.00
	0.23	0.12	0.19	0.06	0.09	0.03	0.02	0.14	0.06	0.25	0.01
M1Zn	34.96	11.55	22.38	7.71	3.04	1.53	0.15	9.00	2.01	5.90	1.16
	0.25	0.08	0.16	0.06	0.07	0.04	0.02	0.08	0.07	0.30	0.04
M5Zn	34.11	11.00	21.11	7.53	3.19	1.45	0.14	8.61	1.89	5.29	5.72
	0.12	0.07	0.16	0.04	0.07	0.05	0.02	0.10	0.05	0.30	0.06
M10Zn	31.80	10.16	19.99	7.09	3.23	1.36	0.13	7.93	1.83	4.57	11.24
	0.09	0.10	0.20	0.05	0.11	0.05	0.01	0.06	0.05	0.41	0.10

Table 8.18. Chemical composition of the Zn-doped matrix glasses. The error of the measurement is shown by the standard deviation of the measurements.

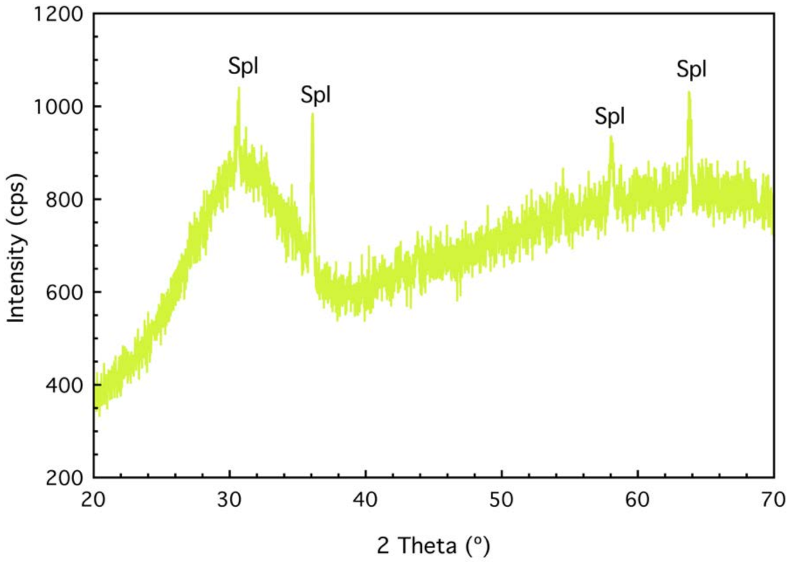

Figure 8.37. XRD profile of the as-quenched M10Zn glass.

The density of the glasses increases almost linearly with Zn addition due to its atomic weight being higher than the average of the glass components (Figure 8.38). The low error of the measurements proves that the glasses are homogeneous. The spinel-like crystals do not affect the density measurements, hence they are probably nanometric – which would be consistent with the low intensity of the XRD reflections – and homogeneously distribution.

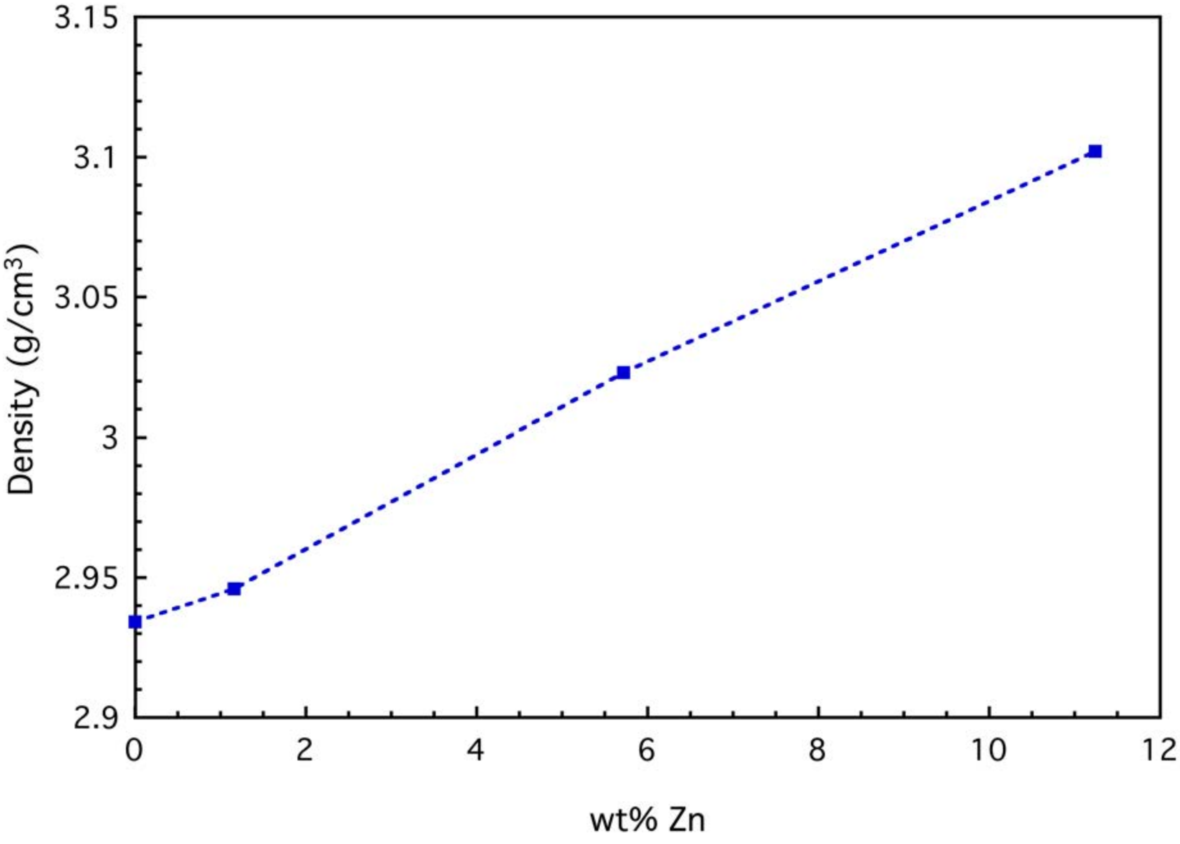

Figure 8.38. Variation of the density of the glasses as a function of the concentration of Zn. The error of the measurement is smaller than the symbols.

8.6.2 Raman spectroscopy

As explained in the previous chapters, the Raman spectra are divided in three regions (Figure 8.39): the low frequency envelope (LF, 350-650 cm^{-1}), which does not change with Zn addition; the middle frequency envelope (MF, 650-800 cm^{-1}) that shifts slightly to lower frequencies as a consequence of the decrease of the concentration of SiO_2; and the high frequency envelope (HF, 800-1250 cm^{-1}). The shape of the HF does not vary with Zn addition, hence it does not seem to significant changes to the structure of the matrix glass. This may be attributed to Zn being an intermediate cation, which may be present in glasses both in tetrahedral and octahedral coordination (Rosenthal and Garofalini, 1987). Depending on Zn's distribution, the polymerization may not have been altered. Zn in octahedral coordination occupies a similar location to Mg in the glass structure according to the similarity of their ionic radii (Shannon et al., 1976). The spectra are noisy, showing the presence of nanolites.

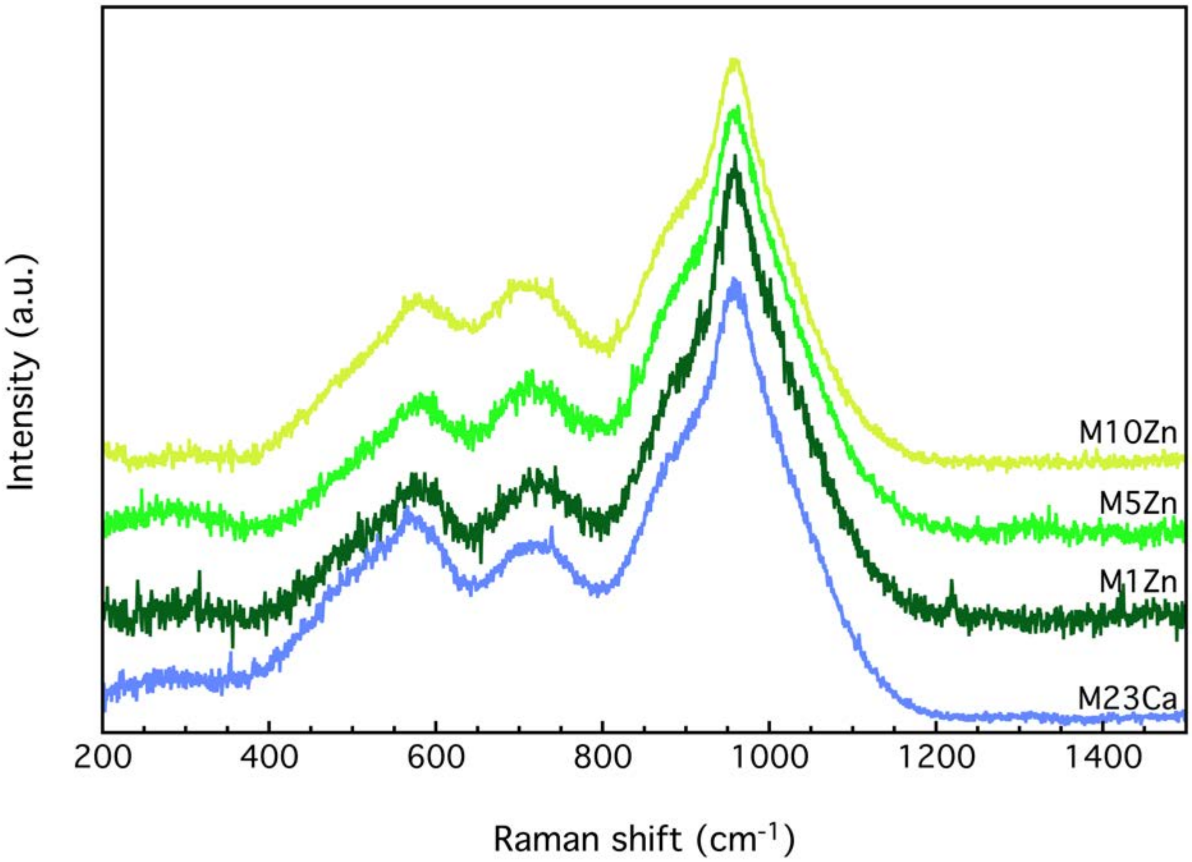

Figure 8.39. Raman spectra of the Zn-doped glasses compared to the P-Ca-basaltic matrix. Zn content decreases from top to bottom.

8.6.3 Thermal analysis and crystallization

The DTA profiles show three groups of events during the heating cycle (Figure 8.40). The first endothermal events – between 630-720 ºC – corresponds to the glass transition range. Tg decreases with Zn addition (Table 8.19) because the more covalent character of the Zn-O bond compared to the Ca-O and Mg-O bonds makes the glass structure more rigid, hence increasing the stress and reducing the energy that is needed for relaxation (Sułowska et al., 2016).

	Tg DTA (ºC)	Tg DIL (ºC)
M23Ca	636	636
M1Zn	697	652
M5Zn	670	639
M10Zn	658	604

Table 8.19. Tg of the Zn-doped glasses.

The group of exothermic events between 770-970 ºC is linked to the crystallization of an assemblage of mineral phases. The XRD profiles show that these phases are a member of the spinel group, diopside, and akermanite (Figure 8.41). The spinel-like phase likely contains some Zn in solid solution with magnetite because the angles of its reflections are intermediate between those of gahnite (Zn_2AlO_4) The second group of endothermal events corresponds to the melting of the aforementioned mineral phases, first akermanite and then diopside as mentioned in chapter 7. The addition of Zn increases the akermanite/diopside ratio due to the incorporation of Zn^{2+} to the akermanite structure (Deer et al., 1992).

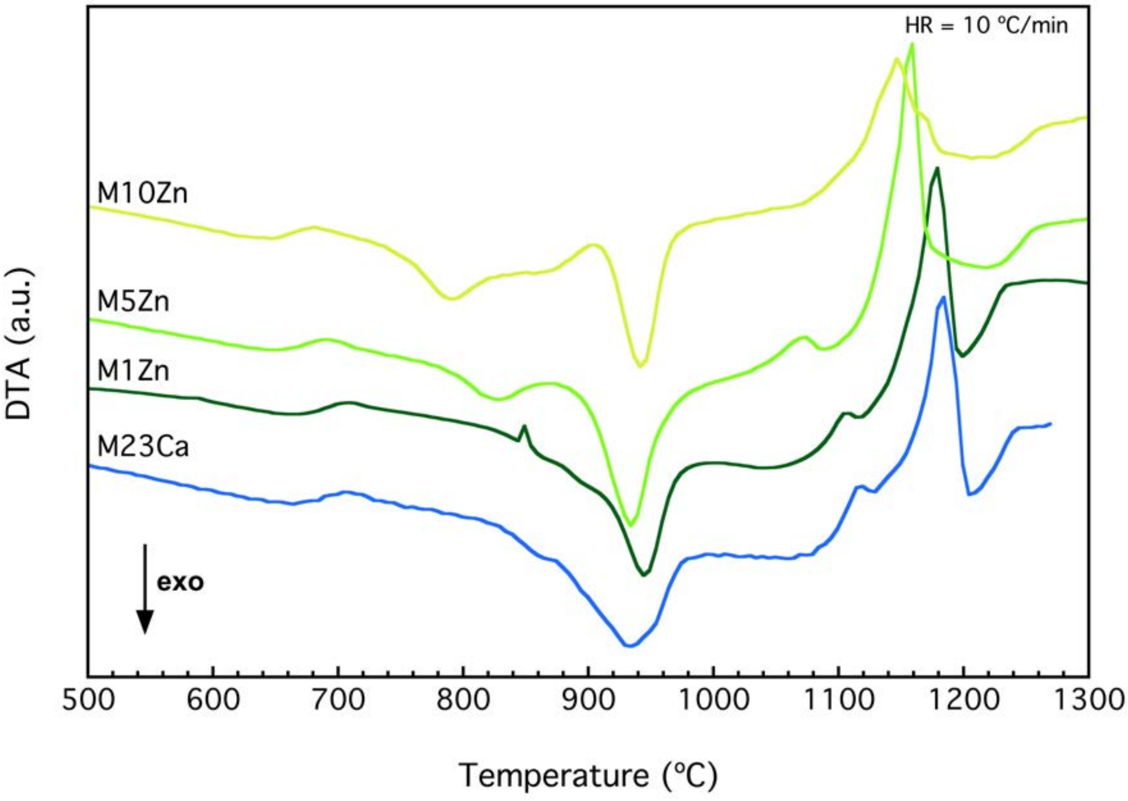

Figure 8.40. Thermal behavior of the Zn-doped glasses.

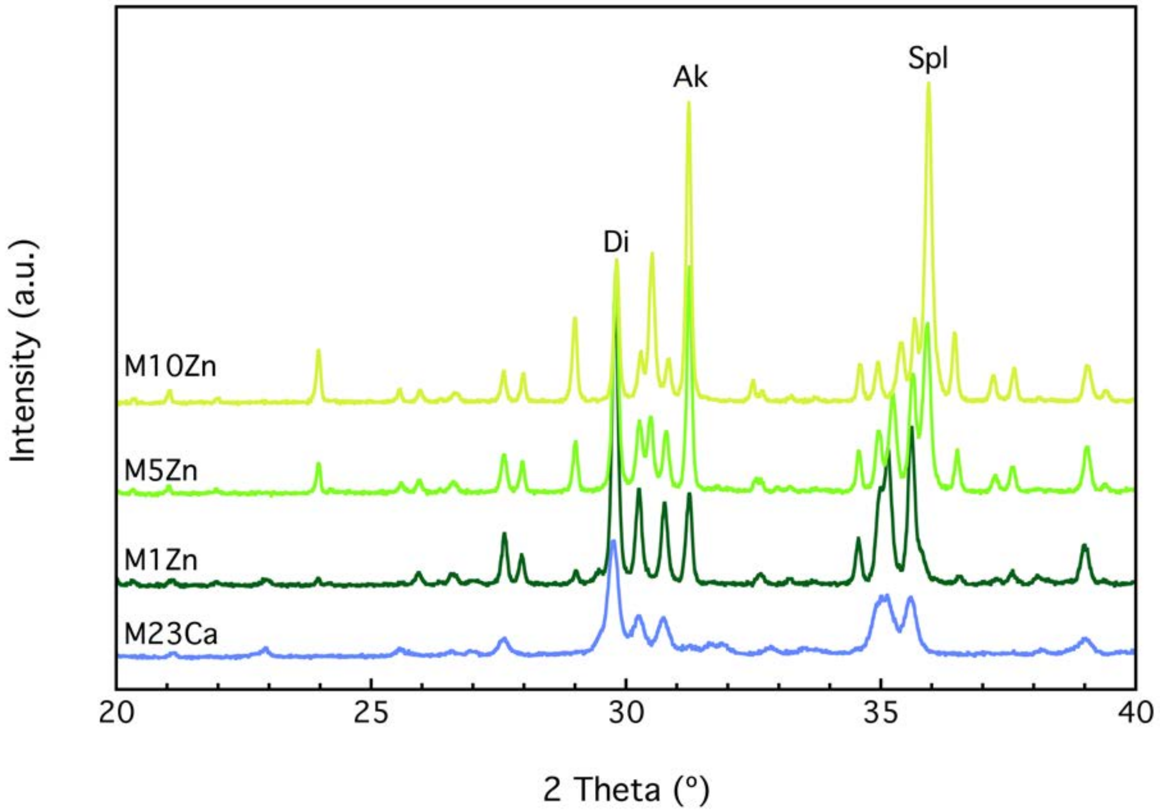

Figure 8.41. XRD profiles of the Zn-doped glasses treated at the temperatures of the exothermic peaks.

8.6.4 Viscosity-temperature curves

The viscosity-temperature curves may be divided in three regions (Figure 8.42). Viscosity decreses with a steep slope in the first region – between $10^{7.9}$ and 10^{12} Pa·s – as the viscous flow is controlled by the deformation of the rigid glass. The decrease of viscosity with Zn addition is consistent with the evolution of Tg. In the second region – between $10^{7.9}$-$10^{5.6}$ Pa·s the slope decreases as the deformation is controlled by the crystallization mentioned in the previous section. In the third section – between $10^{5.6}$-$10^{2.1}$ Pa·s – the flow is dominated by the melting of these crystals and the formation of liquid. Overall, the addition of Zn decreases the viscosity when it is emplaced in the glass structure, pointing to a network-modifying role, unless it is causing crystallization.

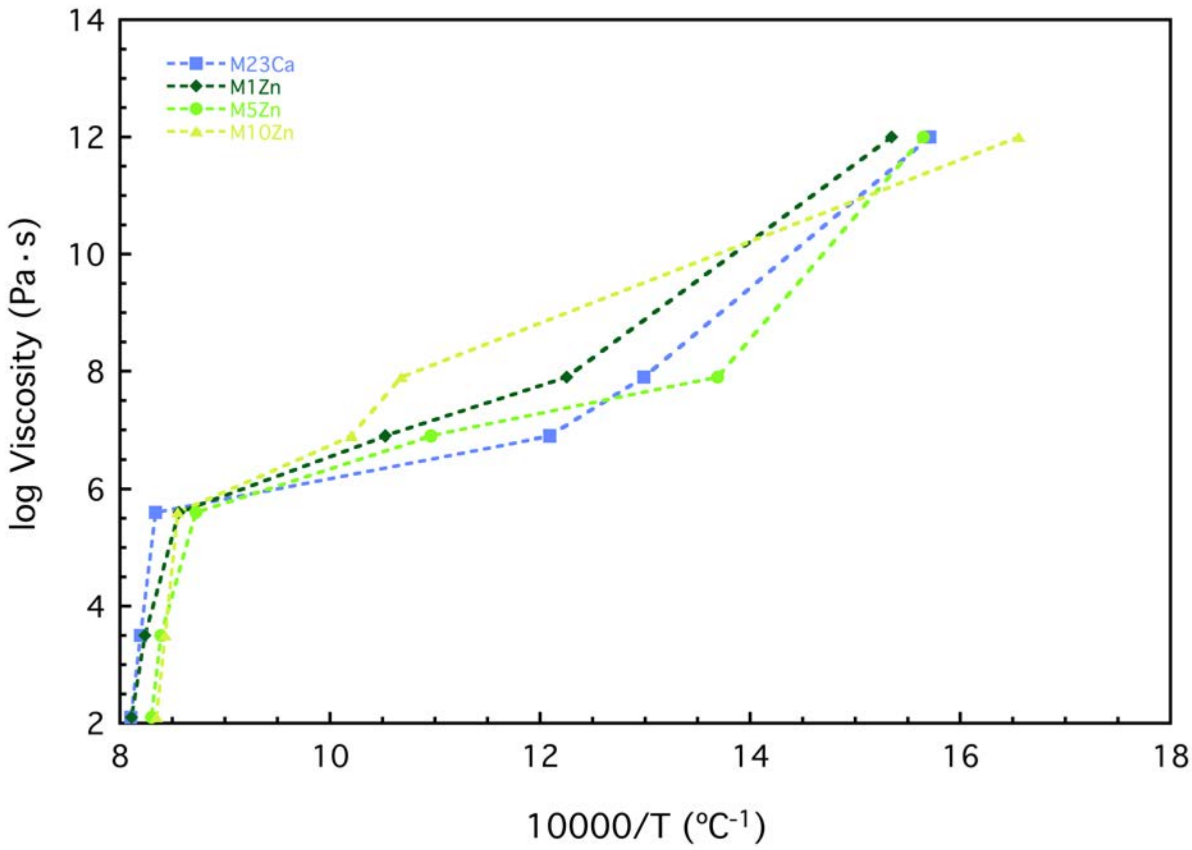

Figure 8.42. Viscosity-temperature curves of the Zn-doped glasses. The lines are only a guide for the eye.

8.6.5 Microhardness

The addition of Zn increases the microhardness of the glass in comparison to the glassy matrix (Figure 8.43). However, upon the onset of spinel crystallization in sample M10Zn microhardness decreases. Although crystallization normally enhances the hardness, it may also cause some porosity and fragilization of the network. This reduction of microhardness is also consistent with the low energy of Zn-O bonds (Sułowska et al., 2016).

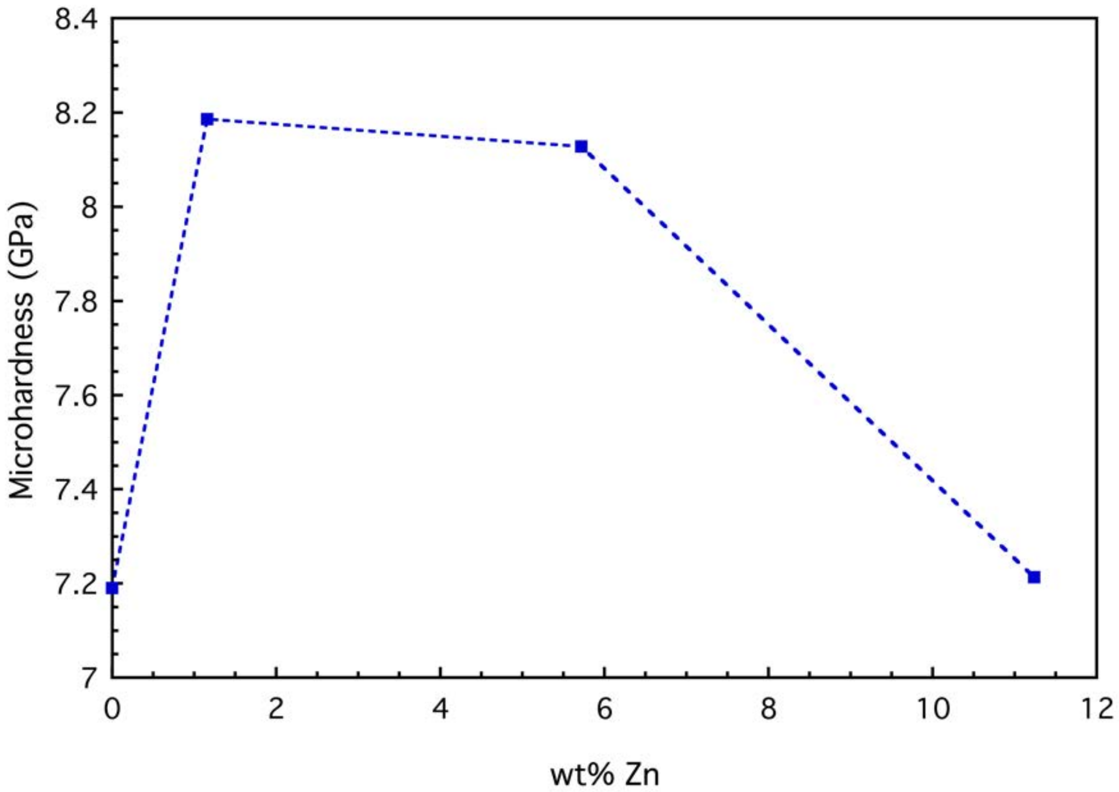

Figure 8.43. Microhardness Vickers of the Zn-doped glasses.

8.6.6 Leaching

The leaching tests confirm the stability of the glasses, as the concentrations of the major components are at least six orders of magnitude below those of the original glasses (Table 8.20). The potentially toxic metals are properly inertized and comply with the requirements to be considered inert (Table 8.21). The concentration of Zn in the leachate increases proportionately to its concentration in the glass. However, even at its highest, the concentration is still more than 2 orders of magnitude below the maximum allowed.

[ppm sol]	**Si**	**Al**	**Ca**	**Mg**	**Na**	**K**	**Fe**	**P**	**Zn**
M23Ca	3.61	1.01	3.6	2.86	10.3	2.06	0.23	BB	$7*10^{-4}$
M1Zn	4.66	0.95	18.92	5.30	31.95	7.66	0.32	0.70	0.06
M5Zn	7.36	1.98	17.45	6.29	31.22	6.55	1.30	1.08	0.11
M10Zn	4.28	1.17	11.60	2.38	8.48	1.70	0.48	0.58	0.27
DIN38414S4	N/A	N/A	N/A	N/A	N/A	N/A	N/A	N/A	4

Table 8.20. Concentrations of the main components of the Zn-doped glasses in the leachate. BB stands for below blank.

[ppb] sol	Ba	Cd	Cr	Cu	Mn	Ni	Pb	Ti
M23Ca	BB	0.77	BDL	15.92	0.36	5.12	0.77	47.90
M1Zn	38.27	0.10	BDL	19.31	7.27	6.36	5.30	67.82
M5Zn	878.63	0.15	3.95	16.87	25.23	7.39	5.13	276.39
M10Zn	660.28	0.10	BDL	14.88	9.67	3.68	4.21	136.34
Limits	20000	40	500	2000	N/A	400	500	N/A

Table 8.21. Concentrations of the trace components of the Zn-doped glasses in the leachate. BB stands for below blank. N/A stands for not applicable. Limits from (Council of the European Union and 2003/33/EC, 2003; DIN-38414S4, 1984).

8.6.7 Conclusions

- The Zn-doped glasses are homogeneous. Their density increases proportionately to the addition of Zn.
- The solubility of Zn in the matrix is between 6 and 12 wt%. A spinel-like phase precipitates upon saturation.
- Tg decreases with Zn addition due to the covalent character of the Zn-O bonds.
- The glasses crystallize into a spinel-like phase, diopside, and akermanite.
- Viscosity decreaess with Zn addition apart from the intermediate range, where the samples crystallize.
- The microhardness increases first and then decreases with Zn addition
- The Zn-doped glasses are chemically stable and may be considered inert.

CHAPTER 9 Valorization of sludge from a wastewater treatment plant by glass-ceramic production

9.1 Introduction

The continued growth of the volume of sewage sludge produced at wastewater treatment plants, its use and storage are a major environmental problem. Solid waste management is a global concern that results in many issues such as high-energy consumption, a disproportionate increase in industrial waste and the pollution of the environment. Many environmental problems arise from the accumulation of industrial and municipal wastes and sludge, mainly related to their volume and contents of potentially toxic elements. All these topics require the development of new solutions to achieve a sustainable development. Using waste as a raw material represents a reduction of both storage space issues with their associated economic costs and the need to mine for raw materials to be used in the manufacture of any new product (Andreola et al., 2016). From this point of view, it is a measure that promotes environmental conservation and a rational use of natural resources.

A current possibility for various types of sludge (including fly ash), toxic and nuclear wastes is the fabrication of glass and glass-ceramics by means of vitrification processes (Bingham and Hand, 2006; Garcia-Valles et al., 2007; Peng et al., 2004; Pioro et al., 2001). Sewage sludge (SS) ashes may be a substitute for clay in brick manufacture (Trauner, 1993; Wiebusch et al., 1999; Wiebusch and Seyfried, 1997). Moreover, the manufacture of bricks using 100% SS ash was achieved at a plant operating in Japan (Okonu and Takahashi, 1997). The literature also includes examples of the use of SS ash in the production of glass-ceramics (Endo and Nagayoshi, 1997; Suzuki et al., 1997), in asphalted paving mixes (Al Sayed et al., 1995) and the effect of adding SS ash to cement mortars (Bhatty and Reid, 1989; Monzó et al., 1999). Glass-ceramics are also considered for the inertization of other residues, such as high level nuclear waste (Asuvathraman et al., 2015).

After the thermal treatments, the waste becomes a stable glass or glass-ceramic suitable for commercial purposes. These processes give a value to the waste, as well as solving the storage problem. The organic content of waste may act as auxiliary power.

Vitrification offers an alternative in the stabilization of hazardous wastes, since the potentially toxic elements are bound in a glassy matrix or in crystalline phases (Alfonso et al., 2016; Arancibia et al., 2013; Cetin et al., 2015; Garcia-Valles et al., 2007).

Glass-ceramics are polycrystalline materials of fine microstructure produced by the controlled crystallization (devitrification) of a glass. To obtain the glass ceramic it is necessary to establish how nucleation and crystal growth processes occur in the chosen glassy matrix. Knowing the nucleation (T_N) and growth temperature (T_{GR}) of phases that will crystallize during glass-ceramic formation is essential for glass technology. The determination of these parameters is critical when the raw materials are wastes because of their chemical complexity, which results in the nucleation and growth of different mineral phases.

Currently, many studies that develop new glass-ceramics focus on obtaining inexpensive materials using basaltic rocks and ceramic waste coming from the manufacture of sanitary materials (Khater et al., 2012). In this case, the glass-ceramic is polymineralic (pyroxenes, anorthite, olivine and magnetite) and has a high hardness. Marangoni and coworkers (Marangoni et al., 2014) obtained self-foaming cellular glass–ceramics, which had high strength and porosity, from mixtures of recycled soda-lime glass and iron-rich basalt scoria. Chinnam and coworkers (Chinnam et al., 2013), in a review paper, stated that making glass-ceramics with waste residues is energetically more efficient than using natural raw materials and concluded that many works suggest that iron rich wastes show potential to be developed as useful glass–ceramics for functional applications in the construction industry.

The aim of this work is to obtain a glass-ceramic product using wastes as a raw material. Its production is based in the determination of the nucleation and crystal growth in a glass obtained using silica-rich sewage sludge from a wastewater treatment plant that depollutes water from municipal and industrial origin.

9.2 Materials and methods

9.2.1 Original Glass

The original glass used in this paper was made and reported in a previous work (Garcia-Valles et al., 2013). Nucleation and crystal growth were studied in an original glass sample produced from sludge of a wastewater treatment plant (WWTP) located in El-Sadat City (near the Nile delta) about 93 km from Cairo (Egypt). Original glass included dry WWTP sludge (91 wt%) from the oxidation tank together with 2 wt% Na_2 CO_3, 5 wt. % Ca CO_3, and 2 wt% CaF_2 (Garcia-Valles et al., 2013). The mixture was placed inside an aluminous crucible and molten at 1450 ºC for 8 h inside a globular alumina furnace equipped with molybdenum disilicide SuperKanthal®. The glass was cast in a metallic mold and annealed at 450ºC for 60 min.

9.2.2 Methods

The chemical composition of the original glass was obtained by X-ray fluorescence (XRF), using a sequential X-ray spectrophotometer Phillips PW2400.

The mineralogical evolution during the heating treatment of the original glass was determined by X-Ray Diffraction (XRD) carried out under vacuum atmosphere in an Anton Paar HTK1200N High Temperature chamber (HT-XRD), coupled to a PANalytical X'Pert PRO MPD Alpha1 powder diffractometer in Bragg-Brentano $\theta/2\theta$ geometry (radius of 240 millimeters, Cu Kα1 radiation (λ = 1.5406 Å), work power 45 kV – 40 mA, scanning range 4 – 80º 2θ with step size of 0.017º and measuring time 50 s. The experiment consisted in heating powdered glass at a rate of 20 °C/min with 1h isothermal step at 28, 200, 400, 600, 700, 800, 825, 850, 875, 900, 910, 920, 930, 940, 950, 960, 970, 980, 990 and 1000 º C. A last set of spectra was recorded at 28 ºC after free cooling. 7 spectra were taken during each one of these steps.

The temperatures of nucleation (T_N) and crystal growth (T_{GR}) are essential parameters in glass-ceramic manufacture. T_N is obtained with Differential Thermal Analysis (DTA) of the original glass. 70 mg of glass particles (between 400-500 µm in diameter) were heated at 15 ºC/min in alumina crucibles at temperatures between 500 – 825 ºC every 25 ºC during 3h isothermal steps, followed by further heating at 15 ºC/min up to 1200 ºC. The equipment was a DTA-TG Netzsch STA 409C model operating under dry air atmosphere with an air flux of 80 ml min^{-1}. The temperature of maximum nucleation rate (T_N) can be obtained from the exothermic peak temperature (T_{ex}) which is related to the number of nuclei per unit volume that were formed in the glass (N) (Xu et al., 1991) [Eq. 1]. This relationship is established by the expression:

$$\ln N = \frac{m * E_c}{R * T_{ex}} + Ct \qquad \text{[Eq. 1]}$$

R = gas constant

Ec = activation energy for crystallization

m = dimensionality of crystal growth

Ct = constant

The size of magnetite crystals been determined by XRD of the original glass heated up to 750 and 800 ° C using the equation of Scherrer (Monshi et al., 2012) [Eq. 2]

$$\tau = \frac{K\lambda}{\beta \cos\theta} \qquad \text{[Eq. 2]}$$

τ is the mean size of the crystalline domains; K is a dimensionless shape factor; λ is the X-ray wavelength; β is the line broadening at half the maximum intensity, after extracting the instrumental line broadening, in radians; θ is the Bragg angle.

To establish the process of growth of the different phases, further thermal treatments were designed according to T_N results. Small glass fragments (2-3 mm) are heated at 15 ºC/min up to the nucleation temperature, where they undergo a 3h isothermal step, and then up to 1100ºC in the DTA cell.

The crystal growth of magnetite from the silicate glass network has been analyzed using Raman spectroscopy. Unpolarized Raman spectra were obtained in a HORIBA Jobin Yvon LabRam HR 800 dispersive spectrometer, equipped with an Olympus BXFM optical microscope, and using a CCD detector cooled at –70ºC. Sample excitation was achieved using the 532 nm line of an argon laser operating at 4 mW with 4 measurement repetitions for 120 s each.

The microstructure and microchemistry of these samples were analysed both in transmission (TEM) and scanning electron microscopies (SEM). TEM characterization was carried out in a field emission transmission electron microscope JEOL 2010F operating at 200 kV. Energy dispersive spectroscopy (EDS) was carried out on an Emispec system in scanning transmission electron microscopy (STEM) mode. SEM study was performed in an ESEM Quanta 200 FEI XTE 328/D8395 coupled to an EDS detector and in a JEOL J-7100 field emission SEM.

Rietveld refinement of the XRD spectrum of the glass-ceramic was performed on a XRD-pattern of a non-oriented sample with FullProf v. 3.00 software (Rodríguez-Carvajal, 1993).

The leachability of chemical elements from the glass and the glass-ceramic were evaluated in order to determine the ability of the glass as a binder for potentially toxic elements according to DIN 38414-S4 (DIN-38414S4, 1984). The test is performed in a sample of 100 g of dry mass, particle size < 10 mm), mixed in 1000 ml of deionized water. The mixture is agitated during 24 h at room temperature and the liquid is separated from the solid using a 0.45 μm pore size filter. The minor elements in the original glass and the leachates of the glass and the glass-ceramic were analysed by inductively coupled plasma optical emission spectrometry (ICP-OES, Optima 3100×, PerkinElmer) and inductively coupled plasma mass spectrometry (ICP-MS, Elan 6000, PerkinElmer).

9.3 Results and discussion

The chemical composition of the sludge from WWTP El-Sadat City is similar to that of a basalt except for phosphorus and heavy metal contents, whose concentration exceed the permissible limit to be used as fertilizers. Sludge composition was reported (Garcia-Valles et al., 2013). The original glass is an aluminosilicate-based glass and its chemical composition is shown in Table 9.1.

Major components (wt %)									
SiO_2	Al_2O_3	Fe_2O_3	CaO	MgO	K_2O	Na_2O	P_2O_5	TiO_2	MnO
48.45	21.82	9.60	11.26	1.29	1.59	3.62	1.38	0.94	0.05

Table 9.1. Chemical composition of the original glass.

9.3.3 Determination of nucleation rates and growth temperatures

DTA investigations on the original glass samples were carried out to determine the temperature ranges of nucleation and crystal growth. These parameters are needed to optimize glass-ceramic manufacture (Xu et al., 1991). The glass transition temperature obtained by dilatometry is 659 ºC (Garcia-Valles et al., 2013). The temperatures of maximum nucleation rate of the glass are the temperatures of the maxima of the curve representing $1000/T_{ex}$ as a function of T_N [Eq. 1]. The curve in Figure 9.1 shows two peaks corresponding to maximum nucleation rate temperatures of two different crystalline phases: magnetite (Fe_3O_4) and plagioclase (Na [Si_3AlO_8] - Ca [$Si_2Al_2O_8$]). Magnetite nucleation starts at 500 ºC (point 1) and reaches its maximum nucleation rate at 600 ºC (point 2). Plagioclase nucleation starts below 650 ºC (point 3) and the maximum nucleation rate occurs at 775 ºC (point 4).

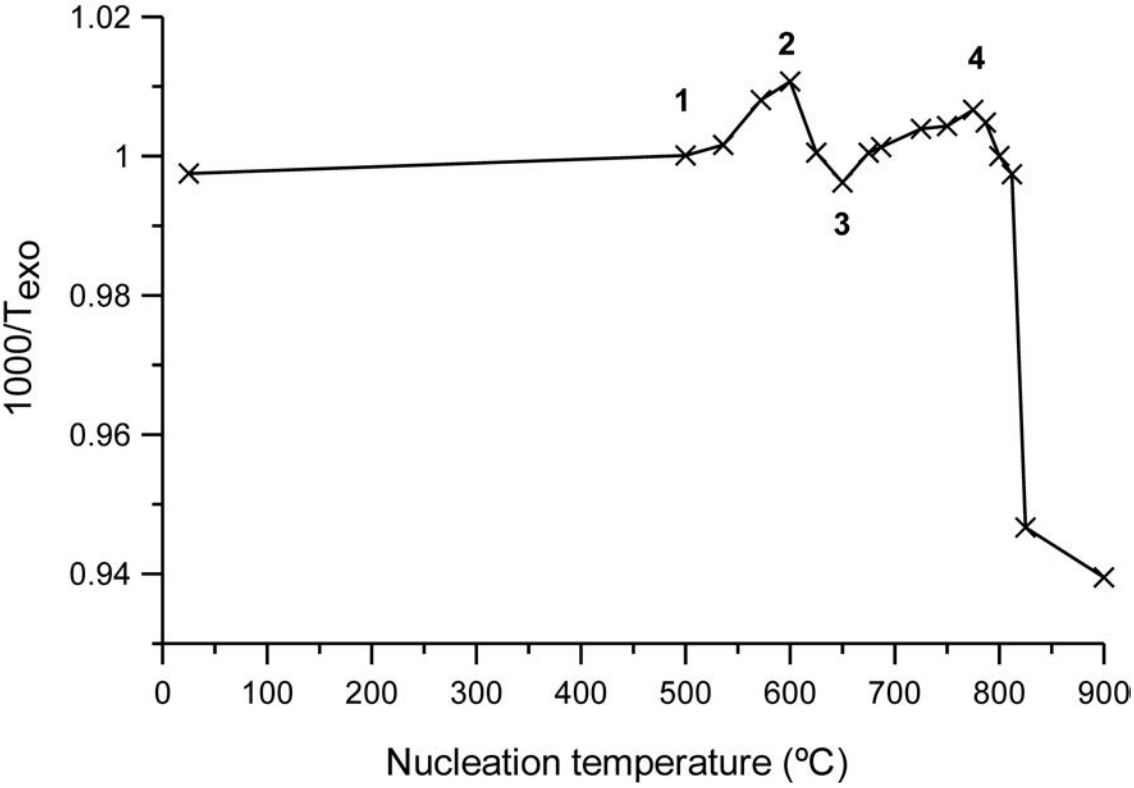

Figure 9.1. Inverse of T_{exo} as a function of T_N. The peaks in the plot correspond to nucleation ranges and its maxima to the temperature of maximum rate of nucleation of each phase.

The Raman spectra of thermally treated glasses at temperatures from 575 to 750 ºC are presented in Figure 9.2. The presence and growth of a band at ~ 675 cm^{-1} with rising temperature shows the progressive ordering during crystallization of the magnetite structure (Shebanova and Lazor, 2003; Wang et al., 1999). The envelope centred at 950 cm^{-1} can be linked to vibrations on the silicate network, dominated in particular by $Si\text{-}O^-$ stretching in structural units with two non-bridging oxygens for tetrahedron (NBO/Si = 2, Q^2) (Neuville, 2006). As temperature increases, the magnetite band becomes progressively more intense than the silicate band.

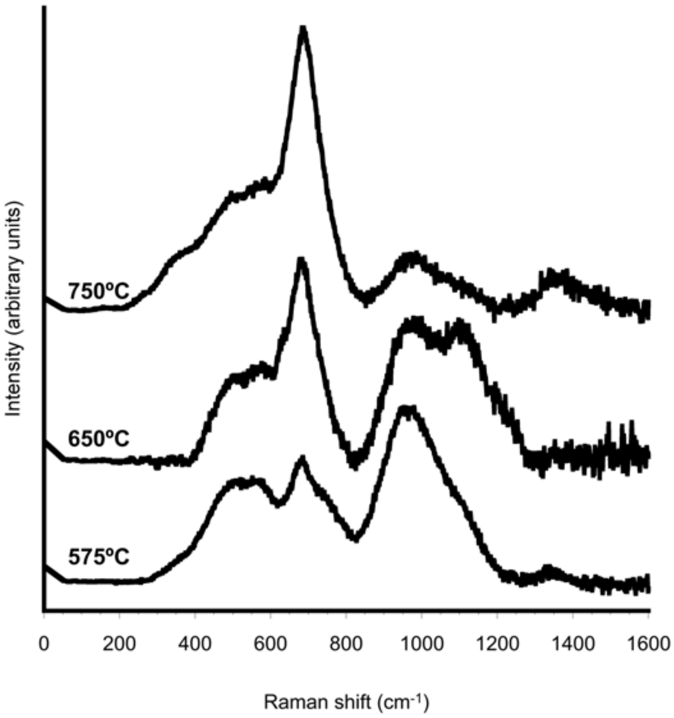

Figure 9.2. Unpolarized Raman spectra at room temperature of glasses previously treated at 575, 675 and 750 ºC.

Figure 9.3 shows evidence of the devitrification sequence of the glass recorded in HT-XRD spectra and enables the determination of the newly formed crystalline phases. Only two phases with different thermal behaviour are formed during heating in the temperature range from 200 to 1000 ºC. The first observed mineral is magnetite and the second, and most abundant, phase is plagioclase. Magnetite starts growing below 700 ºC whereas plagioclase (An_{48}) growth begins at 850 ºC.

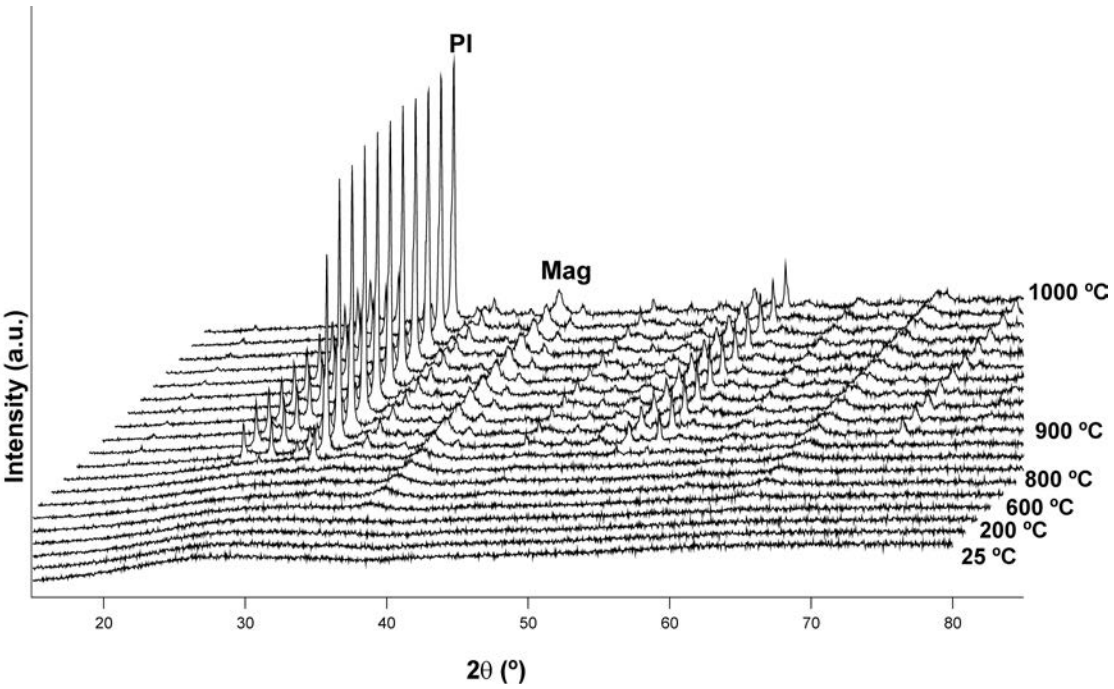

Figure 9.3. HT-XRD patterns of glass evolution between 200-1000 ºC show magnetite (Mag) and plagioclase (Pl) crystallizing during the thermal treatment.

The evolution of the two phases during the formation of the glass-ceramic is established by analysing the intensity of peak d_{311} of magnetite and d_{040} of plagioclase in HT-XRD patterns (Figure 9.3). The sizes of coherent crystals of the two phases are calculated with Scherrer's equation [Eq. 2] (Figure 9.3). In the case of magnetite (Figure 9.4A) the curve shows the induction period, with a rising gradient from below 700 ºC up to 875 ºC; over this temperature the gradient becomes constant while reaching the stable growth zone until the completion of the treatment at 1000 ºC. The average diameters of magnetite crystals are 11 nm at 750 ºC and 13 nm at 800 ºC. The steady growth of magnetite is due to the standard vacuum conditions in the HT-XRD chamber that prevent its oxidation, hence enabling the increase of crystallinity when the sample is heated. Plagioclase (Figure 9.4B) begins its induction period at temperatures below 850 ºC and reaches up to 875 ºC, where the coherent crystals grow from 50 to 60 nm. Its stable growth period ranges from 875 ºC to 925 ºC. The maximum peak intensity is at 910 ºC, followed by a slight decrease and stabilization. The maximum size of coherent plagioclase crystals is 250 nm. The maximum intensity of plagioclase diffraction at 910 ºC is around the same order of magnitude of the temperatures is 960 – 970 ºC, similar to the temperatures reported by Tunali and co-workers (Tunali et al., 2015) for the crystallization of anorthite in ceramic glazes in the CaO-Al_2O_3-SiO_2 system doped with Na_2O and K_2O. This composition is similar to basalt apart from FeO and TiO_2, which in the present study are emplaced in the magnetite structure. The obtained lower temperature can be related to a higher percentage of albite in the plagioclase of this study.

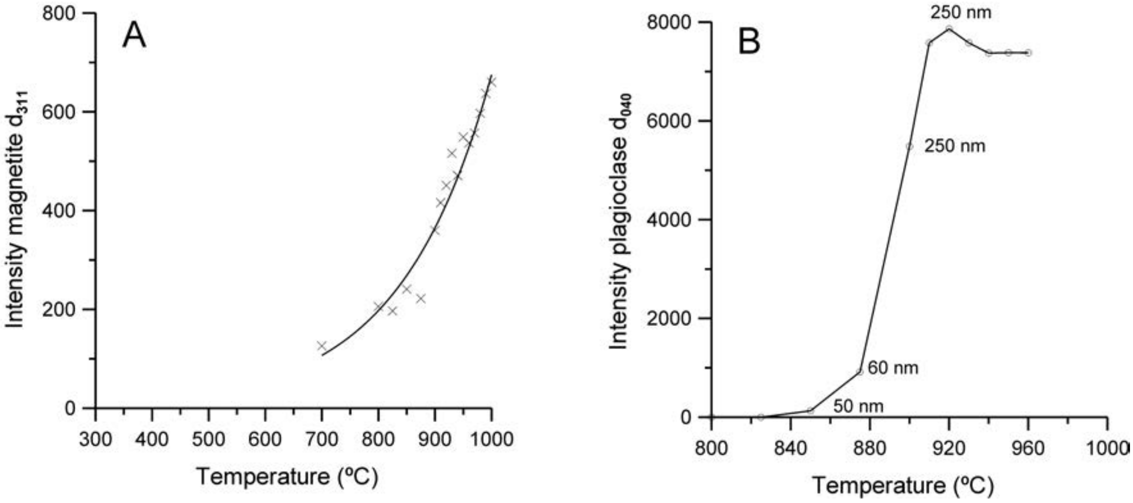

Figure 9.4. Growth diagrams for magnetite (A) and plagioclase (B) determined from the intensity of peak d_{311} of magnetite and d_{040} of plagioclase in HT-XRD patterns.

9.3.4 Microstructural characterization of the thermally treated glasses

Dark cubic crystals of magnetite observed in TEM (Figure 9.5) have a bimodal size distribution; type one includes crystals with maximum length between 10 and 15 nm (Figure 9.5A), which is in good agreement with the calculations using Scherrer's equation [Eq. 2] and type two crystals, which are approximately 125 nm long (Figure 9.5B). Magnetite is included in a lighter matrix formed by plagioclase nuclei (Figure 9.5A). The chemical analysis of magnetite crystals shows mainly iron oxide with a small traces of Cu TEM-EDS; and the matrix composition consists mainly of Si, Al and Ca, with a small content of Na. Electron microscopy observation at TEM corroborates the evolution of the mineral phases previously determined by XRD.

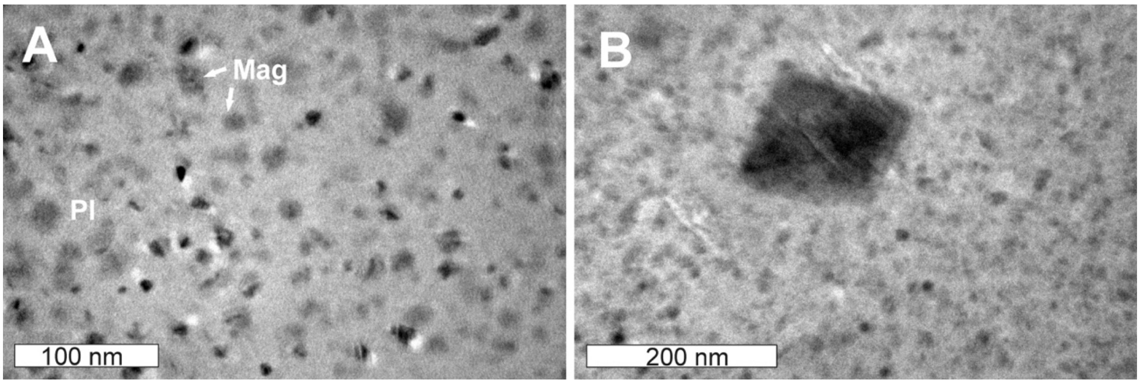

Figure 9.5. TEM micrograph: (A) Magnetite small crystals (10 – 15 nm) embedded in a plagioclase matrix; (B) Large magnetite crystal (approx. 125 nm) mixed with small magnetite crystals and plagioclase nuclei.

In SEM texture observations of the sample treated at 800 ºC (Figure 9.6), magnetite has a spherical shape with diameters between 40 and 80 nm. These crystal sizes are not coherent with XRD or TEM results; hence, they correspond to crystalline aggregates instead of single spherical nuclei of single crystals. Figure 9.6 shows these magnetite aggregates (A) surrounded by plagioclase nuclei (B).

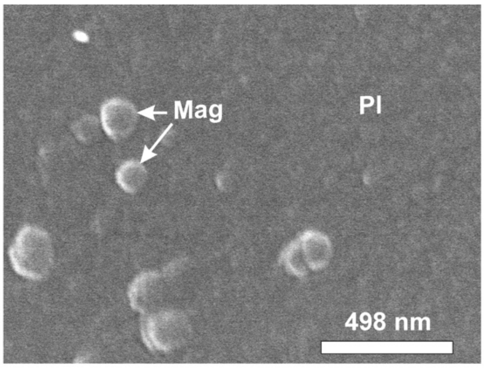

Figure 9.6. SEM micrograph of the original glass treated at 800 ºC during 2 hours. Mag, magnetite, Pl, plagioclase.

After determining magnetite and plagioclase T_N, heat treatments are performed using the DTA furnace as treatment cell to establish the growth process of plagioclase. Small glass samples (approx. 125 mg) were heated at 15 ºC/min at the start of plagioclase nucleation period at 675 ºC. Afterwards, the glass was heated from 850 to 925 ºC (one sample every 25 ºC), corresponding to the interval of linear growth of plagioclase, during 3 hours. Each sample was heated afterwards up to 1100ºC at 15 ºC/min to finish growth.

Representative SEM micrographs of the evolution of original glass during thermal treatment are assembled in Figure 9.7. The boundaries between plagioclase and magnetite are polygonal, due to magnetite not being able to enter the aluminosilicate lattice during the growth of plagioclase crystals. Magnetite is the first formed phase, as it precedes plagioclase growth and the formation of the reticular texture. The size of plagioclase polygons is between 10-30 µm, independently of the treatment temperature, because plagioclase crystals grow around previous magnetite crystals. As the first part of the treatment (heating up to 675 ºC) is the same for all the samples, the number of magnetite and plagioclase crystals is similar in all of them.

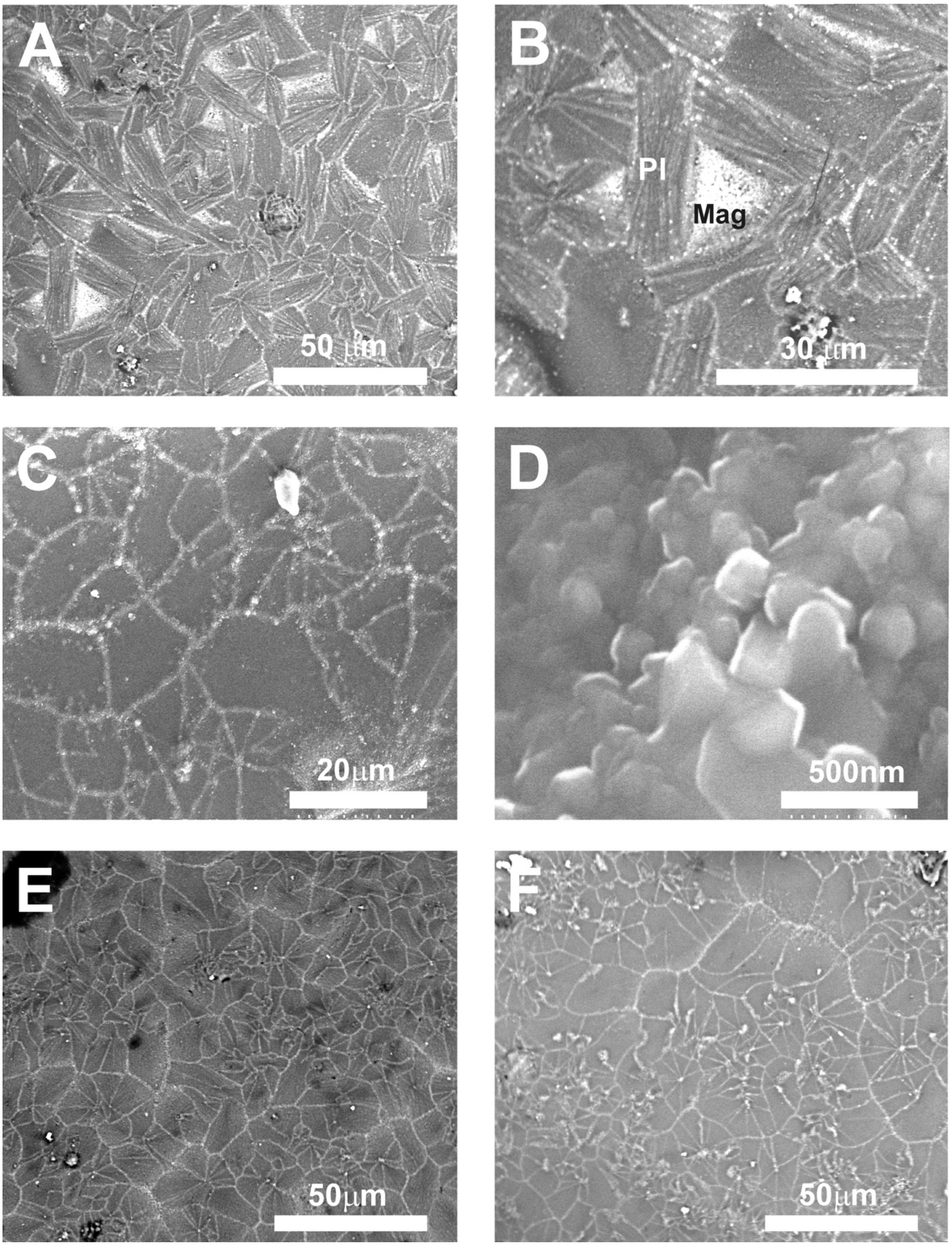

Figure 9.7. SEM images of crystallized glasses with different thermal histories (all images are in backscattering mode except D). A) General texture of glass-ceramic treated at 675 ºC. B) Detail corresponding to the crystal growth of plagioclase and the expulsion of magnetite crystals that are unable to enter the network. C) Sample treated at 850 ºC, plagioclase intergrowth with magnetite parallel to the faces of the growing crystals. D)

Morphologies of magnetite crystals at a plagioclase grain border in the sample treated at 850 ºC. E) Polygonal plagioclase texture from glass treated at 875 ºC; magnetite crystals are located in at plagioclase grain borders. F) Sample treated at 925 ºC.

The magnetite crystals form an intergrowth parallel to the longitudinal border of the polygonal texture. This fact is best viewed in the sample treated at 675° C (Figure 9.7A and Figure 9.7B) because this isothermal treatment temperature is more favourable to magnetite growth than to the crystallization of plagioclase (Figure 9.4B). In exchange, plagioclase is better ordered and more crystalline at temperatures between 850 and 925 ºC (Figure 9.7C, Figure 9.7D, Figure 9.7E and Figure 9.7F) because they lie in the steady to stable plagioclase growth range (Figure 9.4B). In these conditions its ability to expel magnetite to the grain edges is higher. At 850 ºC plagioclase crystals have a maximum length of 150 nm (Figure 9.7C), whereas at 925 ºC they reach approximately 250 nm (Figure 9.7F). Figure 9.7D is an enlargement of Figure 9.7C showing equidimensional, isometric crystals of magnetite. These sizes are in good agreement with the calculations using the Scherrer's equation [Eq. 2].

9.3.5 Glass-ceramic production

According to the previously exposed results, the process to obtain the final glass-ceramic consists in heating the glass at 15 ºC/min during the whole experiment and includes two isothermal stages. The first isothermal step at 600 ºC during 4 h corresponds to the temperature of maximum nucleation rate of magnetite. The second isothermal stage at 775 ºC during 3 h corresponds to both the temperature of maximum nucleation rate of plagioclase and the stable growth stage of magnetite. The final stage consisted in heating the material up to 1100 ºC and a 4h isothermal step to favour crystalline growth.

The Rietveld refinement of the XRD profile (Figure 9.8) confirms that plagioclase (An_{48}) is the main mineral in the glass-ceramic material (90.08 (± 1.22) wt%) whereas the abundance of magnetite is 9.92 (± 0.23) wt%. Concerning its crystallinity, the baseline of the pattern is flat in the raw spectra, thus accounting for low amorphous contents (if any).

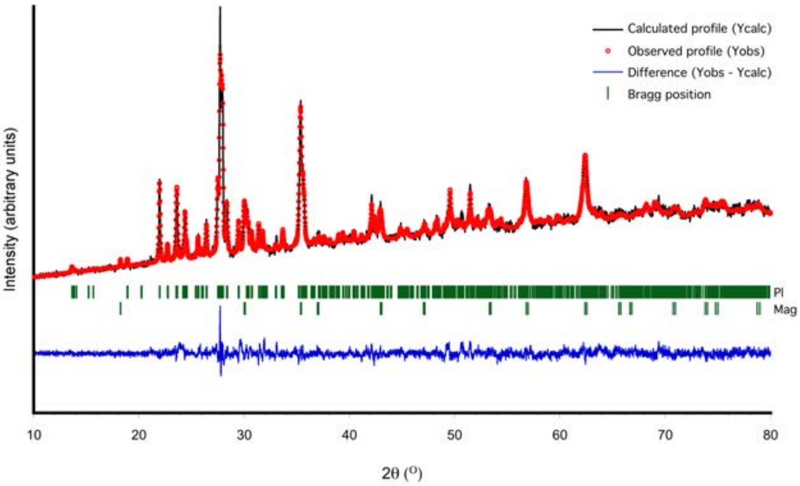

Figure 9.8. Rietveld refinement of the XRD spectrum of the glass-ceramic shows the crystallization of the two phases: magnetite and plagioclase.

The SEM micrographs of the fracture surface of the glass-ceramic show the intergrowth of plagioclase and magnetite (Figure 9). Plagioclase, the main phase, is present in the form of large aggregates (>100μm) as shown in Figure 9A. The smallest magnetite crystals (<0.5 μm) are prefentially located at the edges of plagioclase, whereas larger magnetites (maximum length of 2.6 μm) are dispersed (Figure 9B). A certain porosity is also present. There is no evidence of the existence of an amorphous phase, in good agreement with XRD results.

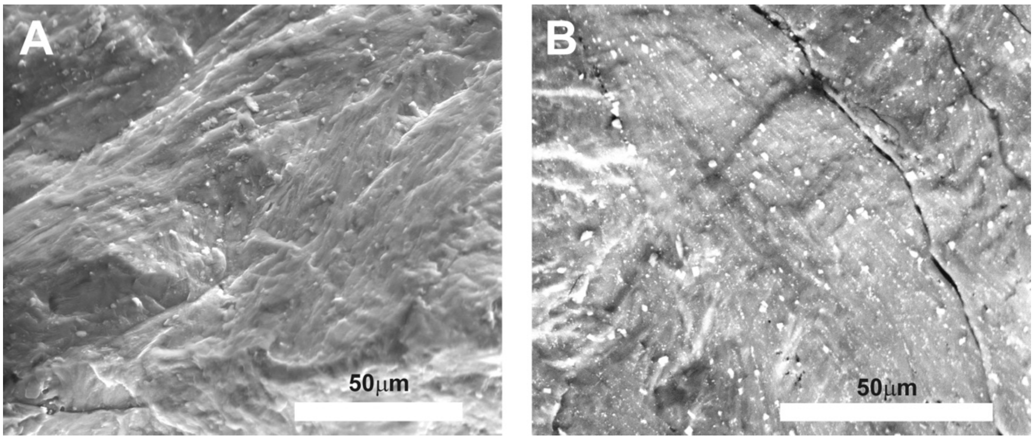

Figure 9.9. Fracture surface of the glass-ceramic as seen on SEM. (A) Plagioclase aggregates can be observed in secondary electron image and (B) magnetite is more evident in backscattered electron image (light colour).

9.3.6 Leachability

The analysis of the leachates (Table 9.2) shows that the contaminant cations are immobilized in both the glass and the glass-ceramic structure because the concentrations of potentially toxic elements in the liquids are either much lower than in the original glass (Zn, Cr, Ni, Pb, Cd) or directly below the detection limit of the ICP-MS equipment (As, Hg). According to these results, both the glass and the glass-ceramic materials comply with the requirements stated in DIN 38414-S4 (DIN-38414S4, 1984) for storage in landfills for inert wastes, as leaching is below the limits established by the norm for all the elements.

Elements	Original glass [mg L^{-1}]	Glass leachate [µg L^{-1}]	Glass-ceramic leachate [µg L^{-1}]	DIN 38414-S4 [µg L^{-1}]	Detection limits [µg L^{-1}]*
As	BDL	BDL	BDL	500	5
Cd	BDL	1.3	BDL	40	0.5
Cu	656	243.4	17.07	2000	5
Cr (total)	611	144.9	BDL	500	10
Hg	BDL	BDL	BDL	100	1
Ni	215	23.1	BDL	400	2.5
Pb	879	243.3	BDL	500	1
Zn	9001	2651.0	58.13	4000	5

*Table 9.2. Concentrations of potentially toxic elements in the original glass, the glass and glass-ceramic leachates, maximum allowed limits according to German standard [26] and detection limits of the ICP-MS equipment. BDL stands for below detection limit. *Refers to detection limits for liquids.*

9.4 Conclusions

Glass-ceramic derived from original glass obtained using silicate sewage sludge containing dangerous concentrations of potentially toxic elements from a WWTP at El-Sadat City is an environmentally friendly new product.

The treatment of the original glass to make a glass-ceramic consists in heating the glass at 15 ºC while observing two nucleation steps. The first lasts 4 h at 600 ºC and correspond to the nucleation temperature of magnetite. The second has a duration of 3 h at 775 ºC for 3h to ensure plagioclase maximal nucleation. Finally, the crystalline growth of the two phases is achieved by heating the material up to 1100 ºC during 4 h.

The data obtained in this research show that the potentially toxic elements contained in the sludge are effectively stabilized and bound in the structure of the minerals formed during the thermal treatment. Plagioclase (90 wt%) and magnetite (10 wt%) are the only mineral phases formed during the thermal treatment. The presence of magnetite is especially interesting because the spinel structure is able to lodge potentially toxic elements such as Zn and Cr. The lower concentrations of potentially toxic elements in the leachate of the glass-ceramic show that they are better stabilized in the newly formed phases than in the glass.

9.5 Future perspectives - Outlook

The fact that the obtained materials can be considered inert opens the possibility of using sewage sludge as a raw material in the production of glasses and glass-ceramics with a commercial value. The dark-coloured glasses and glass-ceramics might be suitable as industrial pavements and wall tiles; the glass-ceramic may substitute slate in roofs.

CHAPTER 10 General discussion

I Don’t Want to Belong to Any Club That Will Accept Me as a Member

Groucho Marx

This thesis proposes the inertization of sewage sludge by vitrification. The research group in which the thesis has been carried out had already published some papers on the vitrification of sewage sludge and industrial waste (Garcia-Valles et al., 2013, 2011, 2007; Martinez, 1995; Pérez et al., 1998, 1996a, 1996b). However, most of the literature focuses on the vitrification of the ashes that result from the incineration of sewage sludge as explained in chapter 2. Ashes are indeed easier to vitrify specially due to their lack of water but have the inconvenient of going through the incineration process with all the implications explained in the introduction. The general focus of most published research is on studying single example wastes or discrete mixtures of wastes. This accumulative knowledge is of extreme importance but leaves a gap for a systematic study of the effect of the variation of composition that is the reason for choosing an approach based on modifying the composition of a basalt to progressively approach that of sewage sludge.

Vitrification has been proven as an effective inertization technique using the leaching tests. The mixtures between basalt and either P, Ca or both comply with the legal limits of the concentrations of PTE in the leachates; hence, the elements are adequately bound in the glass structure. This opens two possibilities: although the initial proposal is to inertize sewage sludge by itself, it could also be mixed with either with basalt or with toxic wastes such as foundry sand and carbonate waste to get closer to the “basalt-like” composition. A significant amount of sewage sludge can be added to basalt and still obtain a material in the high end of at least microhardness, which is promising towards finding potential applications for the glasses and glass-ceramics in the building industry – such as wall tiles or pavement.

The presence of nanolites – nano-oxides of magnetite or other Fe-Ti oxides – has a strong influence in several of the glasses properties. Firstly, it conditions the deformation and viscosity at temperatures as low as Tg, and facilitates the fast crystallization of the glasses at generally low temperatures. Indeed, in some cases the crystallization events seem to start either right at the end of the glass transition or even to overlap it, which may explain both the sometimes contradictory trends in the evolution of Tg and the lack of consistency in the differences between the DTA and the dilatometric Tg – as the difference between them varies from about 20 ºC to more than 100 ºC (Table 10.1). In second place, the nucleation is likely to improve the microhardness of the glasses as crystalline phases are harder than the corresponding amorphous phases of the same composition. Finally, the pervasiveness of the nanolites gives rise to the homogeneous fine microstructure of the glass-ceramics. This microstructure is essential in improving the microhardness of the glasses (Holand and Beall, 2012). The

It is interesting to obtain a composition in the stability field of pyroxene, which is capable of isolating heavy metals in its structure (Morse, 1980).

	wt%	Density (g/cm^3)	Microhardness (GPa)	DTA Tg (ºC)	Tg dil (ºC)
B0	none	2.844	7.663	674	629
B2P	2.55	2.836	7.131	673	638
B4P	4.54	2.832	6.963	661	638
B8P	8.52	2.81	6.556	685	643
B16P	16.47	2.749	6.276	-	643
B32P	32.38	2.636	5.408	-	650
B1Ca	10.58	2.871	7.280	677	637
B2Ca	11.73	2.880	7.112	689	634
B4Ca	13.44	2.902	7.084	688	639
B8Ca	16.52	2.932	7.228	666	637
B16Ca	24.44	2.969	8.194	695	645
GC16Ca	-	-	8.6	-	-
B24Ca	28.84	2.976	8.676	712	651
B32Ca	36.56	-	7.088	-	-
M14Ca	14.04	2.867	7.190	698	620
M23Ca	22.10	2.934	7.244	687	636
M30Ca	30.21	2.979	7.347	684	654
M1Ba	1.27	2.936	7.865	691	654
M5Ba	6.01	3.001	8.905	688	656
M10Ba	12.37	3.084	7.748	692	648
M01Cr	0.12	2.869	7.576	688	625
M1Cr	1	2.914	7.848	687	642
M5Cr	5	2.928	7.986	698	658
M15Cr	15	3.018	6.914-12.950	705	664
M1Cu	1.06	2.950	6.885	682	604
M5Cu	5.23	3.006	7.378	683	575
M05Ni	0.46	2.884	7.763	672	645
M1Ni	1.02	2.897	7.459	679	647
M15Ni	10.91	3.023	7.898	702	667
M1Zn	1.16	2.946	8.186	697	652
M5Zn	5.72	3.023	8.128	670	639
M10Zn	11.24	3.102	7.213	658	604

Table 10.1. Summary of the glass properties: density, microhardness, DTA Tg and dilatometric Tg.

All the glasses made from mixtures including basalt crystallize into a least a certain amount of diopside, apart from other minerals, due to the high concentrations of Mg. However, the waste glasses from SS-like compositions reported in the literature and the case example of the vitrification and glass-ceramic processing of Egyptian sewage sludge have a different output, with the crystallization of minerals such as anorthite, wollastonite, augite, akermanite, donanthite, and gehlenite (Table 10.2). Of these, only augite might host heavy metals, as the others are Na-Ca bearing (alumino)silicates that have a much less flexible lattice.

In the case example of the ninth chapter, the glass-ceramic processing on vitrified sewage sludge yields a plagioclase-magnetite-bearing glass-ceramic. Although the inertization process is effective, the mineralogical composition is not optimal interest for further inertization of potentially toxic elements, as they can enter the structure of the spinel-like phase but not the structure of plagioclase. The crystallization of plagioclase is due to the high concentration of aluminum used as a precipitant in wastewater processing. This highlights a limitation of the vitrification technique: it is essential to standardize the wastewater treatment, including the additives of choice, to get a chance of obtaining a feed of raw materials of limited variability for glass production.

The choice of microhardness as the mechanical property to be measured was based mostly in it being an easily available technique at the laboratory scale. However, a more appropriate way to determine the applicability of the materials in construction would be measuring the resistance to abrasion. Even so, it can be assumed that the hardest materials will have a higher resistance to abrasion. The glasses of this study are in the high end of microhardness values reported in the literature due to their location on the diopside or melilite stability field (Table 10.2).

	Main crystalline phase	Density (g/cm^3)	Microhardness (GPa)	Reference
SS fly ash	Glass	2.83	4.59	(Park et al., 2003)
SS fly ash	Di	2.87	6.23	
SS fly ash	An	2.93	5.86	
SS	Wo, An		6.12-6.54	(Tian et al., 2011)
SS	Wo, An		6.28	
Silceram, iron blast-furnace slag	Di	2.90	7	(Carter et al., 1988)
Peat ash, steel paint slag, clay	n/r	3.04	n/r	(Cimdins et al., 2000)
Vitrified filter dust from waste incinerators	Di	2.89	7.9	(Romero et al., 2000)
Vitrified mixture of 75% MSW incinerator fly ash + 20% SiO_2	Di	2.78	6.73	(Park and Heo, 2002)
10% steel dust and 90% incinerator fly ash	A, Ak, donanthite	3.20	8.5	(Cheng and Chiu, 2003)
100% incinerator fly ash	Gh	2.07	nr	(Cheng et al., 2002)
50% mine tailing + 20% fly ash + Fe_2O_3 + CaF_2	Di	3.00	7.17	(Baowei et al., 2013)
Canary Island basalt glasses			5.16-6.28	(De Vicente Mingarro, 1992)
Canary Island basalt glass-ceramics	Px, Pl, Fe-Ti oxides		6.62-8.66	(De Vicente Mingarro, 1992)
Basalt glass		2.95	7.7	(Jensen et al., 2009)
Basalt glass+crystal mixtures	Di		6.8-8.9	(Jensen et al., 2009)
Holyoke basalt glass			8.9	(El-Shennawi et al., 1999)

Table 10.2. Summary of the properties of selected waste and basalt glasses from the literature.

The incorporation of the heavy metals to the glassy matrix gives extremely variable results in solubility and crystallization. Their solubility increases in the following order: Cr<Ni<Cu<Zn<Ba. The position of Ni in this list is somewhat tentative, as it causes more observable nucleation than Cu at 1 wt%, but none of them cause crystalline XRD reflections. The other elements are ordered according to the wt% of the concentration where there are observable reflections in their XRD profiles.

Ba, as an alkaline earth, is more affine to the silicate matrix. This results in its higher solubility – it is the only element that does not cause crystallization at the highest concentration

– in spite of its large atomic radius. It is likely that the depolymerized network of the matrix is flexible enough to accommodate the Ba ions. Its close link to the silicate network is also shown by the crystallization of celsian at high temperature. In exchange, all the other minerals are transition metals and tend to crystallize in the form of spinel-like oxides. Zn has the second better solubility due to its similarities in charge and ionic radius to Mg^{2+} – whose ionic radius is 0.72 Å (Shannon et al., 1976) – hence it may well occupy the same positions. Although Zn -doped glasses crystallizes into a spinel group mineral upon heating, it is not the specific Zn-spinel gahnite, signaling that a significant amount of Zn may easily remain in the glass. At the studied concentrations, Cu does not form a spinel but shows the Raman signature attributed to nanocrystalline Cu^0. Hence, it is likely that its solubility is not much higher than 5 wt% CuO. Upon a thermal treatment it forms the Cu-spinel phase tenorite, signaling a partitioning in favor of the solid phase. Ni is assumed to have the second lowest solubility due to its tendency to cause nucleation and to the almost complete disappearance of the NBO region in the Raman spectra when trevorite crystallizes. Its interaction with the network might be limited. Finally, Cr has the lowest solubility mainly because it crystallizes into large chromite crystals at concentrations as low as 5 wt%, whereas Ni only crystallized into small dendritic crystals during the quenching of the glass bearing 15 wt% NiO. The suggested trend for the increase solubility follows the same order of the increase of the ionic radii of the elements considering that they were in 6-fold coordination in the glasses (Table 10.3).

Element (coordination)	**Ionic radius (Å)**
Ba^{2+} (6)	1.35
Cr^{3+}(6)	0.62
Cu^{2+} (4)	0.57
Cu^{2+} (6)	0.73
Ni^{2+} (6)	0.69
Zn^{2+} (4)	0.60
Zn^{2+} (6)	0.74

Table 10.3. Ionic radii of the heavy metals of this study (Shannon et al., 1976).

As they are not engaged in the crystallization processes of the aluminosilicates, the addition of transition metals does not change the position of the bulk composition of each glass in the CMAS diagram. Hence, the rest of the glass crystallizes according to the proportions of CaO-MgO-Al_2O_3-SiO_2. However, the PTE are still influencing the macroscopic properties such as viscosity or density.

CHAPTER 11 Conclusions

O Captain! my Captain! our fearful trip is done,

The ship has weather’d every rack, the prize we sought is won,

The port is near, the bells I hear, the people all exulting,

Walt Whitman, Leaves of Grass

The work presented in this PhD thesis focused on the simulation of the vitrification of sewage sludge using a basalt doped with P and Ca. A further step in the inertization of toxic waste is taken by proposing the inertization of different heavy metals to the glass – Ba, Cr, Cd, Ni, Zn – and studying their solubility, and their effect on the glass structure, macroscopic properties and chemical resistance. Potentially toxic elements are ubiquitous in anthropic processes and as such may enter the water systems upon leaching and present a potential danger to human and biosystems health’s.

Basaltic liquids only accept low amounts of P before the onset of an immiscibility that causes the formation of coexisting phosphate and silicate phases. The phosphate phase eventually crystallizes during quenching causing an increase in the viscosity of the melt and forming a glass-ceramics (stanfieldite + amorphous silicate phase). The crystallization of the phosphate also improves the microhardness of the material and likely minimizes the effects of leaching. Stanfieldite has been found to have Mössbauer parameters similar to those of the alluaudite group.

Ca has a higher solubility than P due to its alkaline earth nature; at low concentrations it plays the role of a network modifier. However, upon changing from the stability field of diopside to that of melilite the nucleation of the glass during quenching increases due to the rising of the melting temperature. This effect improves the microhardness of the glasses but ends up causing the crystallization of merwinite.

The combination of the addition of P_2O_5 and CaO to basalt causes a depolymerization of the structure and a sharper differentiation of the Q^n groups. Increasing the concentration of Ca seems to increase the nucleation – due to the transition from the stability field of pyroxene to that of melilite – during quenching, resulting in strengthened glasses. The thermal treatment of the glasses resulted in the crystallization of akermanite, pyroxene, magnetite and minor nepheline. A mostly pyroxene-bearing glass-ceramics was obtained after a treatment at the nucleation and growth temperatures. The nuclei of magnetite promoted the crystallization of diopside and ended up integrating its crystalline lattice.

The glass-ceramic processing on a case example of vitrified sewage sludge yields a plagioclase-magnetite-bearing glass-ceramic. Although this material achieves the inertization process of sewage sludge by itself, the mineralogical composition is not ideal for further inertization of potentially toxic elements, as they can enter the structure of the spinel-like phase but not the structure of plagioclase.

The solubility of the potentially toxic elements is quite low due to most of them being transition metals. Apart from Ba – which is an alkaline earth, none of them dissolves into the glass in the studied concentrations above 5 wt% Zn seems to have a lower affinity for the spinel-like phase than the other transition metals.

In general, studied compositions have good fusibility and low viscosity at temperatures between 1300-1450 ºC. However, all the studied glasses are pervasively nucleated during quenching as a consequence of the high Fe concentration. This nucleation facilitates the crystallization of the glasses and obtaining a fine-grained microstructure in the glass-ceramics. Morever, the presence of nuclei makes the glasses harder. In all the studied cases, the glass-ceramic process yields a fine-grained material based that contain mostly diopside grains. All the studied materials comply with the leaching limits to be considered inert.

FUTURE PERSPECTIVES

In light of the results presented in this thesis, there are some directions in which the research may be furthered. Concerning the mechanical properties of the glasses, it would be interesting to repeat the microhardness measurements in a microdurometer equipped with a Knoop microindenter because its shape is more appropriate for brittle materials than the Vickers microindenter. The determination of other properties such as flexural and compressive strength or the resistance to abrasion might offer a more precise picture of the applicability of the sewage sludge-like glasses.

Another study that may offer some insight on both the structure and the crystallization of the glasses would be working in simplified systems. Combining the existent literature on Ca-Mg and Fe aluminosilicates, it may be interesting to study the formation of glass in the SiO_2-

Al_2O_3-CaO-MgO-Fe_2O_3-P_2O_5 system and then further this research by adding PTEs representing toxic wastes one at a time. Although this composition is already quite complex, its structure is likely to be easier to interpret in the Raman spectra and the crystallization process will imply a smaller amount of mineral phases.

References

Achiba, W. Ben, Lakhdar, A., Gabteni, N., Laing, G. Du, Verloo, M., Boeckx, P., Van Cleemput, O., Jedidi, N., Gallali, T., 2010. Accumulation and fractionation of trace metals in a Tunisian calcareous soil amended with farmyard manure and municipal solid waste compost. J. Hazard. Mater. 176, 99–108. https://doi.org/10.1016/j.jhazmat.2009.11.004

Agarwal, G., Speyer, R.F., 1991. Devitrification hardening of cupola slag glass with CaO and SiO_2 additions. J. Non. Cryst. Solids 135, 95–104. https://doi.org/10.1016/0022-3093(91)90409-Y

Agència de Residus de Catalunya, 2018. Estadístiques de residus municipals.

Al Sayed, M.H., Madany, I.M., Buali, A.R.M., 1995. Use of sewage sludge ash in asphaltic paving mixes in hot regions. Constr. Build. Mater. 9, 19–23. https://doi.org/10.1016/0950-0618(95)92856-C

Albiach, R., Canet, R., Pomares, F., Ingelmo, F., 2001. Organic matter components, aggregate stability and biological activity in a horticultural soil fertilized with different rates of two sewage sludges during ten years. Bioresour. Technol. 77, 109–114. https://doi.org/10.1016/S0960-8524(00)00166-8

Alfonso, P., 1985. Mineralogía y aptitudes vitrocerámicas de materiales magmáticos neógenos de Cataluña.

Alfonso, P., Castro, D., Garcia-Valles, M., Tarrago, M., Tomasa, O., Martinez, S., 2016. Recycling of tailings from the Barruecopardo tungsten deposit for the production of glass. J. Therm. Anal. Calorim. https://doi.org/10.1007/s10973-016-5332-y

Ando, J., 1958. Phase Diagrams of $Ca_3(PO_4)_2$-Mg_3 $(PO_4)_2$ and $Ca_3(PO_4)_2$-$CaNaPO_4$. Bull. Chem. Soc. Jpn. 31, 201–205.

Andreola, F., Barbieri, L., Lancellotti, I., Martín, M.I., Rincòn, J.M., Romero, M., 2016. Thermal approach to evaluate the sintering-crystallization ability in a nepheline-forsterite-based glass-ceramics. J. Therm. Anal. Calorim. 123, 241–248. https://doi.org/10.1007/s10973-015-4960-y

Angelidis, M., Gibbs, R.J., 1989. Chemistry of metals in anaerobically treated sludges. Water R 23, 29–33.

Ansari, M.I., Malik, A., 2010. Seasonal variation of different microorganisms with nickel and cadmium in the industrial wastewater and agricultural soils. Environ. Monit. Assess. 167, 151–163. https://doi.org/10.1007/s10661-009-1038-y

Araña, V., Aparicio, A., Escorza, C.M., Cacho, L.G., Ortiz, R., Vaquer, R., Barberi, F., Ferrara, G., Albert, J., Gaissot, X., 1983. El volcanismo neógeno-cuaternario de Catalunya: caracteres estructurales, petrológicos y geodinámicos. Acta Geol. Hisp. 18, 1–17.

Arancibia, J.R.H., Alfonso, P., García-Valles, M., Martínez, S., Parcerisa, D., Canet, C., Romero, F.M., 2013. Obtención de vidrio a partir de residuos de la minería del estaño en Bolivia. Bol. la Soc. Esp. Ceram. y Vidr. 52, 143–150. https://doi.org/10.3989/cyv.192013

Asuvathraman, R., Joseph, K., Raja Madhavan, R., Sudha, R., Krishna Prabhu, R., Govindan Kutty, K. V., 2015. A versatile monazite-IPG glass-ceramic waste form with simulated HLW: Synthesis and characterization. J. Eur. Ceram. Soc. 35, 4233–4239. https://doi.org/10.1016/j.jeurceramsoc.2015.07.025

Baowei, L., Leibo, D., Xuefeng, Z., Xiaolin, J., 2013. Structure and performance of glass-ceramics obtained by Bayan Obo tailing and fly ash. J. Non. Cryst. Solids 380, 103–108. https://doi.org/10.1016/j.jnoncrysol.2013.09.012

Barbieri, L., Corradi Bonamartini, A., Lancellotti, I., 2000. Alkaline and alkaline-earth silicate glasses and glass-ceramics from municipal and industrial wastes. J. Eur. Ceram. Soc. 20, 2477–2483. https://doi.org/10.1016/S0955-2219(00)00124-2

Barbieri, L., Karamanov, A., Corradi, A., Lancellotti, I., Pelino, M., Rincon, J.M., 2008. Structure, chemical durability and crystallization behavior of incinerator-based glassy systems. J. Non. Cryst. Solids 354, 521–528. https://doi.org/10.1016/j.jnoncrysol.2007.07.080

Barker, T.C., 1977. The Glassmakers: Pilkington 1826-1976. Weidenfled & Nicholson, London.

Beall, G.H., Rittler, H.L., 1976. BASALT GLASS CERAMICS. Am. Ceram. Soc. Bull.

Bell, R.J., Bird, N.F., Dean, P., 1968. The vibrational spectra of vitreous silica, germania and beryllium fluoride. J. Phys. C Solid State Phys. 1, 299–303. https://doi.org/10.1088/0022-3719/1/2/304

Bell, R.J., Dean, P., 1972. Localization of phonons in vitreous silica and related glasses. Int. Conf. Phys. Non-Crystalline Solids 22, 375–382.

Bernardo, E., Dal Maschio, R., 2011. Glass-ceramics from vitrified sewage sludge pyrolysis residues and recycled glasses. Waste Manag. 31, 2245–2252. https://doi.org/10.1016/j.wasman.2011.06.018

Bhatnagar, V.M., 1969. The melting point of synthetic apatites. Mineral. Mag. 37, 288.

Bhatty, J.I., Reid, K.J., 1989. Compressive strength of municipal sludge ash mortars. ACI Mater. J. 86, 394–400.

Bień, J., Celary, P., Morzyk, B., Sobik-Szołtysek, J., Wystalska, K., 2013. Effect of additives on heavy metal immobilization during vitrification of tannery sewage sludge. Environ. Prot. Eng. 39, 33–40. https://doi.org/10.5277/EPE130204

Bingham, P.A., Hand, R.J., 2006. Vitrification of toxic wastes: a brief review. Adv. Appl. Ceram. 105, 21–31. https://doi.org/doi:10.1179/174367606X81687

Bingham, P.A., Hand, R.J., Hannant, O.M., Forder, S.D., Kilcoyne, S.H., 2009. Effects of modifier additions on the thermal properties, chemical durability, oxidation state and structure of iron phosphate glasses. J. Non. Cryst. Solids 355, 1526–1538. https://doi.org/10.1016/j.jnoncrysol.2009.03.008

Binhussain, M.A., Marangoni, M., Bernardo, E., Colombo, P., 2014. Sintered and glazed glass-ceramics from natural and waste raw materials. Ceram. Int. 40, 3543–3551. https://doi.org/10.1016/j.ceramint.2013.09.074

Biscoe, J., Warren, B.E., 1938. X-Ray Diffraction Study of Soda-Boric Oxide Glass. J. Am. Ceram. Soc. 21, 287–293. https://doi.org/10.1111/j.1151-2916.1938.tb15777.x

Borowski, G., 2015. Using vitrification for sewage sludge combustion ash disposal. Polish J. Environ. Stud. 24, 1889–1896. https://doi.org/10.15244/pjoes/36080

Borowski, G., 2013. Application of Vitrification Method for the Disposal of Municipal Sewage Sludge.

Borowski, S., Domański, J., Weatherley, L., 2014. Anaerobic co-digestion of swine and poultry manure with municipal sewage sludge. Waste Manag. 34, 513–521. https://doi.org/10.1016/j.wasman.2013.10.022

Brow, R.K., 2000. Review: the structure of simple phosphate glasses. J. Non. Cryst. Solids 263, 1–28. https://doi.org/10.1016/S0022-3093(99)00620-1

Burkhard, D.J.M., 2001. Crystallization and oxidation of Kilauea basalt glass: Processes during reheating experiments. J. Petrol. 42, 507–527 ST–Crystallization and oxidation of Kil. https://doi.org/10.1093/petrology/42.3.507

Calas, G., Cormier, L., Galoisy, L., Ramos, A., Rossano, S., 1997. Chemical bonding and structural ordering of cations in silicate glasses 51–58.

Cao, J.P., Shi, P., Zhao, X.Y., Wei, X.Y., Takarada, T., 2014. Catalytic reforming of volatiles and nitrogen compounds from sewage sludge pyrolysis to clean hydrogen and synthetic gas over a nickel catalyst. Fuel Process. Technol. 123, 34–40. https://doi.org/10.1016/j.fuproc.2014.01.042

Cao, Y., Pawłowski, A., 2012. Sewage sludge-to-energy approaches based on anaerobic digestion and pyrolysis: Brief overview and energy efficiency assessment. Renew. Sustain. Energy Rev. 16, 1657–1665. https://doi.org/10.1016/j.rser.2011.12.014

Careghini, A., Dastoli, S., Ferrari, G., Saponaro, S., Bonomo, L., De Propris, L., Gabellini, M., 2010. Sequential solidification/stabilization and thermal process under vacuum for the treatment of mercury in sediments. J. Soils Sediments 10, 1646–1656. https://doi.org/10.1007/s11368-010-0290-7

Carter, S., Ponton, C.B., Rawlings, R.D., Rogers, P.S., 1988. Microstructure, chemistry, elastic properties and internal friction of Silceram glass-ceramics. J. Mater. Sci. 23, 2622–2630. https://doi.org/10.1007/BF01111924

Celis, J., Sandoval, M., Barra, R., 2008. Plant Response to Salmon Wastes and Sewage Sludge Used as Organic Fertilizer on Two Degraded Soils Under Greenhouse Conditions. Chil. J. Agric. Res. 68, 274–284. https://doi.org/10.4067/S0718-58392008000300007

Cetin, S., Marangoni, M., Bernardo, E., 2015. Lightweight glass-ceramic tiles from the sintering of mining tailings. Ceram. Int. 41, 5294–5300. https://doi.org/10.1016/j.ceramint.2014.12.049

Chazhengina, S.Y., Rybnikova, Z.P., Svetov, S.A., 2016. Scanning electron microscopy and Raman spectroscopy as combined methods for studying zoning in minerals: The case of spinels from Archean komatiites. Geol. Ore Depos. 58, 628–635. https://doi.org/10.1134/S1075701516080067

Cheng, T.W., 2004. Effect of additional materials on the properties of glass-ceramic produced from incinerator fly ashes. Chemosphere 56, 127–131. https://doi.org/10.1016/j.chemosphere.2004.02.009

Cheng, T.W., Chiu, J.P., 2003. Fire-resistant geopolymer produce by granulated blast furnace slag. Miner. Eng. 16, 205–210. https://doi.org/10.1016/S0892-6875(03)00008-6

Cheng, T.W., Ueng, T.H., Chen, Y.S., Chiu, J.P., 2002. Production of glass-ceramic from incinerator fly ash. Ceram. Int. 28, 779–783. https://doi.org/10.1016/S0272-8842(02)00043-3

Chinnam, R.K., Francis, A.A., Will, J., Bernardo, E., Boccaccini, A.R., 2013. Review. Functional glasses and glass-ceramics derived from iron rich waste and combination of industrial residues. J. Non. Cryst. Solids 365, 63–74. https://doi.org/10.1016/j.jnoncrysol.2012.12.006

Cicconi, M.R., De Ligny, D., Gallo, T.M., Neuville, D.R., 2016. Ca neighbors from XANES spectroscopy: A tool to investigate structure, redox, and nucleation processes in silicate glasses, melts, and crystals. Am. Mineral. 101. https://doi.org/10.2138/am-2016-5663

Cicconi, M.R., Neuville, D.R., Tannou, I., Baudelet, F., Floury, P., Paris, E., Giuli, G., 2015. Letter. Competition between two redox states in silicate melts: An in-situ experiment at the Fe K-edge and Eu L_3-edge. Am. Mineral. 100, 1013–1016. https://doi.org/10.2138/am-2015-5172

Ciecińska, M., Stoch, P., Stoch, A., Nocuń, M., 2015. Thermal properties of 60P2O5-20Fe2O3-20Al2O3 glass for salt waste immobilization. J. Therm. Anal. Calorim. 121, 1225–1232. https://doi.org/10.1007/s10973-015-4586-0

Cieślik, B.M., Namieśnik, J., Konieczka, P., 2015. Review of sewage sludge management: Standards, regulations and analytical methods. J. Clean. Prod. 90, 1–15. https://doi.org/10.1016/j.jclepro.2014.11.031

Cimdins, R., Rozenstrauha, I., Berzina, L., Bossert, J., Bücker, M., 2000. Glassceramics obtained from industrial waste. Resour. Conserv. Recycl. 29, 285–290. https://doi.org/10.1016/S0921-3449(00)00053-7

Cochain, B., Neuville, D.R., Henderson, G.S., McCammon, C.A., Pinet, O., Richet, P., 2012. Effects of the iron content and redox state on the structure of sodium borosilicate glasses: A Raman, Mössbauer and boron k-edge xanes spectroscopy study. J. Am. Ceram. Soc. 95, 962–971. https://doi.org/10.1111/j.1551-2916.2011.05020.x

Colomban, P., Schreiber, H.D., 2005. Raman signature modification induced by copper nanoparticles in silicate glass. J. Raman Spectrosc. 36, 884–890. https://doi.org/10.1002/jrs.1379

Colombo, P., Brusatin, G., Bernardo, E., Scarinci, G., 2003. Inertization and reuse of waste materials by vitrification and fabrication of glass-based products. Curr. Opin. Solid State Mater. Sci. 7, 225–239. https://doi.org/10.1016/j.cossms.2003.08.002

Correll, D.L., 1998. The Role of Phosphorus in the Eutrophication of Receiving Waters: A Review. J. Environ. Qual. 27, 261. https://doi.org/10.2134/jeq1998.00472425002700020004x

Costa, M., Klein, C.B., 2006. Toxicity and carcinogenicity of chromium compounds in humans. Crit. Rev. Toxicol. 36, 155–163. https://doi.org/10.1080/10408440600932003

Coté, B., Massiot, D., Taulelle, F., Coutures, J.P., 1992. 27Al NMR spectroscopy of aluminosilicate melts and glasses. Chem. Geol. 96, 367–370. https://doi.org/10.1016/0009-2541(92)90065-D

Council Directive, 1999. Council Directive 1999/31/EC on the landfill. Off. J. Eur. Communities L182/1-19. https://doi.org/10.1039/ap9842100196

Council of the European Union, 2003/33/EC, 2003. Council Decision establishing criteria and procedures for the acceptance of waste at landfills pursuant to Article 16 of and Annex II to Directive 1999/31/EC. Off. J. Eur. Communities 27–49.

Davis, R.D., 1996. The impact of EU and UK environmental pressures on the future of sludge treatment and disposal. Water Environ. J. 10, 65–69. https://doi.org/10.1111/j.1747-6593.1996.tb00010.x

Davydov, V.I., Burdinskii, V.P., Dobrygin, P.G., Luchnikov, N.V., Kostin, V.V., Filippov, S.N., Kolupaeva, T.I., 1996. Equipment for vitrification of nuclear power plant wastes in a direct-heating ceramic furnace. At. Energy 80, 219–221.

Dayan, A.D., Paine, A.J., 2001. Mechanisms of chromium toxicity, carcinogenicity and allergenicity: Review of the literature from 1985 to 2000. Hum. Exp. Toxicol. 20, 439–451. https://doi.org/10.1191/096032701682693062

De Sousa Meneses, D., Malki, M., Echegut, P., 2006. Optical and structural properties of calcium silicate glasses. J. Non. Cryst. Solids 352, 5301–5308. https://doi.org/10.1016/j.jnoncrysol.2006.08.022

De Vicente Mingarro, I., 1992. Estudio de los mecanismos de nucleación y cristalización en vidrios obtenidos a partir de rocas basálticas canarias. PhD Thesis.

De Vicente Mingarro, I., Callejas, P., Rincon, J.M., 1991. Microestructura y microanálisis de fases minerales cristalizadas en vidrios obtenidos a partir de rocas basálticas. Bol. la Soc. Esp. Mineral. 14, 95–105.

Deer, W.A., Howie, R.A., Zussman, J., 1992. An introduction to the rock-forming minerals, 2nd ed. Longman.

Di Genova, D., Morgavi, D., Hess, K.-U., Neuville, D.R., Borovkov, N., Perugini, D., Dingwell, D.B., 2015. Approximate chemical analysis of volcanic glasses using Raman spectroscopy. J. Raman Spectrosc. 46, 1235–1244. https://doi.org/10.1002/jrs.4751

DIN-38414S4, 1984. Deutsche Einheitsverfahren zur Wasser, Abwasserund Schlammuntersuchung, Bestimmung der Eluierbarkeit von Wasser (S4).

Dingwell, D.B., Knoche, R., Webb, S.L., 1993. The effect of P_2O_5 on the viscosity of haplogranitic liquid . Eur. J. Miner. 5, 133–140.

Domínguez, A., Fernández, Y., Fidalgo, B., Pis, J.J., Menéndez, J.A., 2008. Bio-syngas production with low concentrations of $CO_2$and CH_4 from microwave-induced pyrolysis of wet and dried sewage sludge. Chemosphere 70, 397–403. https://doi.org/10.1016/j.chemosphere.2007.06.075

Dominguez, A., Menendez, J.A., Inguanzo, M., Pis, J.J., 2006. Production of bio-fuels by high temperature pyrolysis of sewage sludge using conventional and microwave heating. Bioresour. Technol. 97, 1185–1193. https://doi.org/10.1016/j.biortech.2005.05.011

Donald, I.W., Metcalfe, B.L., Taylor, R.N.J., 1997. Review The immobilization of high level radioactive wastes using ceramics and glasses. J. Mater. Sci. 32, 5851–5887. https://doi.org/10.1023/A:1018646507438

Dupree, R., Holland, D., Mortuza, M.G., Collins, J.A., Lockyer, M.W.G., 1989. Magic angle spinning NMR of alkali phospho-alumino-silicate glasses. J. Non. Cryst. Solids 112, 111–119. https://doi.org/10.1016/0022-3093(89)90504-8

Dyar, M.D., Jawin, E.R., Breves, E., Marchand, G., Nelms, M., Lane, M.D., Mertzman, S.A., Bish, D.L., Bishop, J.L., 2014. Mössbauer parameters of iron in Phosphate minerals: Implications for interpretation of martian data. Am. Mineral. 99, 914–942. https://doi.org/10.2138/am.2014.4701

Eastmond, D.A., MacGregor, J.T., Slesinski, R.S., 2008. Trivalent chromium: Assessing the genotoxic risk of an essential trace element and widely used human and animal nutritional supplement. Crit. Rev. Toxicol. 38, 173–190. https://doi.org/10.1080/10408440701845401

EEC, 2017. Sewage sludge production and disposal, in: Eurostat Statistical Books. Brussels.

EEC Council, 1998. Commission Directive 98/15/EC of 27 February 1998 amending Council Directive 91/271/EEC with respect to certain requirements established in Annex 1. Dir. 98/15/EC 41, 29–30. https://doi.org/http://eur-lex.europa.eu/legal-content/EN/TXT/?uri=celex:31998L0015

EEC Council, 1991. 91/271/EEC of 21 May 1991 concerning urban waste-water treatment. EEC Counc. Dir. 10. https://doi.org/http://eur-lex.europa.eu/legal-content/en/ALL/?uri=CELEX:31991L0271

El-Shennawi, A.W.A., Mandour, M.A., Morsi, M.M., Abdel-Hameed, S.A.M., 1999. Monopyroxenic basalt-based glass-ceramics. J. Am. Ceram. Soc. 82, 1181–1186. https://doi.org/10.1111/j.1151-2916.1999.tb01893.x

Endo, H., Nagayoshi, Y., 1997. Production of glass ceramics from sewage sludge. Water Sci. Technol. 36, 235–241.

EPA, 1994. Land Application of Sewage Sludge. Fed. Regist.

Erol, M., Küçükbayrak, S., Ersoy-Meriçboyu, A., 2007. Production of glass-ceramics obtained from industrial wastes by means of controlled nucleation and crystallization. Chem. Eng. J. 132, 335–343. https://doi.org/10.1016/j.cej.2007.01.029

European Comission, 2014. Towards a circular economy: A zero waste programme for Europe. European Comission.

European Council, 1986. Directive 86/278/EEC of the European Council on the protection of the environment, and in particular of soil, when sewage sludge is used in agriculture. Off. J. Eur. Communities. L Ser. L 269, 1–13. https://doi.org/2004R0726 - v.7 of 05.06.2013

Evans, A.G., Wilshaw, T.R., 1976. Quasi-static solid particle damage in brittle solids-I. Observations analysis and implications. Acta Metall. 24, 939–956. https://doi.org/10.1016/0001-6160(76)90042-0

Fernandez Navarro, J.M., 1991. El vidrio. Consejo Superior de Investigaciones Científicas.

Ferreiro-Domínguez, N., Rigueiro-Rodríguez, A., Bianchetto, E., Mosquera-Losada, M.R., 2014. Effect of lime and sewage sludge fertilisation on tree and understory interaction in a silvopastoral system. Agric. Ecosyst. Environ. 188, 72–79. https://doi.org/10.1016/j.agee.2014.02.007

Flügel, A., 2007. Glass properties [WWW Document]. URL www.glassproperties.com (accessed 4.19.18).

Folgueras, M.B., Díaz, R.M., Xiberta, J., Prieto, I., 2003. Thermogravimetric analysis of the co-combustion of coal and sewage sludge. Fuel 82, 2051–2055. https://doi.org/10.1016/S0016-2361(03)00161-3

Font, R., Fullana, A., Conesa, J.A., Llavador, F., 2001. Analysis of the pyrolysis and combustion of different sewage sludges by TG. J. Anal. Appl. Pyrolysis 58–59, 927–941. https://doi.org/10.1016/S0165-2370(00)00146-7

Fonts, I., Gea, G., Azuara, M., Ábrego, J., Arauzo, J., 2012. Sewage sludge pyrolysis for liquid production: A review. Renew. Sustain. Energy Rev. 16, 2781–2805. https://doi.org/10.1016/j.rser.2012.02.070

Forsberg, L.S., Ledin, S., 2006. Effects of sewage sludge on pH and plant availability of metals in oxidising sulphide mine tailings. Sci. Total Environ. 358, 21–35. https://doi.org/10.1016/j.scitotenv.2005.05.038

Franus, M., Barnat-Hunek, D., Wdowin, M., 2016. Utilization of sewage sludge in the manufacture of lightweight aggregate. Environ. Monit. Assess. 188, 1–13. https://doi.org/10.1007/s10661-015-5010-8

Fredericci, C., Zanotto, E.D., Ziemath, E.C., 2000. Crystallization mechanism and properties of a blast furnace slag glass. J. Non. Cryst. Solids 273, 64–75. https://doi.org/10.1016/S0022-3093(00)00145-9

Furukawa, T., Fox, K.E., White, W.B., 2011. intensities and structural units in sodium silicate glasses Raman spectroscopic investigation of the structure of silicate glasses . III . Raman intensities and structural units in sodium silicate glasses 8) 3226. https://doi.org/10.1063/1.442472

Fytili, D., Zabaniotou, A., 2008. Utilization of sewage sludge in EU application of old and new methods-A review. Renew. Sustain. Energy Rev. 12, 116–140. https://doi.org/10.1016/j.rser.2006.05.014

Gan, H., Hess, P.C., 1992. Phosphate speciation in potassium aluminosilicate glasses. Am. Mineral. 77, 495–506.

Garcia-Valles, M., Aly, M.H., El-Fadaly, E., Hafez, H.S., Nogues, J.M., Martinez, S., 2011. Producción de materiales vitrocerámicos obtenidos a partir de lodos procedentes de una estación de depuración de aguas residuales urbanas en la Ciudad de El-Sadat (Egipto). Bol. la Soc. Esp. Ceram. y Vidr. 50, 219–228.

Garcia-Valles, M., Avila, G., Martinez, S., Terradas, R., Nogues, J.M., 2007. Heavy metal-rich wastes sequester in mineral phases through a glass-ceramic process. Chemosphere 68, 1946–1953. https://doi.org/10.1016/j.chemosphere.2007.02.034

Garcia-Valles, M., Hafez, H.S., Cruz-Matias, I., Verges, E., Aly, M.H., Nogues, J., Ayala, D., Martinez, S., 2013. Calculation of viscosity-temperature curves for glass obtained from four wastewater treatment plants in Egypt. J. Therm. Anal. Calorim. 111, 107–114. https://doi.org/10.1007/s10973-012-2232-7

Gin, S., Abdelouas, A., Criscenti, L.J., Ebert, W.L., Ferrand, K., Geisler, T., Harrison, M.T., Inagaki, Y., Mitsui, S., Mueller, K.T., Marra, J.C., Pantano, C.G., Pierce, E.M., Ryan, J. V., Schofield, J.M., Steefel, C.I., Vienna, J.D., 2013. An international initiative on long-term behavior of high-level nuclear waste glass. Mater. Today 16, 243–248. https://doi.org/10.1016/j.mattod.2013.06.008

Goldschmidt, V., 1926. Geochemische Verteilungsgesetze der Elemente. 6. Skr. utg. av det Nor. Videnskaps-akademi i Oslo 1.

Gong, M., Zhu, W., Xu, Z.R., Zhang, H.W., Yang, H.P., 2014. Influence of sludge properties on the direct gasification of dewatered sewage sludge in supercritical water. Renew. Energy 66, 605–611. https://doi.org/10.1016/j.renene.2014.01.006

Greaves, G.N., 1985. EXAFS and the structure of glass. J. Non. Cryst. Solids 71, 203–217.

https://doi.org/10.1016/0022-3093(85)90289-3

Greaves, G.N., Fontaine, A., Lagarde, P., Raoux, D., Gurman, S.J., D., R., Gurman, S.J., 1981. Local structure of silicate glasses. Nature 293, 611–616. https://doi.org/10.1038/293611a0

Grigiante, M., Ischia, M., Baratieri, M., Maschio, R.D., Ragazzi, M., 2010. Pyrolysis analysis and solid residue stabilization of polymers, waste tyres, spruce sawdust and sewage sludge. Waste and Biomass Valorization 1, 381–393. https://doi.org/10.1007/s12649-010-9038-2

Guillemet, T.A., Maesen, P., Delcarte, E., Lognay, G.C., Gillet, A., Claustriaux, J.J., Culot, M., 2009. Factors influencing microbiological and chemical composition of South-Belgian raw sludge. Biotechnol. Agron. Soc. Environ. 13, 249–255.

Gupta, R., Garg, V.K., 2008. Stabilization of primary sewage sludge during vermicomposting. J. Hazard. Mater. 153, 1023–1030. https://doi.org/10.1016/j.jhazmat.2007.09.055

Hall, J., 2014. Ecological and economical balance for sludge management options. Eur. Com. 89. https://doi.org/10.1016/j.resconrec.2016.01.007

Hannant, O.M., Bingham, P. a., Hand, R.J., Forder, S., 2008. The structural properties of iron in vitrified toxic waste ashes. Glas. Technol. J. Glas. Sci. Technol. Part a 49, 27–32.

Hannant, O.M., Forder, S.D., Bingham, P.A., Hand, R.J., 2009. Structural studies of iron in vitrified toxic wastes. Hyperfine Interact. 192, 37–42. https://doi.org/10.1007/s10751-009-9944-5

Haugsten, K.E., Gustavson, B., 2000. Environmental properties of vitrified fly ash from hazardous and municipal waste incineration. Waste Manag. 20, 167–176. https://doi.org/10.1016/S0956-053X(99)00325-6

He, M. miao, Tian, G. ming, Liang, X. qiang, 2009. Phytotoxicity and speciation of copper, zinc and lead during the aerobic composting of sewage sludge. J. Hazard. Mater. 163, 671–677. https://doi.org/10.1016/j.jhazmat.2008.07.013

Hehlen, B., Neuville, D.R., 2015. Raman response of network modifier cations in alumino-silicate glasses. J. Phys. Chem. B 119, 4093–4098. https://doi.org/10.1021/jp5116299

Hennet, L., Pozdnyakova, I., Bytchkov, A., Cristiglio, V., Palleau, P., Fischer, H.E., Cuello, G.J., Johnson, M., Melin, P., Zanghi, D., Brassamin, S., Brun, J.F., Price, D.L., Saboungi, M.L., 2006. Levitation apparatus for neutron diffraction investigations on high temperature liquids. Rev. Sci. Instrum. 77. https://doi.org/10.1063/1.2200756

Holand, W., Beall, G.H., 2012. Glass-ceramic Technology, Glass-Ceramic Technology.

https://doi.org/10.1002/9781118265987.fmatter

Hossain, M.K., Strezov, V., Nelson, P.F., 2009. Thermal characterisation of the products of wastewater sludge pyrolysis. J. Anal. Appl. Pyrolysis 85, 442–446. https://doi.org/10.1016/j.jaap.2008.09.010

Hrma, P., Riley, B.J., Crum, J. V., Matyas, J., 2014. The effect of high-level waste glass composition on spinel liquidus temperature. J. Non. Cryst. Solids 384, 32–40. https://doi.org/10.1016/j.jnoncrysol.2013.02.014

Hsiau, P.C., Lo, S.L., 1998. Extractabilities of heavy metals in chemically-fixed sewage sludges. J. Hazard. Mater. 58, 73–82. https://doi.org/10.1016/S0304-3894(97)00121-0

Huang, C., Behrman, E.C., 1991. Structure and properties of calcium aluminosilicate glasses. J. Non. Cryst. Solids 128, 310–321. https://doi.org/10.1016/0022-3093(91)90468-L

Huang, P.Y., Kurasch, S., Srivastava, A., Skakalova, V., Kotakoski, J., Krasheninnikov, A. V, Hovden, R., Mao, Q., Meyer, J.C., Smet, J., Muller, D.A., Kaiser, U., 2012. Direct Imaging of a Two-Dimensional Silica Glass on Graphene.pdf. Nano Lett. 12, 1081–1086. https://doi.org/dx.doi.org/10.1021/nl204423x |

Inglezakis, V.J., Zorpas, A.A., Karagiannidis, A., Samaras, P., Voukkali, I., Sklari, S., 2016. EUROPEAN UNION LEGISLATION ON SEWAGE SLUDGE MANAGEMENT 23, 635–639.

Inguanzo, M., Dominguez, A., Menendez, J.A., Blanco, C.G., Pis, J.J., 2002. On the Pyrolysis of Sewage Sludge: The Influence of Pyrolysis Temperature on Biochar, Liquid and Gas Fractions. J. Anal. Appl. Pyrolysis 63, 209–222. https://doi.org/10.4028/www.scientific.net/AMR.518-523.3412

Ischia, M., Maschio, R.D., Grigiante, M., Baratieri, M., 2011. Clay-sewage sludge co-pyrolysis. A TG-MS and Py-GC study on potential advantages afforded by the presence of clay in the pyrolysis of wastewater sewage sludge. Waste Manag. 31, 71–77. https://doi.org/10.1016/j.wasman.2010.05.027

Jensen, M., Smedskjaer, M.M., Estrup, M., Kristjansson, M., Lönnroth, N., Yue, Y.Z., 2009. Hardness of basaltic glass-ceramics. Glas. Technol. Eur. J. Glas. Sci. Technol. Part A 50, 189–195.

Jung, C.H., Matsuto, T., Tanaka, N., 2005. Behavior of metals in ash melting and gasification-melting of municipal solid waste (MSW). Waste Manag. 25, 301–310. https://doi.org/10.1016/j.wasman.2004.08.012

Kacprzak, M., Neczaj, E., Fijałkowski, K., Grobelak, A., Grosser, A., Worwag, M., Rorat, A., Brattebo, H., Almås, Å., Singh, B.R., 2017. Sewage sludge disposal strategies for sustainable development. Environ. Res. 156, 39–46. https://doi.org/10.1016/j.envres.2017.03.010

Kalampounias, A.G., Papatheodorou, G.N., Yannopoulos, S.N., 2003. Inelastic light scattering from xCaO-(1-x)SiO_2 glasses. J. Non. Cryst. Solids 322, 35–40. https://doi.org/10.1016/S0022-3093(03)00169-8

Kang, J., Wang, J., Cheng, J., Yuan, J., Hou, Y., Qian, S., 2017. Crystallization behavior and properties of CaO-MgO-Al2O3-SiO2 glass-ceramics synthesized from granite wastes. J. Non. Cryst. Solids 457, 111–115. https://doi.org/10.1016/j.jnoncrysol.2016.11.030

Karamanov, A., Gutzow, I., Penkov, I., Andreev, J., Bogdanov, B., 1994. Diopside marble-like sintered glass- ceramics. Glas. Berichte Glas. Sci. Technol. 67, 202–206.

Kavouras, P., Kaimakamis, G., Ioannidis, T.A., Kehagias, T., Komninou, P., Kokkou, S., Pavlidou, E., Antonopoulos, I., Sofoniou, M., Zouboulis, A., Hadjiantoniou, C.P., Nouet, G., Prakouras, A., Karakostas, T., 2003. Vitrification of lead-rich solid ashes from incineration of hazardous industrial wastes. Waste Manag. 23, 361–371. https://doi.org/10.1016/S0956-053X(02)00153-8

Khater, G.A., Abdel-Motelib, A., El Manawi, A.W., Abu Safiah, M.O., 2012. Glass-ceramics materials from basaltic rocks and some industrial waste. J. Non. Cryst. Solids 358, 1128–1134. https://doi.org/10.1016/j.jnoncrysol.2012.02.010

Kikuchi, R., 1998. Vitrification process for treatment of sewage sludge and incineration ash. J. Air Waste Manag. Assoc. 48, 1112–1115. https://doi.org/10.1080/10473289.1998.10463766

Kim, K.D., Lee, S.H., Ahn, H.K., 2004. Observation of nucleation effect on crystallization in lithium aluminosilicate glass by viscosity measurement. J. Non. Cryst. Solids 336, 195–201. https://doi.org/10.1016/j.jnoncrysol.2004.01.001

Kingery, W.D., 1960. Introduction to ceramics, Wiley series on the science and technology of materials. Wiley.

Kreidl, N.J., Weyl, W.A., 1941. Phosphates in Ceramic Ware: Iv, Phosphate Glasses. J. Am. Ceram. Soc. 24, 372–378. https://doi.org/10.1111/j.1151-2916.1941.tb15444.x

Król, D., Poskrobko, S., 2012. Waste and fuels from waste Part I. Analysis of thermal decomposition. J. Therm. Anal. Calorim. 109, 619–628. https://doi.org/10.1007/s10973-012-2397-0

Kunzmann, T., 1999. The aenigmatite-rhonite mineral group. Eur. J. Mineral. 11, 743–756.

Le Losq, C., Cicconi, M.R., Greaves, G.N., Neuville, D.R., 2018. Springer Handbook of Glass. Springer.

Le Losq, C., Neuville, D.R., Chen, W., Florian, P., Massiot, D., Zhou, Z., Greaves, G.N., 2017. Percolation channels: a universal idea to describe the atomic structure and dynamics of glasses and melts. Sci. Rep. 7, 16490. https://doi.org/10.1038/s41598-017-16741-3

Lebedev, A.A., 1921. Polymorphism and annealing of glass. Trans. Opt. Inst. 2, 1–21.

Levin, E.M., McMurdie, H.F., 1975. Phase diagrams for ceramists 1975 Supplement. The American Ceramic Society.

Li, L., Xu, Z.R., Zhang, C., Bao, J., Dai, X., 2012. Quantitative evaluation of heavy metals in solid residues from sub- and super-critical water gasification of sewage sludge. Bioresour. Technol. 121, 169–175. https://doi.org/10.1016/j.biortech.2012.06.084

Lin, D.F., Chang, W.C., Yuan, C., Luo, H.L., 2008. Production and characterization of glazed tiles containing incinerated sewage sludge. Waste Manag. 28, 502–508. https://doi.org/10.1016/j.wasman.2007.01.018

Lin, H.C., Foster, W.R., 1968. Studies in System Bao-Al2O3-Sio2. I. Polymorphism of Celsian. Am. Mineral. 53, 134–144.

Long, D.A., 1977. Raman spectroscopy. McGraw-Hill.

Lu, H., Shi, X., Costa, M., Huang, C., 2005. Carcinogenic effect of nickel compounds. Mol. Cell. Biochem. 279, 45–67. https://doi.org/10.1007/s11010-005-8215-2

Lundin, M., Olofsson, M., Pettersson, G.J., Zetterlund, H., 2004. Environmental and economic assessment of sewage sludge handling options. Resour. Conserv. Recycl. 41, 255–278. https://doi.org/10.1016/j.resconrec.2003.10.006

Magnien, V., Neuville, D.R., Cormier, L., Roux, J., Hazemann, J.L., de Ligny, D., Pascarelli, S., Vickridge, I., Pinet, O., Richet, P., 2008. Kinetics and mechanisms of iron redox reactions in silicate melts: The effects of temperature and alkali cations. Geochim. Cosmochim. Acta 72, 2157–2168. https://doi.org/10.1016/j.gca.2008.02.007

Magnien, V., Neuville, D.R., Cormier, L., Roux, J., Hazemann, J.L., Pinet, O., Richet, P., 2006. Kinetics of iron redox reactions in silicate liquids: A high-temperature X-ray absorption and Raman spectroscopy study. J. Nucl. Mater. 352, 190–195. https://doi.org/10.1016/j.jnucmat.2006.02.053

Majima, T., Tadao, K., Naruse, M., Hiraoka, M., 1978. Studies on Pyrolysis Process of Sewage Sludge, Eighth International Conference on Water Pollution Research. International Association on Water Pollution Research. https://doi.org/10.1016/B978-0-08-020902-9.50052-3

Marangoni, M., Secco, M., Parisatto, M., Artioli, G., Bernardo, E., Colombo, P., Altlasi, H., Binmajed, M., Binhussain, M., 2014. Cellular glass-ceramics from a self foaming mixture of glass and basalt scoria. J. Non. Cryst. Solids 403, 38–46. https://doi.org/10.1016/j.jnoncrysol.2014.06.016

Marinoni, N., D'Alessio, D., Diella, V., Pavese, A., Francescon, F., 2013. Effects of soda-lime-silica waste glass on mullite formation kinetics and micro-structures development in vitreous ceramics. J. Environ. Manage. 124, 100–107. https://doi.org/10.1016/j.jenvman.2013.02.048

Martinez, S., 1995. Reciclaje y tratamiento de residuos 30, 1–3.

Matson, D.W., Sharma, S.K., Philpotts, J.A., 1983. The structure of high-silica alkali-silicate glasses. A Raman spectroscopic investigation. J. Non. Cryst. Solids 58, 323–352. https://doi.org/10.1016/0022-3093(83)90032-7

McMillan, P.F., 1984a. Structural Studies of Silicate Glasses and Melts-Applications and Limitations of Raman Spectroscopy. Am. Mineral. 69, 622–644. https://doi.org/0003-004x/84/070E-0622$0

McMillan, P.F., 1984b. A Raman spectroscopic study of glasses in the system CaO-MgO-SiO2. Am. Mineral. 69, 645–659.

McMillan, P.F., Piriou, B., 1982. The structures and vibrational spectra of crystals and glasses in the silica-alumina system. J. Non. Cryst. Solids 53, 279–298. https://doi.org/10.1016/0022-3093(82)90086-2

McMillan, P.F., Piriou, B., 1975. Glass Ceramics. Academic Press.

Menéndez, J.A., Domínguez, A., Inguanzo, M., Pis, J.J., 2005. Microwave-induced drying, pyrolysis and gasification (MWDPG) of sewage sludge: Vitrification of the solid residue. J. Anal. Appl. Pyrolysis 74, 406–412. https://doi.org/10.1016/j.jaap.2004.10.013

Metcalf, Eddy, 1991. Wastewater engineering - treatment, disposal and reuse, 3rd Editio. ed. McGraw Hill, New York, USA.

Mininni, G., Blanch, A.R., Lucena, F., Berselli, S., 2015. EU policy on sewage sludge utilization and perspectives on new approaches of sludge management. Environ. Sci. Pollut. Res. 22, 7361–7374. https://doi.org/10.1007/s11356-014-3132-0

Mininni, G., Sbrilli, A., Guerriero, E., Rotatori, M., 2004. Dioxins and furans formation in pilot incineration tests of sewage sludge spiked with organic chlorine. Chemosphere 54, 1337–1350. https://doi.org/10.1016/S0045-6535(03)00252-2

Monshi, A., Foroughi, M.R., Monshi, M.R., 2012. Modified Scherrer Equation to Estimate More

Accurately Nano-Crystallite Size Using XRD. World J. Nano Sci. Eng. 2, 154–160. https://doi.org/10.4236/wjnse.2012.23020

Monteiro, S.N., Alexandre, J., Margem, J.I., Sánchez, R., Vieira, C.M.F., 2008. Incorporation of sludge waste from water treatment plant into red ceramic. Constr. Build. Mater. 22, 1281–1287. https://doi.org/10.1016/j.conbuildmat.2007.01.013

Montero, M.A., Jordán, M.M., Hernández-Crespo, M.S., Sanfeliu, T., 2009. The use of sewage sludge and marble residues in the manufacture of ceramic tile bodies. Appl. Clay Sci. 46, 404–408. https://doi.org/10.1016/j.clay.2009.10.013

Monzó, J., Payá, J., Borrachero, M. V., Peris-Mora, E., 1999. Mechanical behavior of mortars containing sewage sludge ash (SSA) and Portland cements with different tricalcium aluminate content. Cem. Concr. Res. 29, 87–94. https://doi.org/10.1016/S0008-8846(98)00177-X

Morse, S.A., 1980. Basalts and phase diagrams : an introduction to the quantitative use of phase diagrams in igneous petrology. Springer, New York.

Mymrin, V., Ribeiro, R.A.C., Alekseev, K., Zelinskaya, E., Tolmacheva, N., Catai, R., 2014. Environment friendly ceramics from hazardous industrial wastes. Ceram. Int. 40, 9427–9437. https://doi.org/10.1016/j.ceramint.2014.02.014

Mysen, B.O., 2003. Physics and chemistry of silicate glasses and melts. Eur. J. Mineral. 15, 781–802.

Mysen, B.O., 1992. Iron and phosphorus in calcium silicate quenched melts. Chem. Geol. 98, 175–202. https://doi.org/10.1016/0009-2541(92)90184-7

Mysen, B.O., Frantz, J.D., 1992. Raman spectroscopy of silicate melts at magmatic temperatures: Na_2O-SiO_2 , K_2O-SiO_2 and Li_2O-SiO_2 binary compositions in the temperature range 25-1475° C. Chem. Geol. 96, 321–332. https://doi.org/10.1016/0009-2541(92)90062-A

Mysen, B.O., Holtz, F., Pichavant, M., Beny, J.M., Montel, J.M., 1999. The effect of temperature and bulk composition on the solution mechanism of phosphorus in peraluminous haplogranitic magma. Am. Mineral. 84, 1336–1345. https://doi.org/10.2138/am-1999-0910

Mysen, B.O., Richet, P., 2005. Silicate Melts: Properties and Structure, 1st ed. Elsevier B.V.

Mysen, B.O., Ryerson, F.J., Virgo, D., 1981. The structural role of phosphorus in silicate melts. Am. Mineral. 66, 106–117. https://doi.org/0003-w4x/ 8 | /0 I 02-0 I 06$02.00

Mysen, B.O., Toplis, M.J., 2007. Structural behavior of Al^{3+} in peralkaline, metaluminous, and peraluminous silicate melts and glasses at ambient pressure. Am. Mineral. 92, 933–946.

https://doi.org/10.2138/am.2007.2334

Mysen, B.O., Virgo, D., Harrison, W.J., Scarfe, C.M., 1980. Solubility mechanisms of H_2O in silicate melts at high pressures and temperatures: a Raman spectroscopic study: discussion. Am. Mineral. 65, 900–914.

Mysen, B.O., Virgo, D., Scarfe, C.M., 1980. Relations between anionic structure and viscosity of silicate melts - A Raman spectroscopic study. Am. Mineral. 65, 690–710.

Navarro, A., Cardellach, E., Cañadas, I., Rodríguez, J., 2013. Solar thermal vitrification of mining contaminated soils. Int. J. Miner. Process. 119, 65–74. https://doi.org/10.1016/j.minpro.2012.12.002

Neuville, D.R., 2006. Viscosity, structure and mixing in (Ca, Na) silicate melts. Chem. Geol. 229, 28–41. https://doi.org/10.1016/j.chemgeo.2006.01.008

Neuville, D.R., Cormier, L., Caurant, D., Montagne, L., 2013. Du verre au cristal : Nucléation, croissance et démixtion, de la recherche aux applications, EDP Scienc. ed.

Neuville, D.R., Cormier, L., Massiot, D., 2006. Al coordination and speciation in calcium aluminosilicate glasses: Effects of composition determined by ^{27}Al MQ-MAS NMR and Raman spectroscopy. Chem. Geol. 229, 173–185. https://doi.org/10.1016/j.chemgeo.2006.01.019

Neuville, D.R., Cormier, L., Montouillout, V., Florian, P., Millot, F., Rifflet, J.C., Massiot, D., 2008a. Structure of Mg- and Mg/Ca aluminosilicate glasses:27Al NMR and Raman spectroscopy investigations. Am. Mineral. 93, 1721–1731. https://doi.org/10.2138/am.2008.2867

Neuville, D.R., Cormier, L., Montouillout, V., Florian, P., Millot, F., Rifflet, J.C., Massiot, D., 2008b. Structure of Mg- and Mg/Ca aluminosilicate glasses: ^{27}Al NMR and Raman spectroscopy investigations. Am. Mineral. 93, 1721–1731. https://doi.org/10.2138/am.2008.2867

Neuville, D.R., de Ligny, D., Henderson, G.S., 2014a. Advances in Raman Spectroscopy Applied to Earth and Material Sciences. Rev. Mineral. Geochemistry 78, 509–541. https://doi.org/10.2138/rmg.2013.78.13

Neuville, D.R., Hennet, L., Florian, P., De Ligny, D., 2014b. In situ High-Temperature Experiments. Rev. Mineral. Geochemistry 78, 779–800. https://doi.org/10.2138/rmg.2013.78.19

Neuville, D.R., Linard, Y., Richet, P., 1996. Rheology of iron aluminosilicate melts. Eos (Washington. DC). 77, F798.

Neuville, D.R., Mysen, B.O., 1996. Role of aluminium in the silicate network: In situ, high-temperature study of glasses and melts on the join SiO_2-$NaAlO_2$. Geochim. Cosmochim. Acta 60, 1727–1737. https://doi.org/10.1016/0016-7037(96)00049-X

Nogueira, T.A.R., Melo, W.J., Fonseca, I.M., Marcussi, S.A., Melo, G.M.P., Marques, M.O., 2010. Fractionation of Zn, Cd and Pb in a tropical soil after nine-year sewage sludge applications. Pedosphere 20, 545–556. https://doi.org/10.1016/S1002-0160(10)60044-6

Novikov, A.N., 2017. Structure and dynamics of aluminosilicate glasses and melts. Université d’Orléans.

Odegaard, H., Paulsrud, B., Karlsson, I., 2002. Wastewater sludge as a resource: Sludge disposal strategies and corresponding treatment technologies aimed at sustainable handling of wastewater sludge. Water Sci. Technol. 46, 295–303.

Okonu, N., Takahashi, S., 1997. Full scale application of manufacturing bricks from sewage sludge. Water Sci. Technol. 36, 243–250.

Oliva, J., Bernhardt, A., Reisinger, H., Domenig, M., Krammer, H.-J., 2009. Klärschlamm-Materialien zur Abfallwirtschaft. Klagenfurt.

Orsini, P., Buri, A., Marotta, A., 1974. Devitrification of Glasses in the Akermanite-Gehlenite System. J. Am. Ceram. Soc. 58, 306–311.

Park, Y.J., Heo, J., 2002. Conversion to glass-ceramics from glasses made by MSW incinerator fly ash for recycling. Ceram. Int. 28, 689–694. https://doi.org/10.1016/S0272-8842(02)00030-5

Park, Y.J., Moon, S.O., Heo, J., 2003. Crystalline phase control of glass ceramics obtained from sewage sludge fly ash. Ceram. Int. 29, 223–227. https://doi.org/10.1016/S0272-8842(02)00109-8

Pascual, M.J., Pascual, L., Duran, A., 2001. Determination of the viscosity-temperature curve for glasses on the basis of the fixed viscosity points determined by hot stage microscopy. Phys. Chem. Glas. 42, 61–66.

Pasquarello, A., Car, R., 1998. Identification of Raman Defect Lines as Signatures of Ring Structures in Vitreous Silica. Phys. Rev. Lett. 80, 5145–5147. https://doi.org/10.1103/PhysRevLett.80.5145

Pavluskin, N., 1986. Vitrokeramik. Grundlagen der Technologie.

Pavšič, P., Mladenovič, A., Mauko, A., Kramar, S., Dolenec, M., Vončina, E., Pavšič Vrtač, K., Bukovec, P., 2014. Sewage sludge/biomass ash based products for sustainable construction. J. Clean. Prod. 67, 117–124. https://doi.org/10.1016/j.jclepro.2013.12.034

Penel, G., Leroy, G., Rey, C., Sombret, B., Huvenne, J.P., Bres, E., 1997. Infrared and Raman microspectrometry study of fluor-fluor-hydroxy and hydroxy-apatite powders. J. Mater. Sci. Mater. Med. 8, 271–276. https://doi.org/10.1023/A:1018504126866

Peng, F., Liang, K., Hu, A., Shao, H., 2004. Nano-crystal glass-ceramics obtained by crystallization of vitrified coal fly ash. Fuel 83, 1973–1977. https://doi.org/10.1016/j.fuel.2004.04.008

Pérez, J.A., Terradas, R., Manent, R.M.M., Martínez, S., 1998. Sinterizzazione di scarti industriali in materiali ceramici. Ceramurgia 28, 11–14.

Pérez, J.A., Terradas, R., Manent, R.M.M., Martínez, S., 1996a. Valutazione degli scarti industriali come materie prime per composizioni di smalti ceramici. Ceramurgia 26, 353–356.

Pérez, J.A., Terradas, R., Seijas, M.M., Manent, R.M.M., Martínez, O., 1996b. Inertization of industrial wastes in ceramics materials. Ind. Ceram. 16, 7–11.

Perez, J., Terradas, R., Manent, R.M.M., Martinez, S., 1996. Inertisation of industrial wastes in ceramics materials. Ceramurgia 28, 11–13.

Pioro, L.S., Sadovskiy, B.F., Pioro, I.L., 2001. Research and development of a high-efficiency one-stage melting converter-burial-bunker method for vitrification of high-level radioactive wastes. Nucl. Eng. Des. 205, 133–144. https://doi.org/10.1016/S0029-5493(00)00349-6

Pokorna, E., Postelmans, N., Jenicek, P., Schreurs, S., Carleer, R., Yperman, J., 2009. Study of bio-oils and solids from flash pyrolysis of sewage sludges. Fuel 88, 1344–1350. https://doi.org/10.1016/j.fuel.2009.02.020

Qian, T., Jiang, H., 2014. Migration of Phosphorus in Sewage Sludge during Different Thermal Treatment Processes. Sustain. Chem. Eng. 2, 1411–1419.

Rawlings, R.D., Wu, J.P., Boccaccini, A.R., 2006. Glass-ceramics: Their production from wastes-A Review. J. Mater. Sci. 41, 733–761. https://doi.org/10.1007/s10853-006-6554-3

Rincon, J.M., 2016. Vitreous and ceramic processing for the recycling of industrial wastes. Key Eng. Mater. 663, 11–22.

Rincón, J.M., Capel, F., 1985. Microindentation behaviour KIC factor determination and microstructure analyses of some Li_2O-SiO_2 glass-ceramic materials. Ceram. Int. 11, 97–102.

Rodríguez-Carvajal, J., 1993. Recent advances in magnetic structure determination by neutron powder diffraction. Phys. B Condens. Matter 192, 55–69. https://doi.org/10.1016/0921-4526(93)90108-I

Roeder, P.L., Reynolds, I., 1991. Crystallization of chromite and chromium solubility in basaltic melts. J. Petrol. 32, 909–934. https://doi.org/10.1093/petrology/32.5.909

Roig, N., Sierra, J., Martí, E., Nadal, M., Schuhmacher, M., Domingo, J.L., 2012. Long-term amendment of Spanish soils with sewage sludge: Effects on soil functioning. Agric. Ecosyst. Environ. 158, 41–48. https://doi.org/10.1016/j.agee.2012.05.016

Romero, M., Rawlings, R.D., Rincón, J.M., 2000. Crystal nucleation and growth in glasses from inorganic wastes from urban incineration. J. Non. Cryst. Solids 271, 106–118. https://doi.org/10.1016/S0022-3093(00)00082-X

Romero, M., Rincón, J.M., 1997. Microstructural characterization of a goethite waste from zinc hydrometallurgical process. Mater. Lett. 31, 67–73. https://doi.org/10.1016/S0167-577X(96)00235-2

Romero, M., Rincón, J.M., Rawlings, R.D., Boccaccini, A.R., 2001. Use of vitrified urban incinerator waste as raw material for production of sintered glass-ceramics. Mater. Res. Bull. 36, 383–395. https://doi.org/10.1016/S0025-5408(01)00501-3

Rosenthal, A.B., Garofalini, S.H., 1987. Structural Role of Zinc Oxide in Silica and Soda-Silica Glasses. J. Am. Ceram. Soc. 70, 821–826. https://doi.org/10.1111/j.1151-2916.1987.tb05634.x

Rulkens, W., 2008. Sewage Sludge as a Biomass Resource for the Production of Energy : Overview and Assessment of the Various Options Sewage Sludge as a Biomass Resource for the Production of Energy : Overview and Assessment of the Various Options †. Energy & Fuels 22, 9–15. https://doi.org/10.1021/ef700267m

Ryerson, F.J., 1985. Oxide solution mechanisms in silicate melts: Systematic variations in the activity coefficient of SiO_2. Geochim. Cosmochim. Acta 49, 637–649. https://doi.org/10.1016/0016-7037(85)90159-0

Ryerson, F.J., Hess, P.C., 1980. The role of P_2O_5 in silicate melts. Geochim. Cosmochim. Acta 44, 611–624. https://doi.org/10.1016/0016-7037(80)90253-7

Ryerson, F.J., Hess, P.C., 1978. Implications of liquid-liquid distribution coefficients to mineral-liquid partitioning. Geochim. Cosmochim. Acta 42, 921–932. https://doi.org/10.1016/0016-7037(78)90103-5

Sánchez, M.E., Menéndez, J.A., Domínguez, A., Pis, J.J., Martínez, O., Calvo, L.F., Bernad, P.L., 2009. Effect of pyrolysis temperature on the composition of the oils obtained from sewage sludge. Biomass and Bioenergy 33, 933–940. https://doi.org/10.1016/j.biombioe.2009.02.002

Sano, A., Kanomata, M., Inoue, H., Sugiura, N., Xu, K.Q., Inamori, Y., 2012. Extraction of raw sewage sludge containing iron phosphate for phosphorus recovery. Chemosphere 89, 1243–1247. https://doi.org/10.1016/j.chemosphere.2012.07.043

Seifert, F.A., Mysen, B.O., Virgo, D., 1982. Three-dimensional network structure of quenched melts (glass) in the systems SiO_2-$NaAlO_2$, SiO_2-$CaAl_2O_4$and SiO_2-$MgAl_2O_4$. Am. Mineral. 67, 696–717.

Seleiman, M.F., Santanen, A., Stoddard, F.L., Mäkelä, P., 2012. Feedstock quality and growth of bioenergy crops fertilized with sewage sludge. Chemosphere 89, 1211–1217. https://doi.org/10.1016/j.chemosphere.2012.07.031

Shannon, B.Y.R.D., H, M., Baur, N.H., Gibbs, O.H., Eu, M., Cu, V., 1976. Revised Effective Ionic Radii and Systematic Studies of Interatomie Distances in Halides and Chaleogenides Central Research and Development Department , Experimental Station , E . L Du Pont de Nemours The effective ionic radii of Shannon & Prewitt [Acta .

Shebanova, O.N., Lazor, P., 2003. Raman study of magnetite (Fe_3O_4): Laser-induced thermal effects and oxidation. J. Raman Spectrosc. 34, 845–852. https://doi.org/10.1002/jrs.1056

Shelby, J.E., 2005. Introduction to Glass Science and Technology.

Shi, J., Feng, H., Ye, C., Hu, L., Xie, J., Yang, H., Liu, X., 2017. Preparation and characterization of $CaO \cdot Al_2O_3 \cdot SiO_2$ glass-ceramics from molybdenum tailings. Mater. Chem. Phys. 197, 57–64. https://doi.org/http://dx.doi.org/10.1016/j.matchemphys.2017.05.028

Siddique, R., Kaur, G., Rajor, A., 2010. Waste foundry sand and its leachate characteristics. Resour. Conserv. Recycl. 54, 1027–1036. https://doi.org/10.1016/j.resconrec.2010.04.006

Sigua, G.C., Adjei, M.B., Rechcigl, J.E., 2005. Cumulative and residual effects of repeated sewage sludge applications: forage productivity and soil quality implications in South Florida, USA. Environ. Sci. Pollut. Res. Int. 12, 80–88. https://doi.org/DOI 10.1065/espr2004.10.220

Singh, R.P., Agrawal, M., 2008. Potential benefits and risks of land application of sewage sludge. Waste Manag. 28, 347–358. https://doi.org/10.1016/j.wasman.2006.12.010

Smekal, A.G., 1951. On the structure of glass. J. Soc. Glas. Technol. 32, 392–395.

Sobiecka, E., Szymanski, L., 2013. Thermal plasma vitrification process as an effective technology for fly ash and chromium-rich sewage sludge utilization. J. Chem. Technol. Biotechnol. 89, 1115–1117. https://doi.org/10.1002/jctb.4221

Sułowska, J., Wacławska, I., Szumera, M., 2016. Comparative study of zinc addition effect on thermal properties of silicate and phosphate glasses. J. Therm. Anal. Calorim. 123, 1091–1098.

https://doi.org/10.1007/s10973-015-5044-8

Sun, K.H., 1947. FUNDAMENTAL CONDITION OF GLASS FORMATION *. J. Am. Ceram. Soc. 30, 277–281. https://doi.org/10.1111/j.1151-2916.1947.tb19654.x

Suzuki, S., Tanaka, M., Kaneko, T., 1997. Glass-ceramic from sewage sludge ash. J. Mater. Sci. 2, 1775–1779. https://doi.org/10.1023/a:1018584202392

Tao, J., Wu, S., Sun, L., Tan, X., Yu, S., Zhang, Z., 2012. Composition of Waste Slyudge from Municipal Wastewater Treatment Plant. Procedia Environ. Sci. 12, 964–971. https://doi.org/10.1016/j.proenv.2012.01.372

Tarragó, M., Esteves, H., Garcia-Valles, M., Martínez, S., Neuville, D.R., 2018. Effect of Ca in P-doped basaltic glass-ceramics: Application to waste inertization. Mater. Lett. 220, 266–268. https://doi.org/10.1016/j.matlet.2018.03.020

Tarrago, M., Garcia-Valles, M., Aly, M.H.H., Martínez, S., Martinez, S., 2017. Valorization of sludge from a wastewater treatment plant by glass-ceramic production. Ceram. Int. 43, 930–937. https://doi.org/10.1016/j.ceramint.2016.10.083

Teixeira, S.R., Magalhães, R.S., Arenales, A., Souza, A.E., Romero, M., Rincón, J.M., 2014. Valorization of sugarcane bagasse ash: Producing glass-ceramic materials. J. Environ. Manage. 134, 15–19. https://doi.org/10.1016/j.jenvman.2013.12.029

Tervahauta, T., Rani, S., Hernández Leal, L., Buisman, C.J.N., Zeeman, G., 2014. Black water sludge reuse in agriculture: Are heavy metals a problem? J. Hazard. Mater. 274, 229–236. https://doi.org/10.1016/j.jhazmat.2014.04.018

Tian, Y., Zuo, W., Chen, D., 2011. Crystallization evolution, microstructure and properties of sewage sludge-based glass-ceramics prepared by microwave heating. J. Hazard. Mater. 196, 370–379. https://doi.org/10.1016/j.jhazmat.2011.09.045

Toplis, M.J., Dingwell, D.B., 1996. The variable influence of P2O5 on the viscosity of melts of differing alkali/aluminium ratio: Implications for the structural role of phosphorus in silicate melts. Geochim. Cosmochim. Acta 60, 4107–4121. https://doi.org/10.1016/S0016-7037(96)00225-6

Toplis, M.J., Dingwell, D.B., Libourel, G., 1994a. The effect of phosphorus on the iron redox ratio, viscosity, and density of an evolved ferro-basalt. Contrib. to Mineral. Petrol. 117, 293–304. https://doi.org/10.1007/BF00310870

Toplis, M.J., Libourel, G., Carroll, M.R., 1994b. The role of phosphorus in crystallisation processes of basalt: An experimental study. Geochim. Cosmochim. Acta 58, 797–810. https://doi.org/10.1016/0016-7037(94)90506-1

Trauner, E.J., 1993. Sludge Ash Bricks Fired to above and below Ash-Vitrifying Temperature. J. Environ. Eng. 119. https://doi.org/https://doi.org/10.1061/(ASCE)0733-9372(1993)119:3(506)

Tunali, A., Ozel, E., Turan, S., 2015. Production and characterisation of granulated frit to achieve anorthite based glass-ceramic glaze. J. Eur. Ceram. Soc. 35, 1089–1095. https://doi.org/10.1016/j.jeurceramsoc.2014.09.039

Umari, P., Gonze, X., Pasquarello, A., 2003. Concentration of Small Ring Structures in Vitreous Silica from a First-Principles Analysis of the Raman Spectrum. Phys. Rev. Lett. 90, 4. https://doi.org/10.1103/PhysRevLett.90.027401

Varitis, S., Pavlidou, E., Kavouras, P., Vourlias, G., Chrissafis, K., Xenidis, a., Karakostas, T., 2015. Devitrification routes of a vitrified chromium-loaded ash. J. Therm. Anal. Calorim. 121, 203–208. https://doi.org/10.1007/s10973-015-4539-7

Vessal, B., Greaves, G.N., Marten, P.T., Chadwick, A. V, Mole, R., Houde-Walter, S., 1992. Cation microsegregation and ionic mobility in mixed alkali glasses. Nature 356, 504–506. https://doi.org/10.1038/356504a0

Vienna, J.D., 2010. Nuclear Waste Vitrification in the United States: Recent Developments and Future Options. Int. J. Appl. Glas. Sci. 1, 309–321. https://doi.org/10.1111/j.20411294.2010.00023.x

Villeneuve, N., Neuville, D.R., Boivin, P., Bachèlery, P., Richet, P., 2008. Magma crystallization and viscosity: A study of molten basalts from the Piton de la Fournaise volcano (La Réunion island). Chem. Geol. 256, 241–250. https://doi.org/10.1016/j.chemgeo.2008.06.039

Vogel, G., 1992. Glass Chemistry, 2nd ed. Springer, New York, USA.

Wang, A., Jolliff, B.L., Haskin, L. a, Et, W., Raman, a L., 1999. Raman spectroscopic characterization of a Martian SNC meteorite: Zagami. J. Geophys. Res. 104, 8509–8519.

Wang, X., Jin, Y., Wang, Z., Mahar, R.B., Nie, Y., 2008. A research on sintering characteristics and mechanisms of dried sewage sludge. J. Hazard. Mater. 160, 489–494. https://doi.org/10.1016/j.jhazmat.2008.03.054

Werner, W., 2012. Section 6. Fertilizers, in: Ulhmann's Encyclopedia of Chemistry. pp. 295–311.

Wiebusch, B., Ozaki, M., Watanabe, H., Seyfried, C.F., 1999. Assessment of leaching tests on construction material made of incinerator ash (sewage sludge): investigation in Japan and

Germany. Water Sci. Technol. 38, 195–205.

Wiebusch, B., Seyfried, C.F., 1997. Utilization of sewage sludge ashes in the brick and tilt industry. Water Sci. Technol. 36, 251–258.

Wojdyr, M., 2010. Fityk: A general-purpose peak fitting program. J. Appl. Crystallogr. 43, 1126–1128. https://doi.org/10.1107/S0021889810030499

World Health's Organization, 2001. Environmental Health Criteria 221: Zinc. Environ. Heal. Criteria. https://doi.org/10.1016/0043-1354(85)90052-1

World Health's Organization, 1998. Environmental Health Criteria 200: Copper.

World Health's Organization, 1991. Environmental Health Criteria 108: Nickel.

World Health's Organization, 1990. Environmental Health Criteria 107: Barium.

World Health's Organization, 1988. Environmental Health Criteria 61: Chromium.

Wyllie, P.J., Tuttle, O.F., 1964. Experimental investigation of silicate systems containing two volatile components. Part III. The effects of SO_3, P_2O_5, HCl, and Li_2O, in addition to H_2O, on the melting temperatures of albite and gran. Am. J. Sci. 262, 930–939.

Xu, X.J., Ray, C.S., Day, D.E., 1991. Nucleation and crystallization of Na_2O-2CaO-$3SiO_2$ glass by differential thermal analysis. J. Am. Ceram. Soc. 74, 909–914. https://doi.org/10.1111/j.1151-2916.1991.tb04321.x mirror libgen.asia torrent arcive mirror

Yadav, A.K., Singh, P., 2015. A review of the structures of oxide glasses by Raman spectroscopy. RSC Adv. 5, 67583–67609. https://doi.org/10.1039/C5RA13043C

Yue, Y.Z., 2008. Characteristic temperatures of enthalpy relaxation in glass. J. Non. Cryst. Solids 354, 1112–1118. https://doi.org/10.1016/j.jnoncrysol.2006.11.027

Zachariasen, W.H., 1932. The atomic arrangement in glass. J. Am. Chem. Soc. 54, 3841–3851. https://doi.org/10.1021/ja01349a006

Zanotto, E.D., Mauro, J.C., 2017. The glassy state of matter: Its definition and ultimate fate. J. Non. Cryst. Solids 471, 490–495. https://doi.org/10.1016/j.jnoncrysol.2017.05.019

Zhou, J., Li, T., Zhang, Q., Wang, Y., Shu, Z., 2013. Direct-utilization of sewage sludge to prepare split tiles. Ceram. Int. 39, 9179–9186. https://doi.org/10.1016/j.ceramint.2013.05.019